The effect of oblique entry into an automotive catalyst on the flow distribution within the monolith

Quadri, Syed

Award date:
2008

Awarding institution:
Coventry University

The effect of oblique entry into an automotive catalyst on the flow distribution within the monolith

By

Syed Saleem Quadri

February 2008

The work contained within this document has been submitted by the student in partial fulfilment of the requirement of their course and award

ABSTRACT

Automotive catalytic converters are increasingly used to reduce emissions from internal combustion engines to comply with emission regulations. Maldistributed flow across the catalyst affects its warm up, light off time, ageing, and conversion efficiency. This thesis concerns flow distribution in automotive catalytic converters and methods to improve CFD predictions.

Previous studies showed that modelling the monolith flow resistance using the Hagen-Poiseuille's formulation under predicted flow maldistribution. The predictions were improved by incorporating an additional pressure loss term $\frac{1}{2}\rho V^2$, where V is transverse velocity just upstream of a monolith channel, for oblique entry of the flow into the monolith known as the entrance effect. Further improvement was obtained by incorporating the critical angle of attack method. However, there was no experimental evidence to support these oblique entry loss formulations. There also remained the possibility that under prediction of flow maldistribution might be due to the failure to predict flow in the diffuser accurately.

A one-dimensional oblique angle flow rig was designed and built to measure the effect of oblique entry flow losses in monoliths. Experiments were performed at different angles of attack (α), using different lengths of substrate and a methodology was developed to obtain the oblique flow entrance losses. The results showed that the pressure loss attributed to the entrance effect increased with the angle of attack. The entrance effect was also found to be dependent on channel Reynolds number and substrate length. The theoretical assumption of $\frac{1}{2}\rho V^2$ predicts accurately at low Reynolds number but looses its validity at high Reynolds number. From the experimental studies, an improved correlation for the entrance effect has been derived as a function of major controlling variables, i.e., angle of attack, length of the substrates and Reynolds number.

A two-dimensional rig was designed to measure the flow field using PIV in a 2-D diffuser placed upstream of two different length substrates. The results showed that

the flow in a wide angle diffuser consisted of a central core, free shear layer and recirculation regions. The near-field region was found similar to that of a plane jet. The flow field was found to be independent of Reynolds number. Increasing the substrate length resulted in a flattening of the axial profiles close to the substrate face.

A CFD study was undertaken to predict maldistributed flow at the exit of the substrate for an axisymmetric catalyst model by incorporating the measured entrance effect correlation. A fixed critical angle of attack ($\alpha_{c,F}$) approach was used whereby the entrance effect is assumed constant for $\alpha > \alpha_{c,F}$. Incorporating the entrance effect with $\alpha_{c,F} = 81^0$ improved the prediction of maldistribution in the flow profiles.

A 2-D CFD study was undertaken to predict the flow distribution in the diffuser and downstream of the substrate. A comparison of the CFD predictions in the diffuser using different turbulence models showed that all the turbulence models used in this study over predicted the width of the central core region and the V2F turbulence model gave velocity predictions that compared best with PIV. Incorporating the entrance effect improved the predictions close to the diffuser-substrate interface and downstream of the substrate.

Acknowledgements

First and foremost, I would like to thank Professor S.F. Benjamin who is also my director of studies. His guidance, frequent discussions and sparkling ideas have given me great assistance throughout this project.

I also wish to thank Dr C. A. Roberts for her encouragement, advise and discussions throughout this project. She was always there to listen and advise throughout this project.

The technical support from Mr. K. Smith, Mr. C.Thorneycroft and Mr. R.Gartside is also acknowledged.

I am grateful to my parents for their love and encouragement throughout my study. Without their support, I would not have been able to complete this project. Finally, I would like to thank my fiancée for her encouragement and support.

Table of Contents

Chapter 3: Introduction to PIV

Chapter 7: Conclusions and Future Work

Nomenclature

Symbols

a	acceleration of the fluid, m/s^2
A	cross-sectional area of the channel, m^2
A_1	inlet area of the oblique angled duct, m^2
A_2	outlet area of the oblique angled duct, m^2
A_{inlet}	inlet area of the 2-D nozzle, m^2
A_{exit}	outlet area of the 2-D nozzle, m^2
AR	area ratio of the 2-D diffuser
b	aspect ratio of the 2-D diffuser and the 2-D nozzle, m
C_s	scattering cross-section, m^2
CR	contraction ratio of the 2-D nozzle, dimensionless
C_{pe}	static pressure coefficient at the point of maximum pressure in the nozzle, dimensionless
C_{pi}	static pressure coefficient at the point of minimum pressure in the nozzle, dimensionless
C_{pr}	static pressure recovery coefficient of the diffuser, dimensionless
d_{diff}	diffraction limited particle image diameter, μm
d_h	channel hydraulic diameter, m
d_p	particle diameter, μm
d_τ	particle image diameter, μm or pixels
f	friction Fanning factor for fully developed flow, dimensionless
$f^\#$	lens F-number (ratio of focal length to lens aperture diameter)
f_{app}	apparent friction Fanning factor, dimensionless
F_i	non-dimensional parameter used in nozzle design
F_e	non-dimensional parameter used in nozzle design
F_X	thrust force (N)
G_i	non-dimensional parameter used in nozzle design
G_e	non-dimensional parameter used in nozzle design
H_1	(inlet 2-D nozzle height)/2, m
H_2	(outlet 2-D nozzle height)/2, m
H_3	(inlet 2-D nozzle height), m
H_4	(outlet 2-D nozzle height), m
I_0	laser intensity incident on the particle W/m^2

K_i	porous medium permeability in STAR-CD, kg/s m^3
K(x)	additional pressure loss term for developing flow, dimensionless
$K(\infty)$	additional pressure loss term for developed flow, dimensionless
K_c	contraction pressure loss coefficient of the substrate, dimensionless
K_e	expansion pressure loss coefficient of the substrate, dimensionless
K_{Obl}	nondimensional pressure loss due to oblique entrance
$K_{Obl,\ theoretical}$	nondimensional theoretical pressure loss due to oblique entrance
m	contraction ratio (m=CR)
m	refractive index
$\dot{m}_1$	mass flow rate at inlet of oblique angled duct kg/s
$\dot{m}_2$	mass flow rate at the exit of the monolith in the oblique angled flow measurements, kg/s
M	magnification
N	number of image samples
L	length of the monolith, m
L_c	length of the 2-D nozzle contour, m
L_d	length of the 2-D diffuser, m
L_e	entrance length in the monolith channel, m
L_t	total length of the 2-D nozzle, m
P	perimeter of the channel, m
p_2	static pressure at the exit of the diffuser, Pa
p_1	static pressure at the inlet to the diffuser, Pa
P_{s1}	static pressure at point 1, Pa
P_{s2}	static pressure at point 2, Pa
P_{t1}	total pressure at point 1 upstream of the monolith, Pa
P_{t2}	total pressure at point 2 downstream of the monolith, Pa
P_M	pressure drop across the monolith due to fully developed flow + developing flow at the entrance of the substrate channels +entrance and exit losses+ oblique entrance losses, Pa
P_L	pressure drop due to fully developed flow + developing flow at the entrance of the channels +contraction and expansion losses, Pa
P_S	total scattered power, W
P_{Obl}	pressure drop due to oblique entrance (entrance effect), Pa

$P_{Obl,\ theoretical}$	theoretical pressure loss due to oblique entrance, Pa
ΔP	pressure drop across the monolith, Pa
$\Delta P_{contraction}$	static pressure drop due to contraction at the channel entrance, Pa
$\Delta P_{expansion}$	static pressure drop due to expansion at the channel entrance, Pa
ΔP^{*}	non-dimensional pressure drop in the monolith, dimensionless
∂P	pressure drop in the monolith, Pa
r_c	local longitudinal radius of curvature, m
Re	Reynolds number based on diffuser inlet height or radius, dimensionless
Re_c	channel Reynolds number, dimensionless
U_1	upstream velocity to the substrate channels in the oblique angled ducts, m/s
U_1	velocity at the inlet to diffuser, m/s
U_2	outlet velocity downstream of the substrate, m/s
$U_{2,\infty}$	velocity far downstream of the nozzle exit, m/s
u_2	flow non-uniformity in the 2-D nozzle, dimensionless
U_c	channel velocity is given by $\varepsilon.U_c$, m/s
U_f	centreline velocity along the nozzle, m/s
U_o	axial component of the oblique flow vector upstream of the substrate channel ($U_o=U_1 Cos\alpha$), m/s
U_g	Gravitational induced velocity, m/s
U_S	Velocity lag of a particle, m/s
U_f	fluid velocity, m/s
Up	particle velocity, m/s
Us	superficial velocity, m/s
$U_{s,i}$	superficial velocity in the direction i, m/s
V	transverse velocity component upstream of the monolith, m/s
V_c	transverse velocity component upstream of the monolith at the critical angle of attack, m/s
$V_{c,V}$	transverse velocity component upstream of the monolith at the critical angle of attack, m/s
$V_{c,F}$	transverse velocity component upstream of the monolith at the fixed critical angle of attack, m/s

V_w	wall velocity, m/s
W_1	inlet height of the diffuser, m
W_2	outlet height of the diffuser, m
x	axial distance along the nozzle contour
x_i	distance of wall velocity minimum from the nozzle inlet, m
x_e	distance of wall velocity maximum from the nozzle exit, m
x_m	location of match point from the start of the nozzle
X^+	dimensionless monolith length
X	channel length (m)
X_i	parameter indicating the contour shape ($X_i = x_m/Lc$)

Greek Symbols

α	angle of attack (degrees)
$\alpha_{c,B}$	critical angle of attack suggested by Betz,(degrees)
$\alpha_{c,V}$	critical angle of attack used by Liu (2003),(degrees)
$\alpha_{c,F}$	fixed critical angle of attack (degrees)
α_1	kinetic energy correction factors for inlet velocity U_1, non-dimensional
α_2	kinetic energy correction factors for exit velocity U_2, non-dimensional
α_i	permeability coefficients in the direction i
β	permeability coefficient in the flow direction
β_i	permeability coefficients in the direction i
ξ_i	three mutually perpendicular directions (i=1, 2, 3)
$\lvert\vec{v}\rvert$	superficial velocity magnitude m/s
μ	dynamic viscosity of the fluid, Pas
θ	half included diffuser angle, degrees,
ε	porosity of the substrate, dimensionless
ρ	density of air kg/m^3
ρ_p	particle density,kg/m^3
Δt	pulse separation time, μs
τ_s	Relaxation time of the particle, seconds

Subscripts

i	point of wall velocity minimum
e	point of wall velocity maximum
∞	far upstream and downstream
f	centreline
1	inlet Plane
2	exit Plane

Abbreviations

1-D	One-dimensional
2-D	Two-dimensional
3-D	Three-dimensional
AD	Axisymmetric decay region
Al_2O_3	Aluminium Oxide
CD	characteristic decay region
CeO_2	Ceria
CFD	Computational Fluid Dynamics
CO_2	Carbon-di-oxide
CO	Carbon monoxide
cpsi	Cells per square inch
EDH	Enhanced Diffuser Header
EGR	Exhaust Gas Recirculation
HC	hydrocarbon
HWA	Hot Wire Anemometry
LSV	Laser Speckle Velocimetry
LHS	Left Hand Side
MARS	Monotone Advection and Reconstruction Scheme
NOx	Oxides of nitrogen
O	Centre of Diffuser
Pb	Lead
PC	Potential Core Region

PIV	Particle Image Velocimetry
PTV	Particle Tracking Velocimetry
psi	Pounds per square inch
Rh	Rhodium
RHS	Right Hand Side
RNG	Renormalisation group
RM	Reference Mass
SFCD	Self-Filtered Central Differencing
SIMPLE	Semi-Implicit Method for Pressure-Linked Equations
SOx	Oxides of sulphur
SNR	Signal to noise ratio
TWC	Three Way Catalytic Converter
VFM	Viscous Flow Meter
YAG	Yttrium Aluminium Garnet

Chapter 1: Introduction and Literature Review

1. Introduction

Automotive catalytic converters are increasingly used to reduce emissions from internal combustion engines and comply with emission regulations. One important factor that determines catalyst performance is flow distribution in the monoliths. This thesis concerns flow distribution in automotive catalytic converters and methods to improve CFD predictions. In this Chapter, a brief overview of the sources of pollutant formation in internal combustion engines and the current emission regulations has been given. Also the factors affecting catalyst performance in particular the flow distribution, are described.

1.1 Sources of pollution in an engine and its composition

Automotive emissions are a major source of air pollution. The increase of the automotive population over the years has resulted in legislation to control their emission levels. The United States first introduced emission legislation for automobiles in 1966. This was later followed by Europe, Japan and Australia. Over the past two decades automotive emissions regulations have increasingly become more stringent in response to a rapid increase in the worldwide automotive population and amid growing environmental concerns.

The exhaust gas from internal combustion engines contains small concentrations of carbon monoxide (CO), hydrocarbons (HC's), oxides of nitrogen (NO_x), oxides of sulphur (SO_x) and particulate matter.

Hydrocarbon emissions are due to a number of sources. One of the sources is the fuel-air mixture trapped in the crevices which escapes the primary combustion process resulting in unburned hydrocarbons. A quenched layer containing unburned and partially burned fuel-air mixture left at the combustion chamber walls is also one of the sources. Another source is believed to be the absorbtion and desorbtion of fuel hydrocarbon components by the lubricating oil resulting in a fraction of the fuel escaping the primary combustion process (Heywood, 1998).

CO is formed due to the incomplete combustion of the fuel as there is insufficient oxygen to completely burn the carbon in the fuel to carbon dioxide. CO is also formed due to uneven mixture distribution within the cylinder.

Oxides of nitrogen (NO,NO_2,N_2O_2 etc) NO_x are formed at the high combustion temperature behind flames due to the chemical reaction involving nitrogen and oxygen molecules which do not attain chemical equilibrium.

Pb is an antiknock additive introduced in fuels. Pb poisons the noble metal (Pt-Rh) in the three way catalytic converter (Williamson et al., 1979). It is also harmful to the brain and nervous system. Legislation has been introduced to prohibit or limit the use of lead additive in fuels.

Particulate matter is more associated with combustion in diesel engines when compared to gasoline engines. It consists of fine particles of solid carbon (soot) on which some organic compounds have been absorbed. The particulate matter results from incomplete combustion of fuel hydrocarbons and lubricating oil. The soot is generated from the fuel molecules via their oxidation and/or pyrolysis products (Heywood, 1998).

Carbon dioxide is a product of perfect combustion. It does not directly affect human health but it is a greenhouse gas that traps the earth's heat and contributes to global warming.

1.2 Emission Legislation

Ever since its introduction emission legislation has become more stringent. The emission legislation in the European Union is specified in the Directive 70/220/EEC. This basis directive has been modified to EURO 1(1992), EURO 2 (1996), EURO 3 (2000), EURO 4 (2005, Current Legislation) and EURO 5 (proposed legislation due to be implemented from September 2009). Since EURO 2 there has been different legislation for gasoline and diesel cars. Diesel cars have more stringent CO standards but are permitted to emit higher levels of NO_x. Gasoline vehicles are exempted from

particulate matter standards in the EURO 4 stage but there is a limit for diesel cars. Table 1.2 gives the proposed limits under EURO 5 legislation. Compared to EURO 4 there has been a further reduction in NO_x and an 80% reduction in particulate matter for diesel cars has been proposed which makes the use of diesel particulate filter compulsory. Even gasoline cars also have a limit for particulate emission. Also the durability of aftertreatment systems has been increased from 80000 km to 160000 km or 5 years whichever is first. There has been no change in the limits for CO as compared to EURO 4. The CO_2 emission limits have been reduced to 140 g/km.

			Limit values									
		RM kg	CO mg/km		(HC) mg/km		NO_x mg/km		(HC+NO_x) mg/km		Particulates mg/km	
Category	Class		Petrol	Diesel	Petrol	Diesel	Petrol	Diesel	Petrol	Diesel	Petrol	Diesel
M	---	All	1000	500	75	---	60	200	---	250	5	5
N1	I	RM<1305	1000	500	75	---	60	200	---	250	5	5
	II	1305<RM-1760	1810	630	100	---	75	260	---	320	8	8
	III	1760<RM	2270	740	120	---	82	310	---	380	12	12

Table 1.1 EURO 5 Emission Legislation (3)

*M and N1 categories stand for passenger cars and light commercial vehicles respectively.

1.3 Three-Way Catalytic Converter

In the early 70's automotive companies were able to comply with the emission limits by changing the engine settings. The possible solutions were running with lean air-fuel ratios, exhaust gas recirculation (EGR) and stratified charge combustion. These measures were able to comply with one or more of the standards but there was not a method which would work for all the emissions.

This resulted in the development of aftertreatment systems in the exhaust stream. One of the most successful devices has been the catalytic converter. A typical catalytic

converter consists of a monolith encased in a metal casing. The substrate consists of large number of small parallel channels through which exhaust gas flows. It can be made of ceramic, usually cordierite, or metal. The washcoat is a porous metal oxide such as aluminium oxide (Al_2O_3) applied onto the substrate in liquid form. The noble metals such as platinum, palladium and rhodium are embedded in the washcoat. The main purpose of the noble metal is to increase of the rate of chemical reaction of the species at lower temperature. The main purpose of the washcoat is to provide a porous medium so that the noble metals are dispersed and to increase the catalyst activity by increasing the effective surface area and to provide thermal stability (Depcik et al., 2005).

Figure 1.1 Structure of TWC (Source from Umicore AG) (Auckenthaler, 2005)

When catalytic converters were first introduced they were designed to convert only HC and CO to carbon dioxide and water through exothermic oxidation reactions. Hence they were referred to as oxidation catalysts. There should be enough oxygen atoms present in order to oxidise CO and HC. Platinum was used as the noble metal to

oxidise the HC and CO. Many oxygen atoms in the exhaust are combined as NO_x and therefore are unaffected by oxidation reactions. The main drawback with oxidation catalysts is that the NO_x passes through the aftertreatment system without being treated. NO reduction can be achieved by running the engine under rich conditions which reduces the engine NO_x emissions and injecting additional secondary air to oxidise to HC's and CO or run the engine slightly lean. The rich condition results in a fuel consumption penalty and increase CO_2 emissions. The use of Rh as a noble metal resulted in reduction of NO_x and release of oxygen atoms which can be used to oxidise CO and HC's. Hence if the engine is run at or close to stoichiometric conditions then all the three harmful exhaust species can be significantly reduced. Such a catalyst is referred to as three way catalyst (TWC).

As emission legislation became increasingly stringent, automotive manufacturers sought to find ways to improve catalyst performance. Hence it became very important to understand the factors and parameters affecting catalyst performance. The areas of interest are cold start characteristics, steady state conversion efficiencies and component durability. Close coupled catalyst are placed closer to the exhaust manifold for quicker light off during cold start and transient cycles.

Three way catalysts operate effectively if the engine operates close to stoichiometric air-fuel ratio. Figure 1.2 shows the operating window for effective catalyst performance. This is achieved by the use of a lambda sensor placed in the exhaust system upstream or downstream of catalytic converter to measure the oxygen concentration in the exhaust flow and hence the A/F ratio. A feedback is sent to the engine management system to adjust the A/F ratio in order to ensure it runs in the operating window.

Figure 1.2: Conversion Efficiency of a Three-way catalytic converter as a function of air-fuel ratio (Depcik et al., 2005)

1.4 Investigative Approaches

Two approaches can be used to understand the factors influencing catalyst performance. One is the experimental approach and the other one is mathematical modelling. The experimental approach is time consuming and costly. It also requires having different rig setups to assess parameters. Also obtaining experimental data is sometimes difficult due to limited access. On the other hand a mathematical modelling approach is very desirable provided accurate predictions can be obtained. It provides cost effective solutions and detailed study of various factors influencing the catalyst performance can be studied. There are commercially available computational fluid dynamics codes (CFD) which can be used for predictions.

1.5 Factors affecting Catalyst Performance

Since the introduction of stringent emission regulations in 1970's, a substantial amount of research has been undertaken to investigate the factors affecting the performance of catalytic converters. The light-off behaviour, post-light-off conversion

efficiency and the flow field upstream of the catalyst are some of the important factors affecting catalyst performance. Below is a brief review of some of the major research areas, with particular emphasis on the importance of the flow field, the main subject of this PhD.

1.5.1 Substrate Materials and Geometry

Since its introduction considerable progress has been made in the design of the substrate structure and materials. Initially the cell density of square celled monoliths was 200 cells per square inch with a wall thickness of 12 milli inches. This has now been increased to 400/6 and 1200/2. The main factors taken into consideration in substrate design are the catalyst conversion efficiency, pressure drop, thermal durability and mechanical strength.

A study by Kaiser and Pelters (1991) showed that as cell density increased, the pressure drop also increased and that at lower cell densities light-off was more rapid but warmed up conversion efficiencies were low. Several studies (Umehara et al., 1997, Schmidtt et al., 1999 and Kikuchi et al., 1999) have been conducted with ceramic substrates on the benefits of higher cell densities and thin wall substrates. The benefits of higher cell densities and thin wall ceramics are an increase in geometric surface area, improved thermal shock resistance, faster light-off time, and lower pressure drop.

The choice of substrate material lies between metallic and ceramic. Metallic substrates have thinner walls and high cell densities when compared to ceramic substrates. They have low heat capacity and thermal mass resulting in faster light-off and improved resistance to high temperature ageing and are increasingly used as close-coupled catalysts closer to the engine. Metallic substrates are costly when compared to ceramic substrates. Ceramic substrates are commonly used as the substrate material as they are economical, readily available and have acceptable properties. They also have the advantage of lower thermal expansion compared to metallic ones. Commonly used ceramic substrates have square cross sectional shaped channels whist metallic substrates have channels of sinusoidal or triangle shape. Both ceramic and metallic substrates can have circular or elliptical cross section.

1.5.2 Washcoat Formulations and Noble metal

Considerable progress has also been made in the development of noble metal and washcoat formulations in order to improve catalyst performance. Pt and Pd are effective in oxidation of HC's and CO whereas Rh reduces the NO_x. Ceria (CeO_2) is usually added to the washcoat formulation to inhibit sintering but can also promote catalyst activity and improve oxygen storage. Several studies have been conducted in order to assess the effect of different loading of noble metals on catalyst performance.

Monroe et al (1987) experimentally studied the effect of Pt and Rh loading on three way automotive catalysts in engine exhausts. Rhodium containing catalysts had lower light off temperatures than catalysts with only Pt. Pt and Rh containing catalysts were more affected by Rh loading than Pt loading. Increasing the Rh loading resulted in faster light off and an increase in NO conversion efficiencies. Increasing the Pt loading resulted in an increase in CO conversion efficiencies.

1.5.3 Catalyst Light-Off

A catalyst is not fully effective when the temperature inside the catalyst is below approximately 250^{o} C for CO and 250^{O}C-340^{O} C for HC emission, also known as the light-off temperature (Burch et al., 1995). The light off temperature is referred to as the temperature at which the conversion efficiency of a catalyst is 50% (T50) or in some cases 80% (Martin et al., 1998). The time taken to reach the light-off temperature is known as light-off time. Hence a significant portion of emissions pass through the catalyst without being treated during cold start. Cold start emission problems can be reduced by moving the catalyst nearer to the engine as this will result in the catalyst being warmed up faster. Such catalysts are known as closed coupled catalysts.

1.5.4 Catalyst Ageing

In the proposed Euro 5 legislation, the durability of a catalytic converter has been increased from 80000 km to 160000 km. Degradation in catalyst performance can occur due to exhaust conditions over its lifetime; this is also known as ageing. The

two main mechanisms contributing to the ageing effect are catalyst poisoning and sintering. Catalyst poisoning is due to sulphur, zinc, calcium and phosphorous which are present in both engine oil and fuel (Martin et al., 1998). Sintering results in the reduction in the precious metal surface area within the channels of a catalyst and occurs at high temperatures.

1.5.5 Flow distribution and pressure drop

1.5.5.1 Flow distribution

Catalytic converters have to be fitted in a confined space in automotive exhaust systems. However there has to be enough catalyst volume in order to achieve the desired amount of conversion efficiency. Due to the packaging constraints, wide angle diffusers are often used upstream of the substrate. Previous research has shown that for diffusers with a total included angle greater than 11 degrees, flow separation occurs (ESDU, 76027). With wide angle diffusers, the flow separates at the inlet as the adverse pressure gradient which would arise should the flow stay attached, cannot be sustained. Hence typically for axisymmetric geometries, there is a non uniform flow entering the substrate with a high velocity and temperature at the centre of the substrate. This non uniform velocity upstream of the substrate has a detrimental effect on the conversion efficiency and durability of the substrates. Maldistributed flow affects catalyst warm up, light off time, ageing, deactivation, conversion efficiency and system pressure flow. It also results in large sections of the catalyst being poorly utilised. Hence a number of studies have been carried out to understand factors associated with flow maldistribution in catalytic converters.

Lemme et al., (1974) found that the non uniform flow upstream of the substrate reduces its durability, as some part of the substrate wears out faster than others. They also found that increasing the resistance of the substrate resulted in a flattening of the velocity profile.

Within the research group at Coventry University, Clarkson (1995) conducted experimental studies of flow distribution in axisymmetric catalytic converter systems on an isothermal steady flow rig. The flow distribution across the monolith was

investigated for various diffuser angles (10^0, 20^0, 30^0, and 80^0) and also for 180^0 expansions and at two Reynolds numbers. The velocity profiles at the exit, total pressure drop across the assembly and wall static pressure distribution were obtained from the tests. The results showed that the maldistribution increases with increasing Reynolds number and diffuser angle. The flow maldistribution decreased as the monolith brick length was increased.

Clarkson's (1995) work was continued by Haimad (1997) who studied experimentally the effect of inlet flow conditions on catalyst performance. A contracting nozzle was designed to provide uniform inlet flow at the entry to the diffuser. Comparisons were made on the effect of uniform inlet flow and fully developed flow at the inlet to diffuser on flow distribution across the monolith. The results showed that flow maldistribution was reduced with uniform inlet flow (Haimad 1997).

Wendland and Matthes (1986) conducted water flow visualization studies using a suspension of small opaque particles with flow illuminated by a light sheet. Photographs were then taken of the particle streaks. The results showed that the jet from the exhaust pipe separates at the diffuser entrance and results in a constant diameter jet at the centre surrounded by recirculating fluid. The flow separation was visible even with shallow diffuser angles (total included angle of 8^o). The constant diameter jet proceeds to about 20 mm from the substrate face and then expanded to cover the inlet face of the substrate.

Wendland et al., (1992) conducted a study with different Pt/Rh catalyst concentrations and different combinations of inlet and outlet headers. They used tapered and truncated inlet and outlet header configurations. The main aim of this study was to investigate the effect of inlet and outlet header configurations on catalyst performance. Truncating both inlet and outlet headers had little or no effect on catalyst performance. Offsetting the outlet pipe seemed to have no effect on catalyst performance.

Wollin (2001) investigated the effect of pulsating flow conditions on flow distribution using a mechanical pulse generator. The flow was pulsed at 16, 32, 64 and 100 Hz and velocity profiles at the substrate exit, pulse shapes in the centre of the inlet pipe

and at the exit and pressure drop were measured. The results showed that flow maldistribution was less sensitive to Re under pulsating flow conditions. As the frequency increased the flow became more uniform and the pressure drop decreased.

1.5.5.2 Pressure Drop

High exhaust back pressure has a detrimental effect on engine performance and a significant amount of it is due to the pressure loss in the catalytic converter. Engine performance is degraded by approximately 0.3 kW per kPa of backpressure (Pannone et al., 2001). Wendland et al., (1991) conducted an experimental study on the sources of pressure loss in catalytic converters. They showed that the total pressure loss is due to the pressure loss in the substrate and the losses in inlet and outlet headers. The total pressure loss in the substrate is due to:

- Hydrodynamic and thermal boundary layer developing in the entrance region
- Fully developed laminar boundary flow
- Contraction and expansion losses at the entry and exit of monolith channels

The fully developed laminar flow in the substrate channels was given by the Hagen-Poiseuille (H-P) equation. The H-P equation is based on a one-dimensional version of Darcy's equation and throughout this thesis, reference to Darcy's equation assumes the H-P formulation. The contraction and expansion losses are due to abrupt contraction at the entrance of a substrate channel and abrupt expansion at the channel exit. The developing flow in the entrance region is taken into account by a correlation by Shah (Shah, 1978).

An experimental study (Benjamin et al., 1996) was conducted to investigate the validity of Darcy's equation and the Shah correlation for monolithic brick resistance for 1D flows. The experimental results showed that Darcy's equation is fairly accurate at lower Reynolds number but does not accurately predict the pressure loss at high Reynolds number. This is due to the fact that pressure loss due to developing flow at the entrance of monolith is not taken into account by Darcy's equation. The correlation given by Shah (1978) was found to provide better prediction of pressure loss as it takes into account the developing flow and better predicts the pressure loss.

Ekstrom et al (2002) conducted an experimental study to measure the pressure drop along the monolith. The measurements were made for both room-air flow and hot-air flow. A highly turbulent flow was made incident on the substrate. A turbulent grid was installed to break large eddies and control turbulent length scale. The Hagen-Poiseuille equation was used in order to predict the pressure drop along the monolith. Higher pressure drop was found with the turbulence grid indicating that the turbulence can influence the monolith channel flow behaviour when the turbulent scales were small enough. They also found the need to have a better correlation for the pressure drop along the monolith as the Hagen-Poiseuille equation did not predict the pressure drop accurately.

Khiran et al., (2003) performed an experimental study on the pressure loss characteristics in catalytic converters. The results also showed that Shah's model best predicted the pressure drop along the substrate which was in agreement with a similar study conducted by Benjamin et al., (1996). The axial static pressure profile was measured through the channels of a 400 cells per square inch monolith. The results showed that the flow in the channels was laminar but the shape of profile was different from the expected laminar flow profile. The roughness inside the channel inner surfaces was thought to have an effect on the developed pressure profile. Static pressure measurements were taken upstream and downstream of the monolith and entrance and exit losses were calculated. The results showed that the loss coefficients had a combined laminar-turbulent behaviour. The experiments were more repeatable as the length of the substrate increased.

1.5.5.3 Flow Tailoring Devices

There have been various studies to investigate ways to improve the velocity distribution upstream. Most of the techniques used to improve the velocity uniformity aim to avoid separation in the diffuser and flatten velocity profiles.

Howitt et al., (1974) and Lemme et al., (1974) found that using flow tailoring devices improved the flow distribution upstream of the substrate but this resulted in an increase in pressure drop.

Shuai et al., (2001) used particle image velocimetry (PIV) to visualise the flow field upstream of an axisymmetric catalytic converter using two inlet cone configurations. The two inlet cone configurations were a standard 90^0 diffuser and an enhanced diffuser header (EDH) with a shallow angle of 12^0. The main function of enhanced diffuser header developed by Wendland et al., (1991) was to reduce pressure loss. The flow field was investigated at different Reynolds number. The flow visualisation using PIV showed that for the upstream part with a small cone angle of 12^0 there was almost no flow separation. When compared with a conventional 90^0 diffuser, the vortex in the EDH was smaller and weaker. The use of EDH resulted in an improved flow distribution upstream and reduced the pressure loss. CFD simulations were performed and compared well with the PIV measurements both upstream and downstream of the substrate. The pressure drop was modelled using Darcy's equation and the results showed a general agreement but an improved pressure drop model along the substrate was required to accurately predict flow maldistribution as reported by the authors.

Haimad (1997) studied the effect of using radial vanes in order to improve the flow distribution upstream of the catalyst. The results showed that using radial vanes improved the flow distribution but resulted in additional pressure drop.

Guojiang et al., (2005) conducted an experimental study to improve the flow distribution upstream of the monolith using a flow tailoring honeycomb spherical arc. The radius and the diameter of the openings of the spherical arc were varied and hot-wire anemometry measurements were made at the exit downstream of the substrate. The flow maldistribution was then compared for a substrate without the honeycomb arc. The results showed that the flow distribution was improved by installing a honeycomb spherical arc upstream of the monolith but it resulted in a higher pressure drop.

Wollin et al (1999) and Benjamin et al (2001, a) investigated the effect of using contoured ceramic substrates on the flow distributions under steady and pulsating conditions. The maximum velocity at the centre of the substrate was lower when compared to an equal volume standard substrate but there were secondary peaks

generated towards the walls. The flow distribution at pulsation frequencies of 16 and 32 Hz were similar to steady state cases but the flow distribution was more uniform at higher frequencies.

1.5.5.4 CFD Predictions

A monolith consists of thousand of channels and it requires a considerable amount of computational resources and time in order to predict the flow distribution in each channel. An alternate and a widely popular approach has been to use the equivalent continuum methodology wherein the resistance across the substrate is based on the Hagen-Poiseuille relationship. There have been a considerable number of numerical studies in order to predict catalyst performance. CFD studies by Lai et al., (1991) and Kim et al., (1992) showed the importance of uniform flow upstream of the substrate and the influence of the wide angled diffusers on flow uniformity. The results showed that smaller diffuser angles reduced both the pressure drop across the system and flow maldistribution. They also found that increased monolith resistance reduces flow maldistribution but increases pressure drop.

Kim et al., (1999) performed CFD simulations using a variable cell density method and improved the flow maldistribution and conversion efficiency. The brick resistance of the monolith is dependent on the channel velocity and channel diameter and the central core (about 35% of the total frontal area of the monolith) receives more than 50% of the flow resulting in higher velocity at the centre The periphery of the monolith (20% of the total frontal area) receives 5 to 10% of the flow resulting in lower velocity at the edges. A uniform velocity profile upstream of the monolith resulted in higher conversion efficiency. CFD simulations were performed by having a higher cell density at the centre and lower cell density at the edges. The higher cell density at the centre restricted the flow entering the channel and resulted in comparatively lower velocity. The lower cell density at the edges resulted in a comparatively higher velocity. As a result the non-uniformity in the velocity profile upstream of the substrate was reduced resulting in higher conversion efficiency. The pressure loss along the monolith was also reduced by about 7% to 15% when compared to a uniform density brick.

Guojiang et al., (2005) performed CFD simulations to study the effects of upstream flow distribution on the conversion efficiency. The pressure along the brick was modelled using Shah's equation. They also found that the conversion efficiency decreases as the non-uniformity upstream of the monolith increases.

Berkman et al (2002) conducted CFD simulations in order to assess the need for transient flow simulations for close-coupled and underbody converters. The transient simulations required more computational resources and time when compared to steady-state simulations. In order to perform transient simulations, accurate time-dependent boundary conditions were required. The mass flow rate and the temperature were made dependent on the crank angle. They found that the steady-state simulations were adequate for underbody converters since the gas pulsations were weaker. But for close coupled catalysts, the exhaust gas flow was a strong function of crank angle. Steady-state simulations were more suitable for the optimum design of the catalytic converters as it was much easier to analyse the parameters affecting converter efficiency. They also found that the most important factor affecting converter efficiency is the flow uniformity upstream of the monolith.

Much work has been undertaken at Coventry University to predict the flow maldistribution across the substrate. Clarkson (1995) used an equivalent continuum approach wherein the resistance across the substrate was based on the Hagen-Poiseuille relationship. Comparisons were made with experimental results under isothermal conditions in order to validate the model. Different turbulence and near-wall models and different differencing schemes available in STAR-CD were used to predict the flow distribution. The CFD predictions were better when a two layer near-wall approach with RNG-k-epsilon turbulence model and a second order differencing scheme was used. The CFD model under predicted the flow maldistribution across the monolith brick.

Clarkson's (1995) work was continued by Haimad (1997) and she based the resistance across the substrate on Shah' correlation. The CFD predictions showed that the flow maldistribution was flatter when compared with the predictions from Darcy's equation.

A numerical study by Benjamin et al (2001, b) investigated the effect of oblique entry flow into the monolith channels. They found that due to the use of wide angled diffusers there is flow separation at the throat accompanied by large recirculation regions in the diffusers. This results in parts of the flow entering the monolith channels obliquely. They surmised that this oblique entrance results in an additional pressure loss also known as the entrance effect. A theoretical study on flat plate heat exchangers by Kuchemann and Weber (1953) suggested that this oblique entrance results in an additional pressure loss of magnitude equal to $\frac{1}{2}\rho V^2$. Kuchemann and Weber's (1953) assumption of $\frac{1}{2}\rho V^2$ will be referred to as the "theoretical entrance effect" in this thesis. Wollin et al (2001) added this additional pressure loss to Darcy's equation. Having the additional pressure loss term due to oblique entrance considerably improved the predicted velocity profile and the peak velocities at the centre were close to the experimentally determined value. The predictions at high angles of attack corresponding to a region of ≈ 30 mm from the wall and also the flow distribution near the walls did not, however, compare well with the experimental results.

Liu (2003) used a critical angle ($\alpha_{c,V}$) approach where the oblique entrance loss was limited such that it could not exceed the pressure drop in the monolith. Without limiting the oblique entrance loss with this approach, the flow resistance at high angles of attack was very large. This resulted in very little flow entering the channels at these positions. The predictions improved considerably when the critical angle method was used.

1.6 Aims and Objectives

CFD studies by Clarkson (1995), Haimad (1997), Wollin (2001) and Liu (2003) have been performed using an equivalent continuum approach wherein the resistance across the substrate is based on the Hagen-Poiseuille relationship. Previous research from Haimad (1997) and Wollin (2001) showed that this approach under predicts the flow maldistribution. The prediction of flow distribution was improved by incorporating an additional pressure loss term for oblique entry of the flow on the

monolith channels. By using a critical angle of attack ($\alpha_{c,V}$) approach (Liu (2003)), the predictions improved considerably but the peak velocities at the centre were slightly underpredicted. Although the predictions were improved, there was no experimental justification for using $\frac{1}{2}\rho V^2$ and the critical angle of attack approach ($\alpha_{c,V}$). Indeed, it could be argued that underprediction of the flow maldistribution could in part be due to the inability of CFD to correctly predict the separation and flow field within the diffuser. The lack of non-intrusive measurements techniques has resulted in very little information on flows in diffusers under the influence of monoliths however the rapid development of Particle Image Velocimetry (PIV) has now made it possible to study this. This thesis aims to study the flow distribution in the diffuser using PIV and to experimentally determine oblique entry losses utilising a novel rig design. Measurements will then be compared with CFD predictions.

The aim of this thesis is to improve the prediction of flow maldistribution across monoliths.

The specific objectives are as follows:

- To investigate the effect of oblique entry flow at the front face of the substrate under isothermal conditions and to measure the additional pressure loss term using a specially designed rig.
- To visualise the flow field upstream of the substrate using Particle Image Velocimetry (PIV) and investigate the impact of flow separation and oblique entrance on the substrate channels using a two-dimensional flow rig.
- To compare CFD predictions in the diffuser region upstream of the monolith with whole field velocity vector data obtained from PIV and to investigate the accuracy of different turbulence models for various diffuser-monolith flow combinations.
- To improve the CFD methodology for predicting flow distribution under steady flow conditions by incorporating the additional pressure loss term due to the entrance effect deduced from the oblique entry experiments.

In order to realise these objectives, a one-dimensional oblique angle flow rig to perform the oblique angle flow measurements and a two-dimensional rig for the PIV were designed. CFD predictions were then compared with the measurements.

The one-dimensional oblique angle flow rig design and measurements are reported in Chapter 2. The basics of the PIV technique are described in Chapter 3. Chapter 4 describes the design and set-up of the two-dimensional flow rig for PIV and velocity measurements using hot-wire anemometry (HWA). PIV measurements for the flow in the diffuser in the presence of substrates are reported in Chapter 5. Steady CFD simulations of the flow in axisymmetric and 2-D catalyst models have been performed in Chapter 6. The axisymmetric predictions are compared with the velocity profiles at the exit of the substrate. The 2-D predictions are compared with the PIV measurements for flow in a diffuser upstream of the substrate and also with the flow maldistribution at the exit of the substrate using HWA. Conclusions derived from thesis and recommendations for future work are listed in Chapter 7.

Chapter 2: Oblique Angle Flow Measurements

2.1 Introduction

As discussed in Chapter 1, previous research (Clarkson (1995), Haimad (1997), Wollin (2001) and Liu (2003) has shown that the current CFD models under predict flow maldistribution. A possible explanation for this is that oblique entry pressure losses at the entrance to the monolith have not been accounted for. This phenomenon is due to the use of wide angled diffusers which cause flow separation at the throat of the diffuser accompanied by large recirculation regions. This results in a central jet upstream of the substrate which spreads out near the catalyst face causing the flow to impinge obliquely at the catalyst face away from the centre-line of the jet. To account for this, an extra-pressure loss based on theoretical assumptions, was introduced by Benjamin et.al (2001, b). Whilst this improved CFD predictions, some discrepancies were evident. This Chapter describes an experiment designed to quantify these losses which can then be incorporated as a formulation into the CFD code.

2.2 Pressure loss in the monolith

For uni-directional flow, Wendland et al. (1991) described the sources of pressure loss in monoliths as due to

- Hydrodynamic and thermal boundary layer development in the entrance region
- Fully developed laminar boundary flow
- Contraction and expansion losses at the entry and exit of monolith channels

2.2.1 Fully Developed Flow

The Reynolds number in a monolith channel is generally between 10 and 1000. Therefore the flow is laminar. Assuming that the flow is fully developed inside a channel, the pressure drop, resulting from viscous shear at the walls, is given by Darcy's Equation or the Hagen-Poiseuille Equation

$$\frac{\Delta P}{L} = -2f\,Re_c \frac{\mu U_c}{{d_h}^2} \qquad 2.1$$

where ΔP is the pressure drop across the monolith, L is the length of the monolith, Re_c is the channel Reynolds number, U_c is the channel velocity, f is Fanning friction factor for fully developed flow, μ is the dynamic viscosity of the fluid and d_h is the channel hydraulic diameter. The channel hydraulic diameter is given by

$$d_h = \frac{4A}{P} \qquad 2.2$$

where A is the cross sectional area of the channel and P corresponds to its perimeter.

2.2.2 Developing Laminar Flow

Darcy's Equation assumes that there is no developing flow at the entrance of the channel for unidirectional flow. As the fluid enters the channel the velocity profile is approximately uniform and a hydrodynamic boundary layer develops due to the viscous shear forces at the walls of the channel. This developing flow causes an additional pressure drop. The flow only becomes fully developed after a distance known as the entrance length L_e. This additional pressure drop is taken into account by a correlation by Shah (1978).

The total pressure drop due to developing and fully developed flow is given by

$$\Delta P^* = \frac{\Delta P}{\frac{1}{2}\rho U_c^2} = (f_{app}\,Re_c)(4X^+) \qquad 2.3$$

$$X^+ = \frac{X}{d_h\,Re_c} \qquad 2.4$$

where f_{app} is the apparent Fanning friction factor for the total pressure loss over the channel's length taking into account the developing flow and X is the channel length. Equation 2.3 can also be written as

$$\Delta P^* = (f\,Re_c)(4X^+) + K(X) \qquad 2.5$$

where K(X) represents the additional dimensionless pressure loss term for the developing flow. K(X) is zero at the channel entrance and increases to a constant

value K(∞) when the flow is fully developed. Shah (1978) gave a relation to predict the $f_{app}Re_c$ factor in ducts of arbitrary cross sections

$$f_{app}\,Re_c = \frac{3.44}{\sqrt{X^+}} + \frac{(f\,Re_c) + K(\infty)/(4X^+) - 3.44/\sqrt{X^+}}{1 + C(X^+)^{-2}} \qquad 2.6$$

For a circular cross section fRe_c=16, C=0.000212 and K(∞)=1.25 and for a square cross-section fRe_c=14.227, C=0.00029 and K(∞)=1.43.

2.2.3 Contraction and expansion losses at the entry and exit of monolith channels

The flow entering the channel experiences a contraction due to the change in cross sectional area. There is a static pressure drop $\Delta P_{contraction}$ which is due to

- 'Reversible pressure drop caused by the area change and the resulting flow acceleration' (Persoons, 2006).
- 'An irreversible pressure drop given by the entrance pressure loss coefficient K_c.' (Persoons, 2006).

$$\Delta P_{contraction} = (1-\varepsilon)\frac{\rho U_c^2}{2} + K_c\frac{\rho U_c^2}{2} \qquad 2.7$$

The first term represents the reversible pressure drop and the second term represents the irreversible pressure drop.

At the channel exit the flow expands resulting in a static pressure rise $\Delta P_{expansion}$ which is due to

- 'Reversible pressure rise caused by the flow deceleration' (Persoons, 2006)
- 'An irreversible pressure drop given by the exit pressure loss coefficient K_e.' (Persoons, 2006)

$$\Delta P_{expansion} = -(1-\varepsilon)\frac{\rho U_c^2}{2} + K_e\frac{\rho U_c^2}{2} \qquad 2.8$$

Hence the combined irreversible pressure drop due to contraction and expansion losses is given by $\frac{(K_c + K_e)\rho U_c^2}{2}$ where K_c and K_e are a function of area ratio ε.

A study by Wendland et al (1991) showed that the contribution of contraction and expansion channel losses are around 5% of the total pressure drop for a 400 cpsi monolith.

2.2.4 Entrance Effect

Due to the use of wide angled diffusers there is generally a constant diameter jet entering the diffuser which spreads out near the front face of the monolith. The flow thus impinges on the front face of the monolith at various angles of attack depending on the radial distance from the centre-line as shown in Fig. 2.1.

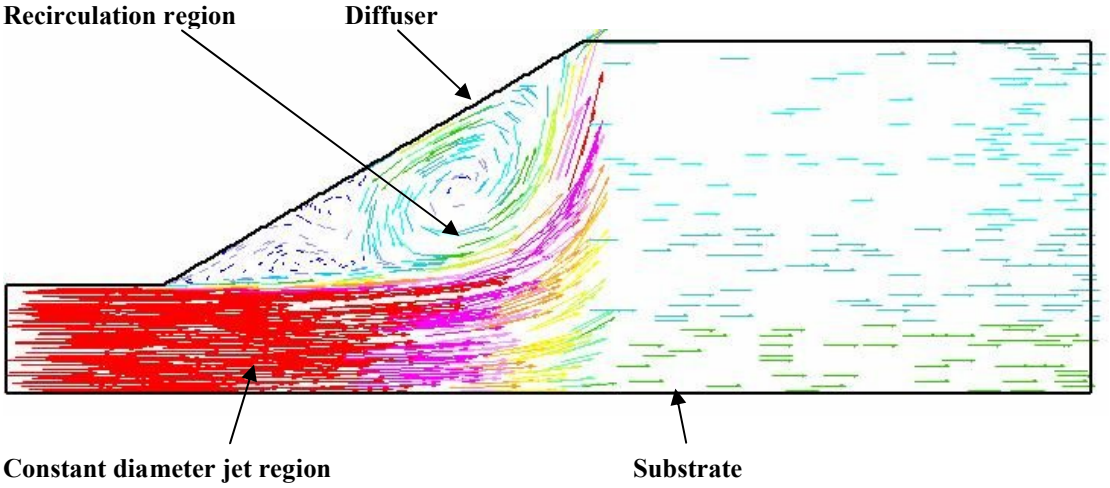

Figure 2.1: CFD predictions showing flow separation and recirculation region

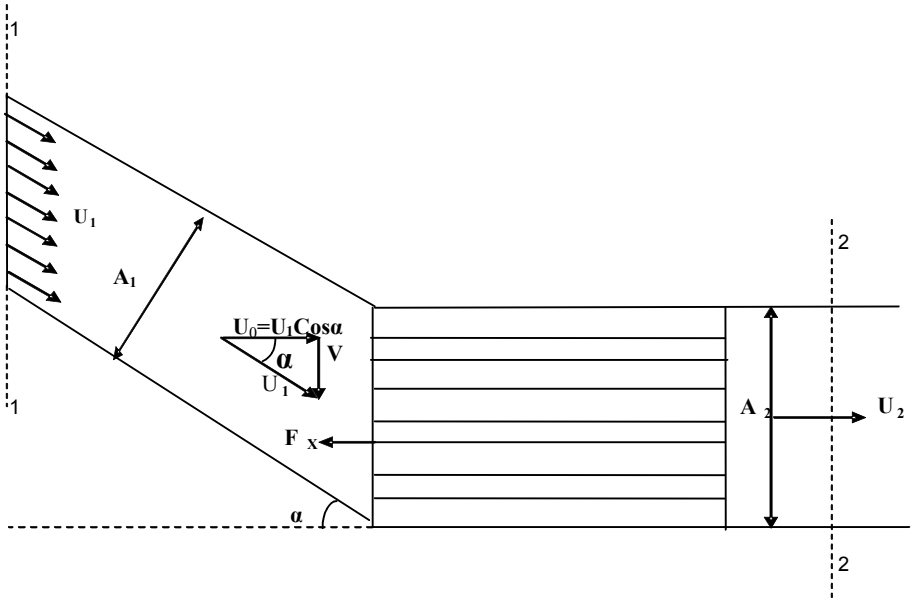

Figure 2.2: Oblique entry flow incident on a two-dimensional flat plate heat exchanger

Kuchemann and Weber (1953) studied the pressure loss formulation due to oblique entrance in the case of two-dimensional flat plate heat exchangers. Fig. 2.2 shows the geometry of the flow incident on a flat plate heat exchanger. The flow was analysed assuming that the flow through each element is the same and also assuming no friction losses. As the flow proceeds from an inlet duct area A_1 to a larger duct area A_2, the flow is retarded resulting in an increase in static pressure. This results in a thrust force (F_X) due to the suction pressures at the leading edge of the plates as the flow accelerates into the block. The magnitude of this thrust force per unit area is equal to $\frac{1}{2}\rho V^2$ where V is the transverse velocity component. The static pressure rise is equal to this thrust force (F_X) per unit area. Kuchemann and Weber (1953) argued that heat exchanger blocks are not aerodynamically streamlined bodies and hence the suction forces generated at the leading edges are not sustained due to the large adverse pressure gradients. This causes flow separation and pressure loss. The pressure loss, also known as entrance effect, is a function of angle of attack. Kuchemann and Weber (1953) proposed that with flow separation, F_X=0. Hence, pressure loss due to oblique entry $P_{Obl} = \frac{1}{2}\rho V^2$.

Kuchemann and Weber (1953) proposed two different approaches in order to formulate the pressure loss due to oblique entry. In the first approach the magnitude of additional pressure loss due to oblique entry was equal to $\frac{1}{2}\rho V^2$ irrespective of the angle of attack. The second approach is based on an assumption from Betz (Kuchemann and Weber, 1953). Betz assumed that there are no oblique entry losses if the static pressure rise in the inlet duct is less than the subsequent pressure drop in the block as long as no overall pressure increase is required. He assumed that up to a Betz critical angle of attack ($\alpha_{c,B}$) there are no oblique entry pressure losses. At the Betz critical angle, the pressure rise in the inlet duct is equal to the pressure drop in the block and above the Betz critical angle the oblique entry loss is given by [$\frac{1}{2}\rho V^2$- pressure drop in the block]. The analogy can be applied to monolith like structures assuming that the flow in the adjacent channels is identical (Benjamin (2001, b)). However, to date there has been no direct experimental evidence to support this.

2.2.5 Total Pressure Drop

The total pressure drop across the monolith can thus be described by:

$$\Delta P = \Delta P_{\text{fully developed}} + \Delta P_{\text{developing flow}} + \Delta P_{\text{contraction}} + \Delta P_{\text{expansion}} + P_{\text{oblique}} \qquad 2.9$$

Substituting the expressions from section 2.1.2 to 2.1.4 we have

$$\Delta P = ((f\,Re_c)(4X^+) + K(X))\frac{1}{2}\rho U_c^2 + (K_c + K_e)\frac{1}{2}\rho U_c^2 + \frac{1}{2}\rho V^2 \qquad 2.10$$

The above expression takes into account the contraction and expansion channel losses and assumes the losses due to oblique entrance are as proposed by Kuchemann and Weber (1953). It also assumes that there are no density changes throughout the system.

2.3 Methodology

The aim of this study was to quantify the pressure loss formulation due to oblique entrance. This required the development of a rig illustrated in Figs. 2.3 and 2.4. The contracting nozzle provides uniform flow into the monolith. The angle of attack was varied by placing ducts at various angles upstream of the monolith. Figs. 2.3 and 2.4 also illustrate the change in length and cross-section of the ducts (upstream pipes) as the angle of attack increases.

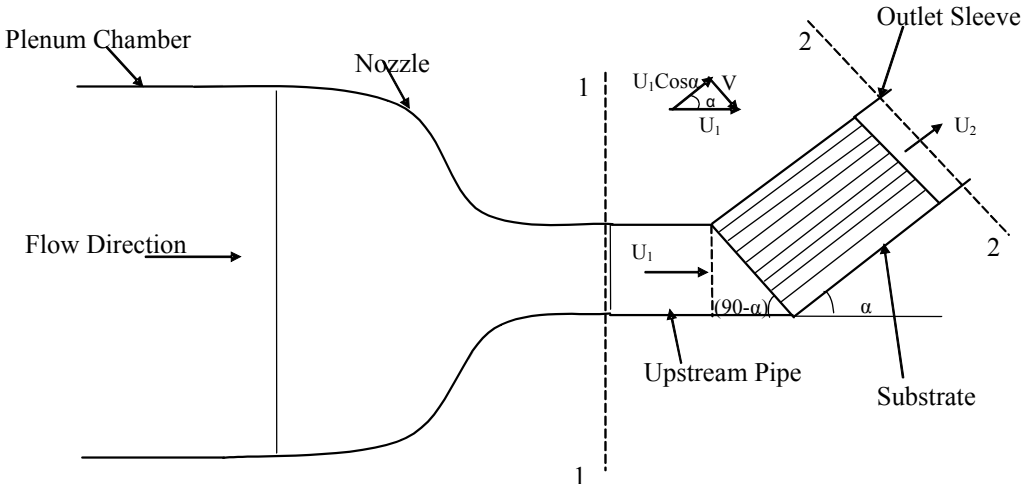

Figure 2.3: Schematic diagram of small angle of attack

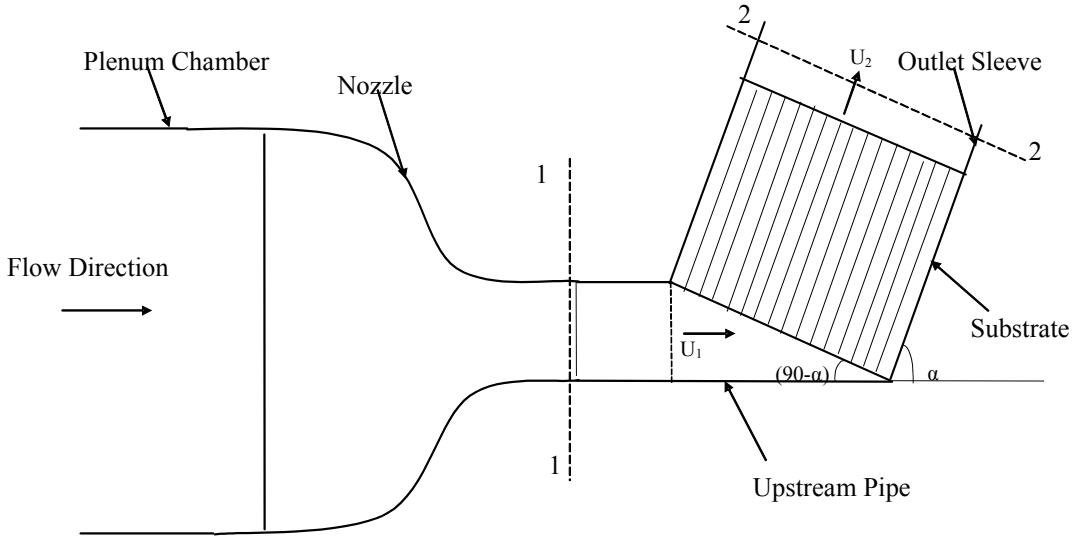

Figure 2.4: Schematic diagram of high angle of attack

Static pressure drop measurements were taken between points 1 and 2. Hence we have the total pressure drop across the system as

$$P_{t1}-P_{t2}-P_M=0 \qquad 2.11$$

where

P_{t1}=total pressure at point 1 upstream of the monolith

P_{t2}=total pressure at point 2 downstream of the monolith

P_M=Pressure drop across the monolith due to fully developed flow + developing flow at the entrance of the substrate channels +contraction and expansion losses at the entry and exit of monolith channels + oblique entrance losses

Equation 2.11 can be rewritten as

$$P_{t1}-P_{t2}-P_L-P_{Obl}=0 \qquad 2.12$$

where P_L= Pressure drop due to fully developed flow + developing flow at the entrance of the substrate channels + contraction and expansion losses at the entry and exit of monolith channels

P_{Obl}=Pressure drop due to oblique entrance

Now

$$P_{t1} = P_{s1} + \frac{1}{2}\rho\alpha_1 U_1^2 \qquad 2.13$$

$$P_{t1} = P_{s2} + \frac{1}{2}\rho\alpha_2 U_2^2 \qquad 2.14$$

where P_{s1} and P_{s2} are the static pressure at points 1 and 2 respectively measured using an Airflow Development inclined paraffin manometer. α_1 and α_2 are the kinetic energy correction factors at 1 and 2. Assuming the flow to be one-dimensional (see Sections 2.4.2 & 2.4.3), α_1 and α_2 are unity. U_1 and U_2 are the average velocities at 1 and 2. There are losses in the upstream pipe to the substrate. As the angle of attack increased the length of the upstream pipe also increased. This results in an additional pressure drop. This effect may be assumed to be small and thus ignored although it is implicitly accounted for within the measurement of (P_{s1}-P_{s2}).

Hence Equation 2.12 can be rewritten as

$$(P_{s1} - P_{s2}) + \frac{1}{2}\rho(U_1^2 - U_2^2) - P_L - P_{Obl} = 0 \qquad 2.15$$

The velocity downstream of the monolith U_2 was obtained from the conservation of mass equation.

$$\dot{m}_1 = \dot{m}_2$$

$$\rho A_1 U_1 = \rho A_2 U_2$$

$$U_2 = \frac{A_1 U_1}{A_2} \qquad 2.16$$

2.3.1 Zero Degree Angle of Attack

To evaluate P_L in Equation 2.15, measurements are needed at zero degree angle of attack. When the angle of attack is zero there is no oblique entrance loss and P_{Obl} is zero. Also the pressure drop across the monolith is a function of upstream or downstream velocity (Haimad, 1997).

Hence for zero degree angle of attack, Equation 2.15 becomes

$$P_L = (P_{s1} - P_{s2}) + \frac{1}{2}\rho(U_1^2 - U_2^2) \qquad 2.17$$

For zero degree angle of attack $A_1=A_2$, so $U_1=U_2$ and

$$P_L=P_{s1}-P_{s2}$$

2.3.2 Oblique angle of attack measurements

The pressure loss due to oblique entrance is thus obtained from Equation 2.15

$$P_{Obl} = (P_{s1} - P_{s2}) + \frac{1}{2}\rho(U_1^2 - U_2^2) - P_L \qquad 2.18$$

2.3.3 Non Dimensional Parameters

The oblique pressure loss, P_{Obl}, non-dimensionalised against the inlet dynamic pressure is given by

$$K_{Obl} = \frac{P_{Obl}}{\frac{1}{2}\rho U_1^2} \qquad 2.19$$

With the assumption that the magnitude of P_{Obl} is $\frac{1}{2}\rho V^2$ where V is the transverse velocity upstream of the substrate, then.

$$P_{Obl,\ theoretical} = \frac{1}{2}\rho V^2 \qquad 2.20$$

and the theoretical K_{Obl} can be defined as

$$K_{Obl,Theoretical} = \frac{\frac{1}{2}\rho V^2}{\frac{1}{2}\rho U_1^2} = Sin^2\alpha \qquad 2.21$$

2.4 Isothermal one-dimensional steady flow rig

This section describes the design of the rig in order to quantify P_{Obl}. The two different configurations used in this study are as shown in fig 2.5 and 2.6. Compressed air was supplied to the test rig from two receivers via a main valve (1). A pressure gauge monitored the pressure (2) and a pressure regulator reduced the pressure from ~100 psi to ~40 psi. A second pressure gauge monitored the pressure. A filter (5) was used to avoid oil contamination. The mass flow rate was controlled using a gate valve (6).

A viscous flow meter (VFM) (10) connected to digital micro manometer FC016 from Furness Controls was used to measure the mass flow rate through the system. A 50 mm flexible plastic pipe connected the VFM to a 12 litre cylindrical plenum (11). A pressure relief valve rated 0.5 bar was fitted at the back of the plenum. This was fitted into the plenum chamber by Wollin (2001) in order to protect the rig during pulsating flow experiments. The plenum contained a flow straightener in order to reduce the non uniformities and swirl in the flow. A contracting nozzle (12) with an outlet diameter of 55 mm was connected to the plenum to provide a uniform velocity profile. Previous studies had diffuser and monolith brick assemblies connected to the contracting nozzle.

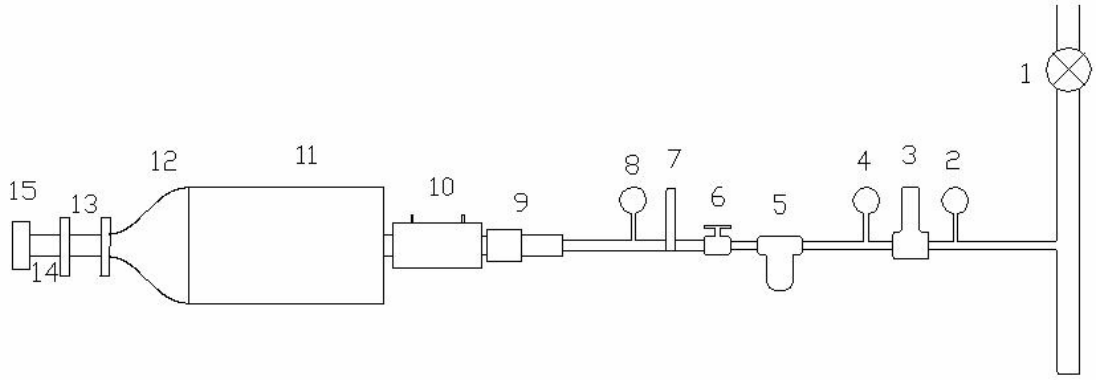

Figure 2.5: Zero degree angle of attack configuration

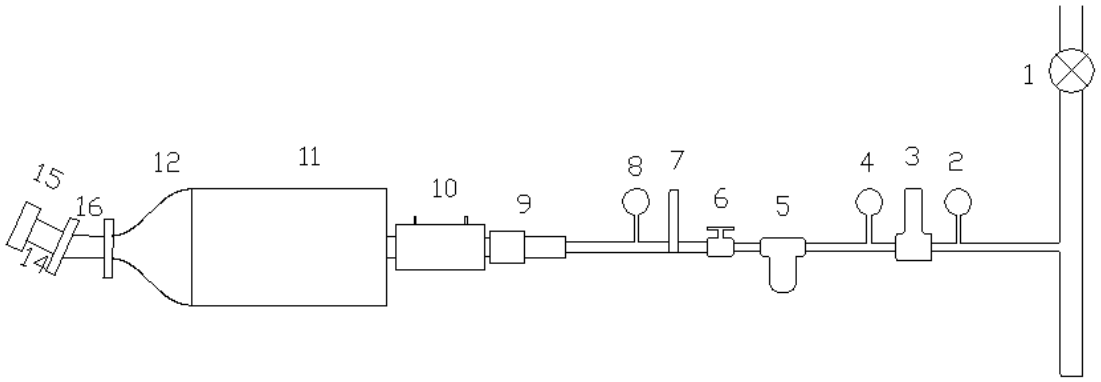

Figure 2.6: Oblique angle of attack configuration

1. Main Valve 2. Pressure Gauge 3. Pressure Regulator 4. Pressure Gauge 5. Filter 6. Gate Valve 7.Safety Relief Valve 8. Pressure Gauge 9. Flow Straightener 10. Viscous Flow Meter 11. Cylindrical Plenum 12. Axisymmetric Nozzle 13. Zero Degree Angled Duct 14. Monolith 15 Outlet Sleeve 16. Oblique Angled Duct with variable lengths for different angles of attack

In order to perform this study, it required a rig setup to perform zero degree angle of attack measurements (Fig. 2.5) and also measurements for different angle of attacks (Fig. 2.6). Ducts with 0^0,30^0,45^0,55^0,60^0,70^0,75^0 angles were connected to the contracting nozzle upstream of the monolith. Five different lengths of the substrates were used for this study. This was done to check the influence of length of the substrate on the entrance effect. Unwashcoated ceramic substrates from NGK with lengths of 17 mm, 27 mm, 40 mm and 100 mm, and a 69 mm length substrate from Johnson Matthey were used. All the substrates had a nominal cell density of 400 cpsi, hydraulic diameter of 1.12 mm and a porosity of 0.77.

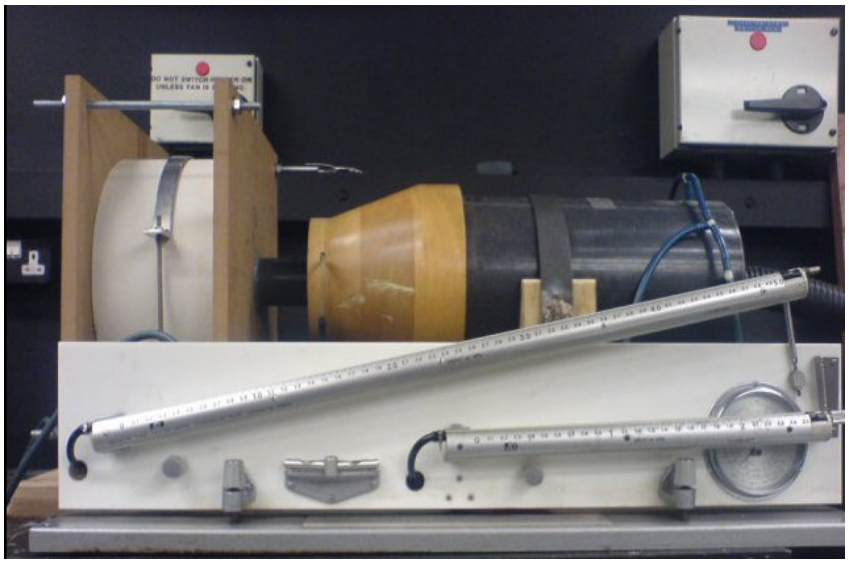

Figure 2.7: Setup for Zero degree angle of attack

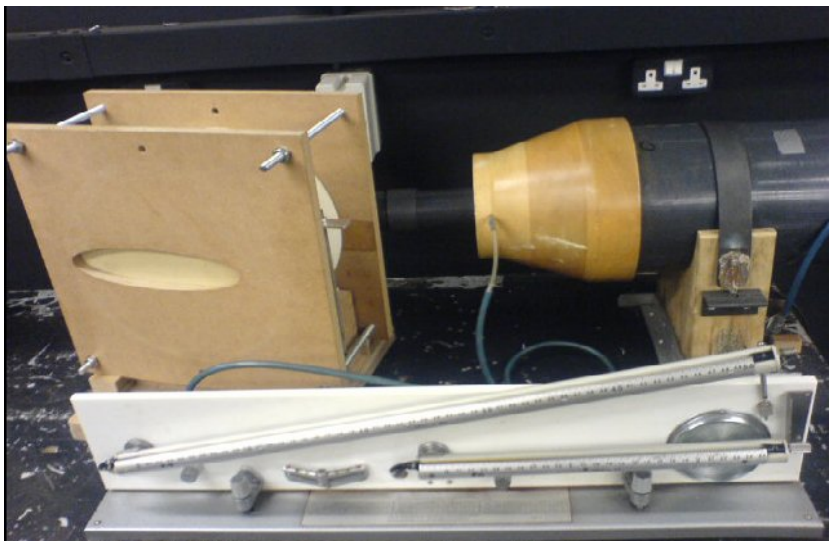

Figure 2.8: Setup for an oblique angle of attack (75^0)

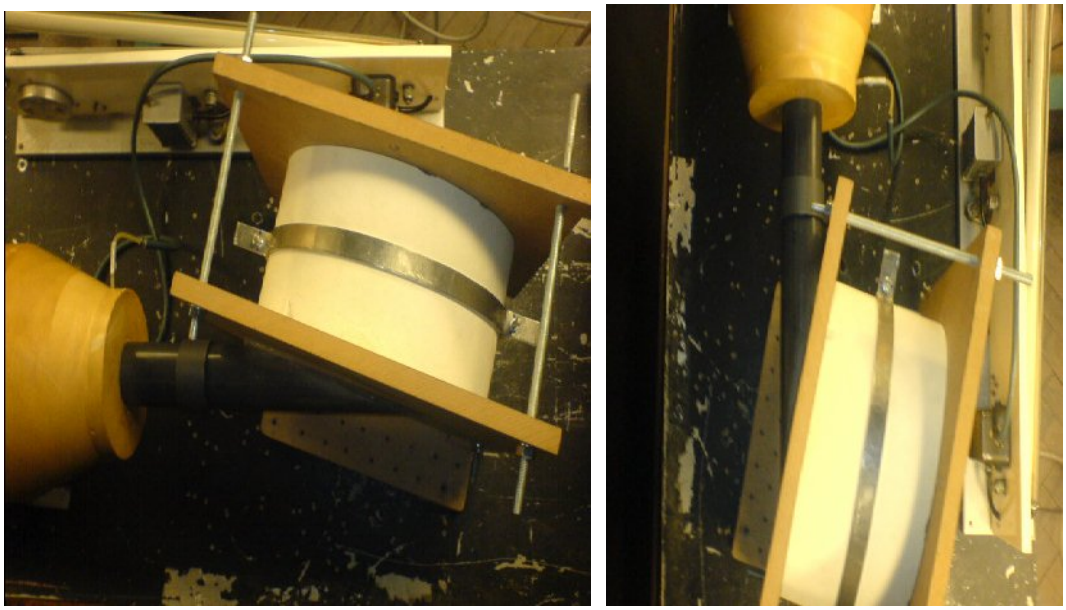

Figure 2.9: Setup of oblique angle of attack (75^0) (Top View)

Figure 2.10: Oblique angled duct (60^0) Front and Back View

Figs. 2.6-2.9 show the rig set-up for zero and oblique angle of attack configurations. Fig. 2.10 shows the oblique angled duct at 60^0 angle of attack showing the front and back view of the oblique angled duct. The back view cross-section shows that the oblique angled duct has an elliptical cross-section.

2.4.1 Instrumentation and data collection

The velocity profiles at the exit of nozzle and downstream of the substrate were measured using a TSI IFA 300 constant temperature hot-wire anemometry system (HWA). This measured the inlet velocity incident on the substrate channels. The probes used were 5µm platinum plated tungsten wire (Dantec 55 P11) and were

calibrated using a fully automatic TSI 1129 calibration rig. The static pressure drop measurements were obtained using an FC 016 Furness Controls digital manometer with a pressure range of 0-199.9 mm of water (0-1960 Pa) and an accuracy of ± 1% of the manometer reading. The static pressure drop measurements were also obtained using an Airflow Development paraffin inclined manometer. The inclined manometer had an accuracy of ± 1Pa for 0-500 Pa, ± 2 Pa for a pressure range of 0-1000 Pa and an accuracy of ± 10 Pa for the pressure range 0-5000 Pa depending upon the slope of the manometer. The digital manometer was more accurate at low pressures and the paraffin inclined manometer had a better accuracy at higher pressures. Hence for the pressure range between 0-2000 Pa, the FC 016 digital manometer was used and for a pressure range above 2000 Pa, the inclined manometer was used.

2.4.2 Calibration of the rig

The rig was calibrated by removing the monolith from Fig. 2.5 assembly and measuring the velocity profiles downstream of the nozzle. Velocity profiles at the exit of the nozzle along x and y axes were measured using a TSI HWA system and a 2-D traversing system at different mass flow rates by operating the gate valve. The x and y axes corresponds to the two mutually perpendicular horizontal and vertical directions across the nozzle exit. The velocity profiles (Figs. 2.11 and 2.12) showed that the flow is uniform along the x and y axes. Mass flow rate and average upstream velocity was calculated from the velocity profiles obtained from a Fortran script developed by Clarkson (1995) using the trapezium method. A best line fit was plotted which gives the pressure drop across the VFM correlated against velocity from the nozzle (Fig. 2.13).

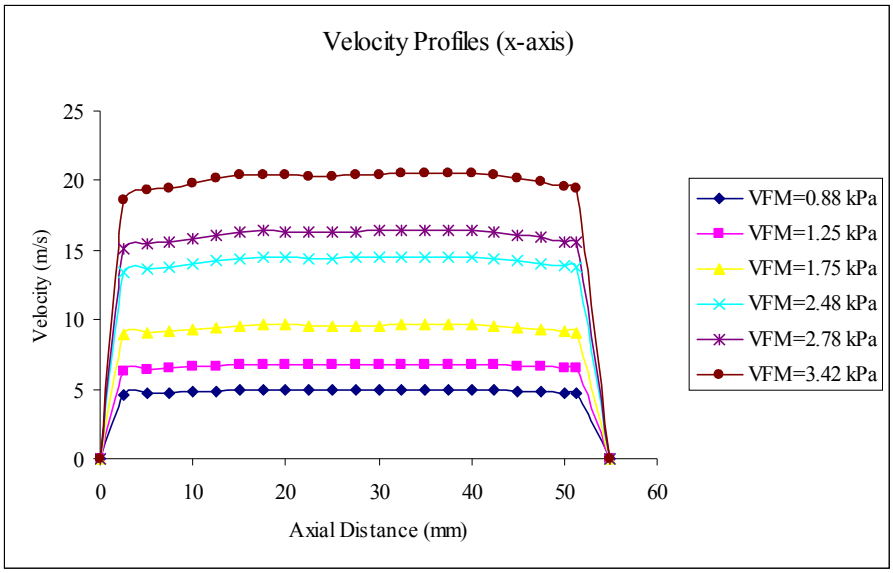

Figure 2.11: Nozzle Velocity Profiles along x-axis

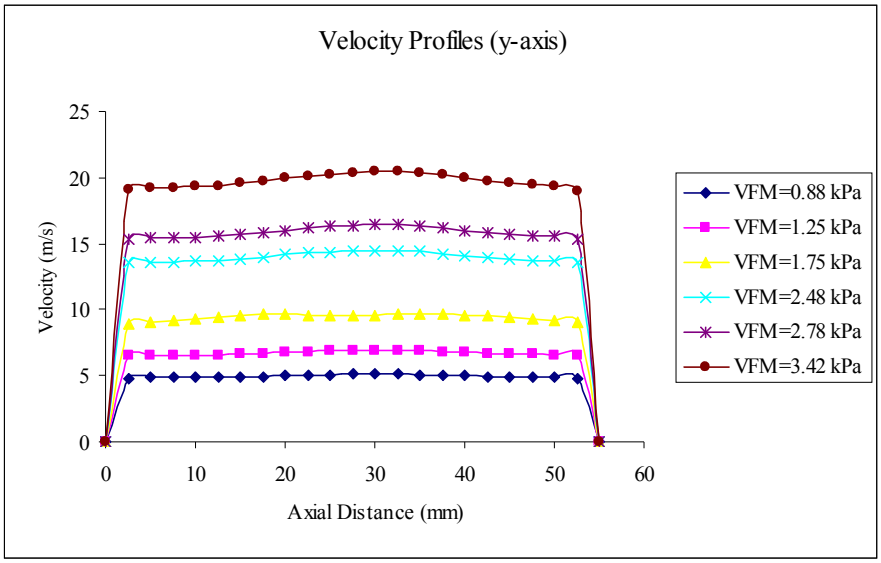

Figure 2.12: Nozzle velocity profiles along y-axis

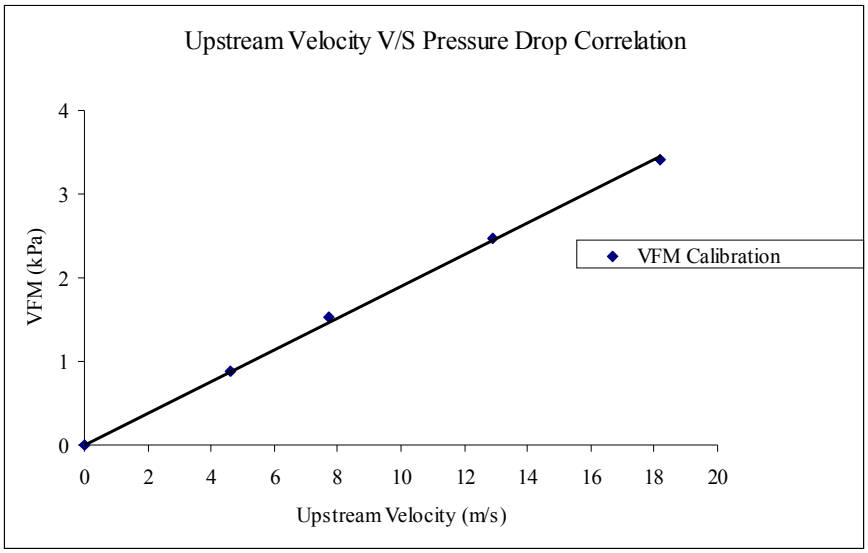

Figure 2.13: Upstream Velocity against pressure drop correlation for VFM

2.4.3 Hot-wire velocity profiles at the exit of oblique angled ducts

One of the assumptions in the methodology to measure entrance effect is that the flow velocity entering the substrate channels is uniform. The flow at the exit of the nozzle is uniform as seen from hot-wire profiles in Figs. 2.11 & 2.22. The effect of the oblique angled ducts on the flow entering the channels was checked. This was done by obtaining hot-wire velocity profiles downstream of the channels; the flow profiles at the exit will be uniform if the flow entering the channels is uniform.

Fig. 2.10 shows that the effect of using an oblique duct is an elliptical flow area. Since there is no change in the minor-axis of ellipse (y-axis) for all the angles of attack, the flow profiles are expected to be uniform. But the major-axis (x-axis) increases, as the angle of the oblique duct increases. Hot-wire velocity profiles were obtained along the major-axis of the oblique angled ducts for 27mm and 152 mm substrate lengths.

Figs. 2.14-2.19 show the velocity profiles along the major-axis of the oblique angled ducts for 27 mm and 152 mm substrate lengths. As the angle of attack increases, the major-axis of the ducts also increases and hence the x-axis in Figs. 2.14-2.19 is different for different angle of attacks. For the 27 mm substrate and 30^0 angle of attack, the flow profile is approximately uniform (Fig. 2.14). As the angle of attack increases there is skewness in the flow profiles (Figs. 2.15 & 2.16). There is more flow entering the duct on one side. This might be due to the fact that the flow has to travel further along the duct on one side and hence the associated boundary layer will be thicker. The skewness for the 75^0 angled ducts is higher than for 60^0 angled ducts. The skewness in the flow profile increases as the angle of oblique angled duct increases. The skewness also increases as the Reynolds number increases.

The effect of substrate length on the uniformity can be assessed by comparing the hot-wire profiles for 152 mm substrates with those for 27 mm. For 152 mm substrate, there is some skewness in the flow profiles even for 30^0 angled ducts (Fig. 2.17). This could be due to the effect of increased resistance of the brick on the flow. Increased skewness is also observed for 60^0 and 75^0 angled ducts (Figs. 2.18 & 2.19). Hence the skewness in the flow upstream of the channels increases as the length of the substrate increases.

Overall, the velocity profiles were considered to be acceptably flat. The research described in this thesis considered a maximum substrate length of 100 mm after these initial investigations so that the skewness would be expected to less than that observed for 152 mm substrate in Figs. 2.17-2.19.

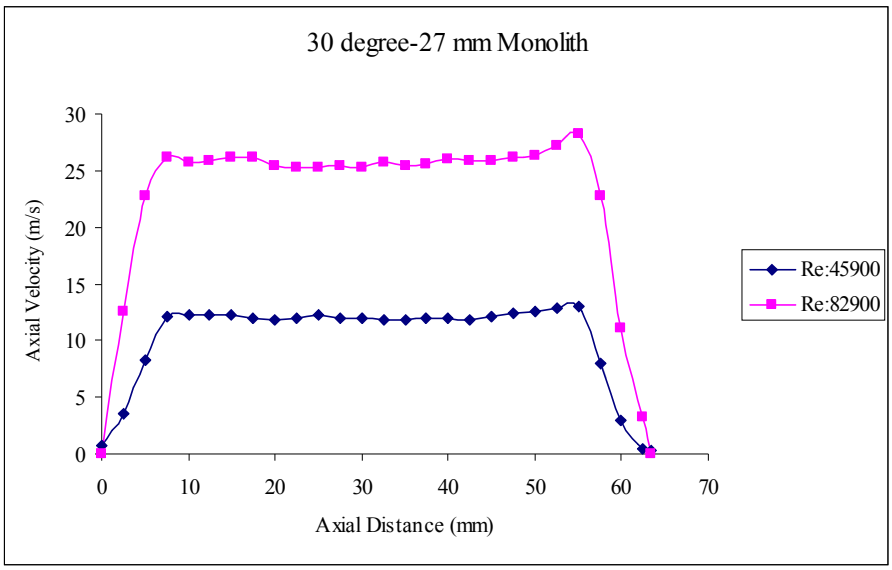

Figure 2.14: Hot-wire velocity profiles for 27 mm substrate at 30^0 angle of attack

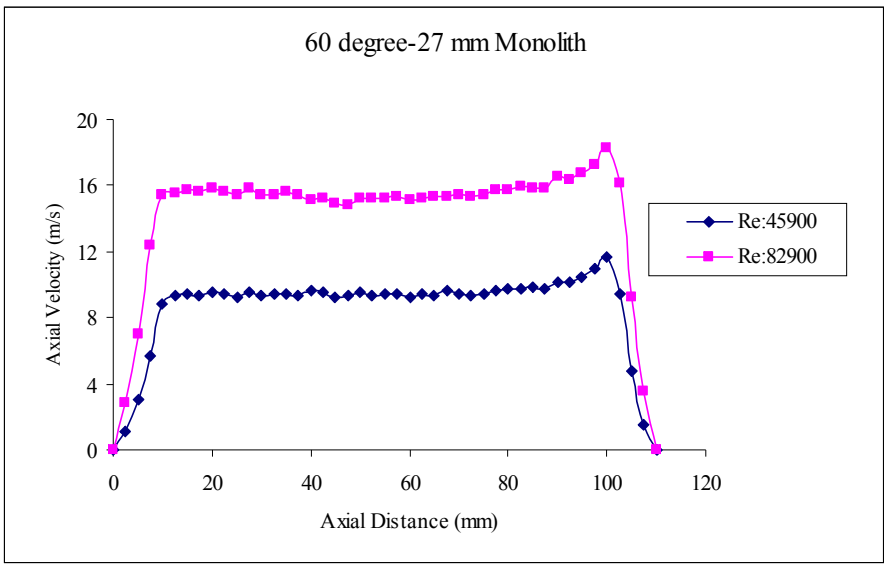

Figure 2.15: Hot-wire velocity profiles for 27 mm substrate at 60^0 angle of attack

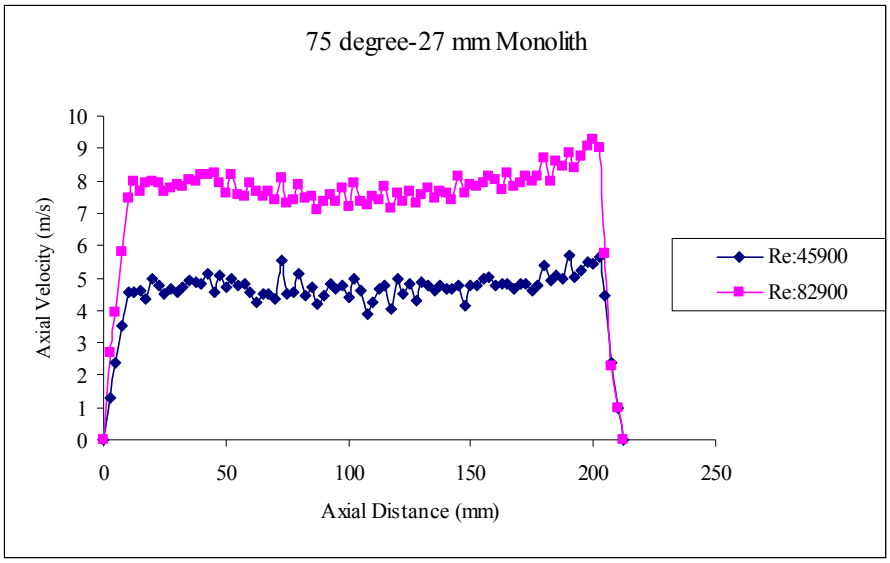

Figure 2.16: Hot-wire velocity profiles for 27 mm substrate at 75^0 angle of attack

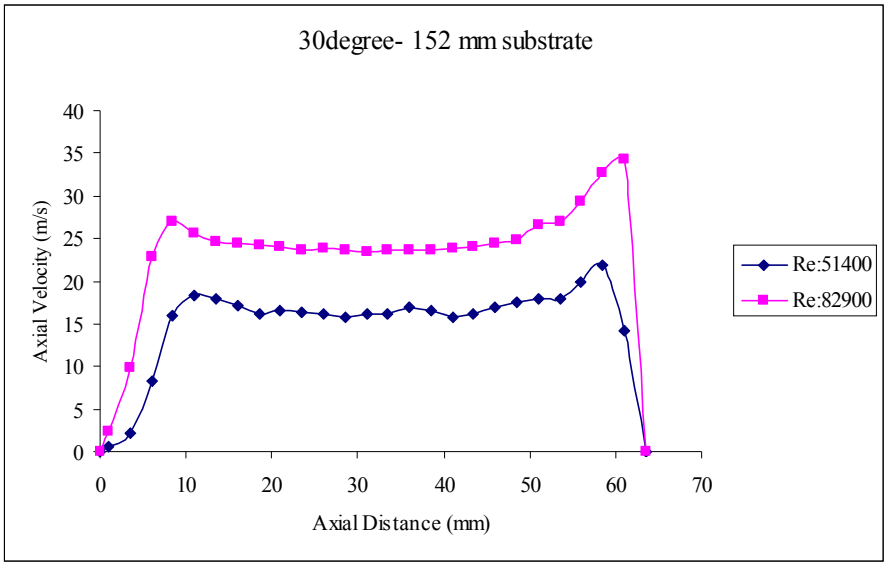

Figure 2.17: Hot-wire velocity profiles for 152 mm substrate at 30^0 angle of attack

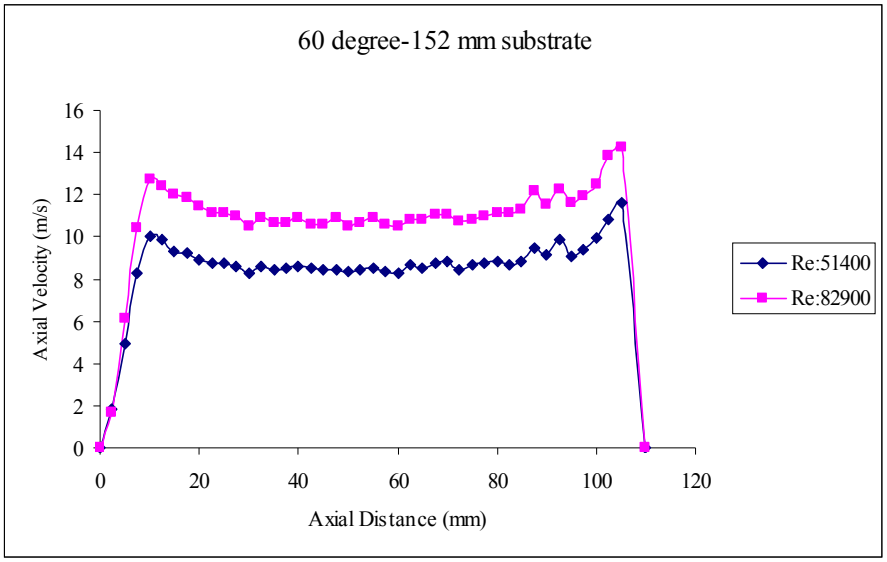

Figure 2.18: Hot-wire velocity profiles for 152 mm substrate at 60^0 angle of attack

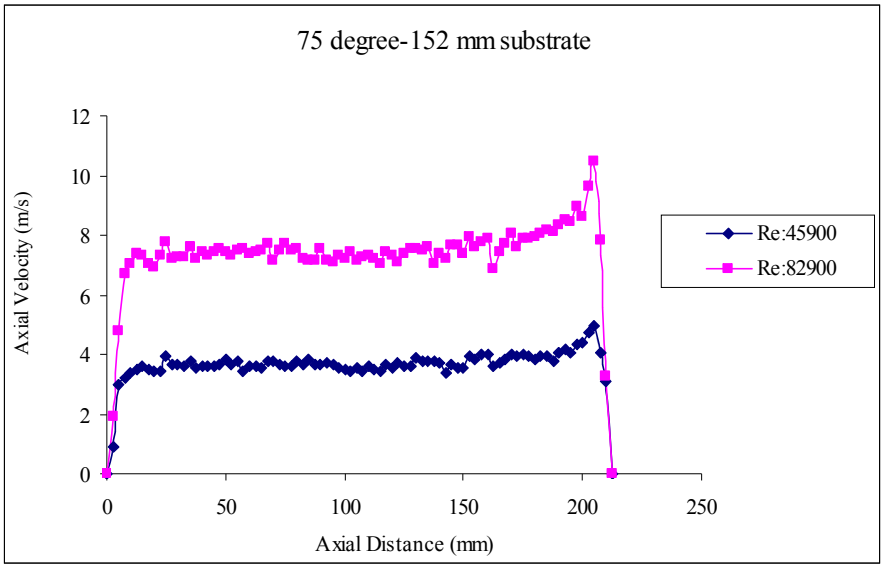

Figure 2.19: Hot-wire velocity profiles for 152 mm substrate at 75^0 angle of attack

2.5 Experimental Results

2.5.1 Zero Degree Angle of Attack

The experiments for zero degree angle of attack were performed for five different lengths of the substrate (17 mm, 27 mm, 40 mm, 69 mm and 100 mm). The mass flow rate was varied and the static pressure drop measurements over a range of Reynolds number were obtained. The experiment was also repeated in order to assess repeatability. The variations in static pressure drop measurements were less than 2%. The measurements were averaged out and a best fit curve, second order polynomial, was fitted to the averaged curve. The polynomial equation obtained gives the monolith pressure drop as a function of upstream or downstream velocity. This upstream or downstream velocity is equal to εU_c where U_c is the channel velocity. The polynomial equation forms the basis of further calculations during oblique angle of attack measurements. The measured pressure drop across the monolith was then compared with Darcy's Equation (H-P) and Shah's correlation (1978). As explained earlier, Darcy's Equation neglects the pressure drop due to developing flow. Shah's correlation takes into account the pressure drop due to developing flow but ignores the pressure drop due to contraction and expansion channel losses. Wendland et.al (1991) showed that the contribution of contraction and expansion losses is around 5% to the overall pressure drop.

In Figs. 2.20-2.24 monolith pressure drop P_L was plotted against the upstream velocity rather than the Reynolds number because the polynomial equation obtained will be used in oblique angle of attack measurements. Figs. 2.20-2.24 show that the monolith pressure drop P_L increases as the length of the substrate increases. For short substrates the flow is still developing when it exits the substrate channels. Hence the contribution of the developing boundary layer cannot be neglected. Darcy's Equation ignores the pressure drop due to developing flow and it looses its validity even at low velocities. As the length of the substrate increases, the predictions using Darcy's Equation are better at low velocities. At high channel velocities the pressure drop due to developing flow cannot be ignored. The entrance length for developing boundary layers increases as the channel velocity increases. For long length substrates (40 mm, 69 mm and 100 mm) the flow is fully developed when it exits the substrate channels at high channel velocities. Shah's correlation better predicts the pressure drop for long length substrates at high channel velocities. At high channel velocities predictions using Shah's correlation worsen as the length of the substrate decreases (17 mm & 27 mm), as the flow is still developing when it exits the substrate channels. The results are in good agreement with a similar study performed by Benjamin et al (1996).

Note that in Figs. 2.20-2.24, upstream velocity refers to U_1.

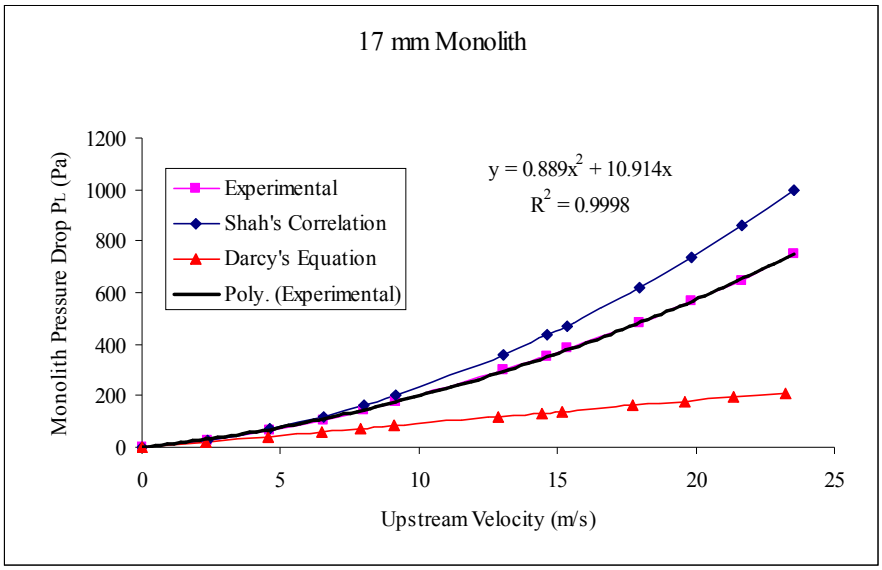

Figure 2.20: Monolith pressure drop for 17 mm monolith as a function of upstream velocity

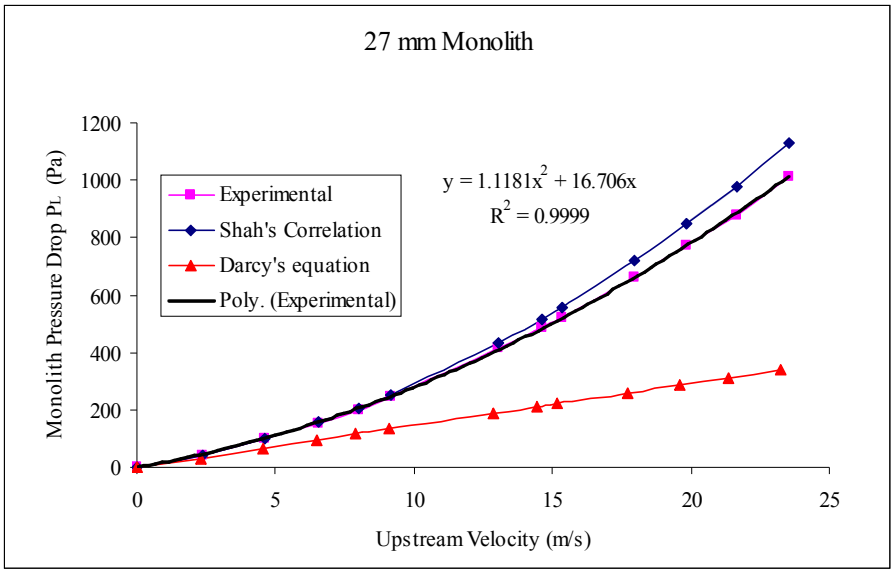

Figure 2.21: Monolith pressure drop for 27 mm monolith as a function of upstream velocity

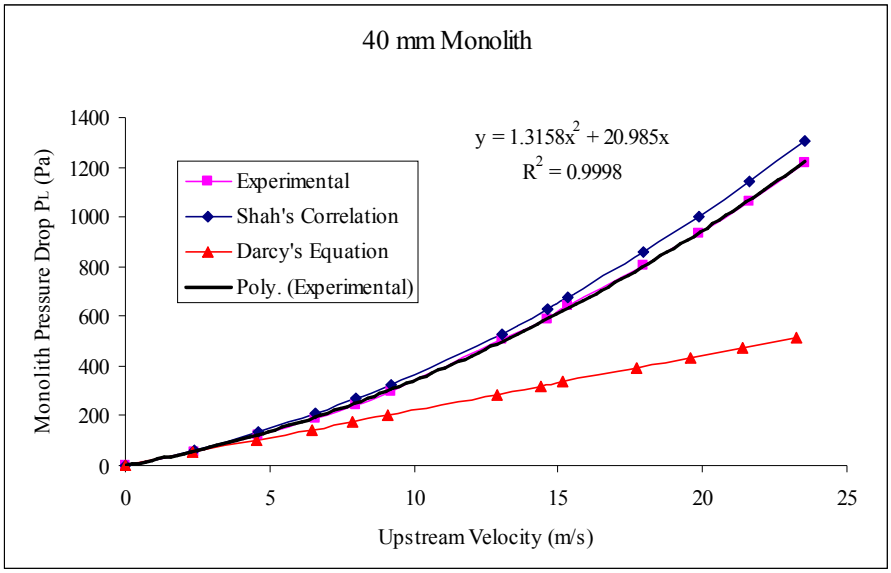

Figure 2.22: Monolith pressure drop for 40 mm monolith as a function of upstream velocity

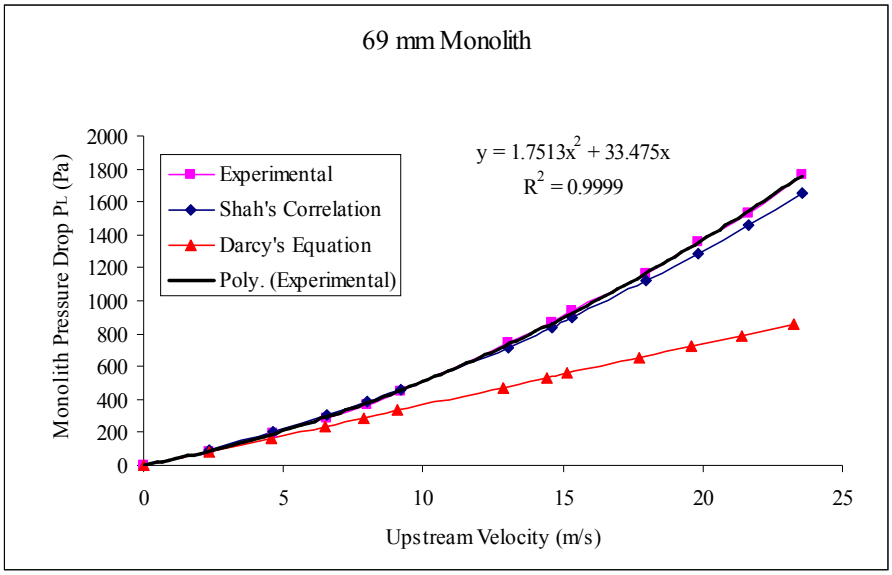

Figure 2.23: Monolith pressure drop for 69 mm monolith as a function of upstream velocity

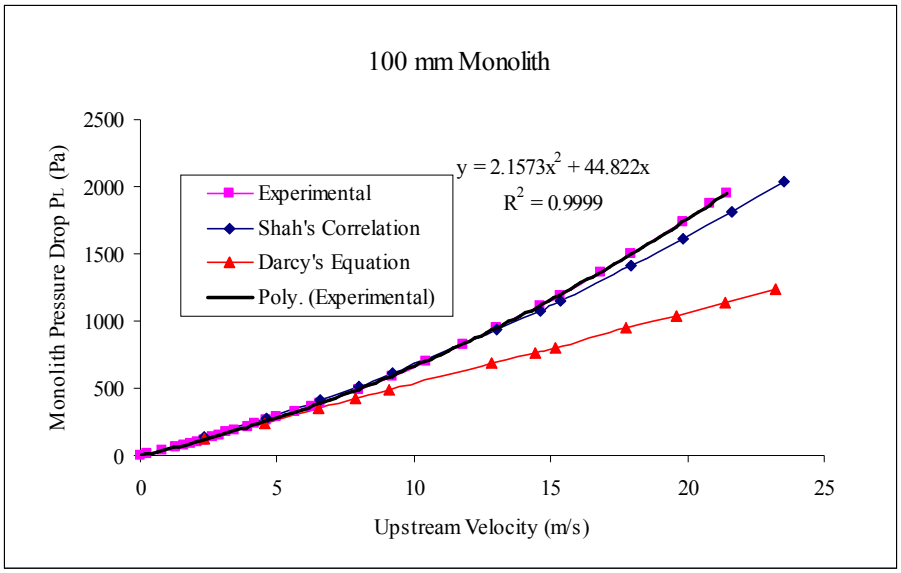

Figure 2.24: Monolith pressure drop for 100 mm monolith as a function of upstream velocity

2.5.2 Oblique angle of attack measurements

Once the zero degree angle of attack pressure drop measurements were obtained, experiments were performed for 30^0, 45^0, 55^0, 60^0,70^0 and 75^0 oblique angled duct configurations and for five different lengths of the substrates (17mm, 27 mm, 40 mm, 69 mm and 100 mm). The static pressure drop measurements were obtained over a range of Reynolds number. The pressure drop due to oblique entrance was calculated from Equation 2.18. The pressure drop attributable to the monolith P_L was obtained using the polynomial equations obtained from the zero degree angle of attack measurements. In the case of oblique angle flow measurements, the downstream velocity U_2 is equal to εU_c. Hence P_L is expressed as a function of U_2 to obtain P_{Obl} in Equation 2.18. As the angle of attack increases, the cross-sectional area of substrate on which the flow is incident also increases and the channel velocity in the substrate reduces for the same total flow rate. Hence the downstream velocity and the pressure drop due to the monolith also reduce as the angle of attack increases. The entrance effect was calculated for all angles of attack configurations. The results were also compared with the theoretical assumption that the magnitude of this pressure loss is $\frac{1}{2}\rho V^2$ where V is the transverse velocity upstream of the substrate.

2.5.2.1 Discussion

Figs. 2.25-2.30 show the pressure loss due to oblique entrance, P_{Obl}, for different angles of attack and different lengths of the substrate at various upstream velocities. At low angles of attack (30^0 &45^0), the flow undergoes a small change in direction when entering the substrate channels and hence the magnitude of the entrance effect is comparatively small and increases with the angle of attack and Reynolds number. This can be quite clearly observed from Figs. 2.31-2.35 in which the Reynolds number is based on the upstream velocity U_1 and the duct (inlet pipe) diameter. From Equation 2.18, the entrance effect is derived from the monolith pressure drop. As the angle of attack increases, the cross-sectional area of the monolith on which the flow is incident also increases. Hence for the same mass flow rate, the channel velocities in the substrate are higher for low angles of attack ducts (30^0 & 45^0) as compared to high angles of attack ducts. The monolith pressure drop (P_L) is thus higher for low angles of attack ducts. The magnitude of P_{Obl} (Figs. 2.25, 2.26) was less than zero at low flow rates and low angles of attack. This was due to errors in the measurement technique and the methodology followed to calculate P_{Obl}. A detailed error analysis is given in Section 2.6. Measurement errors were estimated and found to be high at low Reynolds number and small angles of attack (30^0 & 45^0) but were significantly reduced at high Reynolds number and high angles of attack around ±5% of entrance effect magnitude for 75^0 angle of attack at Re=82900. For short substrates (27 mm and 40 mm), the magnitude of P_L is smaller when compared to a 100 mm substrate. Hence the errors induced in P_{Obl} are small for shorter substrates.

The measured entrance effect was also compared with the theoretical assumption of $\frac{1}{2}\rho V^2$ given by Kuchemann and Weber (1953). The theoretical assumption of $\frac{1}{2}\rho V^2$ compared well for 17 mm substrate at all flow rates. However for the remaining substrates the theoretical assumption compared reasonably well at low flow rates (U_1<13 m/s) but seemed to loose validity at high flow rates (Figs. 2.25-2.30). The prediction using $\frac{1}{2}\rho V^2$ worsens at high flow rates (U_1>13 m/s) and also as the length of the substrate increases. The rate of increase in the magnitude of entrance

effect is considerable at high Reynolds number. This can be assumed to be due to the behaviour of eddies at the channel entrance and the associated pressure loss due to their formation at high Reynolds number. This effect can be observed from the Figs. 2.25-2.30. For example, the measured entrance effect is much higher when compared to $\frac{1}{2}\rho V^2$ for the 100 mm substrate at high flow rates (U_1>13 m/s) for all angles of attack.

In this study the experimental data is not compared with Betz's approach (Kuchemann and Weber (1953)) as it applies to heat exchangers which were designed so as to sustain the suction peaks at their leading edges. Thus the oblique entrance losses were neglected up to relatively high angles of attack. This is clearly not the case for catalyst monoliths as seen from the experimental data and so this approach is not appropriate.

Figs. 2.25-2.30 also show the effect of the substrate length. As the length of the substrate increases, the entrance effect also increases. This might be due to the fact that, as the length increases, the monolith pressure drop increases and as a result, the behaviour of eddies might change inside the channel entrance resulting in a higher pressure loss.

The rate of increase in the magnitude of the entrance effect decreased as the angle of attack increased (Figs. 2.31-2.35) as suggested by Equation 2.21. Fig. 2.36 shows the ratio of entrance effect to monolith pressure drop plotted against $\frac{1}{2}\rho V^2$. As seen in Fig. 2.36 the ratio is greater than 1 at high angles of attack (70^0 and 75^0).

Due to rig limitations, the oblique angle flow measurements could not be performed at very high angles of attack above 75^0 as this would have required a monolith with a larger diameter than is currently available. CFD simulations shown later were performed on an axisymmetric catalyst model incorporating the entrance effect by assuming that above a fixed critical angle, the entrance effect loss was constant. This is called the fixed critical angle of attack approach ($\alpha_{c,F}$). This will be discussed in detail in Chapter 6.

.

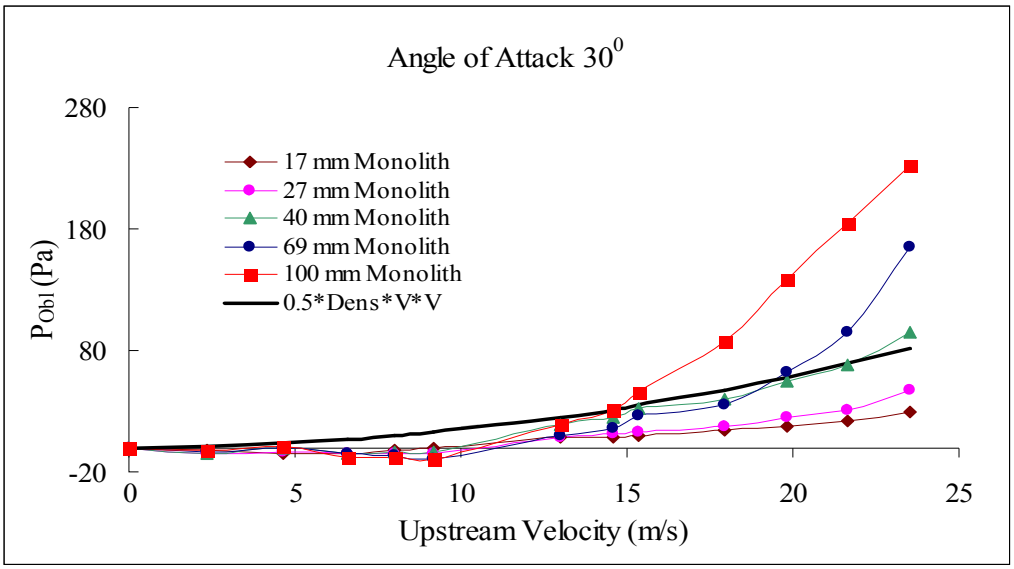

Figure 2.25: P_{Obl} charts for 30^0 angle of attack (Upstream Velocity≡U_1)

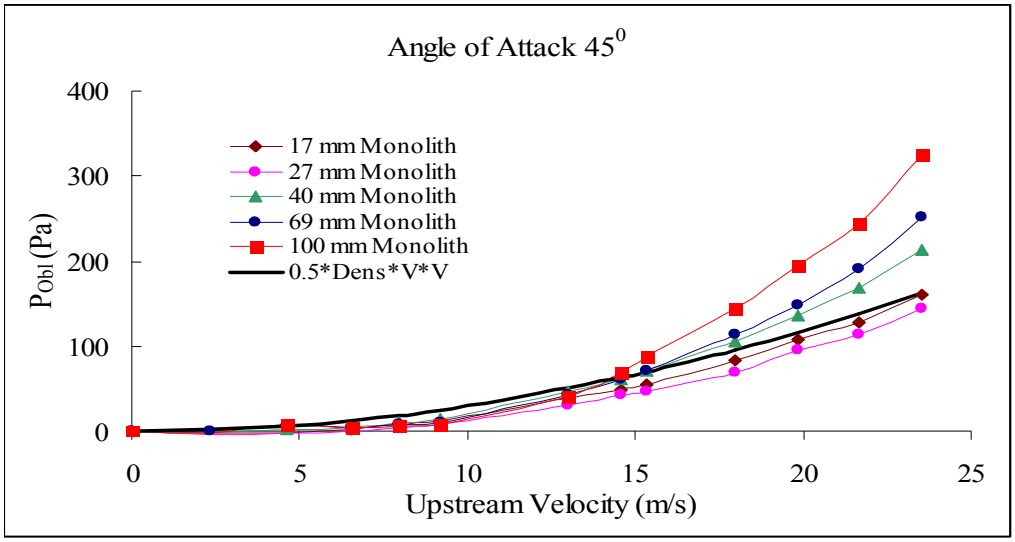

Figure 2.26: P_{Obl} charts for 45^0 angle of attack (Upstream Velocity≡U_1)

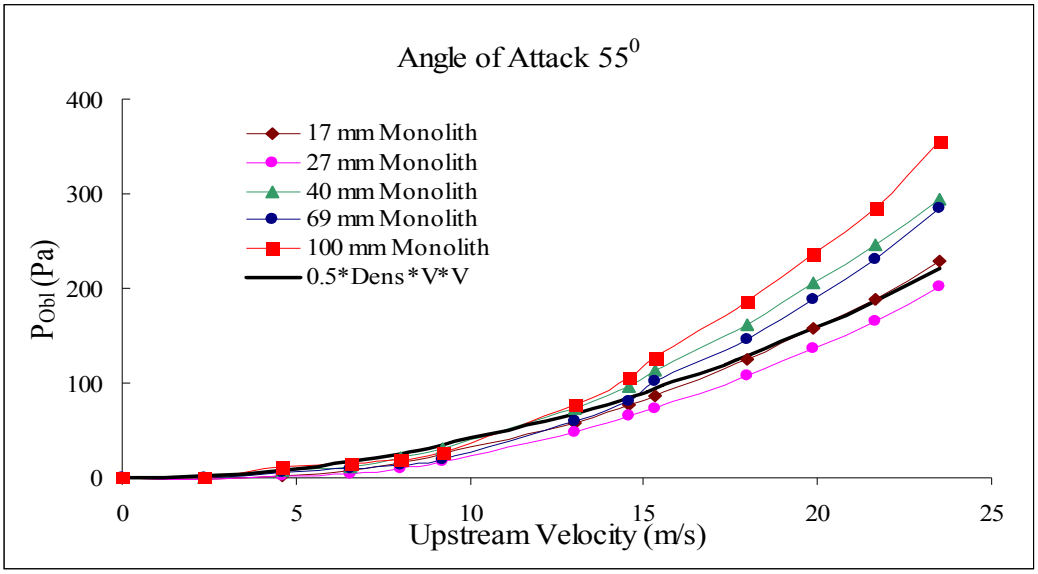

Figure 2.27: P_{Obl} charts for 55^0 angle of attack (Upstream Velocity≡U_1)

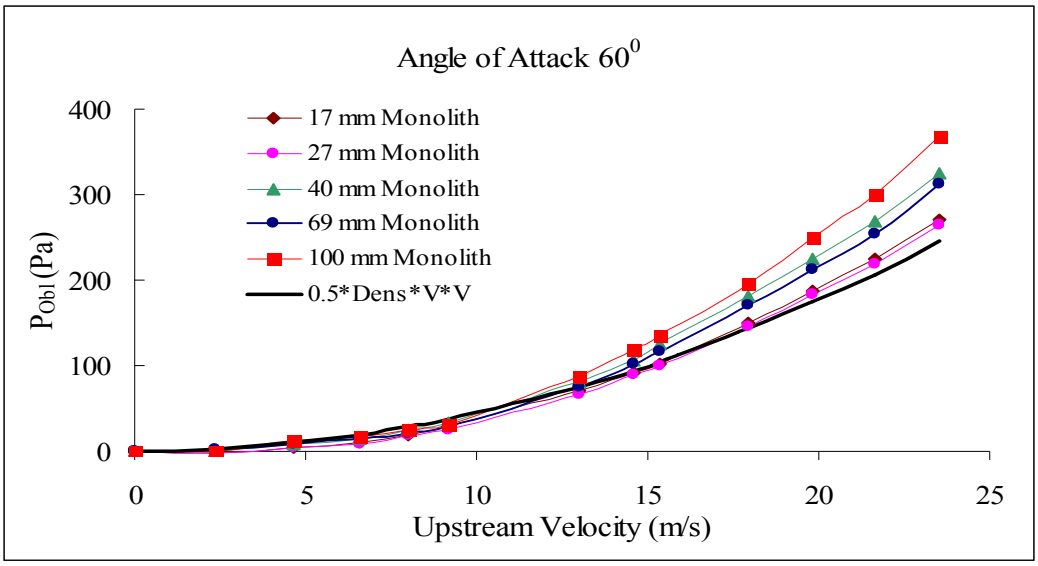

Figure 2.28: P_{Obl} charts for 60^0 angle of attack (Upstream Velocity≡U_1)

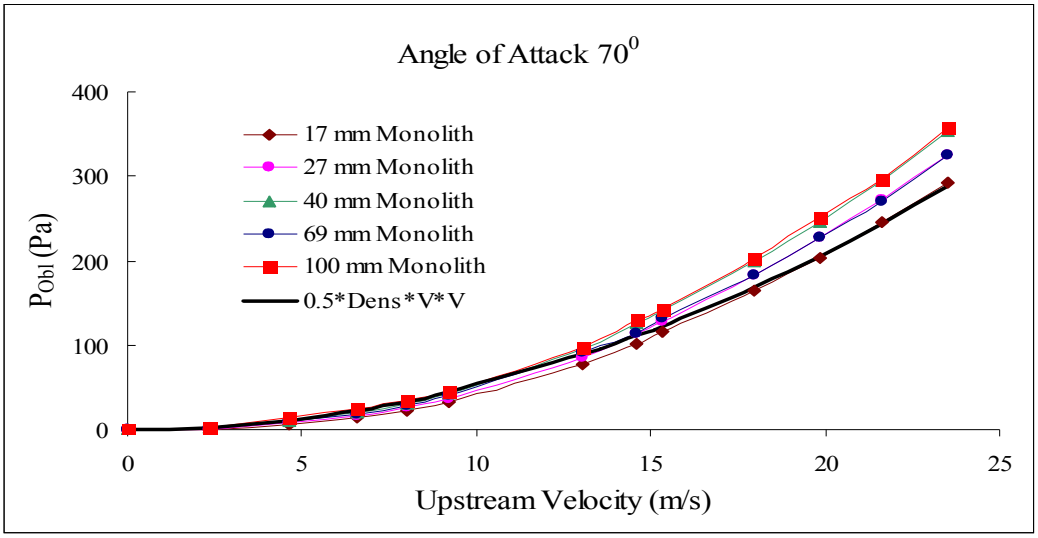

Figure 2.29: P_{Obl} charts for 70^0 angle of attack (Upstream Velocity≡U_1)

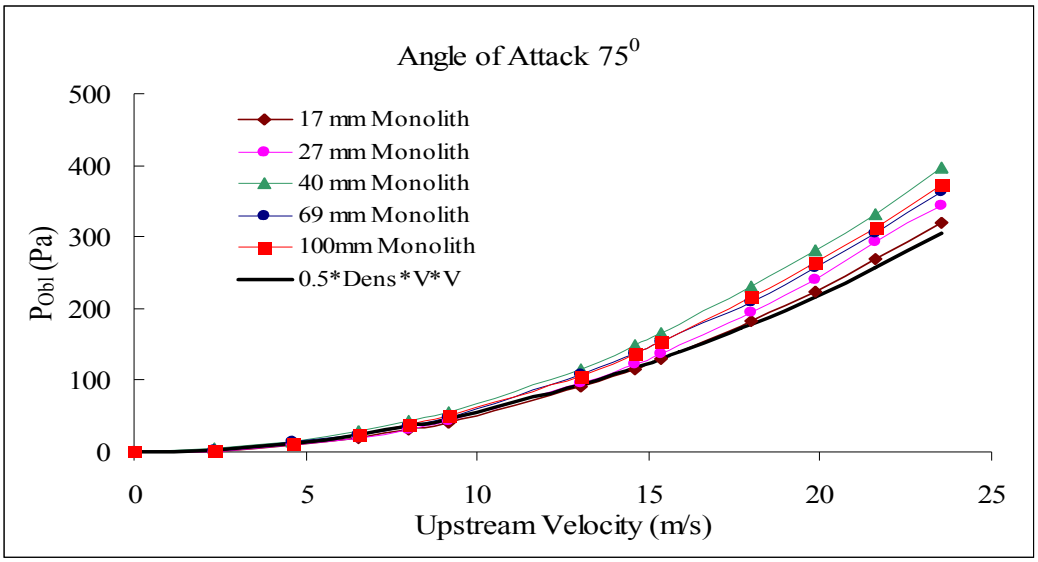

Figure 2.30: P_{Obl} charts for 75^0 angle of attack (Upstream Velocity≡U_1)

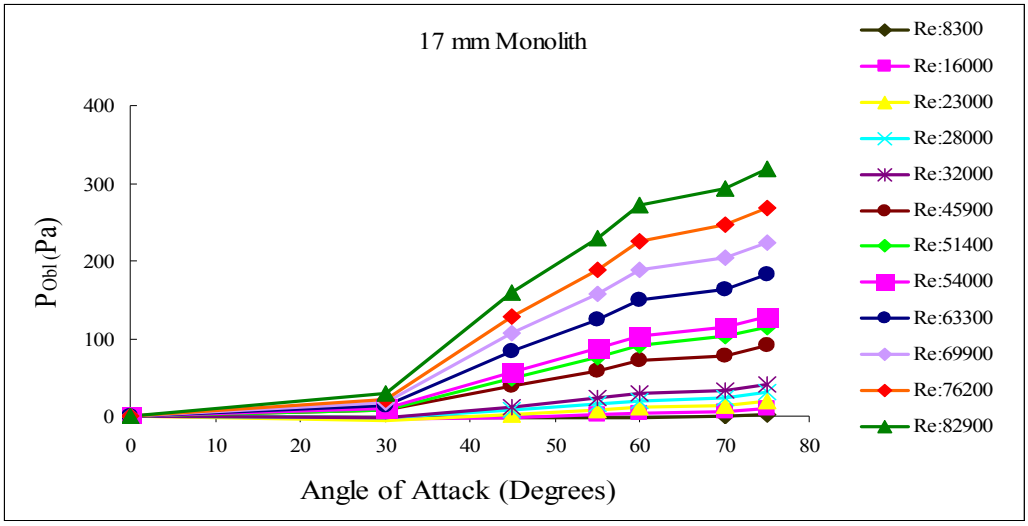

Figure 2.31: Entrance effect against angle of attack for 17 mm substrate

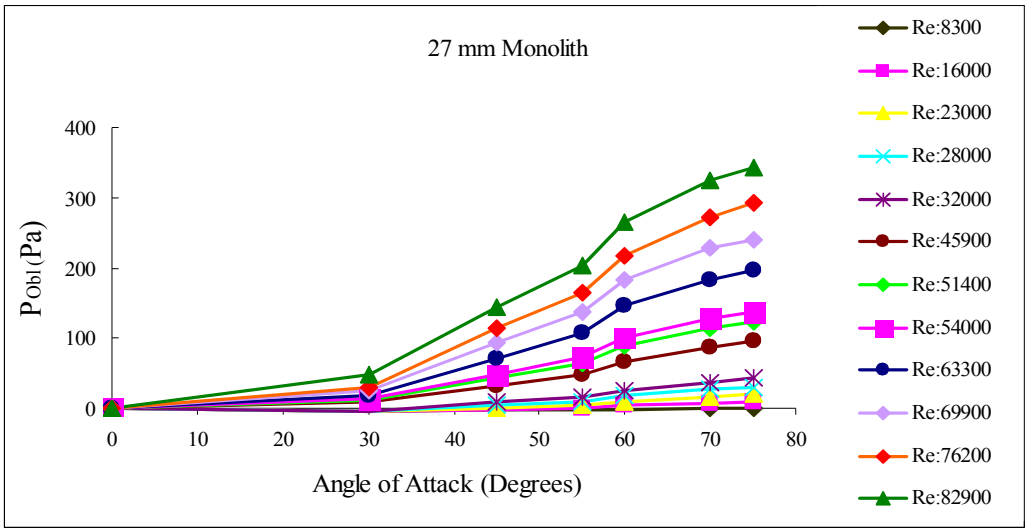

Figure 2.32: Entrance effect against angle of attack for 27 mm substrate

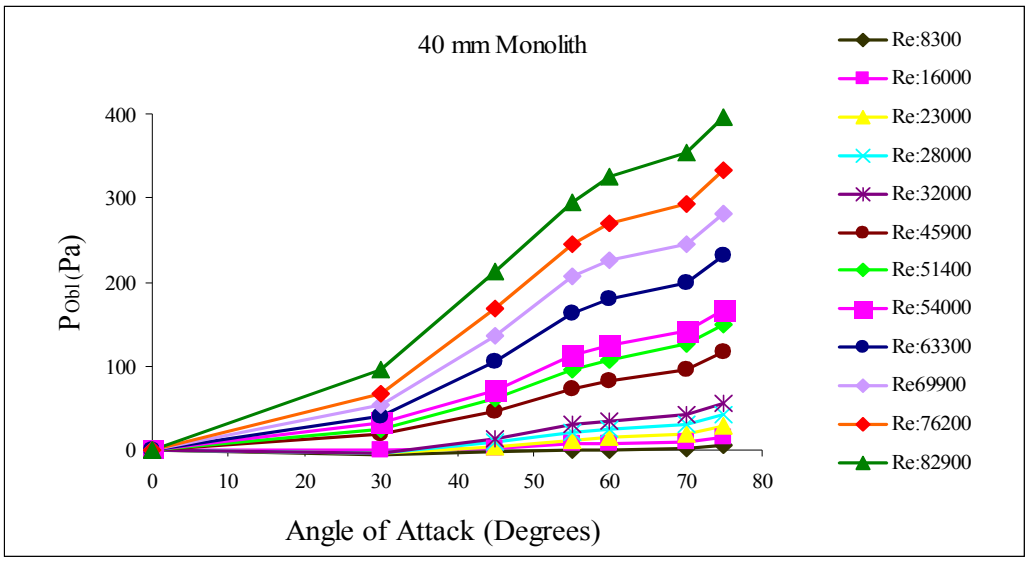

Figure 2.33: Entrance effect against angle of attack for 40 mm substrate

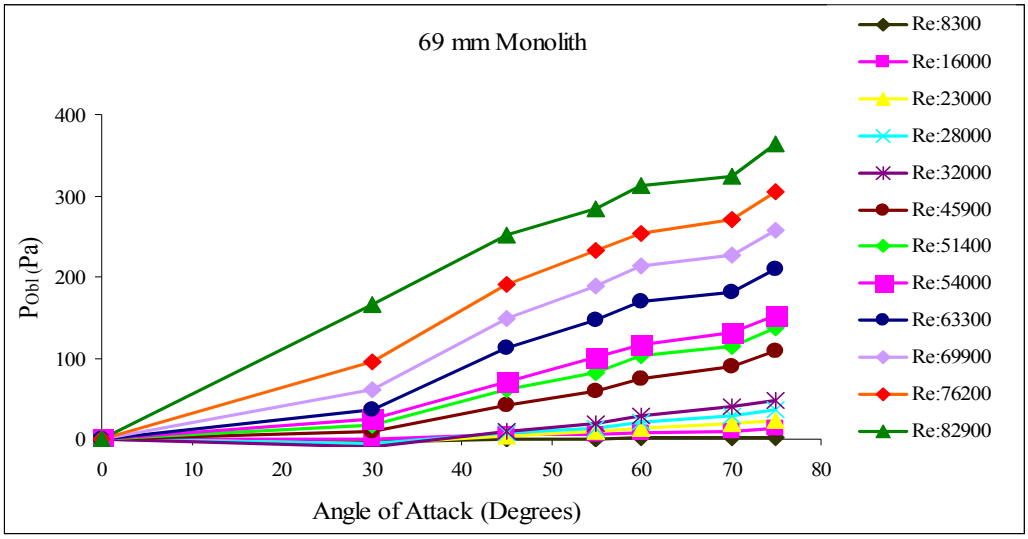

Figure 2.34: Entrance effect against angle of attack for 69 mm substrate

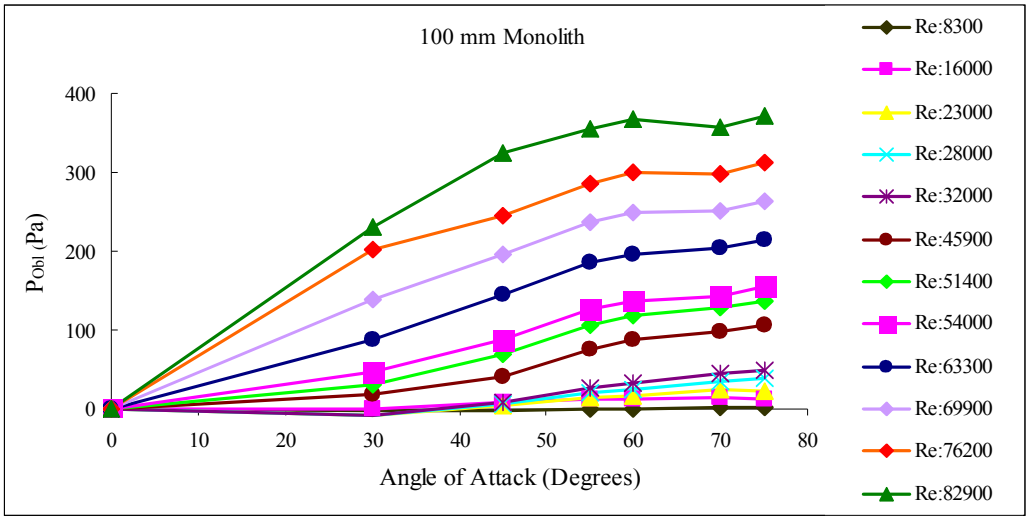

Figure 2.35: Entrance effect against angle of attack for 100 mm substrate

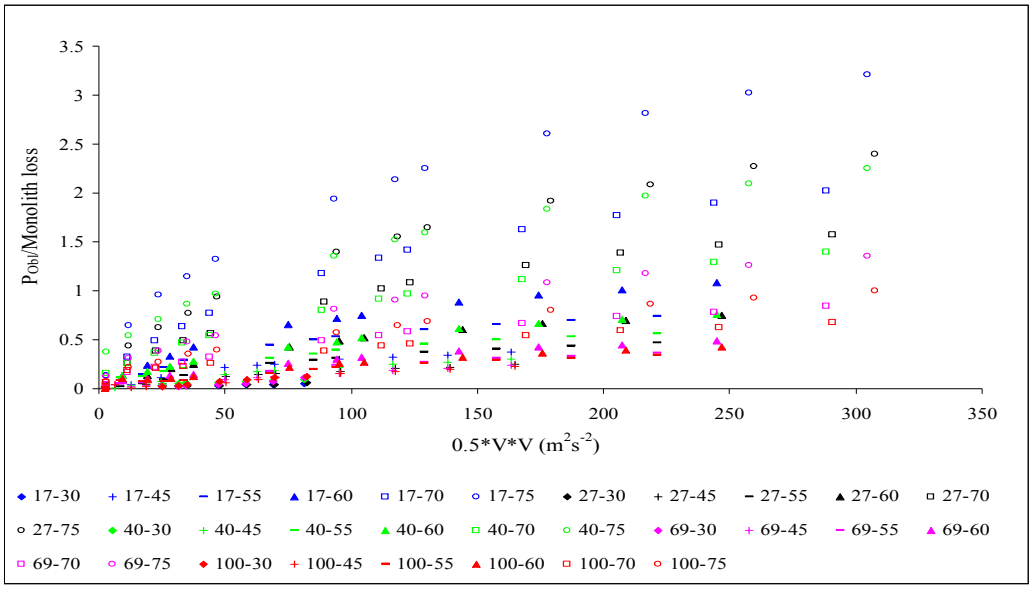

Figure 2.36: Comparison of ratio entrance effect to monolith loss against $\frac{1}{2}\rho V^2$

(Legends in Figure 2.36 refer to Length of the substrate (mm)-Angle of attack (degrees))

2.6 Error Analysis

In 2.5, it was mentioned that at low angle of attack and with large monolith losses, the errors in deducing P_{Obl} are large. This section discusses this issue. Considering the 100 mm substrate, the oblique pressure drop is calculated from Equation 2.18.

$$P_{Obl} = (P_{s1} - P_{s2}) + \frac{1}{2}\rho(U_1^2 - U_2^2) - P_L$$

The monolith pressure drop can be expressed as a function of upstream or downstream velocity and for a 100 mm monolith is given by P_L=2.1.573U_2^2+44.822U_2, where U_2 is the velocity downstream of the substrate

The errors in P_{Obl} are due to errors in static pressure drop measurements, errors due to the velocity measurements using HWA and errors due to the monolith pressure drop P_L. The monolith pressure drop P_L is expressed as a function of velocity downstream of the substrate. The static pressure drop measurements were obtained using FC 016 Furness Controls digital manometer with a pressure range of 0-199.9 mm of water (0-1960 Pa) and an accuracy of ± 1% of the manometer reading. The inclined paraffin manometer had an accuracy of ± 10 Pa for pressure ranges 0-5000 Pa depending upon the slope of the manometer. The velocity measurements using HWA had a 1% error in them. An error analysis was carried out wherein the error magnitudes were taken into account in calculating entrance effect. An error calculation example is shown in Appendix A.

It was found that the errors induced in P_{Obl} were more due to errors in U_1 and U_2 and P_L (which is again dependent on U_2). The contribution of static pressure drop measurement errors (P_{s1}-P_{s2}) had a smaller effect on the overall error magnitude in P_{Obl}. The errors at low angles of attack and low Reynolds number are high due to the fact that P_{Obl} is obtained from the difference of two relatively large numbers. As the angle of attack increased the monolith pressure drop reduced and hence the uncertainty in the entrance effect is reduced significantly and was around ±5% of the entrance effect magnitude for 75^0 angle of attack at Re=82900. It was also found that for short substrates, the magnitude of the monolith pressure drop is smaller when compared to a 100 mm substrate and hence the errors induced are reduced for shorter substrates. The error uncertainties in P_{Obl} for different lengths of substrate are plotted

in Figs. 2.37-2.61. The error charts show that as the length of substrate increases, the error uncertainty also increases and they are the highest at low angles of attack and low Reynolds number. The P_{obl} predicted curve in Figs. 2.37-2.61 is the correlation obtained from the experimental data and is discussed in Section 2.7. "P_{obl} Theoretical" refers to the entrance effect assumption of $\frac{1}{2}\rho V^2$ as suggested by Kuchemann and Weber (1953).

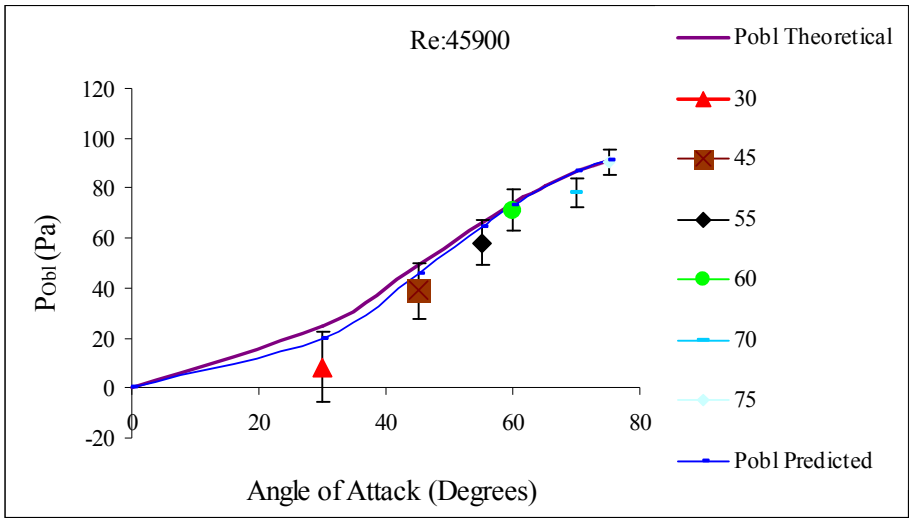

Figure 2.37: P_{Obl} Error Chart for Re: 45900 (17 mm substrate)

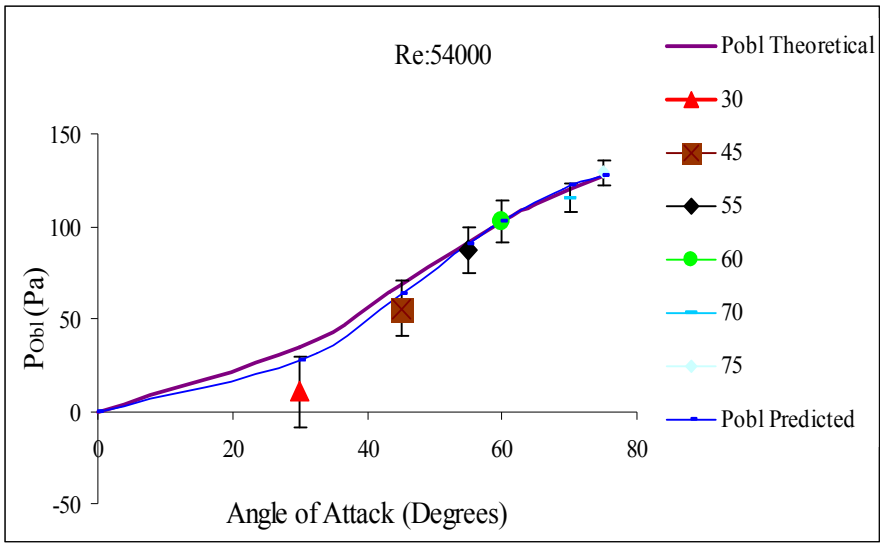

Figure 2.38: P_{Obl} Error Chart for Re: 54000 (17 mm substrate)

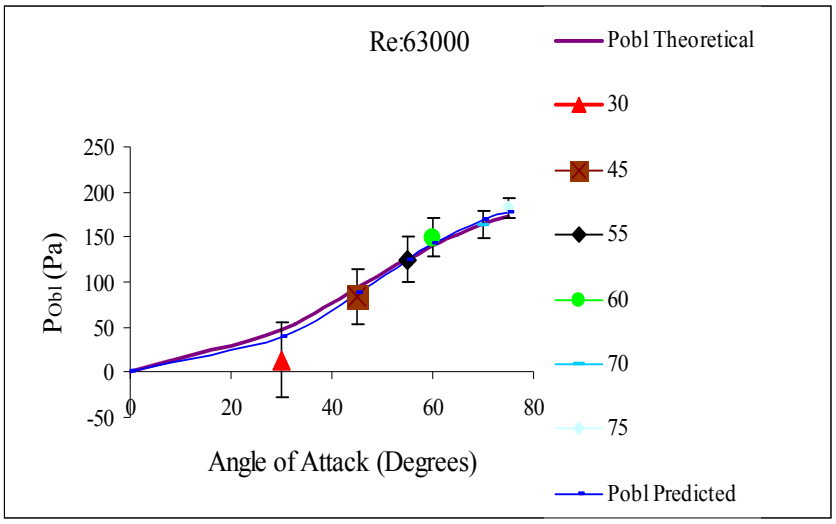

Figure 2.39: P_{Obl} Error Chart for Re: 63300 (17 mm substrate)

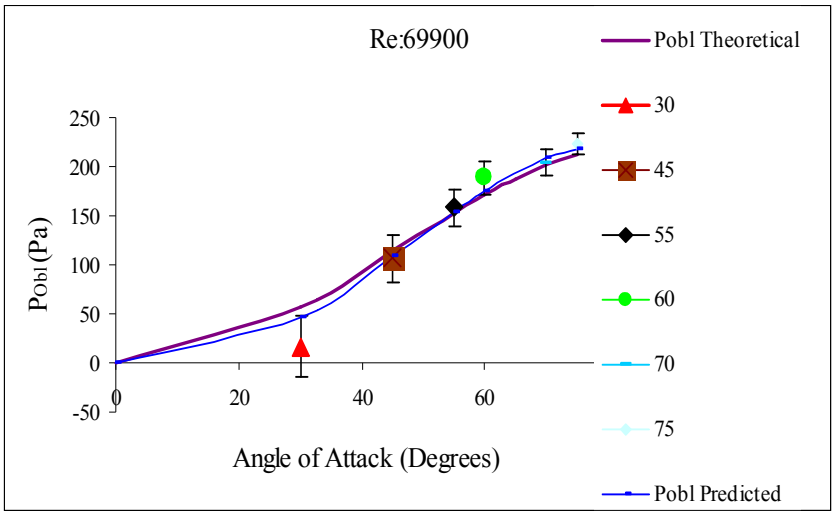

Figure 2.40: P_{Obl} Error Chart for Re: 69900 (17 mm substrate)

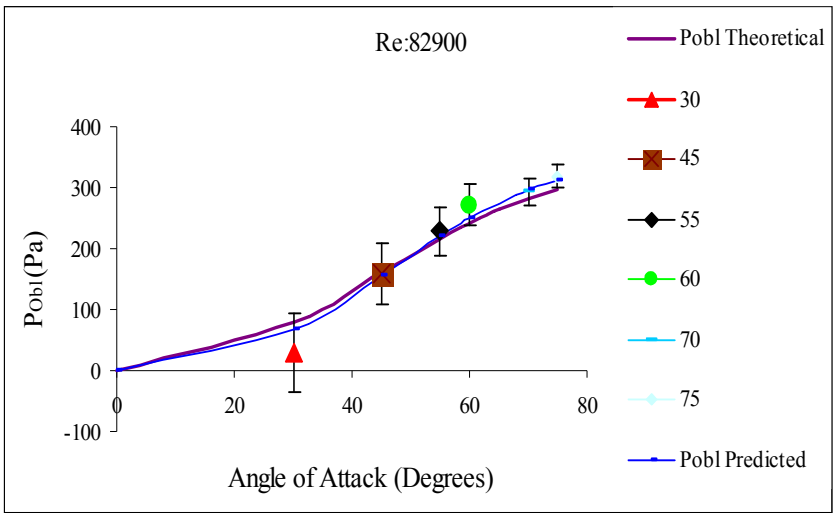

Figure 2.41: P_{Obl} Error Chart for Re: 82900 (17 mm substrate)

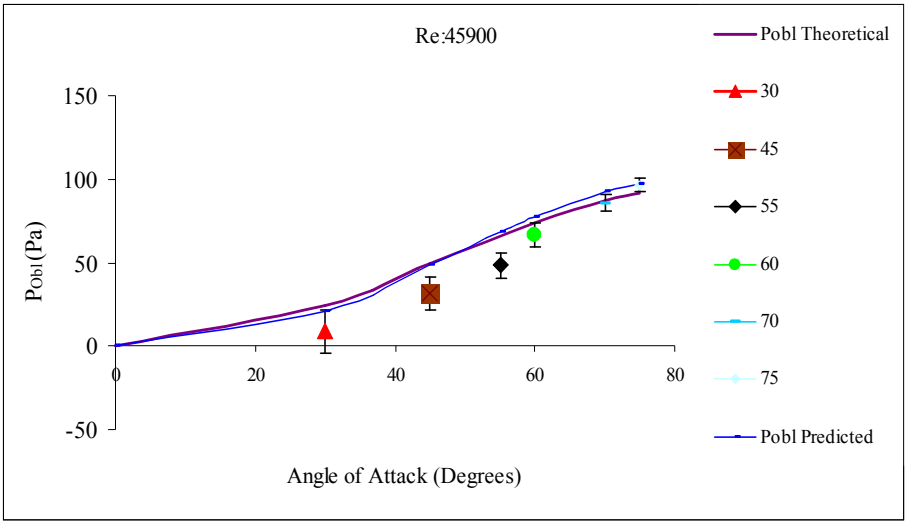

Figure 2.42: P_{Obl} Error Chart for Re: 45900 (27 mm substrate)

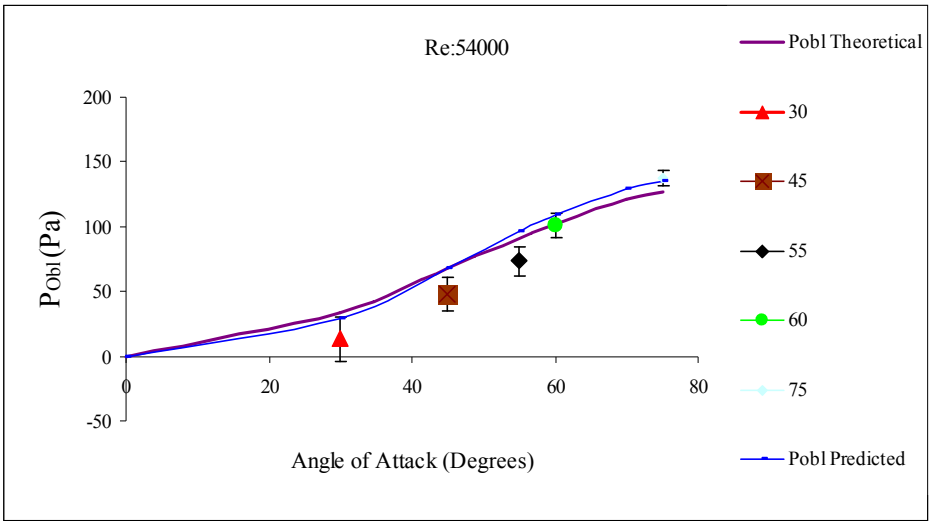

Figure 2.43: P_{Obl} Error Chart for Re: 54000 (27 mm substrate)

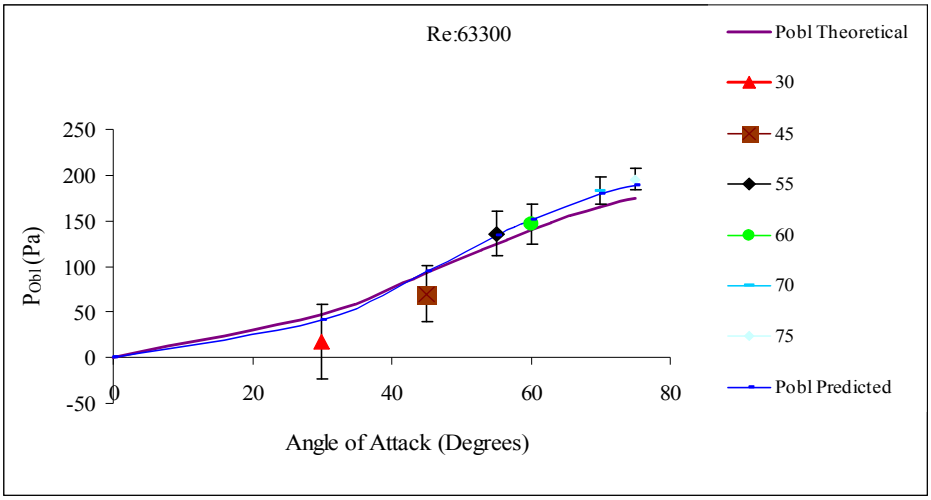

Figure 2.44: P_{Obl} Error Chart for Re: 63300 (27 mm substrate)

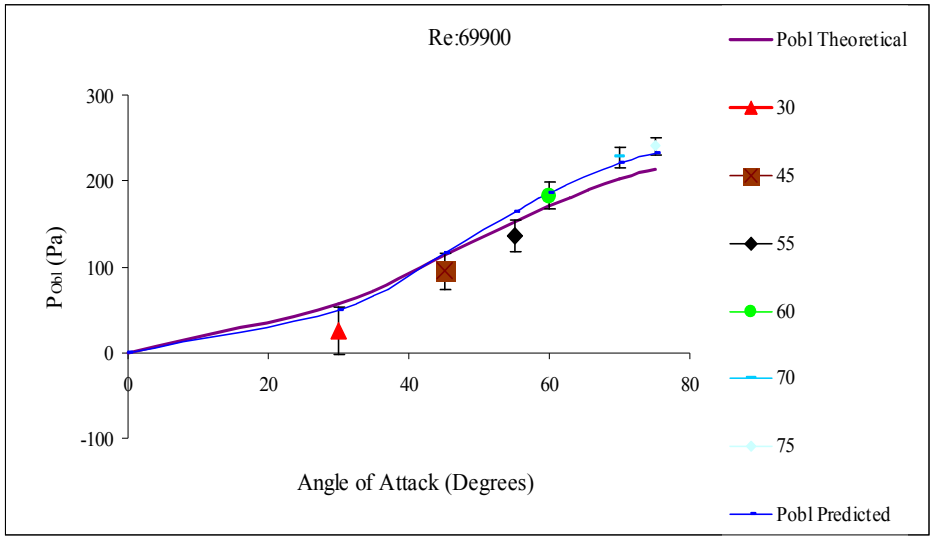

Figure 2.45: P_{Obl} Error Chart for Re: 69900 (27 mm substrate)

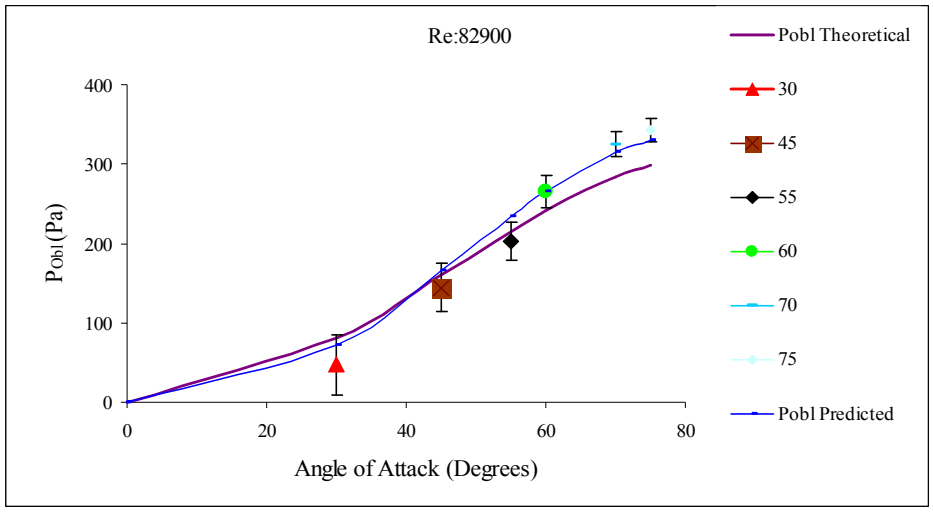

Figure 2.46: P_{Obl} Error Chart for Re: 82900 (27 mm substrate)

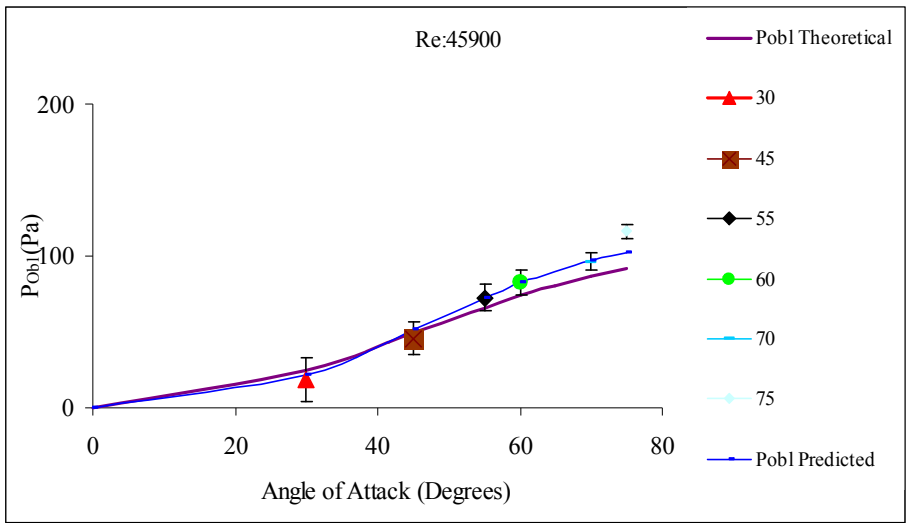

Figure 2.47: P_{Obl} Error Chart for Re: 45900 (40 mm substrate)

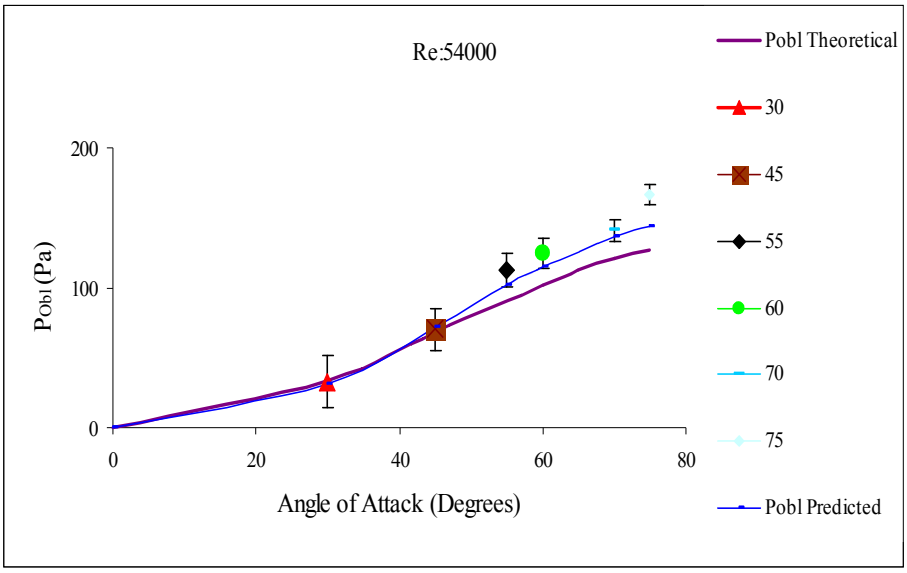

Figure 2.48: P_{Obl} Error Chart for Re: 54000 (40 mm substrate)

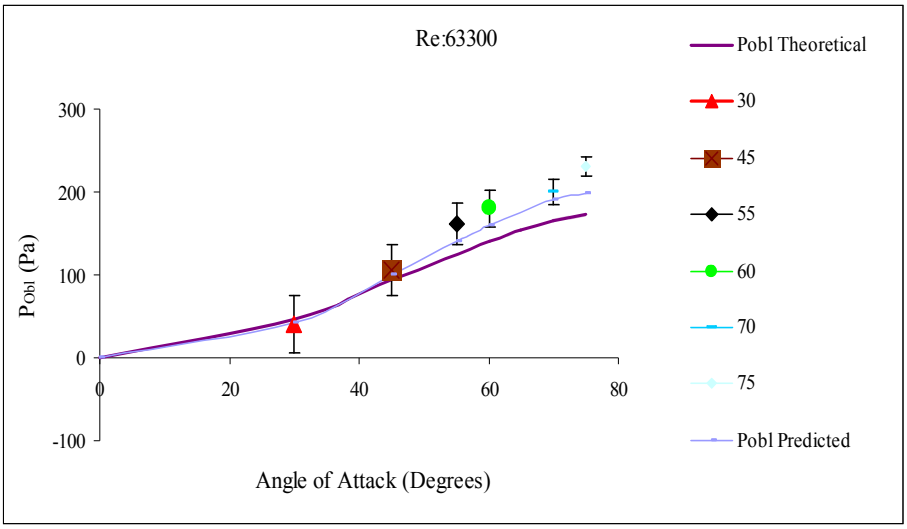

Figure 2.49: P_{Obl} Error Chart for Re: 63300 (40 mm substrate)

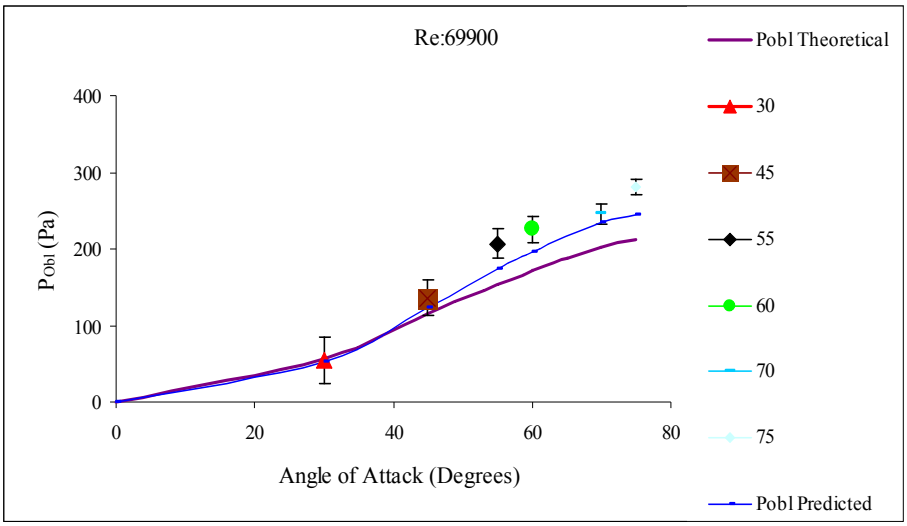

Figure 2.50: P_{Obl} Error Chart for Re: 69900 (40 mm substrate)

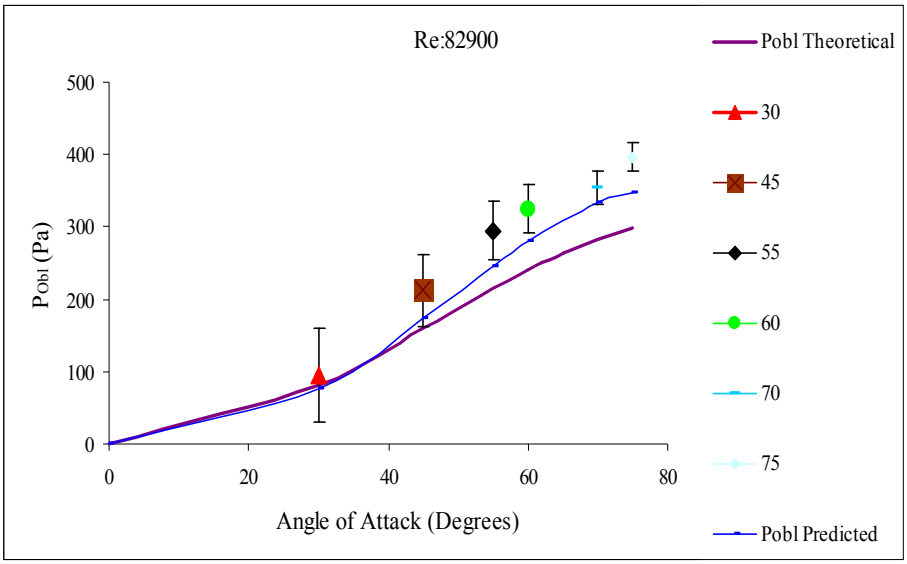

Figure 2.51: P_{Obl} Error Chart for Re: 82900 (40 mm substrate)

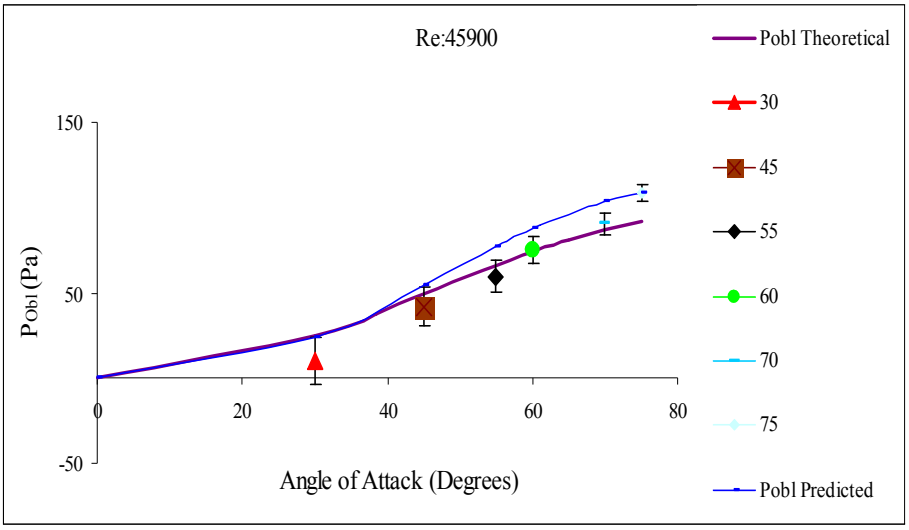

Figure 2.52: P_{Obl} Error Chart for Re: 45900 (69 mm substrate)

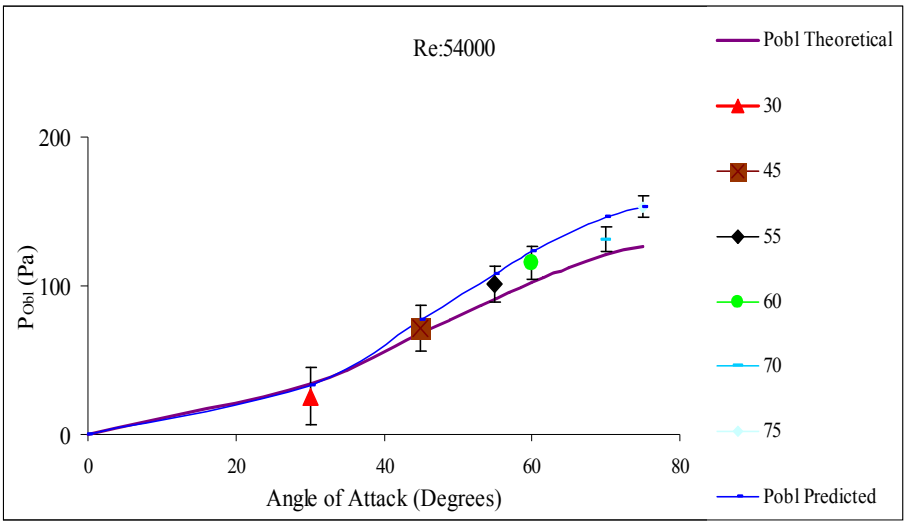

Figure 2.53: P_{Obl} Error Chart for Re: 54000 (69 mm substrate)

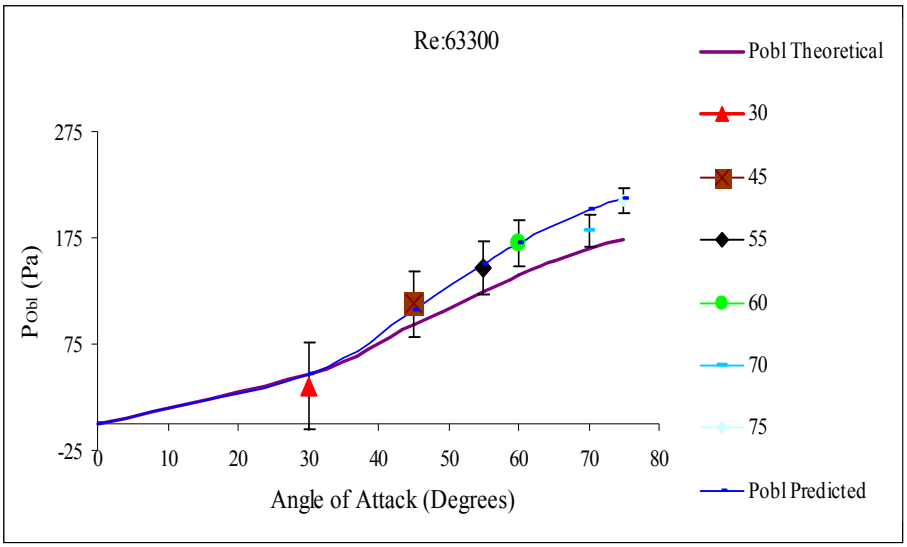

Figure 2.54: P_{Obl} Error Chart for Re: 63300 (69 mm substrate)

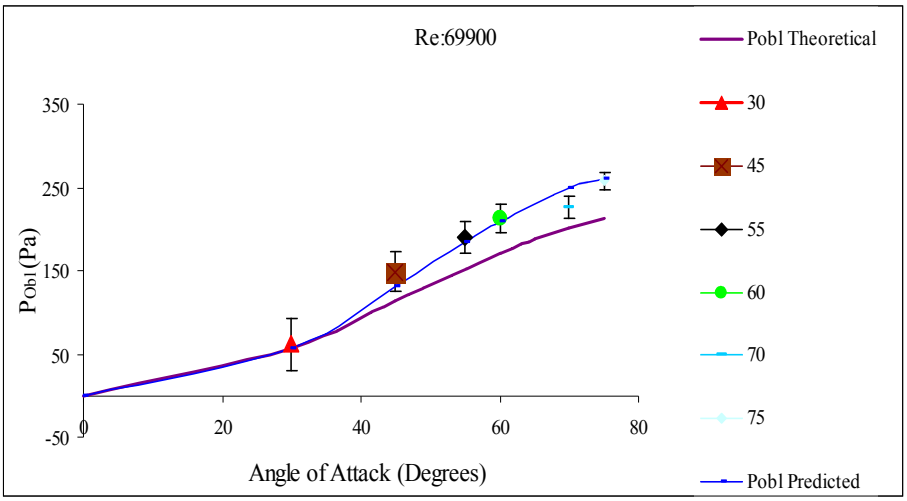

Figure 2.55: P_{Obl} Error Chart for Re: 69900 (69 mm substrate)

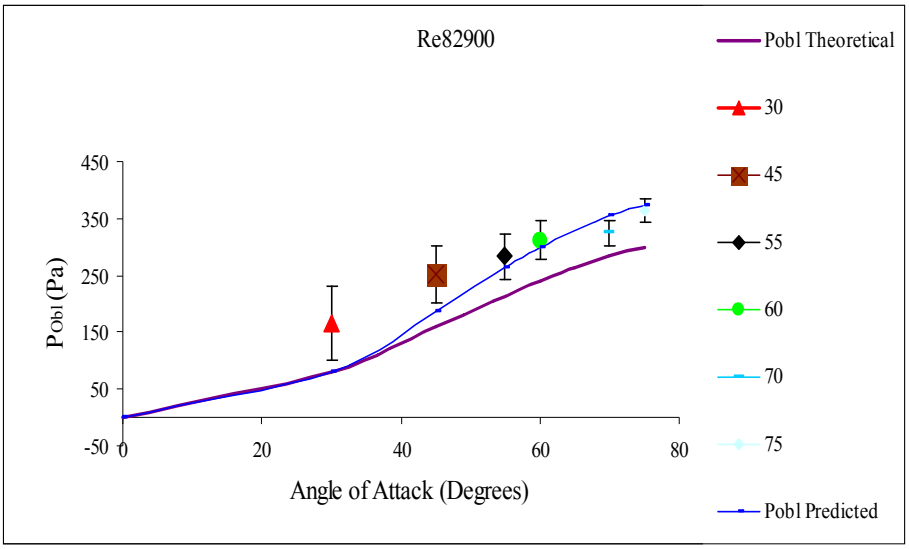

Figure 2.56: P_{Obl} Error Chart for Re: 82900 (69 mm substrate)

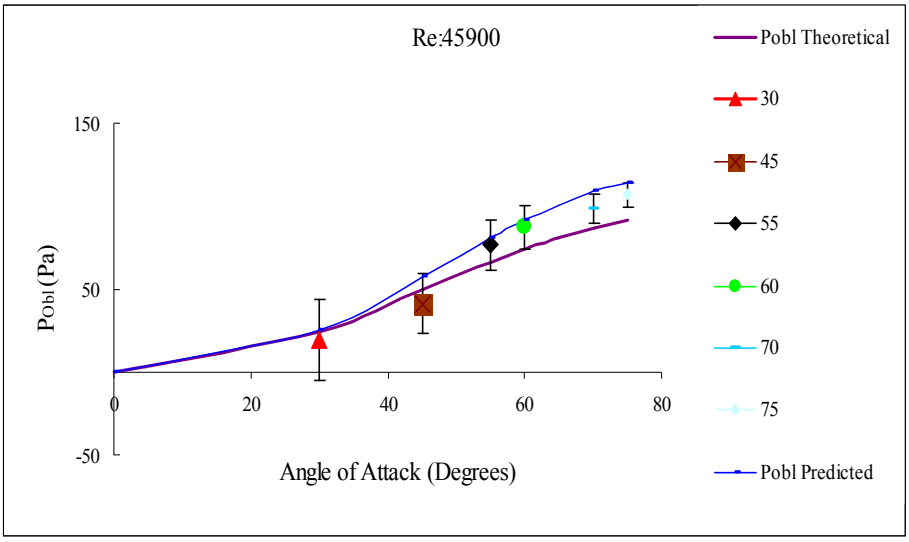

Figure 2.57: P_{Obl} Error Chart for Re: 45900 (100 mm substrate)

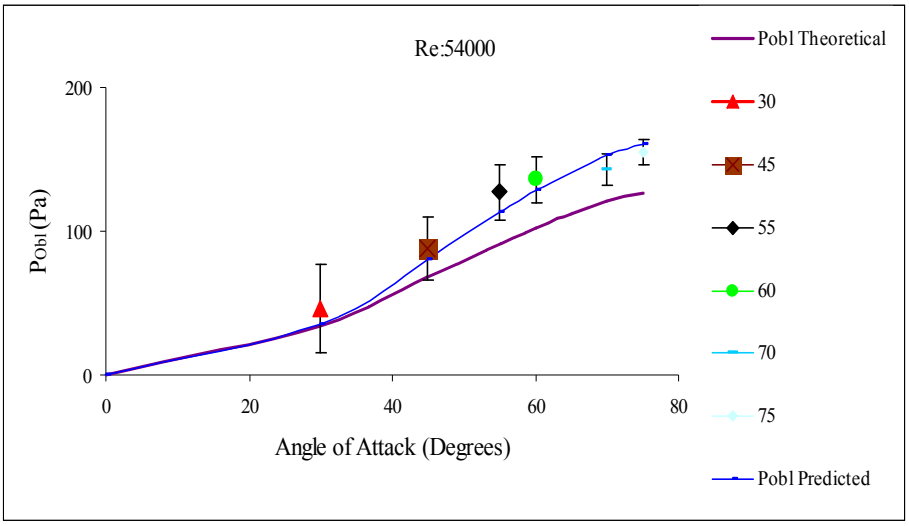

Figure 2.58: P_{Obl} Error Chart for Re: 54000 (100 mm substrate)

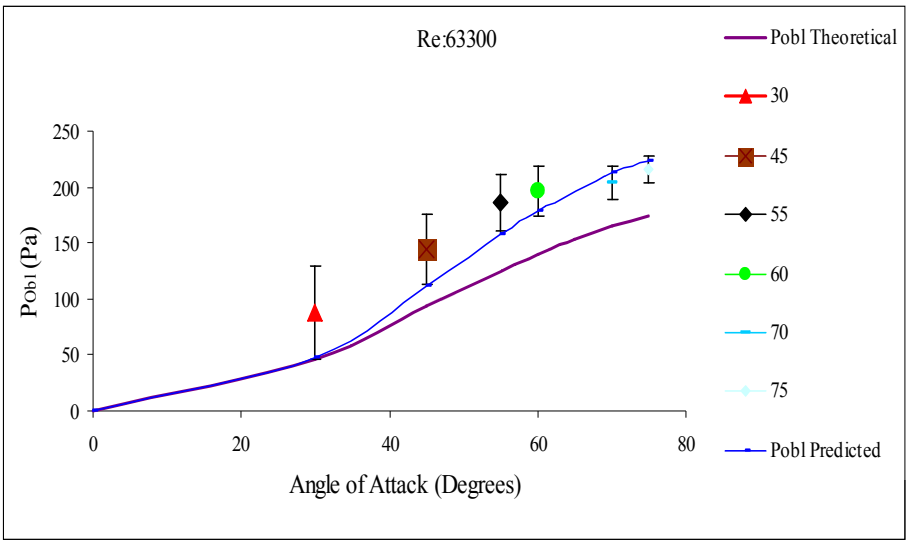

Figure 2.59: P_{Obl} Error Chart for Re: 63300 (100 mm substrate)

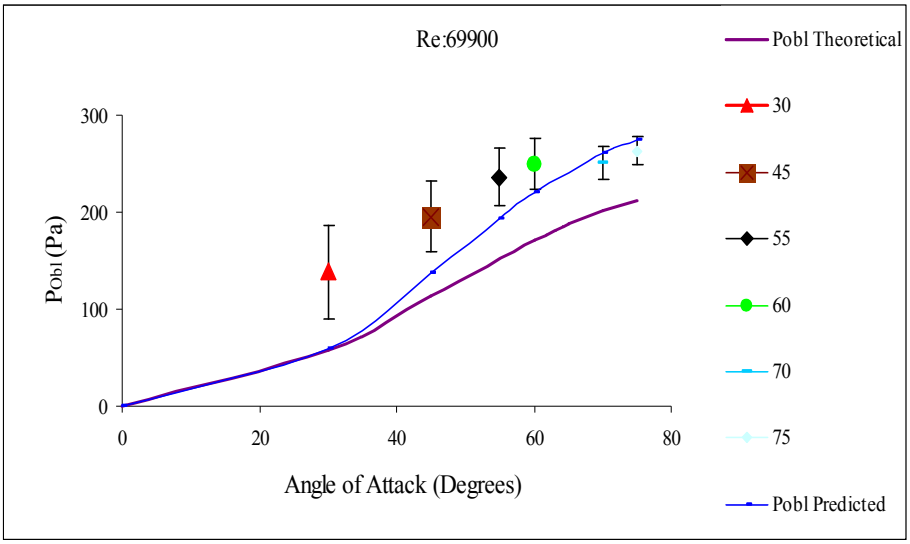

Figure 2.60: P_{Obl} Error Chart for Re: 69900 (100 mm substrate)

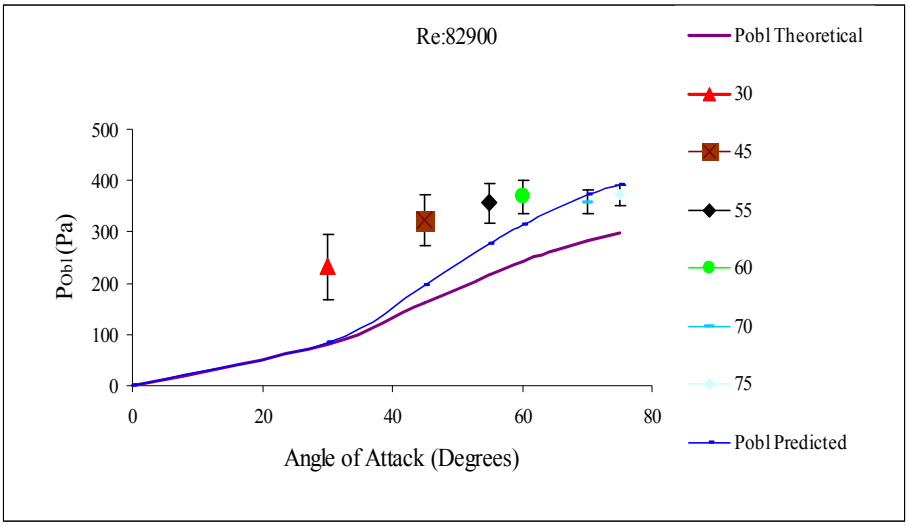

Figure 2.61: P_{Obl} Error Chart for Re: 82900 (100 mm substrate)

2.7 Non-Dimensional Analysis

An attempt was made to obtain a general relationship for the entrance effect from the major controlling variables. Such an expression would be useful for design engineers when developing similar type of systems and also could be used to perform CFD simulations by incorporating the additional pressure loss through a functional relationship. The theoretical assumption of $\frac{1}{2}\rho V^2$ by Kuchemann and Weber (1953) seemed to predict the measured entrance effect accurately at low flow rates but lost validity at high flow rates (Figs. 2.25-2.30). CFD studies performed by Benjamin et al., (2001, b) and Liu (2003) showed that the flow distribution predictions were

considerably improved using the theoretical assumption of $\frac{1}{2}\rho V^2$, however some discrepancies were still evident suggesting an improved correlation is needed to accurately predict entrance effect and further improve CFD predictions. The experimental values of P_{Obl} for five lengths of substrate were used to deduce the relationship.

The entrance effect was non-dimensionalised against the inlet dynamic pressure and the non-dimensionalised entrance effect is given by Equation 2.19:

$$K_{Obl} = \frac{P_{Obl}}{\frac{1}{2}\rho U_1^2}$$

The $K_{Obl,theoretical}$ from Equation 2.21 is given by

$$K_{Obl,theoretical} = \frac{\frac{1}{2}\rho V^2}{\frac{1}{2}\rho U_1^2} \qquad 2.21$$

Also from Fig. 2.2. $$\mathrm{Sin}\alpha = \frac{V}{U_1} \qquad 2.22$$

Equation 2.21 is given by

$$K_{Obl,theoretical} = \mathrm{Sin}^2\alpha \qquad 2.23$$

Results from Section 2.5.2.1 showed that the entrance effect was dependent on the angle of attack, Reynolds number and the length of the substrate. Hence initially $K_{Obl,}$ expressed in terms of independent dimensionless groups might be given by:

$$K_{Obl} = f[(\mathrm{Sin}^2\alpha),(Re_c),(\frac{L}{d_h})]$$

Various forms of expression correlating the variables were assessed by performing a multivariable nonlinear regression analysis using DataFit software by Oakdale Engineering. It was found that using a power-law relationship given by Equation 2.24 provided the best predictions (Figs. 2.62-2.67). Figure 2.62 shows the predictions using Equation 2.24 against the experimental data.

$$K_{Obl} = A[(\mathrm{Sin}^2\alpha)^B,(Re_c)^C,(\frac{L}{d_h})^D] \qquad 2.24$$

where A=0.447, B=1.233, C=0.0756 and D=0.1287

Predictions using Equation 2.24 are shown in Figs. 2.37-2.61 which show that the correlation seems to successfully collapse the experimental data taking into consideration the error uncertainties involved in the measurements. The nondimensional entrance effect with the error uncertainties was also plotted against the experimental data (Figs. 2.63-2.67). The legends in Figs. 2.63-2.67 show length of substrate-angle of attack-channel Reynolds number for each data set. At low angles of attack and long length substrates, the predictions seem to be poor for 30 and 45 degrees angles of attack corresponding to 69 mm and 100 mm substrates, but this may be largely attributed to the error uncertainties involved in the measurements.

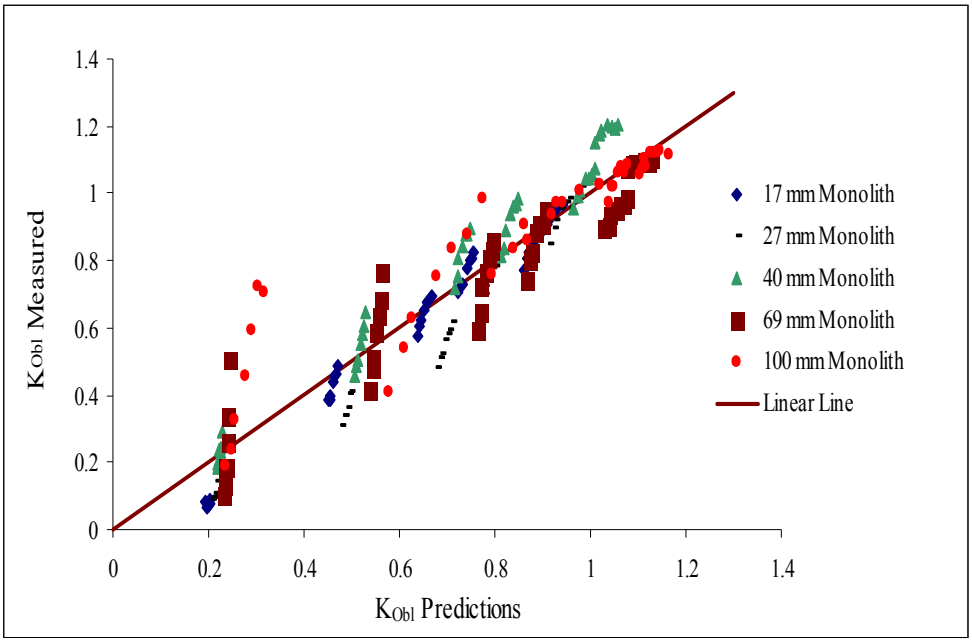

Figure 2.62: Entrance effect correlation chart

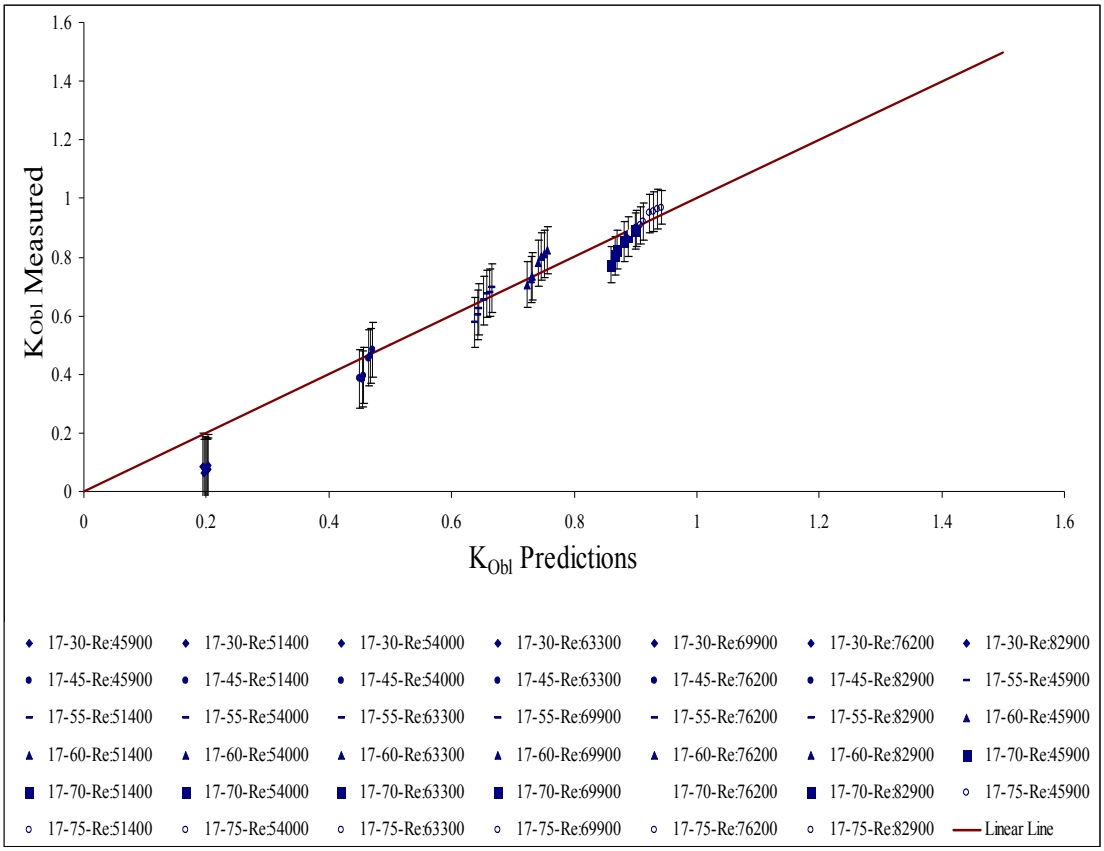

Figure 2.63: Entrance effect correlations for 17 mm substrate

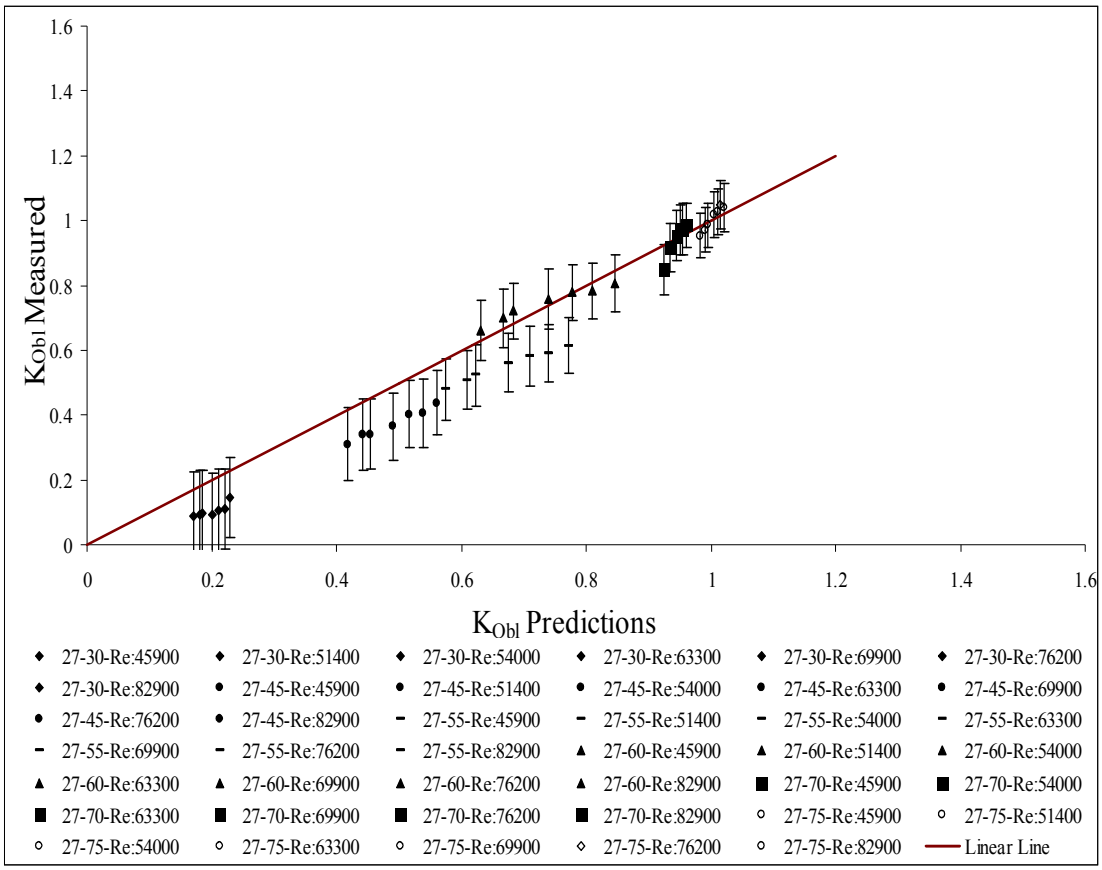

Figure 2.64: Entrance effect correlation for 27 mm substrate

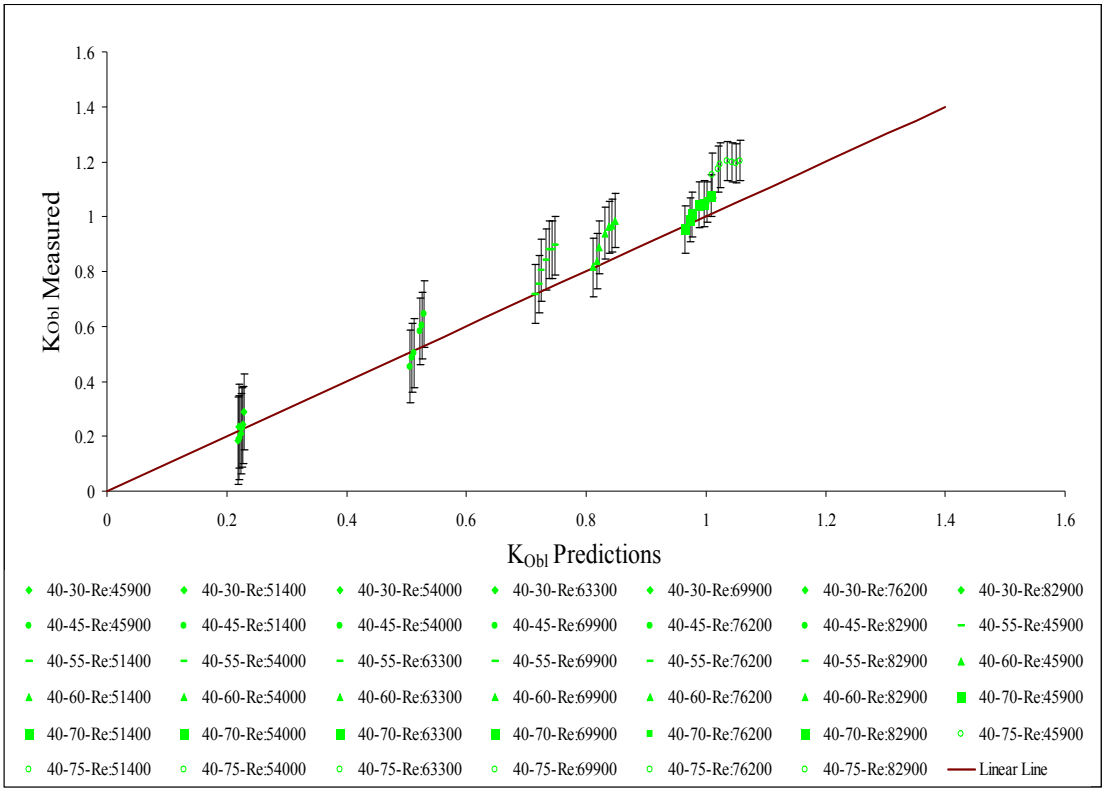

Figure 2.65: Entrance effect correlation for 40 mm substrate

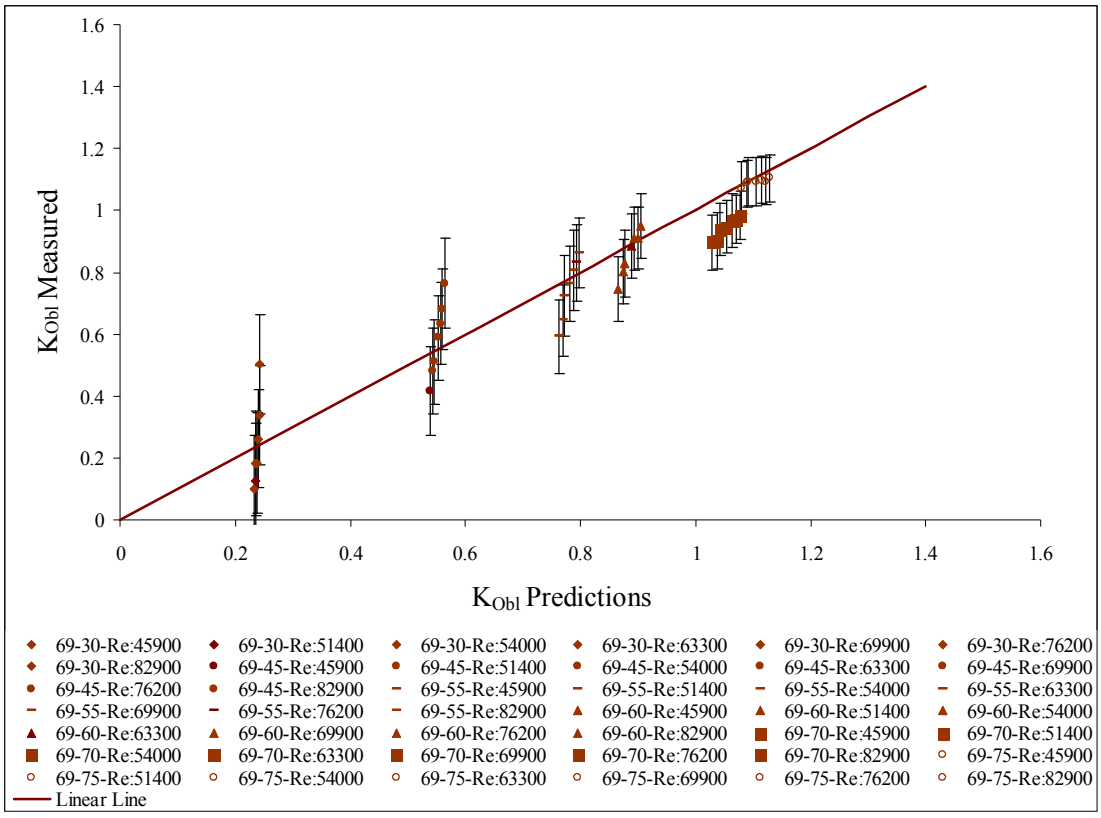

Figure 2.66: Entrance effect correlation for 69 mm substrate

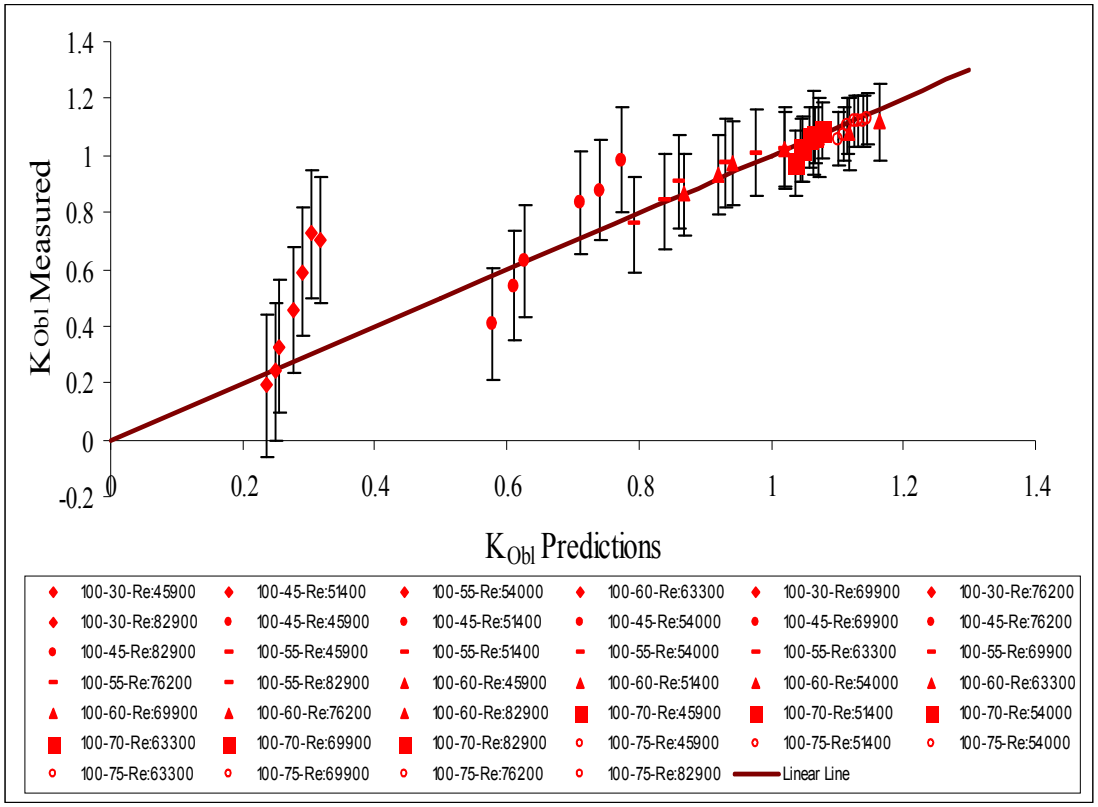

Figure 2.67: Entrance effect correlation for 100 mm substrate

Due to the limitations on the maximum available substrate size, it was not possible to perform the experiments at angles of attack above 75^0. Hence, it is possible there exists a critical angle effect above 75^0. This has been investigated by incorporating the entrance effect in CFD simulations on an axisymmetric model and comparing predictions with experimental results. This is discussed in Chapter 6. The fixed critical angle approach is based on the assumption that there is no further loss due to entrance effect above the critical angle and the magnitude of the entrance effect is constant after the critical angle of attack ($\alpha_{c,F}$). The CFD results showed that the predictions improved using a fixed critical angle approach and a fixed critical angle ($\alpha_{c,F}$) of 81^0 provided the best results. This has not been investigated experimentally; however, a fixed critical angle ($\alpha_{c,F}$) of attack of 81^0 is assumed in this study. Hence incorporating the fixed critical angle approach, the correlation for non-dimensional entrance effect is given by

For $\alpha > \alpha_{c,F}$

$$K_{Obl} = A[(\mathrm{Sin}^2\alpha_{c,F})^B, (\mathrm{Re}_c)^C, (\frac{L}{d_h})^D] \qquad \alpha_{C,F}=81^0 \qquad .25$$

Hence we have for $\alpha \leq \alpha_{c,F}$

$$K_{Obl} = A[(Sin^2\alpha)^B, (Re_c)^C, (\frac{L}{d_h})^D] \qquad 26$$

Equations 2.25 & 2.26 can be written in terms of P_{Obl} and using the critical angle of attack approach, we obtain

For $\alpha \leq \alpha_{c,F}$, $$P_{Obl} = (\frac{1}{2}\rho U_1^2)A[(Sin^2\alpha)^B, (Re_c)^C, (\frac{L}{d_h})^D \qquad 2.27$$

For $\alpha > \alpha_{c,F}$, $$P_{Obl} = (\frac{1}{2}\rho U_1^2)A[(Sin^2\alpha)^B, (Re_c)^C, (\frac{L}{d_h})^{DD} \qquad \alpha_{c,F}=81^0 \qquad 2.28$$

where A=0.447, B=1.233, C=0.0756 and D=0.1287.

Equations 2.27 and 2.28 have been plotted for different lengths of the substrate and are shown in Figs. 2.68-2.69. The predictions show the significance of the fixed critical angle of attack approach as there is no additional pressure loss due to oblique entrance above the fixed critical angle ($\alpha_{c,F}$).

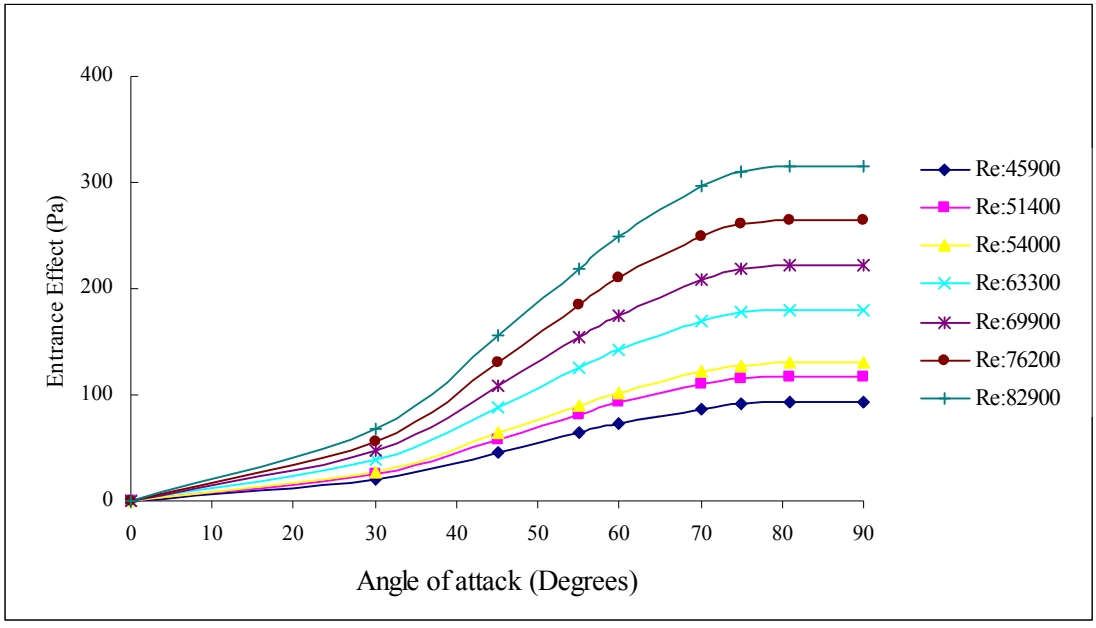

Figure 2.68: Prediction charts of entrance effect including fixed critical angle ($\alpha_{c,F}$) for 17 mm monolith (cf Figure 2.31)

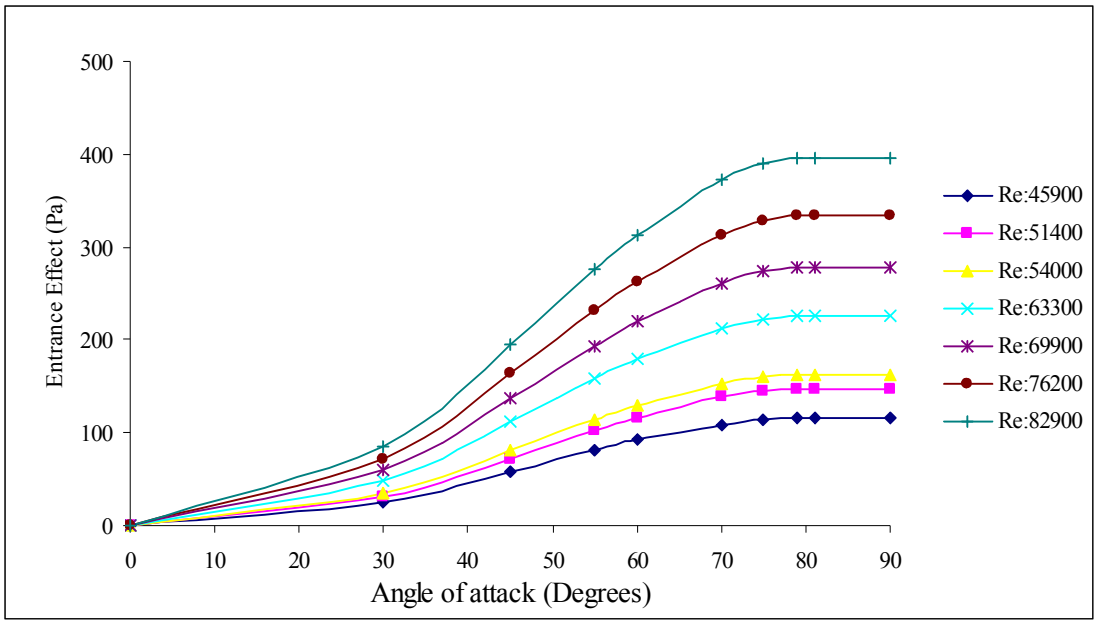

Figure 2.69: Prediction charts of entrance effect including fixed critical angle ($\alpha_{c,F}$) for 100 mm monolith (cf Figure 2.35)

2.8 Summary

An experimental study has been performed to investigate the effect of oblique entry of flow on substrate channels and to quantify the pressure loss due to this. Experiments have been performed on a one-dimensional isothermal oblique angle flow rig using different lengths of the substrates and at different angles of attack. A methodology was derived to obtain the pressure loss due to oblique entrance also known as the entrance effect.

The results for the zero degree angle of attack showed that for short substrates (17 & 27 mm monoliths), the flow is still developing when it exits the substrate channels. Hence the contribution of the developing boundary layer cannot be neglected. Darcy's Equation (H-P) ignores the pressure drop due to developing flow and it looses its validity even at low velocities for short length substrates. As the length of the substrate increases, the predictions using Darcy's Equation are better at low velocities. Shah's correlation better predicts the pressure drop for long length substrates at high channel velocities. This is in good agreement with a similar study performed by Benjamin et al (1996). The results for the oblique angles of attack show that as the angle of attack increases, the entrance effect pressure loss also increases.

The entrance effect was also found to be directly dependent on the angles of attack, channel Reynolds number and length of the substrates. The theoretical assumption of $\frac{1}{2}\rho V^2$ for the entrance effect by Kuchemann and Weber (1953) predicted accurately at low flow rates but looses validity at high Reynolds number.

From the experimental studies, a correlation for the entrance effect has been derived by taking into consideration the major controlling variables, angle of attack, length of the substrates and Reynolds number by forming non-dimensional groups. The obtained correlation successfully collapsed the data. The entrance effect correlation would be useful for design engineers when developing similar types of system. It could also be used to perform CFD simulations by incorporating the additional pressure loss due to entrance effect. This is considered in Chapters 6 and 7 in predicting flow maldistribution for axisymmetric and 2-D catalyst models respectively.

Chapter 3: Introduction to PIV

3.1 Introduction

A 2-D Particle Image Velocimetry (PIV) system supplied by TSI was used to investigate the flow field in a 2D planar diffuser. The desire to measure instantaneous spatial velocity data over an entire flow field prompted the development of Particle Image Velocimetry. The developments in the last 20 years of pulsed lasers and of fast digital image analysis, has enabled a great deal of progress in velocity field measurement methods derived from visualisation techniques (Adrian, 1991, Buchave, 1992). Particle Image Velocimetry is one of them. A brief description of the basics of the PIV technique is first described in this Chapter.

In particle image velocimetry (PIV), the fluid motion is made visible by adding small tracer particles in the flow and these particles are illuminated by a sheet of laser light using a cylindrical lens. Fig. 3.1 shows an overview of a PIV system.

Figure 3.1: Overview of a PIV system (Gilbert.R.A.D, 2002)

Two images of each particle are recorded at a short time interval. The PIV images are analysed by a system composed of reading optics, a computer and analysis software. The image is then divided into interrogation regions and for each of these interrogation regions the images from the first and the second pulse of light sheet are correlated to produce an average particle displacement vector. The local flow velocity

is determined from the displacement of the images of the tracer particles between successive illuminations. The time delay separating the illuminations and the magnification of the recording medium are needed to make the method quantitative.

PIV is a more direct determination of velocity than either pitot probes, which measure pressure, or hot wire probes, which measure heat loss. However it is indirect as it is a measure of the velocity of the tracer particles and not the fluid itself. Therefore the properties of the particles following the flow are of paramount importance. PIV provides accurate quantitative information on the instantaneous spatial structure of the flow.

Particle Image Velocimetry can be divided into three different groups depending upon the methods used to determine the displacement of seed particles, namely: laser speckle Velocimetry (LSV), low density PIV and high density PIV. Due to the relative accuracy of low and high density PIV as well as the difficulty in obtaining the necessarily high seeding density required for LSV, it is no longer widely used (Adrian, 1991).

Low density PIV also known as particle tracking velocimetry (PTV) is used when the seeding density is low enough that individual particles can be tracked. The average distance between particle image pairs is much larger than the mean displacement so that the expected number of particle image pairs in the interrogation area is low. Because of the large distance between particle image pairs with respect to the mean displacement it is fairly easy to identify particle-image pairs that correspond to the same tracer particle in the flow and hence obtain the local flow velocity. PTV yields better results than the conventional statistical analysis methods (auto-correlation / cross-correlation) due to a higher detection rate which can be achieved within the measurement window. PTV could arguably yield better positional accuracy than PIV because it allows one to one tracking of the same particle between two image frames (Grant, 1997).

High density PIV is applied when the seeding density is too high to apply PTV effectively. Either individual particles cannot be identified or the mean spacing between the particles is below the average displacement making the tracking of

individual particles too difficult. As a result the images are divided into interrogation areas and the mean displacement of particles in that area represents the velocity vector. The tracer particles have to be small enough in order to follow the flow and large enough so that they can scatter enough light and the recording medium is able to capture the flow. In order to follow the flow, the tracer particles have to be chemically very stable.

3.2 PIV process

The basic processes in PIV can be divided into image acquisition, processing, data validation and data analysis (Fig. 3.2). A brief explanation of each of the processes are initially given below and explained in detail in Sections 3.3-3.4.

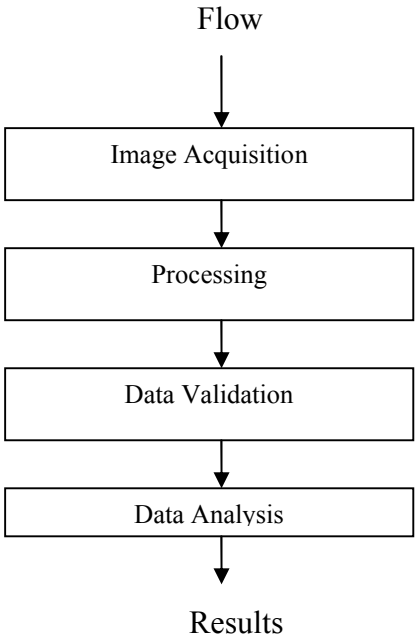

Figure 3.2: A typical PIV process

Image Acquisition: The main task in this process is to capture the image for PIV processing. This is also the most important step in the PIV process. If the obtained data is bad then efforts in processing and applying data validation techniques to improve the quality will be fruitless. It is always advisable to spend quite a lot of effort in optimising the actual physical set-up. The laser and the camera are aligned perpendicular to each other and also perpendicular to the flow. The rig set-up and the optical access for the PIV are done prior to image acquisition. The image acquisition process consists of the tracer particles, flow illumination, image recording parameters

and also the timing parameters. There is an overlap of the above mentioned parameters with the PIV processing and often it is a case of optimising the overall setup.

Processing and Validation: This is the method by which the velocity vector field is generated from the raw image data. The processing steps can be broken down to image conditioning, generating grids and masking spots, performing correlation, locating peaks and performing validation. Each of the steps is explained in detail later. There are several algorithms that could be used for the processing steps grid generation, spot masking, correlation and peak location. The best choices depend on the flow, velocity gradients, seeding and allowable processing time. Once the raw data is processed and a correlation map is obtained, the data can be improved using post-processing tools. A good validation procedure will only remove spurious vectors, and can be used to replace data voids, where appropriate using suitable validation tools. The available tools are the mean and median filters and double correlate filters. No smoothing tool is used in this study as it only makes the data look better.

Analysis & Presentation: This is the step where the vector field information is used to analysis the flow properties and to derive other quantities such as vorticity and turbulence statistics. Tecplot 10 software is used in this study to plot the vectors and contour plots and also to extract data into other formats like MS Excel. The turbulence statistics are automatically calculated in Tecplot.

The flow chart in Fig. 3.3 shows the best practice method to be followed in order to obtain high quality data.

Figure 3.3: Flow Chart of a typical PIV process (TSI Insight 3G Manual)

The different stages in the PIV process are explained in detail below.

3.3 Image Acquisition

The image acquisition process can be divided into tracer particles, flow illumination, recording and the pulse separation time. Each process is explained in detail below.

3.3.1 Tracer Particles

Particle Image Velocimetry technique is based on the assumptions that the tracer particles will follow the fluid motion, and are distributed uniformly in the interrogation region. The energy necessary to illuminate fine particles and produce images of sufficient exposure and clarity is also a major issue in PIV. A brief description into the particle sizes and light scattering capabilities of tracer particles is given below.

The ideal tracer particles introduced into the flow should follow the motion of the fluid accurately and they must scatter sufficient light to be accurately recorded. The two important considerations with regards to the tracer particles are the dynamic response of the tracer particles with respect to the fluid motion and also light scattering properties.

If the density of the fluid ρ and the density of the tracer particles ρ_p do not match then it results in gravitational forces induced on the particle behaviour. This effect becomes more important for flows with strong velocity gradient. The gravitational induced velocity U_g from Stokes drag law assuming spherical particles in a viscous fluid at a very low Reynolds number is given by (Raffel et al, 1998)

$$U_g = d^2_p(\rho_p - \rho)g/18\mu \qquad 3.1$$

where g is the acceleration due to gravity, μ is the dynamic viscosity of the fluid and d_p is the diameter of the particle.

The estimation of the velocity lag of a particle in a continuously accelerating fluid is given by:

$$U_S = U_p - U_f = d^2_p(\rho_p - \rho)a/18\mu \quad 3.2$$

where U_p is the particle velocity and a is the acceleration of the fluid.

One more aspect of tracer particles to be considered is the relaxation time τ_s. The relaxation time is a critical measure for the tendency of particles to attain velocity equilibrium with the fluid and is given by (Raffel et al, 1998)

$$\tau_s = d^2_p\rho_p/18\mu \quad 3.3$$

Since a large relaxation time may cause delay for particles to reach the flow velocity, a continued phase lag will occur when the fluid velocity is fluctuating and hence has to be limited. This becomes more important when PIV is applied to measure turbulent or unsteady flows with large velocity fluctuations.

Due to the difference in density between fluid and tracer particles, the diameter of particles should be very small in order to ensure good tracking of the fluid motion. But particle diameter has to be big enough so as to scatter enough light for the recording medium. So the choice of optimal diameter for seeding particles is a compromise between an adequate tracer response of the particles in the fluid requiring small diameters and a high signal-to-noise ratio (SNR) of the scattered light signal necessitating large diameters (Melling 1997). Olive oil particles with a diameter of 1-2 μm have been used for this study and they are induced in the flow using a six-jet atomiser from TSI.

3.3.1.1 Scattering characteristics of tracer particles

The second important characteristic of the tracer particles is their light scattering properties. The scattering of light by small particles depends upon the ratio of the refractive index of the particle to that of the surrounding medium, the particle size and shape and the observation angle relative to the incident light.

The quality of the PIV recordings is directly proportional to the light scattering capability of the particles. It is often more effective and economical to increase the image intensity by properly choosing the scattering particles than by increasing laser power. A convenient measure of the light scattering capability is the scattering cross

section C_s, defined as the ratio of the total scattered power P_s to the laser intensity I_0 incident on the particle (Melling 1997):

$$C_s=P_s/I_0 \qquad 3.4$$

Figure 3.4: Scattering cross-section as a function of particle size
Source: Melling 1997.

Fig. 3.4 shows the variation of C_s as a function of the ratio of the particle diameter d_p to the laser wavelength λ for spherical particles with a refractive index m=1.6. The scattering cross-section for a diatomic molecule such as nitrogen or oxygen and two larger particles are given in Table 3.1 These examples indicate the difference between the light scattering cross sections of molecules and those of particles of diameter 1-10 μm. It can be seen that larger particles generally scatter more light and give higher SNR, when the particle diameter is less than 1 μm (~ 2λ for green light with λ = 532 nm) the scattering capability decreases drastically with the particle diameter. Particle diameters from 1 to 10 μm have a good SNR and are appropriate for PIV experiments. In addition to the scattering capability or SNR, it is also required that the particle size should be as uniform as possible because the excessive intensity of light scattering from larger particles will induces a high background noise to the light scattering from the smaller particle. Generally for spherical particles with diameters larger than the wavelength of the incident light Mie scattering theory can be applied. In PIV the light is scattered at 90^0 to the incident light sheet so not only the angular distribution of the scattered light intensity from the seeding particles is of interest but also the overall scattering cross-section. Studies of scattering from spherical particles have shown that the scattered light intensity at 90^o scattered is a strong function both of the size parameter d_p/λ and of the refractive index m (Melling 1997).

Table 3.1: Comparison of the approximate values for a diatomic molecule such as nitrogen or oxygen and two larger particles. Source: Melling, A. (1997)

3.3.2 Flow illumination

Lasers are widely used in PIV because of their ability to emit monochromatic light with high energy density which can be easily spread into thin light sheets for illuminating and recording the tracer particles (Raffel et al 1998).

3.3.2.1 Neodym-YAG laser

Nd:YAG lasers (Nd:$Y_3Al_5O_{12}$) are the most important solid-state laser for PIV in which the beam is generated by Nd3+ ions and YAG crystals (yttrium-aluminium-garnet). They are currently the most widely used in PIV applications because of their robustness, high amplification, and good mechanical and thermal properties. The YAG crystal is doped with an active medium, in this case triply ionized neodymium, which replaces another element of roughly the same size, typically yttrium. Generally the crystalline host is doped with around 1 % neodymium by weight. The YAG crystal is pumped with energy from white light flash lamps within the laser head unit (Raffel et al 1998).

Nd:YAG lasers can be operated in both continuous and pulsed mode. They can be operated in pulsed mode by including a quality switch (Q-switch) inside the cavity. The Q-switch alters the resonance characteristics of the optical cavity. Initially the laser medium is pumped while the Q-switch prevents feedback of light into the gain medium. As a result after certain time the amount of stored energy increases and reaches a maximum value. At this point the Q-switch opens allowing a very short burst of high intensity laser light to emit (Raffel et al 1998). The fundamental wavelength of 1064 nm is frequency doubled using special crystals. After separation of the frequency-doubled portion approximately one-third of the original light energy

is available at 532 nm. The PIV system used in this project was supplied by TSI and consists of a 532 nm Nd:YAG laser with a pulse duration of 5ns, pulse energy of 120 mJ and a repetition rate of 15 Hz.

3.3.2.2 Generating a light sheet

The beam delivered from the laser is passed through a cylindrical lens in order to generate a light sheet (Fig. 3.5). A combination of cylindrical and spherical lens can be used to obtain desired height and thickness of the light sheet. The thickness of the light sheet is normally chosen to be as small as possible. A relatively thin light sheet helps to eliminate out of plane motion being recorded. The laser light sheet thickness in this study was approximately around 1 mm.

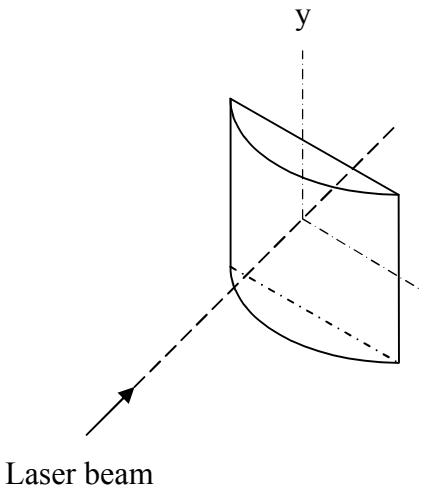

Figure 3.5: Sketch of a cylindrical lens

3.3.3 Recording

Typically two pulses of laser light are used to record pairs of particle images. Earlier PIV recordings were done on photographic film. With the advent of modern digital recording, the use of photographic film in recording PIV images quickly became obsolete. The advantage of using photographic film is its tremendous resolving power; a 12.5 cm × 10 cm piece of film can contain as many as 3 Gbytes of information. Although the photographic process is inconvenient and the interrogation of the photograph slow, the density of information storage makes it possible to record large regions of a flow field and yet resolve flow structures at the sub millimeter level

[Prasad et al 1992]. However, the process of developing and digitizing the film is time consuming and inconvenient.

In the last few years advances in CCD (charged couple device) cameras and videos are attractive and feasible for PIV measurements. Although even today's CCD cameras don't match the spatial resolution of photographic film, the use of modern cross-correlation algorithms means that the results are still highly accurate. The recording and evaluation of the PIV images can be completely decoupled in time and space so that many combinations of recording and evaluation methods can be defined and effectively used.

The illuminated flow field is recorded using a CCD device. The CCD array consists of a regular arrangement of light sensitive pixels which register light intensity. The scattered light intensity from the tracer particles is focussed onto the CCD array and the individual pixels convert the light into the form of charged electrons. The charge represents the digital intensity at each pixel and translates into a raw data image. The powerview 4M plus CCD device used was supplied by TSI with the PIV systems. It has an inter-line transfer CCD which provides a fast transfer of image data and hence results in shorter pulse separation time. The frame rate for the powerview 4M plus camera is 17 frames per second. The two successive particle images separated by time Δt, can be recorded either on two individual image frame (single-exposed mode) or on a single image frame (double-exposed mode). The double-exposed mode has an inherent disadvantage called directional ambiguity, which means one cannot determine which particle image is from the first exposure and which one is from the second exposure. However, this mode is superior for high-speed flows because a small exposure interval Δt, can be easily obtained since there is no need to switch the recording medium. For the single-exposed mode, the directional information is preserved since the sequence of the frames is known. But it requires the exposure interval Δt not to exceed the frame rate of cameras. Because of the large Δt, the application of single-exposed mode is limited and only suitable for the measurements of low-speed flow. To overcome this limitation, frame straddling technique was developed. This technique uses a high-performance progressive-scan-interline CCD chip as the sensor. The chip consists of an array of photosensitive cells and an equal number of storage cells. Upon the first illumination of the frame A, the light sensitive

pixels of the CCD are used to capture the image. Before the start of the next illumination the data is transferred to adjacent vertical shift registers making the active column ready for the capture of frame B. Data in the vertical shift registers is transferred to a PCI-Frame Grabber card in the PC whilst the active column collects the current illuminated image. Using this technique, the exposure interval Δt can be reduced. But the image data transfer rate limits the use of PIV for high speed flows. Each double frame 8 bit image occupies approximately 4Mbytes of RAM and the cameras and the lasers are available which operate at higher frequencies than 15 Hz, it is the data transfer from the CCD registers to the PC where the problem lies. Cameras and frame grabber boards have been developed with their own dedicated memory in order to attempt to over-come this problem in high speed PIV systems.

3.3.4 Particle Image Diameter

Accurate recording of the flow field requires careful selection of the camera lens. Nikon 105 mm focal length lenses with f-numbers ranging from 32-2.8 have been used in this study. Choosing the lens object distance and f-number ($f^{\#}$) are some of the most important factors in the physical set-up.

In order to perform the experiment, the field of view to be studied within the flow field has to be decided. Then it is possible to check whether the CCD available can be used to image the field of view. This again depends on the particle image diameter, d_τ, which is given by (Raffel et al, 1998)

$$d_\tau = \sqrt{M^2 d_P^2 + d_{diff}^2} \qquad 3.5$$

where M is the magnification of the camera, d_p is the physical particle diameter and d_{diff} is the diffracted limited image diameter.

The magnification M, is given by the image size (CCD array size) divided by the field of view and the diffraction limited image diameter is given by

$$d_{diff} = 2.44(1 + M)f^{\#}\lambda \qquad 3.6$$

where the f-number ($f^{\#}$) is set on the camera and is defined as the ratio of the focal length to the diameter of the aperture and λ is the wavelength of the incident light (532nm).

Westerweel (1997) suggested a particle image diameter of 2 pixels for digital PIV analysis. Another parameter to be taken into consideration is the depth of field. It is defined as the distance over which the image remains in focus, i.e., focal depth. All particles remain in focus when the light sheet thickness is smaller than focal depth and so standard practise is to choose a depth of field slightly larger than the light sheet thickness (Adrian, 1991). The depth of field is given by the following Equation (Raffel et al, 1998)

$$\delta z = 4(1 + M^{-1})^2 f^{\#2} \lambda \qquad 3.7$$

The depth of field, particle image diameter, field of view, magnification are all inter-dependant parameters and an initial study of the particle image diameters for different fields of view is discussed in Chapter 4.

3.3.5 Pulse separation time

In PIV, the two main timing parameters are the data acquisition rate (temporal resolution) and the pulse separation time. The maximum data acquisition rate is determined by the camera and laser repetition rate. The maximum repetition rate for the laser is 15 Hz and when in the PIV frame straddle mode the camera starts acquiring two consecutive single frame images. Hence the data acquisition rate is halved to 7.5 Hz. The pulse separation time (Δt) is one of the most important parameter in optimising the set-up for PIV and this is set by the user. The velocity of the fluid is calculated from the recorded tracer displacement within the known time separation. A timing sequence illustrating the way in which the camera and the laser work in relation to the data acquisition rate and pulse separation time is given in the Fig. 3.6. Some of the commonly used parameters in optimising the pulse separation time are explained below. The laser pulse delay is the amount of time to wait from the start of pulse sequence to until the first pulse and the PIV exposure is the time the first frame of the PIV camera is open. The trigger delay is used when the PIV cameras are

triggered externally. It is the time from the start of a sequence until the camera is triggered. In this study the camera was not triggered externally and the triggered delay option has not been used.

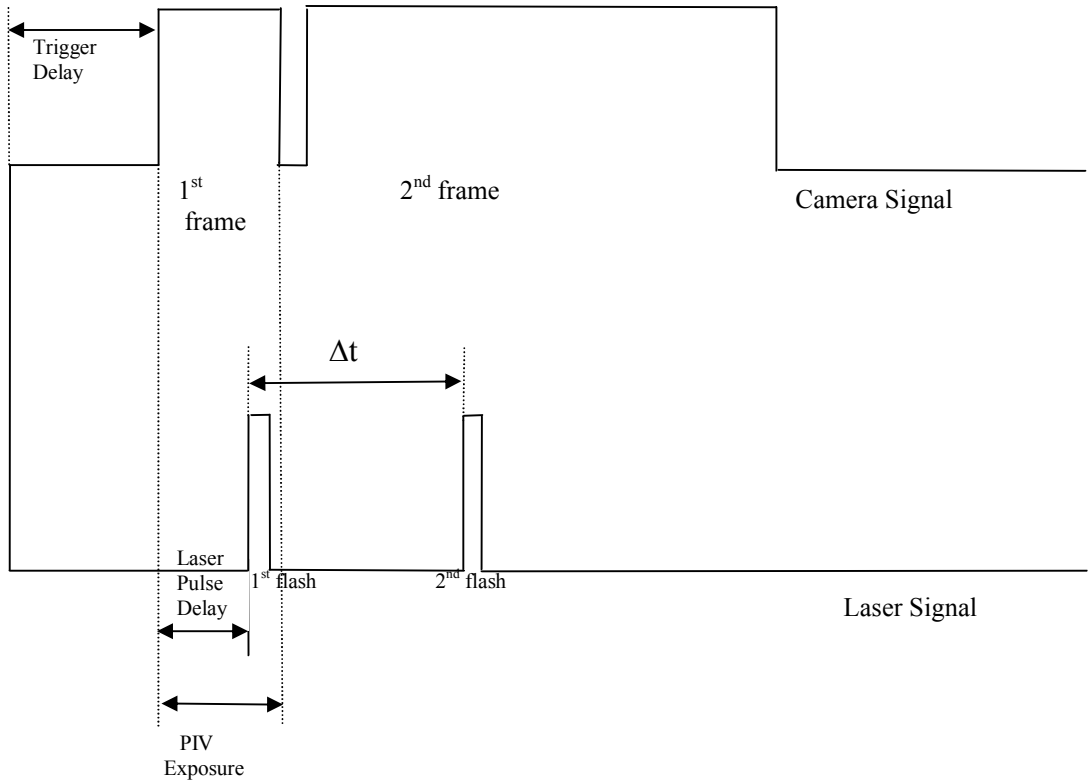

Figure 3.6: Timing sequence diagram

Adrian and Keane (1990) suggested the one-quarter rule which states that the magnitude of each particle displacement in an interrogation cell should be less than one-quarter of the interrogation cell dimension. For an interrogation cell size of 32x 32 pixels the maximum displacement should be less than 8 pixels. Hence Δt should be chosen such that the pixel displacement satisfies the one-quarter rule.

If there is significant out of plane motion, Equation 3.7 should be used to determine the acceptable limit of out of plane motion (Raffel et al 1998). It is important to carefully select the number of images required and this is dependent on the type of flow field being investigated. This was again investigated by a trial and error method wherein the flow field was observed for a range of number of image samples 50,100,150. The results from this study are discussed in Appendix B.

3.4 Processing and validation

This section looks into the processing and calculation of the vector field for the obtained images. The raw images obtained can be reconditioned and the background noises present in the data can be cancelled out. This again depends on the experiment setup and the quality of the data.

3.4.1 Cross Correlation method

In cross-correlation PIV, two images of the tracer particles within the fluid are taken separated by a short duration Δt. As the tracking of individual particles is difficult a statistical analysis procedure is adopted. Each image is divided into a grid of small interrogation areas. The corresponding interrogation areas within each of the two images are then cross correlated. The cross-correlation function is a pattern-matching routine which determines the displacement to shift the first area, to best overlap the second area. By scaling the displacement by the magnification of the camera lens and dividing by Δt, an average velocity for the fluid within the interrogation area can be obtained. This process is repeated at each grid point within the image, resulting in map of velocity vectors to describe the flow.

The cross-correlation function can be considered to be of two parts. Correlations between the images of particles in the first interrogation area with the images of same particles in the second image and correlation between the images of particles in the first interrogation area with images of different particles in the second area which are called random correlations. The random correlations contribute towards noisy peaks in the correlation plane. If the displacement pairs are constant then correlations between same particle pairs combine to produce a prominent peak. The location of this peak relative to the centre of the plane corresponds to the constant displacement while the height of the peak depends on the number of particle pairs. The signal-to-noise ratio (SNR) is defined as the height of the highest peak to the next highest peak and is a measure of the quality of the correlation. A high SNR ratio is an indication of the quality of the data. A value of 2 corresponds to a strong correlation resulting in valid vectors whereas a value of 1 might correspond to noise. This again depends on the experimental set-up and it is possible to set the threshold value below which the

vector will be rejected on the basis that it is noise. A threshold of 1.4 was set to obtain good quality vectors.

For the SNR ratio to be large, a number of conditions must be met:

- Time separation of images Δt should be long enough to resolve the displacement of the particles to sufficient accuracy, yet short enough that the particles do not move out with the light sheet. It should also satisfy the one-quarter rule of thumb suggested by Keane et al (1990). Keane et al (1990) suggested that if an interrogation area of 32×32 pixels is considered the maximum displacement in the interrogation region should be less than 8 pixels.
- The size of the interrogation area must be sufficiently small that the velocity gradient across it can be neglected, but large enough that there are sufficient particle pairs to contribute the correlation.
- The number of particles within each interrogation cell has an impact on the accuracy of the calculated velocity vector because the greater the number of particles contributing to the correlation peak, the stronger the signal to noise ratio. Raffel et al (1998) state that 5 particle images are required within each cell to achieve 95% valid detection in cross-correlation mode. Also the seeding has to be homogeneous so that statistical analysis can be applied.
- The out-of-plane motion should be small so that there are enough particles common to the interrogation area of each image. The out of plane motion should be less than 30% of the light sheet thickness (Raffel et al 1998).
- Another factor affecting the SNR is the cell overlap, defined as a percentage of the cell size. Cell overlap is the amount by which each interrogation cell is overlapped with subsequent ones, and is seen as a way of increasing vector grid density and hence perceived flow information. 50% is the most commonly adopted value. By implementing an overlap, the raw image information is used more than once at each location, resulting in the higher data yield.

In the INSIGHT-3G software used in this study, the cross correlation method is broken down to image conditioning and background image process, generating grids,

masking spots, performing correlation, locating peaks and performing validation. The back ground image process consists of subtracting the acquired images from the back-ground images. This is done to remove noise sources from raw data and improve the SNR. Image conditioners are applied to clarify the images to be processed. It is always advisable to optimise the experimental setup and avoid using the image conditioning and back ground image processes (TSI Insight 3G Manual). The experimental setup was optimised by using a high quality optical glass window in the test rig and by painting the back of the diffuser black so that a dark background is obtained.

3.4.2 Grid Engine

In the INSIGHT 3G software the generation of the grids is done by the grid engine. The grid engine breaks the input images into small interrogation spots for processing and initializes the vector field. For each grid point, the process manager copies the pixels from the input images into the spots and passes the spots to the SpotMask Engine. With frame straddle image capture, Spot A is from Frame A and spot B is from Frame B. The process grid is a list of Grid points and each Grid point defines the pixels from Spot A and Spot B. The grid engine can process the vector field in single as well as in multiple passes. The standard grid engine in INSIGHT 3G is the Nyquist grid which is a single pass grid engine with 50% overlap (TSI Insight 3G Manual). The Nyquist grid is defined as the grid whose frequency is twice the largest frequency contained in the image to be displayed (Perny et.al, 1982).

In multiple-pass processing, the vector processing is done in two or more passes. After the first processing pass, the vector field from the previous pass can be used to optimise the spot grid for the next processing pass. The spots are offset by the particle image displacement distance obtained from the first processing pass. This results in an increase in the SNR as the pairs lost due to in plane motion are minimised. The multiple pass processing grid is known as recursive Nyquist grid where the processing is done in two or more passes. The first processing pass computes the vector field with 50% overlap. The vector field is validated and the results from the first processing pass are used to optimise the spot offsets for the second processing pass.

There is also the option of using deformation grids for the flow with large velocity gradients. Due to the high velocity gradients all the particles in an interrogation region do not move exactly with the same distance and the correlation peak will have a splintered or elongated peak. The deformed grid method is based on a similar idea to multiple pass processing. The first processing pass is the standard Nyquist process. The second processing is same as the recursive Nyquist grid wherein the vector information from the first pass is used to optimise the vector field. In the third processing pass, the four corner neighbouring vectors are used to deform the spot in an attempt to eliminate the gradient in the raw image data. This enhances the correlation peak.

3.4.3 Spot Mask Engine:

The Spot mask engine conditions the spots for processing and passes the spots to the correlation engine. It is used to modify or condition the spots and can increase the signal to noise ratio of the correlation map. The Gaussian Mask engine used in this study multiplies each pixel in spot A by a Gaussian weighting function so that the spot is bright in the centre and dark around the edges. This weighting gives more value to the centre pixels and less to the edge pixels (TSI Insight 3G manual).

3.4.4 Correlation Engine:

Within each cell, the spatial correlation between the first and second frame of the image pair is calculated via Fast Fourier Transforms (FFTs). This results in a correlation map with a peak intensity positioned at the point where the average displacement within the cell lies. Since the input data is discretized, the correlation values exist only for integral shifts. The maximum value in the correlation plane yields the mean displacement to an accuracy of ± ½ pixels. The FFT correlator in INSIGHT 3G which computes the correlation using Fast Fourier Transform (FFT) has been used in this study.

3.4.5 Peak Engine:

One of the most crucial features of digital PIV evaluation is that the position of the correlation peak should be measured to sub pixel accuracy. Three point estimator methods are used to estimate the displacement from the correlation data at the sub pixel level. The most common three point estimators are the Peak centroid fit, parabolic peak fit and the Gaussian peak fit. Of all the three the Gaussian peak fit is most frequently used because the particle images if properly focussed describe Airy intensity functions which are approximated well by a Gaussian intensity distribution. The correlations between two Gaussian functions also result in a Gaussian function (TSI Insight 3G Manual).

3.4.6 Validation

The validation process can be used both to check the quality of the data and remove any spurious vectors present. In most modern PIV software, the process of identifying spurious vectors is automated (as manually checking 1000 vector maps, each containing 4000 vectors could be somewhat time consuming). Inclusion of spurious data in calculations can have dramatic consequences. There are a number of ways in which validation can take place, and are discussed below.

3.4.7 Pre-defined limits

Defining allowable vector limits for the velocity field requires some previous knowledge of the flow itself, as implementing it excludes any velocity vectors outside the defined range. This should be used with caution because, unless the flow is very well behaved (e.g. unidirectional), it is possible that real vector data will be excluded. This validation technique is not so useful where there is a large range of velocities within the flow, because it is likely that spurious vectors will fall within the range of the velocities present. The selection of the limits depends again on the type of flow being investigated and using them can be avoided if there is a sudden change in behaviour of the flow and also if the problem being investigated is a new one and there is no pre knowledge of the type of flow being investigated.

3.4.8 Consideration of Local Flow Conditions

The most trusted method of flow validation is that which considers the neighbouring vectors. This method was proposed first by Westerweel (1993), who stated that if a vector deviates substantially in direction or magnitude compared to its neighbouring vectors, flow continuity is not satisfied and the vector must be spurious. He proposed a technique whereby at each vector location the average magnitude and standard deviation of the surrounding velocities (usually 8 vectors) be calculated. Then the vector in question was compared to the average of its neighbours, plus or minus a factor multiplied by the standard deviation of the neighbouring vectors. If it was outside the defined range, the vector was deemed spurious and removed.

Westerweel's (1993) method was further improved and it was found that using the median information from the neighbouring vectors resulted in better accuracy. The median and the mean value of the surrounding vectors are used to remove the spurious vectors. The median validation tool was applied first and then the mean validation tool was applied with a tolerance of 4 m/s (This was suggested by Dr. Martin Hyde, from TSI, private communication).

3.4.9 Replacing Removed Data

It is important that if data is removed from a vector field because it is deemed to be spurious, that it has to be replaced. If the data is not replaced, it can affect any calculated statistics in the event that zeros are included. The most popular form of data replacement is linear interpolation. This method calculates the average magnitude of the surrounding vectors and replaces the missing vector with such value. This ensures flow continuity but if there are too many spurious vectors removed, the effect of replacing via linear interpolation can be to smooth the flow field. However, it must be remembered that, if the data quality is poor, then the initial experimental set-up should be revised and re-optimised, as there is little point trying to create good data. Note that smoothing has not been used, as this type of post-processing takes no consideration of the actual quality or validity of the data. It only serves to make the

flow continuity look better than has actually been recorded for presentation purposes on screen.

3.5 Summary

The PIV process has been explained in detail together with the optimisation of the various parameters. The most important steps in the process are the physical setup of the light sheet, seeding, camera and timing. By ensuring a good experimental setup and interactively checking the quality of data, the timing parameters can be optimised to obtain good quality vectors. The procedure shown in Fig. 3.3 is used to perform the experiments during this project. The parameters generally employed during the experimental investigation are listed in Table 3.3

Parameter	**Type/Value**
Acquisition	
Laser	Nd:Yag
Laser Power	120 (mJ)
Pulse Separation Time (Δt)	10-250 (μs)
$f^{\#}$	4-8
Processing	
Grid Engine	Recursive Nyquist Grid
Initial Grid Size	64 × 64 pixels
Final Grid Size	32 × 32 pixels
Maximum Displacement	8 pixels
Correlation Engine	FFT correlator
Peak Engine	Gaussian peak
Validation	Linear interpolation, Mean & Median tools

Table 3.3: Typically employed PIV parameters

Chapter 4: Two-Dimensional Flow Rig

4.1 Introduction

The aim of this study was to measure the flow field upstream of the substrate in a diffuser using PIV for comparison with CFD predictions. When PIV is applied to conical diffusers for 3-D flows, it requires a curved optical window which results in errors caused by optical distortion. Considerable progress has been made in PIV over the last 20 years and using Stereoscopic PIV and latest algorithms, PIV can now be successfully applied to conical diffusers for 3-D flows. However, at the start of this study it was decided to study 2-D diffuser-monolith flows. Here the term 2-D diffuser refers to a plane walled diffuser rather than an axisymmetric system. Analysing 2-D flows has certain advantages when compared to 3-D flows. 2-D flows will still retain many of the flow features associated with 3-D flows and axisymmetric systems (Benjamin et al, 1996). With the use of 2-D flows the flow behaviour can be better understood and results in fewer measurements. The computational resources to simulate 2-D flows are low when compared to 3-D flows. Hence in order to investigate the flow field in the diffuser upstream of substrates, a 2-D steady flow rig was built. This required the design and manufacture of a 2-D plenum chamber, 2-D contracting nozzle and 2-D diffuser.

4.2 Two-Dimensional Diffuser

Present exhaust systems have a diameter of around 55 mm upstream of the diffuser-substrate assembly. Also due to confined space, wide angle diffusers generally around 60 degrees are used upstream. The design of the 2-D diffuser was based on a 55 mm inlet height and 60 degree total included angle (Fig. 4.1). It was thought that visualizing a large area of the flow field would be helpful in understanding the flow upstream of the monolith. Hence the limiting factor in selecting the outlet height was the available substrate size. Generally substrates have a diameter around 120-150 mm. A large monolith of around 300 mm in diameter was obtained from NGK. The 2-D diffuser was designed so that the diffuser has a jet flow at the centre with separated regions on each side of the central jet as observed in many real world conditions.

The 2-D diffuser was designed by using the ESDU reference manual (ESDU 76027). ESDU provides validated engineering design data and optimise design iterations so that the validation of the final design is quicker and easier. This ESDU design assumes an open diffuser and the geometry was chosen to ensure that flow separation and jet flow were obtained. The flow field in the ESDU design will be different from that to be studied on the rig which features a large resistance (substrate) downstream but it was considered a useful starting point. The static pressure recovery coefficient for diffusers with jet flow and an inlet aspect ratio of $b/W_1 \geq 6$ is approximately around 0.25 (ESDU 76027). A diffuser inlet height of 55 mm (comparable with the nozzle exit height discussed in Section 4.3) and a 60 degree total angle diffuser ensured jet flow in the diffuser. Fig. 4.1 shows the schematic of a 2-D diffuser

The length of the diffuser L_d is given by Equation 4.1 and was 108.2 mm

$$L_d = \frac{W_2 - W_1}{2 * \tan\theta} \qquad 4.1$$

where W_1 and W_2 are the inlet and the outlet heights respectively and θ is the half included angle

The static pressure recovery coefficient is given by

$$C_{pr} = \frac{p_2 - p_1}{\frac{1}{2}\rho U_1^2} \qquad 4.2$$

where p_2 and p_1 are the static pressure at the inlet and exit of the diffuser.

Some of the other factors of interest in the design process are explained below. The pressure changes due to sudden enlargement of area in a duct are functions of both Reynolds number and the area of enlargement for Re<4000 whereas for higher Reynolds number the pressure changes depend on area ratio ($AR = \frac{W_2}{W_1}$) only. If the velocity profile at the plane of sudden enlargement of area in a duct is not uniform the total pressure loss coefficient is increased. Two dimensional mean flow can be assumed if the aspect ratio (b/W_1) is greater than 4 to 5 (Schetz et al 1999). An aspect ratio of 4 was chosen in order to achieve two-dimensional flow.

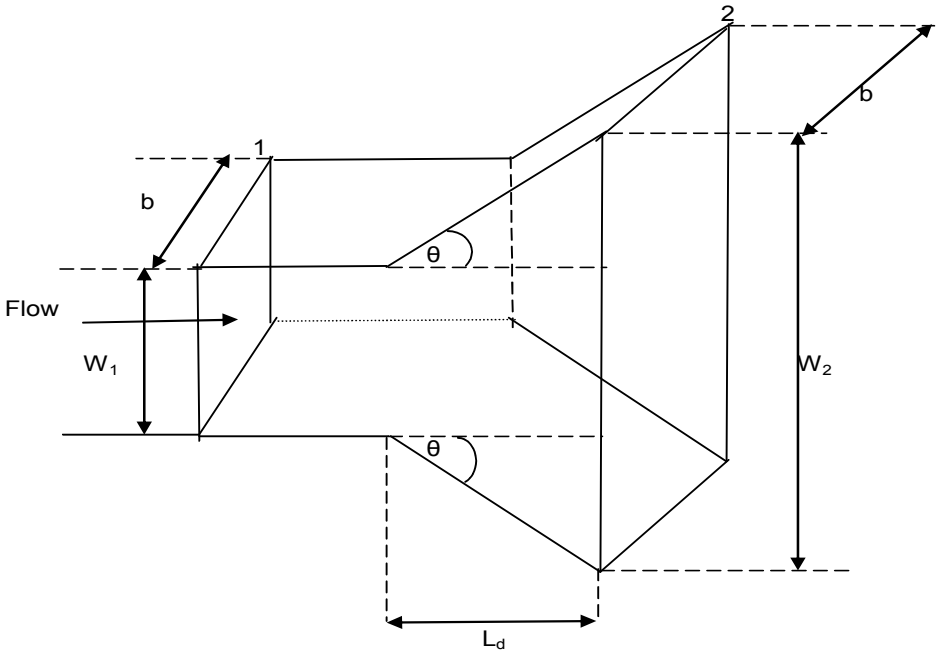

Figure 4.1 Schematic diagram of 2-D diffuser

4.3 Two-Dimensional Contracting Nozzle

The function of a contracting nozzle (Fig. 4.2) is to provide uniform velocity at its exit and reduce the turbulence. It also provides a well defined inlet boundary condition for the CFD simulations. In a similar study on an axisymmetric catalyst system (Haimad (1997)) showed that a uniform flow at the inlet to the diffuser results in a reduction in the maldistribution in the flow at the exit of the substrate. In converging ducts, the area decreases along its axis which results in an increase in flow velocity and a decrease in static pressure. Due to the flow acceleration all the non uniformities and turbulence in the flow are reduced and a well defined contour-shaped converging duct will give a uniform velocity at its exit.

Some of the important criteria when designing a contraction nozzle as mentioned by Morel (1977) are:

- Exit flow uniformity to a prescribed level
- Boundary layer separation
- Minimum exit boundary layer thickness

Contraction ratio (CR), contour shape and the nozzle length determine whether the nozzle has the desired properties. There was concern regarding boundary layer separation due to adverse pressure gradient at the two ends (inlet and exit) of the nozzle. This was avoided by increasing the length of the nozzle but for minimum boundary thickness the length should be minimised. Also the flow was less likely to separate at the exit as the convex curvature at the exit has a stabilising effect whereas the concave curvature at the inlet has a destabilising effect (Bell et al, 1989).

2-D contractions require around 25% more length than axisymmetric systems in order to achieve the same uniformity. Also thick boundary layers at the plane wall have to be avoided as they result in strong secondary flows (Mehta et al, 1979).

The contour shape for the 2-D nozzle was designed using Morel's method (Morel 1977). A suitable contraction ratio (CR) of 4 was chosen at the start and the design criterion for the nozzle was to have 1% flow non-uniformity at the exit and no boundary layer separation. Fig. 4.2 shows the parameters controlling the wall contour of the 2-D nozzle.

Figure 4.2 Wall contour constructed of two matched cubic arcs (Morel, 1977)

The overall design process in obtaining the wall contour and length of the nozzle are explained below. The inlet, H_2 and CR are initially fixed and the desired non-uniformity u_2, C_{Pi} and C_{Pe} are chosen and from them the length L_t and the contour shape (Fig. 4.3) are derived from the method suggested by Morel (1977). A detailed procedure in designing the 2-D contracting nozzle using Morel's method is given in Appendix C.

The specifications of the designed 2-D contracting nozzle are given below:
Contraction ratio=4
Inlet nozzle height=220 mm
Outlet nozzle height=55 mm
Aspect ratio=4
Total nozzle length (Including settling chamber lengths) L_t=202.93 mm

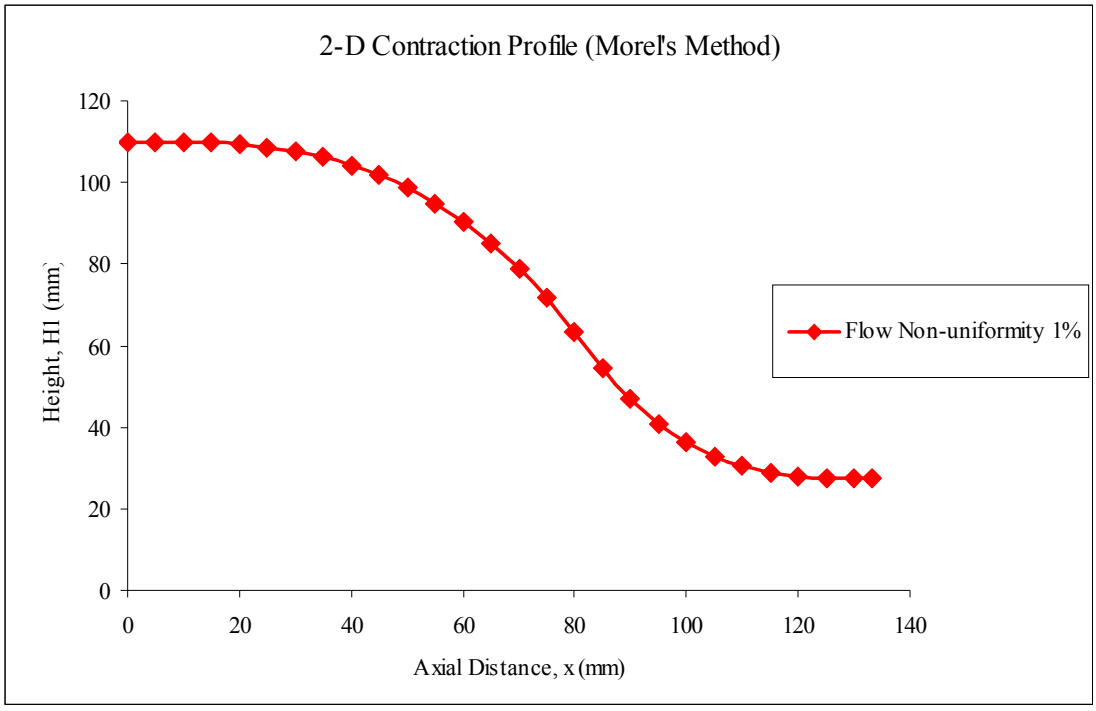

Figure 4.3 Wall Contour shape of the 2-D contracting nozzle

4.4 Plenum Chamber

The 2-D nozzle was fabricated using Bendy MDF. The next stage of the design process was to design a 2-D plenum chamber to be connected upstream of the 2-D nozzle. The dimensions at the exit of the plenum were already known as it was connected upstream of the 2-D nozzle. The plenum chamber had a square cross-section of 220 × 220 mm. Previous axisymmetric studies Haimad (1997) on the rig used a 12 litre cylindrical plenum. Using this as a reference point the required length of the plenum chamber was obtained which was about 1.21 m.

4.5 Isothermal 2-D flow rig

The oblique angle one-dimensional flow rig as described in Fig. 2.3 was modified in order to perform 2-D flow studies as shown in Fig. 4.4. There were no changes to the one-dimensional isothermal flow rig used up to the VFM [10]. The 2-D plenum chamber [11] was mounted vertically and connected to the VFM by a 50 mm flexible circular pipe. The designed 2-D nozzle [12] was connected to the 2-D plenum chamber. The 2-D diffuser [13] with two sides made of optical glass was connected downstream of the 2-D contracting nozzle. The two sides of the 2-D diffuser were made of high transmission crown glass in order to visualise the tracer particles from a pulsed laser and to capture the visualisation by cameras. A substrate [14] of rectangular cross-section was located downstream of diffuser and a 30 mm outlet sleeve [15] was placed downstream of the monolith. The designed nozzle had to be tested to verify that a uniform velocity profile was obtained at its exit. The testing of the nozzle is done by disconnecting the diffuser, substrate and outlet sleeve in Fig. 4.4. The instrumentation and testing are described in the following sections.

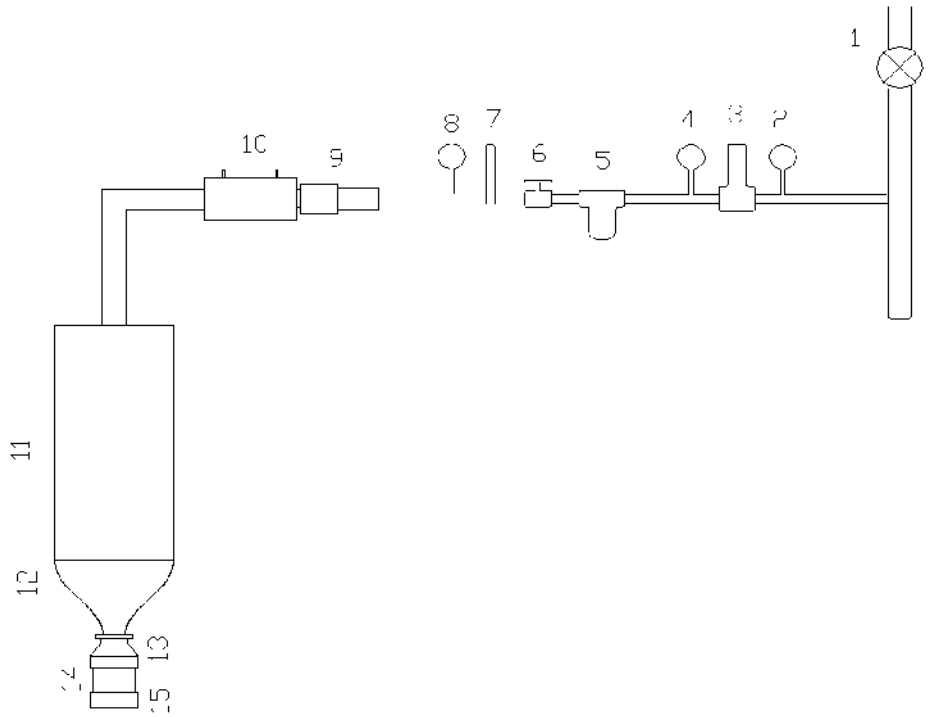

Figure 4.4 2-D isothermal flow rig

1. Main Valve 2. Pressure Gauge 3. Pressure Regulator 4. Pressure Gauge 5. Filter 6. Gate Valve 7.Safety Relief valve 8. Pressure Gauge 9. Flow Straighteners 10. Viscous Flow Meter 11. Two-Dimensional Plenum 12. Two-Dimensional Nozzle 13. 60^0 2-D diffuser 14. 2-D Monolith 15 Outlet Sleeve

4.6 Instrumentation and data collection

The velocity profiles at the exit of nozzle were measured using a TSI IFA 300 constant temperature, hot-wire anemometry system (HWA). The probes used were 5μm platinum plated tungsten wires (Dantec 55 P11). The probes were calibrated using a fully automatic TSI 1129 calibration rig. A sampling size of 2048 points per channel and a sampling rate of 2000 Hz were set for all the measurements. The data points were separated by a distance of 2.5 mm.

4.7 Velocity Profile at the exit of the Nozzle

The designed nozzle was tested to verify that it provides uniform velocity profile at the exit. There was no flow straightener in the plenum chamber at the start of this study. The x-axis corresponds to the axial coordinates and y-axis to the lateral coordinates. Initial velocity profiles taken at the exit of the nozzle showed more than

1% non-uniformity along the y-axis and the velocity profile was inclined to one side of the nozzle along the x-axis and also the non-uniformity along the x-axis was very high without the flow straighteners. Initially it was thought that the nozzle would smooth all the non-uniformities from the inlet flow. This was not the case especially along the x-axis. In order to reduce the non-uniformities the settling chamber at the exit of the nozzle was increased giving the flow more time to smooth out. An outlet sleeve of 20 mm was attached at the exit of the nozzle and this increased the overall length of the nozzle. Further measurements were taken at the tip of this exit sleeve. To reduce non-uniformities further, a flow straightener was placed in the plenum chamber. The flow straightener consisted of a bunch of straws of diameter 2 mm and of length 15 cm approximately which were grouped together and placed closed to the inlet of the plenum chamber. This had very little effect on the velocity profiles along both x and y-axes. The non-uniformities were reduced however when the flow straightener was placed closed to the exit of the plenum chamber (inlet to the nozzle). However the non-uniformities along the y-axis were still more than 1% and there was a slight inclination of the flow on one side of the nozzle along x-axis. The length of flow straightener was then increased to further smoothen the velocity profiles by having a honeycomb structure (5 cm in length and 10 mm channel hydraulic diameter approximately) and fine gauze mesh attached to the straws. This considerably improved the velocity profiles and the non-uniformities along the y-axis were now less than 1%. The inlet to the plenum chamber was a 50 mm circular flexible plastic pipe discharging into the square cross-sectional chamber. The flexible pipe was connected straight and normal to the plenum chamber and any bends were avoided. Also a splitter (radial vane) at the inlet to the plenum chamber was connected so that it spread the flow uniformly across the peripheral regions of the plenum chamber as this was thought to be the cause of inclination along the x-axis. The final velocity profiles along the x and y-axes obtained are shown in Figs. 4.5 & 4.6. Along the x-axis at the edges there seemed to be some variation in the velocity. This could have been due to the flow separation at the edges or due to irregularities in the flow straightener but the profiles were still thought to be acceptable.The profiles across the y axis were very flat.

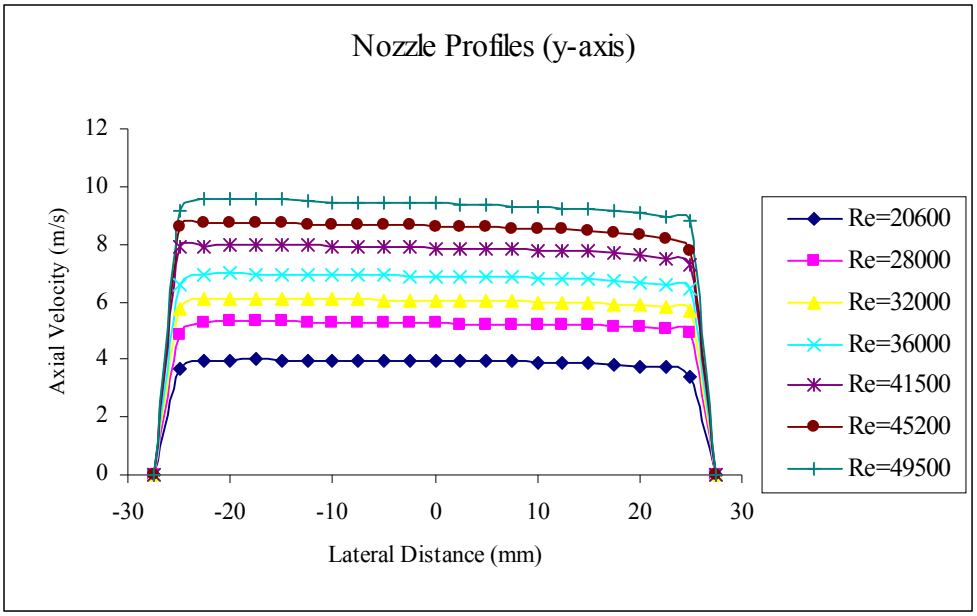

Figure 4.5 Velocity profiles at the exit of the nozzle along y-axis

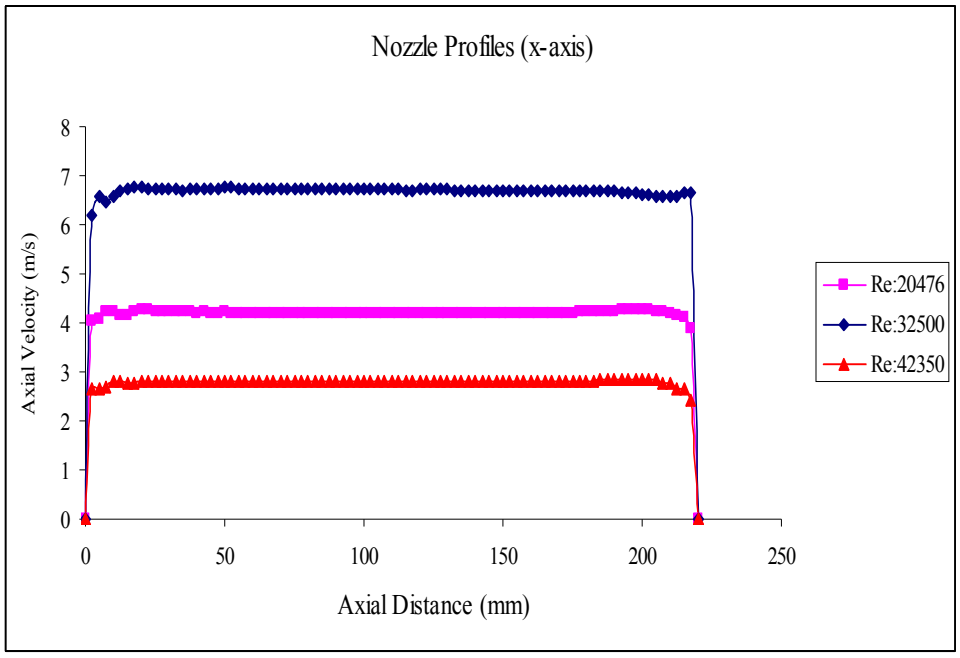

Figure 4.6 Velocity profiles at the exit of the nozzle along x-axis

4.8 2-D Nozzle CFD Model

At the start of this study it was thought to be a useful exercise to perform CFD analysis of the nozzle to get used to using the STAR-CD software and so as to provide a comparison with the experimentally determined velocity profiles. The mesh was constructed in the PROSTAR pre-processing software. Within this, the single block

method was used with the wall shape contour obtained using the SPLINE command (Fig. 4.7). The flow direction was along the x-axis and the two side faces were defined as symmetry planes along the z-axis. A uniform axial velocity was applied at the inlet boundary condition and the exit plane was defined as a pressure boundary. The k-ε high Reynolds number turbulence model with a standard wall function was used. The mesh comprised of 3500 cells and had a cell width of 4 mm in the z-direction. The velocity profiles were obtained at the exit plane and the results showed a uniform velocity profile at the exit and non-uniformity was within the acceptable level. A comparison with the experimentally determined values shows good agreement as shown in Fig. 4.8.

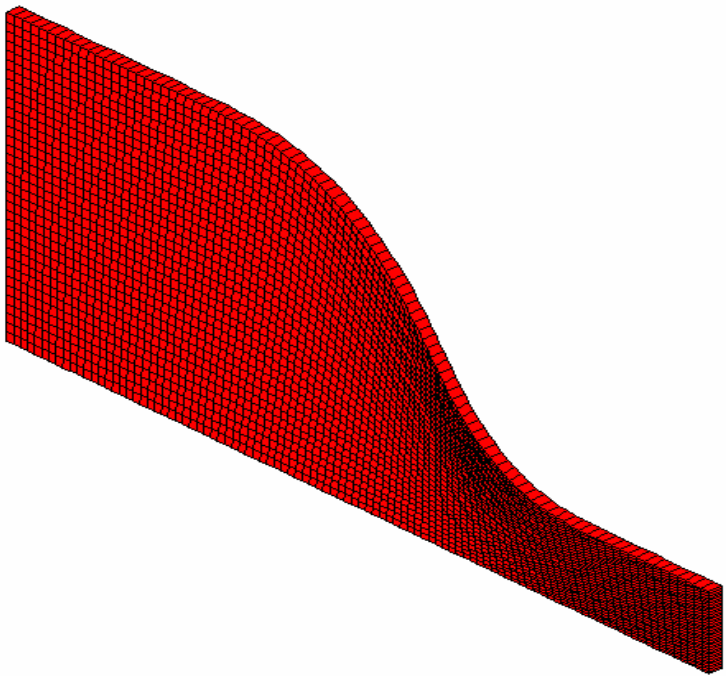

Figure 4.7 Mesh of 2-D contracting nozzle

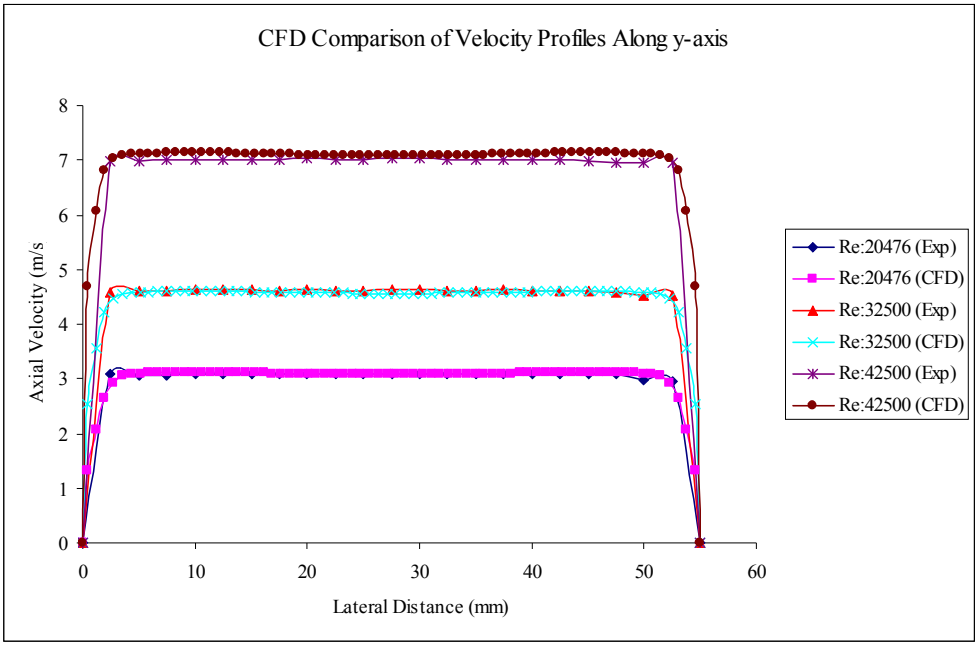

Figure 4.8 Comparison of experimentally determined and CFD model predictions

4.9 Assembling the 2-D rig

The diffuser-substrate assembly with the outlet sleeve was connected back to the nozzle as shown in Fig. 4.4. Hot wire velocity measurements were made 30mm downstream of the substrate for five different flow rates and two substrate lengths. One of the limitations of the 2-D rig is the maximum flow rate that can be obtained. As the pressure regulator was initially designed for axisymmetric flow rig studies the maximum velocity was around 35 m/s for a 55mm diffuser inlet diameter. But for 2-D flows with an aspect ratio of 4, the maximum velocity at the diffuser inlet was 8.5 m/s. This was thought to be acceptable as it is in the velocity range normally found in underbody catalytic converters. Although the entrance effect as seen from oblique angle flow measurements is significant at high velocities this was still thought to be acceptable as the main purpose of the PIV studies was to study the flow distribution upstream in the presence of the substrate.

At the start of this study a 152 mm monolith supplied by Johnson Matthey PLC with a porosity of 0.77 was used. However, due to the large resistance and low flow rates the maldistribution in the flow measured at the exit of outlet sleeve was substantially uniform. It was, therefore, decided to use a shorter brick with less resistance to produce a larger maldistribution in the flow for the same flow rate. Hence a 27 mm

monolith and 100 mm monolith supplied by NGK with a channel hydraulic diameter 1.12 mm and 0.77 porosity were used in this study.

4.10 Hot wire velocity profiles from the exit of the substrate

Velocity profiles were obtained using hot wire anemometry at the exit of the substrate. This gave a measure of maldistributed flow across the substrate and would be useful for comparing with CFD predictions. As the flow exits the substrate it interacts with neighbouring channels and results in jet mixing. It is very difficult to capture the jets from individual channels due to their close vicinity. Hence the hot wire profiles were measured at various distances from the substrate exit. It was found that the flow profiles were smooth at about 25 mm from the exit of the substrate. Also in a similar study Clarkson (1995) showed that at a distance of 30 mm from the exit of the substrate the flow distribution is developed enough to be smooth. Figs. 4.9 and 4.10 shows the flow distribution 30 mm from the exit for two substrate lengths (27 mm and 100 mm) and at five different flow rates. The Reynolds number is based on the equivalent hydraulic diameter (0.088 mm) at the rectangular nozzle exit slot. From the flow distribution profiles there is a central region where the velocity is almost uniform and starts decreasing towards the periphery. As will be discussed in the next chapter this is due to the formation of a central core region in the diffuser and the separation of the flow at the diffuser inlet.

The flow profiles have been non-dimensionalised against the velocity at the inlet to the diffuser. The maldistribution in the flow profiles is defined as the ratio of the maximum velocity to the mean velocity. The maldistribution in the flow increases as the Reynolds number increases (Figs 4.11 & 4.12) and similar results were also observed by Haimad (1997). The maldistribution increases as the length of the substrate decreases. Increasing the length of the substrate, results in a comparatively uniform flow at the exit.

A significant amount of flow is found in the near wall region. This is due to the wall effect and will be explained in more detail with the help of vectors obtained from the PIV experiments in the next chapter. There are considerable problems associated with hot-wire measurements near a wall (Lomas, 1986). Several effects cause errors when

a hot wire sensor is used to make velocity measurements near a wall. The radiation heat loss from the sensor to cooler wall unbalances the Wheatstone bridge and this appears to increase the fluid velocity. Then there is the hydrodynamic interaction between wall, sensor and the support needles which cause additional errors. These errors are again a function of sensor-to-wall distance, support needle orientation and fluid velocity and exist to about 2 mm from the wall (Lomas (1986)).

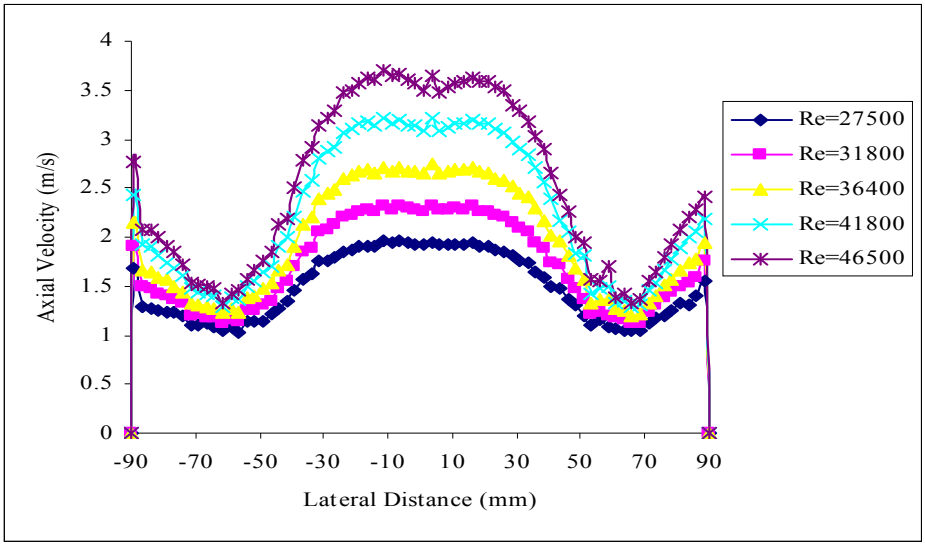

Figure 4.9 Flow distribution 30 mm from the exit of 27 mm substrate at five flow rates

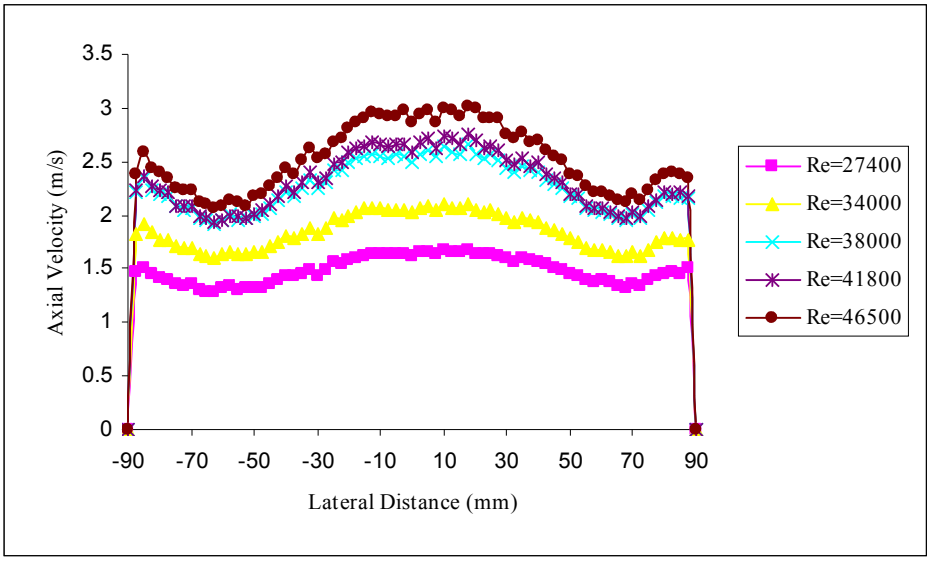

Figure 4.10 Flow distribution 30 mm from the exit of 100 mm substrate at five flow rates

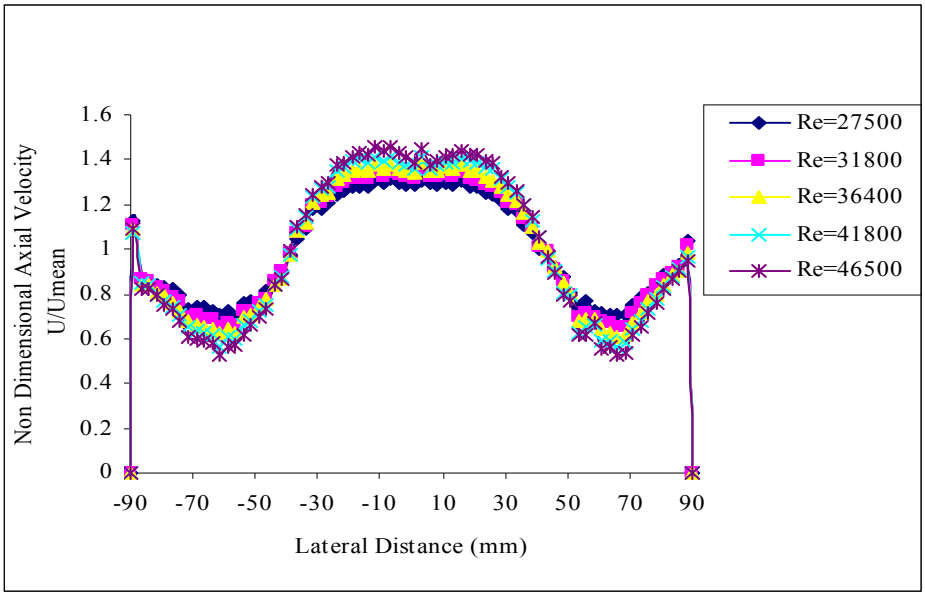

Figure 4.11 Non-dimensional flow distribution chart 30 mm from the exit of 27 mm substrate at five flow rates.

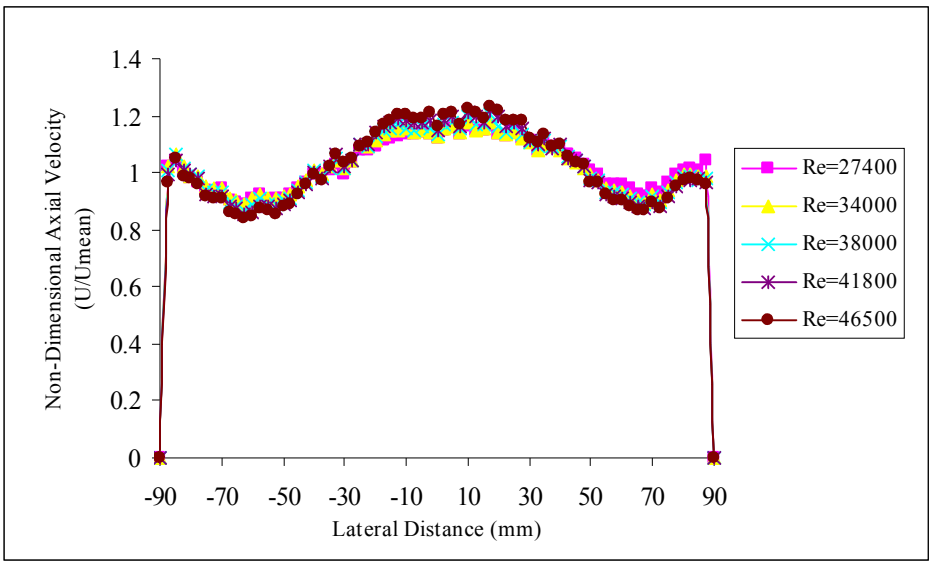

Figure 4.12 Non-dimensional flow distribution chart 30 mm from the exit of 100 mm substrate at five flow rates.

4.11 Laser Safety Considerations

Laser safety calculations were performed and are shown in Appendix D. The PIV pulsed laser was a 120mJ Nd:YAG laser. The laser safety considerations and the nominal hazard distances for viewing the laser beam directly and also viewing the diffused reflections with and without the cylindrical lens were calculated. The results are tabulated in Appendix D.

4.12 2-D PIV Experimental Set-up

The 2-D rig consisting of plenum chamber, contracting nozzle, diffuser and the substrate was mounted vertically. The laser was mounted on a bench vice and aligned perpendicular to the rig and the camera using plumb lines. A spherical lens of 1000 mm focal length was used in combination with the cylindrical lens to obtain a light sheet. The rig is placed at approximately 750 mm from the laser resulting in minimum thickness across the field of view. The camera was mounted on a custom designed traverse with the ability to traverse horizontally and vertically. The camera was also aligned perpendicular to the rig using plumb lines. Figs. 4.13-4.17 show the experimental set up for the PIV investigation.

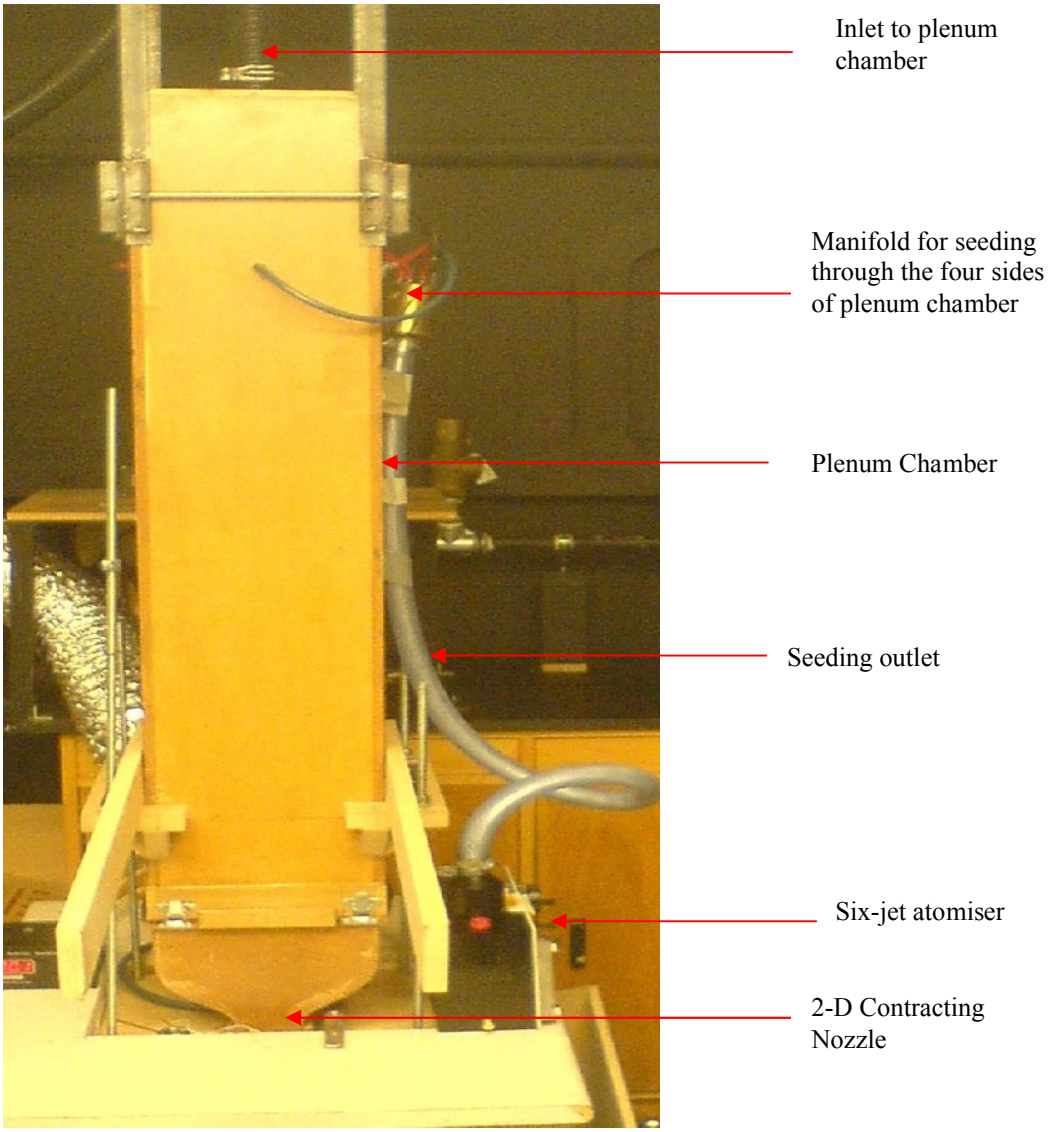

Figure 4.13 2-D rig showing the plenum chamber and the contracting nozzle

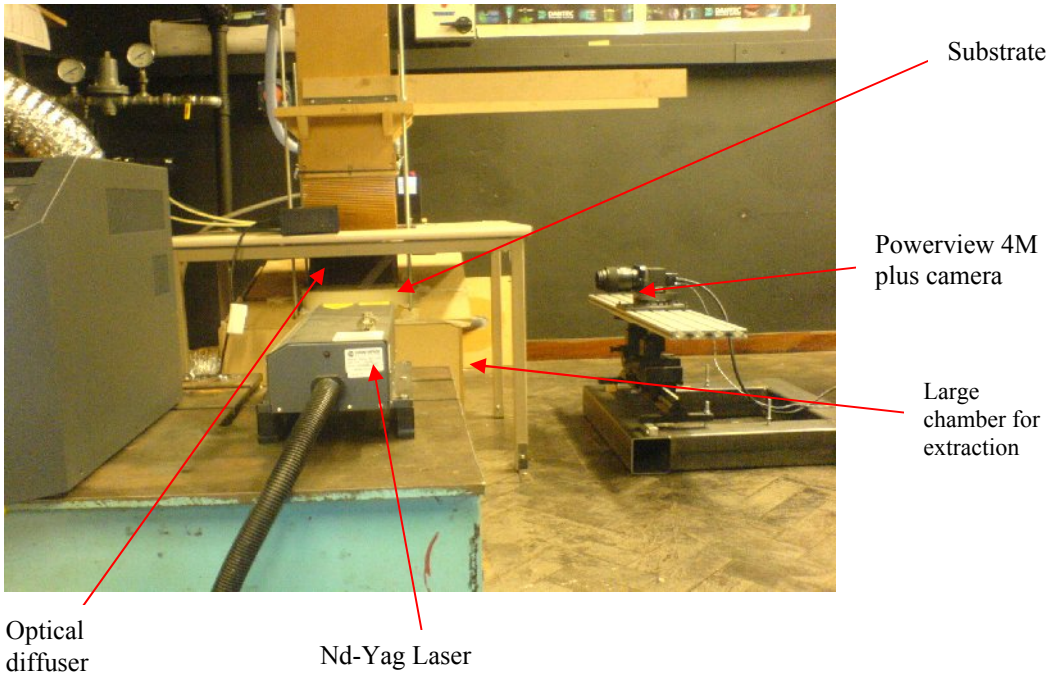

Figure 4.14 Overview of the Laser, Camera and the rig setup

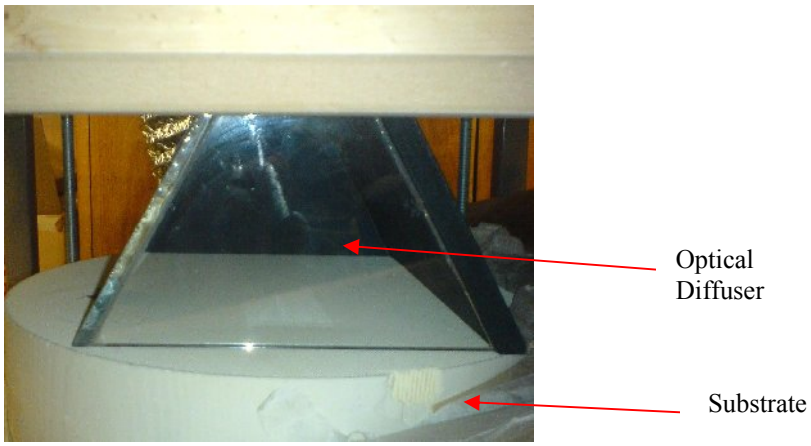

Figure 4.15 Diffuser with optical window

Figure 4.16 Model 9306A Six-Jet atomizer (TSI Manual)

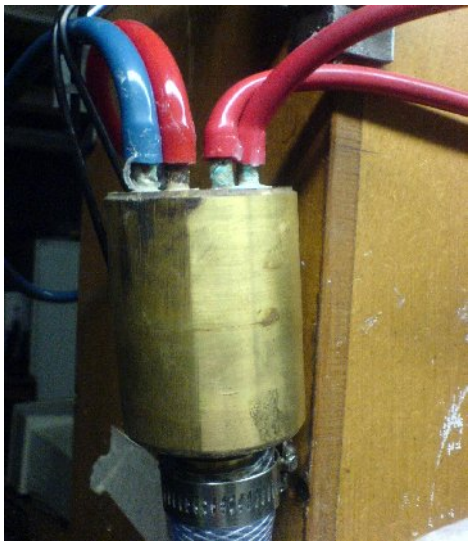

Figure 4.17 Manifold for seeding through the four sides of plenum chamber

4.13 Optimising the seeding and the particle image diameter

Initially the single jet atomiser was used to get used to the PIV software INSIGHT 3G, calibration, operating of the camera and processing of the captured PIV images. The laser was used in the frame straddle mode wherein the first laser pulse was fired at the end of the frame A and then the second laser pulse was fired at the start of the frame B separated by the pulse separation time Δt.

Olive oil was used for seeding and the atomiser pressure was set to 25 psi. The seeding particles were inserted into the flow using a TSI six-jet atomiser. In order to achieve uniform seeding, it was decided to have a manifold design (Fig. 4.17) through which the flow would be inserted from the four sides of the plenum chamber. The amount of seeding can be controlled using the number of jets opening in the six jet atomiser. Also to extract the seeded particles a large chamber was placed downstream of the outlet sleeve as shown in Fig. 4.14. This was done to avoid any interference to the flow from the extraction of the seeding particle and also avoid the interference of seeding particles in the plane of the camera. The selection of the seeding particle is very important to obtain good data from PIV. Table 4.1 shows the flow rate per jet from the six-jet atomiser at different inlet pressures.

Input Pressure		Aerosol Output
psi	kPa	(L/min)
5	34.5	2.4
10	68.9	3.7
15	103	4.7
20	138	5.7
25	172	6.6
35	241	8.3
45	310	10.2

Table 4.1 Aerosol flow rate per jet (TSI Six-Jet atomiser manual)

The particle diameter of the olive oil particles is about 1-2 μm. It was desired to observe the complete flow field of the diffuser, which required a field of view of 180 mm x 180 mm. Westerweel (1997) suggested a particle image diameter of 2 pixels for digital PIV analysis. An initial study of the particle image diameters for different size fields was made using Equations 3.5 and 3.6. The powerview 4M camera has a pixel resolution of 2048 × 2048 pixels and the pixel size is 7.4 μm × 7.4 μm. Table 4.2 shows the calculated particle image diameter for different fields of view and $f^{\#}$ numbers.

Field of view (mm × mm)	Magnification (M)	$f^{\#}$	λ (nm)	d_{diff} (μm)	d_p (μm)	d_τ (μm)	d_τ (pixels) based on 7.4 μm/pixel
180 × 180	0.0071	2.8	532	3.66	1.00	3.66	0.49
180 × 180	0.0071	4	532	5.23	1.00	5.23	0.71
180 × 180	0.0071	5.6	532	7.32	1.00	7.32	0.99
180 × 180	0.0071	8	532	10.46	1.00	10.46	1.41
180 × 180	0.0071	11	532	14.38	1.00	14.38	1.94
90 × 90	0.0190	2.8	532	3.70	1.00	3.70	0.50
90 × 90	0.0190	4	532	5.29	1.00	5.29	0.71
90 × 90	0.0190	5.6	532	7.41	1.00	7.41	1.00
90 × 90	0.0190	8	532	10.58	1.00	10.58	1.43
90 × 90	0.0190	11	532	14.55	1.00	14.55	1.97
60 × 60	0.0638	2.8	532	3.87	1.00	3.87	0.52
60 × 60	0.0638	4	532	5.52	1.00	5.52	0.75
60 × 60	0.0638	5.6	532	7.73	1.00	7.73	1.04
60 × 60	0.0638	8	532	11.05	1.00	11.05	1.49
60 × 60	0.0638	11	532	15.19	1.00	15.19	2.05

Table 4.2: Particle image diameters for different fields of view and $f^{\#}$ numbers

From Table 4.2, it can be seen that the particle image diameter increases as the field of view, i.e., interrogation area decreases. For large fields of view, the $f^{\#}$ number or the seeding particle size had to be increased in order to obtain the recommended 2 pixel image diameter. Increasing the $f^{\#}$ number resulted in low intensity images. The use of larger particles must be employed with caution and its ability to follow the flow must be considered. Initial tests were performed by using $f^{\#}$ number in the range of 4-8 and the results showed that a particle image diameter of 1 pixel resulted in good quality vectors. This was a compromise between the requirement for a large fields of view and the optimum particle image diameter.

4.14 2-D Calibration

The 2-D calibration enables a calibration factor to be obtained to compute the flow velocity in metres per second. The laser is set to low power (60 mJ) during the calibration process and triggered externally from the INSIGHT 3G software. The calibration target (Fig. 4.18) with a side mirror is placed inside the optical diffuser and is aligned manually with the laser beams. Once the calibration plate was aligned, the aperture and the camera lens were adjusted so that the calibration target was in focus. The next step was to check the obtained field of view. This desired field of view can be obtained by moving the camera traverse away or towards the calibration target and then refocusing the camera lens. This can be a trial and error procedure till the desired field of view is obtained. Once the desired field of view was obtained, the calibration numbers per pixel for that field of view were obtained. The distance between the calibration points was 5 mm. This was entered manually and then depending on the distance from the calibration target the calibration numbers per pixel were obtained.

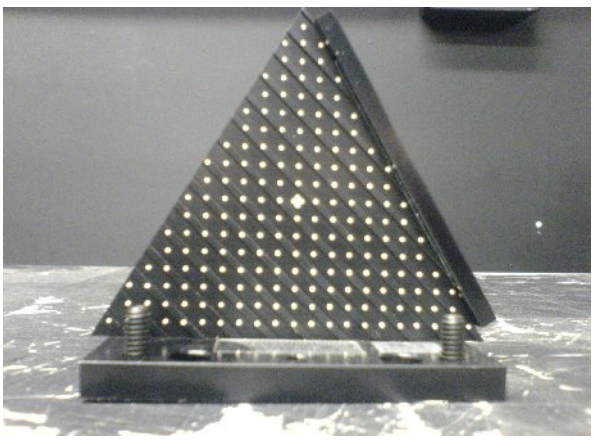

Figure 4.18 Calibration target

4.15 Summary

A 2-D rig has been built to study the flow field in the diffuser using PIV and flow distribution across the substrate. A 2-D contracting nozzle and 2-D planar diffuser has been designed for this purpose. The 2-D contracting nozzle has been designed and tested to obtain a uniform inlet profile at the inlet to the diffuser. Hot-wire velocity profiles of the flow distribution at the exit of the substrate obtained at five different flow rates showed that the flow is symmetric. The hot-wire velocity profiles gave a measure of maldistribution in the flow across the substrate and will be compared with the predictions from CFD. The experimental setup for the PIV investigation of flow in a diffuser upstream of substrate has been discussed in this chapter. The important parameters like the laser setup, camera timing, seeding and PIV processing have been explained in relation to the equipment. The PIV results for different fields of view will be discussed in detail in Chapter 5.

Chapter 5: PIV Results and Discussion

5.1 Fields of View

Three different fields of view namely full-field of view (180 mm × 90 mm), half-field of view (90 mm × 60 mm) and near-wall field of view (45 × 40 mm) were investigated. The half-field of view of the diffuser with an area of interest of 90mm × 60 mm provided the best compromise allowing identification of all the important flow structures, whilst at the same time providing good quality vectors. The field of view of the equipment is generally square but since the region downstream of the diffuser is opaque only the rectangular field of view from which useful data can be obtained is represented here.

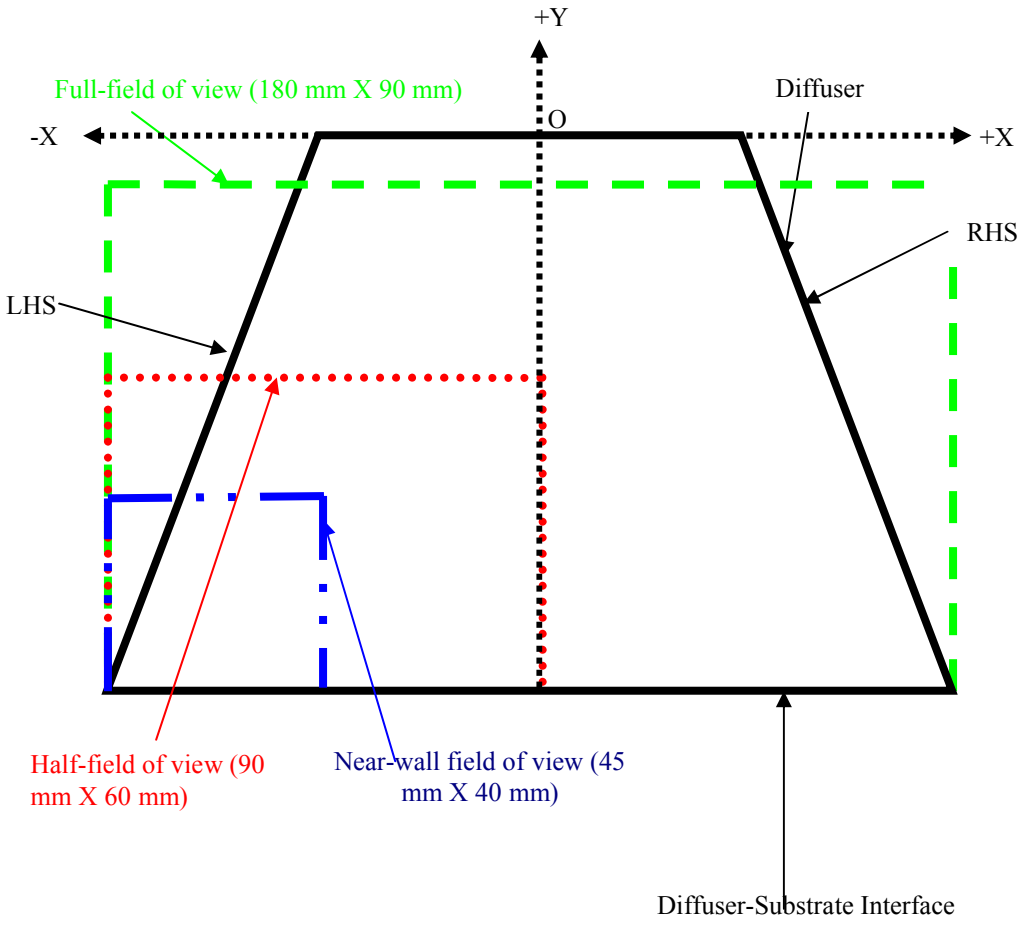

Figure 5.1: Field of view regions for PIV measurements

LHS: Left Hand Side, RHS: Right Hand Side, O: Centre of Diffuser at its inlet, Y: Axial distance from the diffuser-substrate interface, +X: Lateral distance towards RHS, -X: Lateral distance towards LHS

The full view of the diffuser with a field of view 180 mm × 90 mm gave a measure of the symmetry of the flow field. Since the right wall of the diffuser acted as the laser terminator there was a large amount of scattering of laser light in the near-wall region. As discussed earlier, a particle image diameter of 1 pixel was thought be adequate to obtain good quality data. For full-field of view, this was ensured by increasing the $f^{\#}$ number to 8. The seeding density was also increased by opening the number of the jets in the six-jet atomiser. These resulted in more particle pairs available for cross-correlation and hence improve the quality of the data. As will be discussed later, most of the flow features can be seen from the full-field of view results. Once the symmetry is established the half-field of view measurements can be used to provide more detailed information.

Experiments were also conducted by concentrating on the near-wall region in order to understand the flow behaviour at the diffuser wall and the diffuser-substrate interface. The near-wall field of view consisted of a region of 45 mm × 40 mm as shown in the Fig. 5.1. The $f^{\#}$ was set to 5.6 for the half and near-wall field of view.

5.2 Characteristics of plane rectangular jets

It is probably useful at this stage to discuss the main characteristics of diffuser flow and plane rectangular jets to aid in interpretation of the PIV results. The diffuser with a wide angle of 60^0 provides jet flow at the centre and a recirculation region on either side of its longitudinal axis (Fig. 5.2). The flow at the centre of wide angle diffuser behaves like a plane jet and has the general characteristics of plane jets in their near field region. Hence an overview of the characteristics of the plane jets has been provided. There have been a number of studies on the behaviour of plane jets from rectangular slots by Trentacoste et al, 1967, Sforza et al, 1965, Quinn, 1991, 1994, Sfeir, 1979, Marsters, 1981. Turbulent incompressible jets are characterized by three distinct regions which can be classified as:

Potential Core Region (PC): In this region the mixing initiated at the jet boundaries has not influenced the entire flow field. The mean velocity is approximately constant close to the nozzle exit velocity and decreases monotonically beyond it (Fig. 5.3). A short potential core length implies a rapid mixing in the near field.

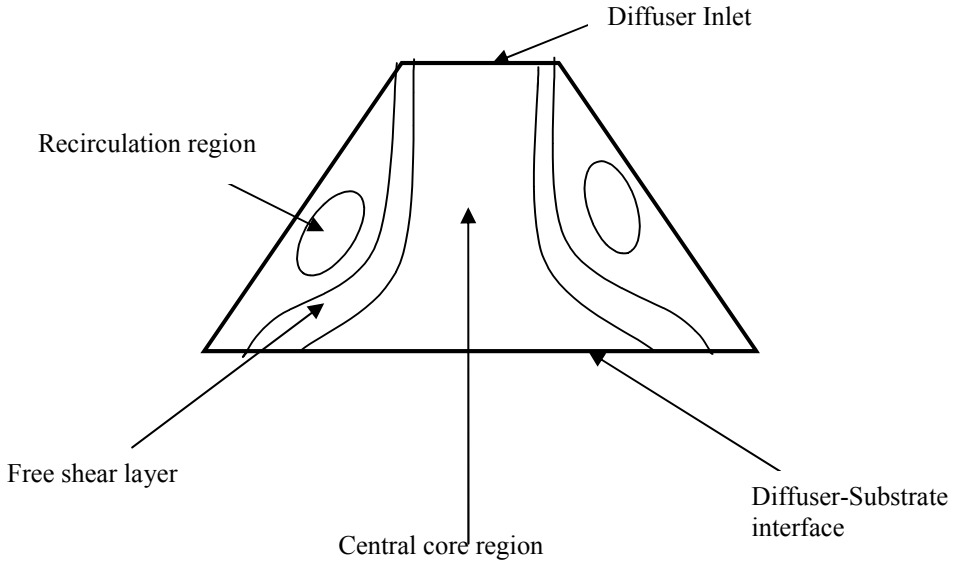

Fig 5.2: Schematic of the flow in the diffuser.

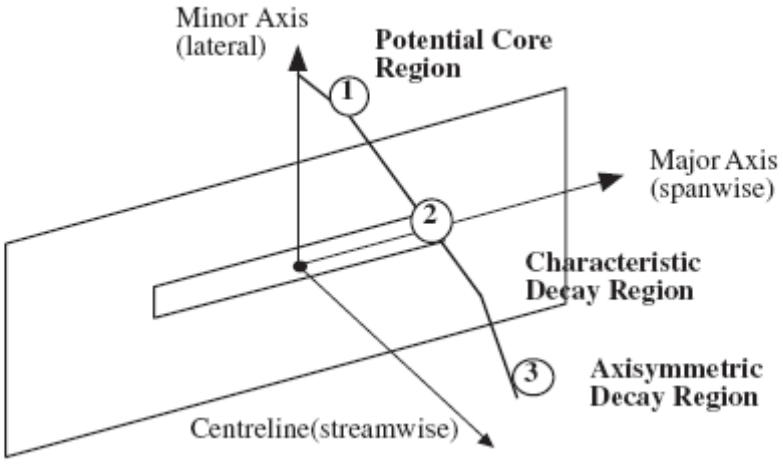

Figure 5.3: Rectangular jet configuration showing the centre line velocity decay regions in the three regions (Ref: Holdo, A.E. & Simpson, A.F., Simulation of high-aspect-ratio jets, 2002, International journal for numerical methods in fluids, 39:343-359).

Characteristic decay region (CD): In this region the centreline velocity decays and this decay is dependent upon orifice configuration. The velocity profiles in the plane of minor axis of the orifice are found to be similar along the symmetry planes whereas those in the plane of the major axis are non-similar (Trentacoste, 1967). In this region, large scale vortices interact and result in momentum transport (Pope, 2000).

Axisymmetric decay region (AD): In this region the centreline velocity decay is linear and the entire flow field approaches axi-symmetry and is independent of orifice geometry. The velocity profiles in both the major and minor axis planes are found to be similar along the symmetry planes (Trentacoste, 1967).

The flow behaviour in the PC and the CD region is dependent on the orifice geometry. Orifices with sharp-edges tend to result in more mixing in the near field region compared with smooth contoured orifices in the near field region. This has been investigated for both round and rectangular jets (Quinn, 1991, 2006). Saddle backed spanwise profiles of mean velocity have been observed from previous studies of turbulent flows from rectangular slots (Fig. 5.4). Similar saddle shape velocity profiles have also been observed in round jets from sharp edge orifices (Quinn, 2006). These saddle-backed velocity profiles have a greater velocity at the periphery of the flow field and migrate inward as the flow proceeds in the stream-wise direction. Various authors have tried to explain the reason for the occurrence of these saddle shaped velocity profiles. Van der Hegger Zignen (1958) explained the saddle-backed characteristic by assuming a system of closed vortex rings surrounding the jet. The velocity induced by these vortex rings when superimposed upon a uniform axial velocity results a saddle shape velocity profile in the plane of symmetry parallel to the slit. Trentacoste et al (1967) mentioned that this might be partially correct but argued that it does not explain the complete saddle-shaped phenomenon observed in their experimental data. They also found that these saddle shaped velocity distributions disappear at a point corresponding to the onset of the AD region. The velocity profiles are found to be similar in both lateral and spanwise directions in this region. They also pointed to the fact that the nonsimilarity is found in the PC region and also in the transverse direction of the CD region where these saddle–shapes persist. Sfier (1979) also used the encircling vortex concept to explain the saddle-shaped velocity profiles. They also pointed out the difficulty of detecting the presence of these vortex rings in a thin layer surrounding the jet.

Figure 5.4 Saddle shaped profiles from a rectangular slot.
(Ref: Trentacoste N, Sforza P. Further experimental results for three dimensional jets, AIAA 1967; 5(5):112–122.)

Marsters (1981) investigated the occurrence of saddle shapes in rectangular jet flows. He found from turbulence measurements that the turbulence stresses increased in the shear layer on the long sides of the jets. Marsters (1981) also pointed out that the increase in the turbulence stresses alone cannot explain the occurrence of saddle-shaped profiles. He concluded that the mechanism which produces saddle-backed velocity profiles has not been determined.

Several studies (Foss et al 1968, Rockwell et al, 1977) have introduced the idea of vortex stretching and secondary flows to explain saddle-shaped profiles. The presence of solid boundaries result in significant differences between mechanisms operating in bounded flows and those in free jets. They thought that the presence of strong vorticity interactions and important secondary flow effects must be involved in forming saddle-shaped profiles and unequal spanwise and lateral spreading rates.

A brief overview of the characteristics of the plane rectangular jets in the near field region has been provided to aid in the interpretation of PIV results in the next sections.

5.3 PIV Measurements for 27 mm substrate

5.3.1 Summary of the experimental set-up

PIV experiments were conducted for two different lengths of substrate 100 and 27 mm. Due to reflection from the surface close to the diffuser-substrate interface accurate measurements of vectors very close to the diffuser-substrate interface (approximately 2 mm) were not possible for all the three fields of view. Hence the PIV results do not contain the region of 2 mm upstream of the diffuser-substrate interface. Initially the experiments were conducted for the full-field of view of the diffuser and for the 27 mm monolith length. Experiments were conducted in order to find the number of PIV images required by varying the sample size and examining the results. Generally for a complex flow field and depending upon the uniformity of seeding a large sample size with 500 images is required. The flow being considered was relatively simple and seeding was uniform as it was fed through at the inlet of the plenum chamber, then passing through the flow straighteners and the contracting nozzle. The results plotted in Appendix B showed that a sample size of 50 was adequate to achieve high quality data. A comparison of different grid algorithms was also done and the results are plotted in Appendix E. From the results, it was found that the use of higher grid methods had no influence on the quality of data. The recursive Nyquist grid method with an initial grid size of 64 × 64 pixels and a final grid of 32 × 32 pixels has been used to process all the experimental data. The choice of grid engine is explained in Chapter 3. The full-field of view measurements gave a measure of the symmetry of the flow field. Once the symmetry is established the half-field of view can be used to explain most of the features of the flow field. The near-wall field of view gives a better understanding of the flow behaviour in the near-wall region and the diffuser-substrate interface.

The calibration procedure was repeated for all the fields of view and the camera focussing and the seeding density adjusted in order to obtain good quality vectors. The region of interest option in the INSIGHT-3G software is used to specify the area of interest which in the case of a full-field of view is 180 mm × 90 mm. This results in only this area being processed once the images are acquired. It was found that the seeding had to be increased for the full-field of view of the diffuser in order to obtain

good vectors. This was done by opening five of the six jets in the atomiser. The quality of the vectors improved considerably by having four or more jets open. This is explained by the availability of more particle pairs for cross-correlation. As mentioned before there was laser light scattering on the right wall of the diffuser which resulted in spurious data in the near-wall region of the right diffuser wall. Experiments were conducted at five different flow rates and processed using the INSIGHT-3G software and post-processed using Tecplot 10.

5.3.2 Experimental results

Fig. 5.5 shows the vector plot of the full-field of view flow field and Figs. 5.6-5.7 show the contour and line-contour for the velocity magnitude and Figs. 5.8 and 5.9 show the contour plot for axial and tangential velocity at Re:41800 respectively. Experiments were also conducted for the half-field of view and near field of view of the diffuser at different flow rates. The seeding density was again optimised by adjusting the number of open jets. Opening of three jets was adequate enough to obtain good quality vector for both the fields of view. Fig. 5.10 shows the vector plot of the half-field of view flow field and Figs. 5.11 and 5.12 show the contour and line-contour plot for the velocity magnitude and Figs. 5.13 and 5.14 show the contour plot for axial and tangential velocity at Re:41800 for the half-field of view measurements. Fig. 5.15 shows the vector plot of the near field of view flow field and Figs. 5.16-5.17 show the contour and line-contour plot for the velocity magnitude and Figs. 5.18-5.19 show the contour plot for axial and tangential velocity at Re:41800 for the near field of view measurements. Figs. 5.20-5.34 show the non-dimensionalised axial velocity profiles at different locations downstream of the diffuser at five different flow rates obtained from the half-field of view measurements. In the non-dimensional plots the axial velocity is non-dimensionalised against the average inlet velocity at the diffuser inlet (nozzle exit). Fig. 5.35 shows the angle of attack as the flow approaches the diffuser-substrate interface. The flow features observed from the three fields of view are explained in detail below.

5.3.3 Discussion

The axial velocity profiles at the inlet of the diffuser consist of a nearly constant central core region and a thin wall shear layer region of approximately 1.5 mm. The flow separates at the inlet of the diffuser and results in the formation of recirculation regions. Hence the flow field consists of a central core region, a free shear layer region and a recirculation region. Fig. 5.2 shows a schematic of the three regions in a diffuser. The flow in the central core region behaves like a plane jet from a rectangular nozzle and has most of the characteristics of plane jets (Trentacoste et.al, 1967); see for example Figs. 5.7, 5.8, 5.11, 5.13, and 5.20-5.29.

The vector plots of the flow field (Figs. 5.5, 5.10 and 5.15) show the flow behaviour in the presence of the substrate. The flow profile at the diffuser inlet (nozzle exit) is a top hat with a small boundary layer region. So the centreline velocity is only very slightly higher than the average velocity. As the flow exits the nozzle there is a small vena-contracta and a central core where the velocity is almost constant. Due to the vena- contracta there is an acceleration of the flow in the central core region. This is similar to the behaviour of a free rectangular jet in the PC region. Due to this inward acceleration of flow, the velocity in the central core region is initially higher than the velocity at the nozzle exit. The non-dimensional centreline velocity is greater than 1 up to a distance of 68 mm from the diffuser inlet and starts decreasing afterwards. This can be observed from the axial velocity profiles in Figs. 5.20-5.24 where the non-dimensional velocity is higher than 1. Beyond 68 mm, saddle shapes develop wherein the velocity at the ends of the central core region is greater than the centreline axial velocity. Similar saddle shape features have also been found in rectangular and round plane jets (Marsters, 1981). Several authors (Trentacoste et.al (1967), Sfier, 1979, Marsters, 1981 and Quinn, 199) have tried to explain the phenomena of saddle shapes as due to encircling vortices which result in more flow entrained in the region around the sides of jet. As yet no conclusive evidence has been found on this. The saddle shapes develop and become more prominent at around 73 mm from the inlet to the diffuser (Figs 5.26 & 5.82). The flow profiles loose their saddle shape due to the substrate resistance as the flow becomes more uniform under its influence at distances 15 mm from the diffuser-substrate interface. (Figs. 5.30-5.34 & 5.86-5.89). Also from the non-dimensional axial profiles there seems to be no Reynolds number effect on

the flow in contrast to the HWA measurements. The HWA velocity measurements (Fig. 4.11) downstream of the substrate showed that as the Reynolds number increases flow maldsitribution also increases.

As noted above along the longitudinal axis, the width of the central core region is found to be reduced slightly at the inlet of the diffuser and is approximately symmetric. There is however a slight skewness of the profiles. This is mainly due to the skewness first observed at the inlet of the diffuser (Fig. 4.5). The skewness increases initially due to the mixing of flow and the saddle back features start developing as the flow proceeds further downstream of the diffuser. This can be observed in Figs. (5.6, 5.7, 5.78-5.82).The skewness observed will have a very little effect on the symmetry of the flow entering the substrate as the resistance of the substrate flattens the profiles. This can be seen because the axial velocity profiles close to the substrate (Figs 5.5, 5.10, 5.31-5.34, 5.86-5.89) are more uniform.

At the nozzle exit, a wall shear layer develops and its initial thickness is due to the development of a thin boundary layer within the nozzle. The thickness of the wall shear layer at the nozzle exit is approximately 1.5 mm. The incoming wall shear layer separates at the inlet of the diffuser and develops as a free shear layer downstream of the diffuser. The free shear layer forms the transition region between two streams of different velocity namely the central core and the recirculation region. The free shear layer entrains the fluid from the separated region and the central core region as it grows downstream of the diffuser. The width of the free shear layer increases as it grows downstream of the diffuser and can be seen from contour and line contour plot of velocity magnitude (Figs 5.6, 5.7, 5.11, 5.12).

Flow separation at the diffuser inlet results in the formation of a recirculating flow between the free shear layer and the diffuser walls. The primary recirculation zone consists of vortex pairs with the velocity at the centre of each vortex being zero. Large pressure losses can occur as the mechanical energy of the fluid is used to drive these large unsteady eddying motions which dissipate into heat energy. Velocity gradients in the flow create turbulence which is then dissipated by viscosity into heat. Figs. 5.6 and 5.11 illustrate these vortices.

As the jet flow approaches the substrate it faces resistance which is highest at the centre of the substrate, because the velocity at the centre is high and the pressure drop in the monolith is greatest. Hence at the front face of the monolith, there is a region of high pressure at the centre and a region of lower pressure towards the periphery. This transverse pressure distribution tends to force the fluid away from the high velocity areas towards the low velocity areas resulting in a flattening of the velocity profile. The uniformity depends on the resistance of the substrate and increases as the substrate resistance increases. Due to the spreading of the jet the flow vectors away from the centre-line approach the substrate at an angle to the channels. The angle of attack increases as the jet spreads towards the periphery. The flow at high angles of attack experiences difficulty in entering the substrate channels due to the "entrance effect loss" discussed in Chapter 2. This reduces the mass flow into these channels; the remaining flow being pushed towards the periphery, some of which feeds the recirculating vortices.

The near-wall field of view of the diffuser provides detail of the flow field near the wall and the diffuser-substrate interface. Fig. 5.15 shows the vector plot of the half-field of view flow field and Figs. 5.16 and 5.17 show the contour and line-contour plot for the velocity magnitude. Figs. 5.18 and 5.19 show the contour plots for axial and tangential velocity at Re: 41800 for the near-wall field of view measurements. The flow at the periphery reaches a stagnation point at approximately 7 mm from the diffuser-substrate interface (Figs. 5.15 & 5.16). At the stagnation point the pressure is high and the flow divides. This higher pressure forces both flow into the channels near the periphery and also feeds flow back towards the diffuser inlet, feeding the recirculating vortex. Therefore there is more flow entering the substrate channels in the near-wall region when compared to the flow in a region of 10-30 mm from the wall. This effect cannot be observed from Fig. 5.34 but is evident from the hot-wire velocity profiles 30 mm from the substrate (Fig. 4.10) and also the CFD predictions which will be explained later in Section 6.5.3.5.

The tangential velocity contour plots are shown in Figs. 5.9, 5.14 and 5.19. Initially at the centre of the diffuser the magnitude of the tangential component is zero and as the jet starts spreading the tangential component increases. The tangential component of the flow is at its maximum in the region of high angles of attack at the diffuser-

substrate interface. This effect can be seen from the contour plots for tangential velocity in Fig. 5.14. The full-field contour plot contains two regions where the tangential component magnitude is highest near the diffuser-substrate corresponding to the flow at high angles of attack (Fig. 5.9)

5.4 PIV measurements for 100 mm substrate

5.4.1 Experimental results

PIV measurements were also made for 100 mm substrate for the three different fields of view. This demonstrates the repeatability of the technique and also the behaviour of the flow in the presence of increased resistance. The full-field of view, half-field of view and the near-wall field of view of diffuser experiments were conducted at five different flow rates. Fig. 5.36 shows the vector plot of the full-field of view flow field and Figs. 5.37-5.38 show the contour and line-contour plots for the velocity magnitude and Figs. 5.39 and 5.40 show the contour plot for axial and tangential velocity at Re:41800 respectively. The seeding density was again optimised by adjusting the number of open jets. Fig. 5.41 shows the vector plot of the half-field of view flow field and Figs. 5.42 and 5.43 show the contour and line-contour plot for the velocity magnitude. Figs. 5.44 and 5.45 show the half-field contour plots for axial and tangential velocity at Re: 41800. Figs. 5.51-5.65 show the non-dimensionalised axial velocity profiles at different locations downstream of the diffuser at five different flow rates obtained from the half-field of view measurements. Figs. 5.66-5.76 show the non-dimensionalised tangential velocity profiles at different locations downstream of the diffuser at five different flow rates obtained from the half-field of view measurements. The axial and tangential velocity profiles were non-dimensionalised against the inlet velocity at the nozzle exit. Fig. 5.77 shows the angle of attack as the flow approaches the diffuser-substrate interface.

5.4.2 Discussion

The flow behaviour is similar to the one observed with the 27mm substrate up to about 50 mm from the diffuser-substrate interface (Fig. 5.80). The flow separates at the inlet to the diffuser and results in the formation of primary recirculation regions. The quality of data in the near-wall region of the right wall of the diffuser for the full-

field of view was not very good. This was again due to scattering of light on the right wall of the diffuser. The full-field of view measurements showed that the flow was mostly symmetrical and can be seen in (Figs 5.37, 5.39, 5.40). Figs. 5.51-5.65 show the non-dimensionalised axial velocity profiles at different locations downstream of the diffuser at five different flow rates obtained from the half-field of view measurements. The non-dimensional profiles show the central core region and also the point of crossover where the flow has changed its axial direction. The point of crossover moves towards the periphery downstream of the diffuser due to the spreading of jet and the recirculation region. The initial increase in the centreline velocity and the occurrence of saddle shapes in the axial velocity profiles are evident in Figs. 5.51-5.55. From the contour plots and the axial velocity profiles there is a small skewness towards the left hand side of the diffuser. This is due to the skewness first observed in the profiles at the diffuser inlet (Fig. 4.5) (nozzle exit). Also the flow starts spreading as it moves downwards and the width of free shear layer increases.

The non-dimensional tangential velocity profiles (Figs. 5.66-5.76) also illustrate the spreading of the jet downstream of the diffuser. The flow at the centre and near to the diffuser inlet has zero or very low magnitude of the tangential velocity. As the jet starts to spread, the flow vectors are at an angle to the initial flow direction. This results in a tangential component which increases further downstream. In the recirculation region the flow is changing direction and as result the tangential component changes from negative to positive. As the flow starts spreading downstream of the diffuser the tangential component increases (Figs. 5.69 and 5.70). Figs. 5.70-5.76 show that the tangential component increases initially and starts decreasing towards the periphery of the diffuser. The increase is due to the spreading of the jet in the central core region and free shear region and the decrease is due to the flow in the recirculation region.

The flow at the periphery reaches a stagnation point at approximately 7 mm from the substrate and there is more flow entering the substrate channels in the near-wall region when compared to the flow in a region of 10-30 mm from the wall. This effect cannot be observed from Fig. 5.76 but is evident from the hot-wire profiles downstream of the substrate (Fig. 4.11) and also the CFD predictions which will be explained later in Section 6.5.3.5

Comparison of 27 mm and 100 monoliths (Figs. 5.78-5.89) shows the effect of the higher substrate resistance. The flow field is largely unaffected due to increased resistance up to about 68 mm from the diffuser-substrate interface. Due to the increased resistance, the front face of the 100 mm substrate will experience a higher static pressure at the centre when compared to the 27 mm substrate. Hence there is a larger pressure differential between the high pressure at the centre and low pressure at the peripheral region and hence more flow is forced towards the periphery of the diffuser. This result in a flattening of the velocity profile upstream and can be seen in Figs. 5.82-5.89. The flattening of the profile due to the higher resistance is at its maximum close to the diffuser-substrate interface as seen in Fig. 5.89.

5.5 PIV plots for 27 mm monolith

The units for the contour plots in this section are in m/s

5.5.1 Full-field of view plots for 27 mm monolith

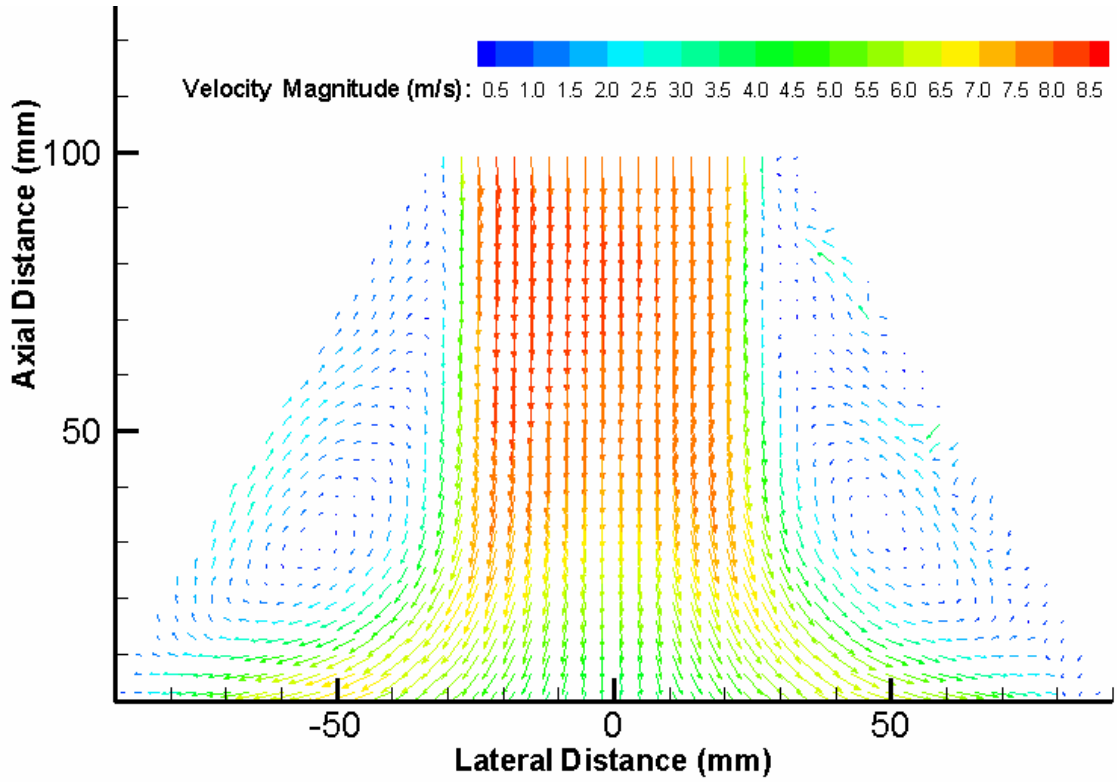

Figure 5.5: Full-field of view vector plot at Re: 41800 for 27 mm monolith

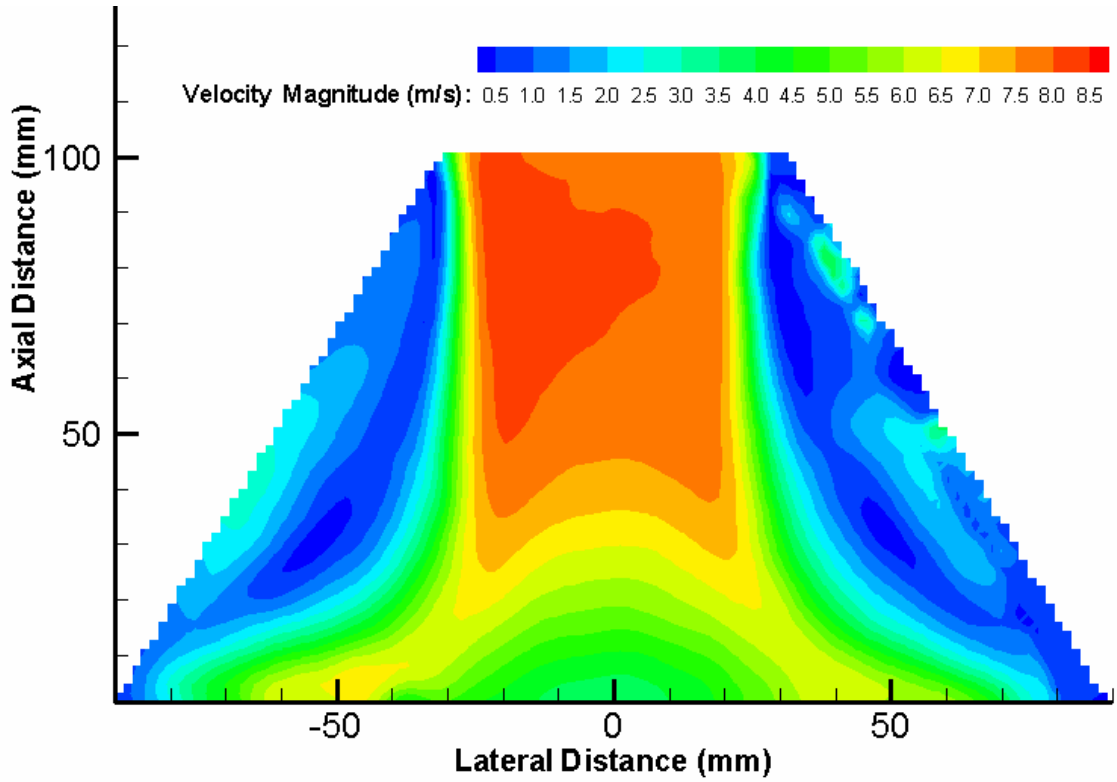

Figure 5.6: Full-field of view contour plot for velocity magnitude at Re: 41800 for 27 mm monolith

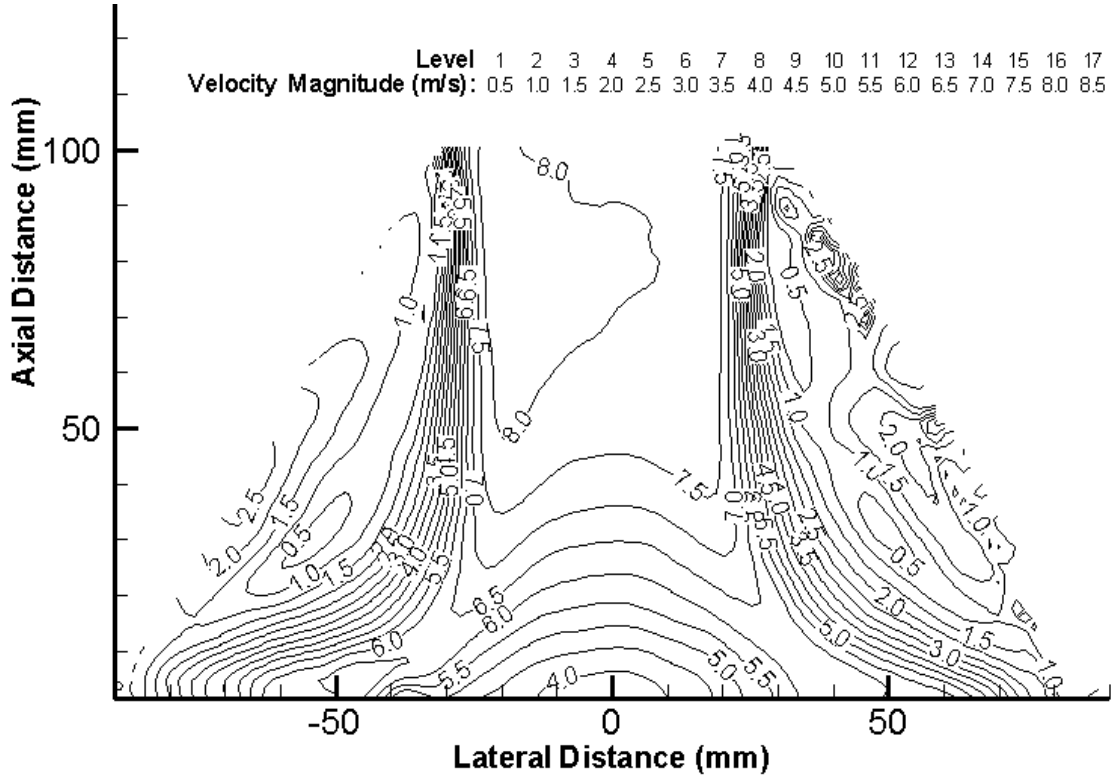

Figure 5.7: Full-field of view line-contour plot for velocity magnitude at Re: 41800 for 27 mm monolith

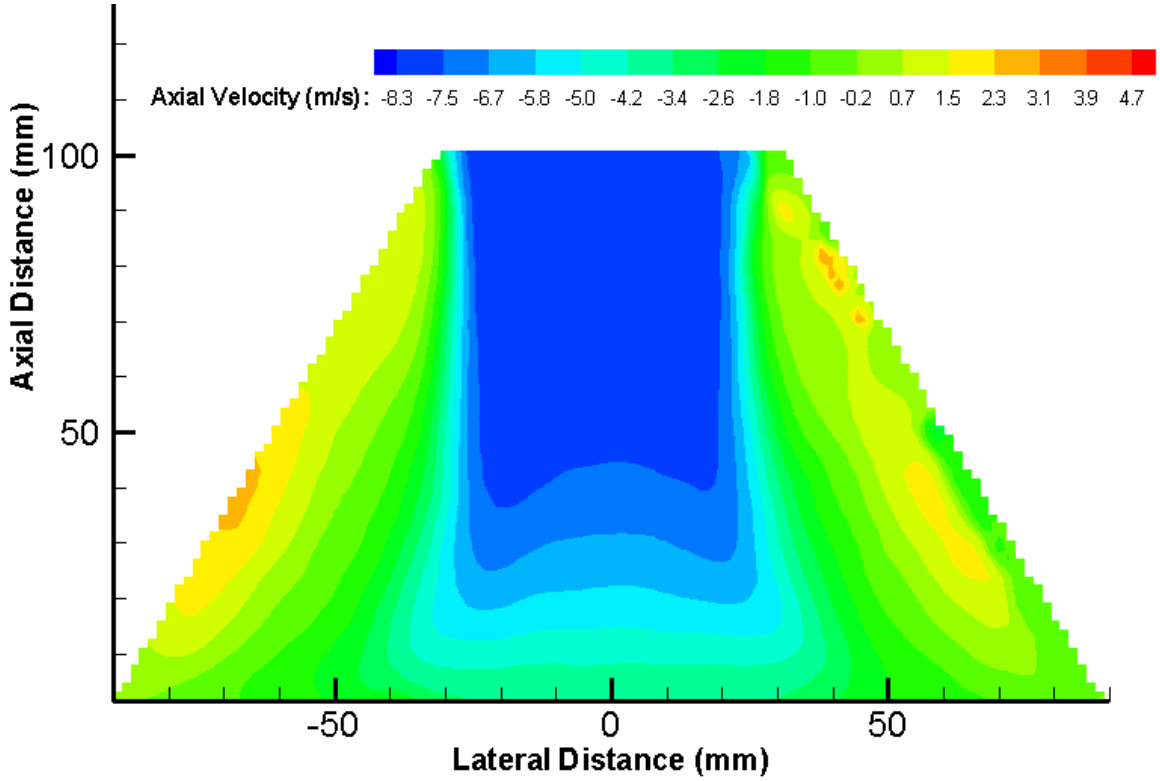

Figure 5.8: Full-field of view contour plot for axial velocity at Re: 41800 for 27 mm monolith

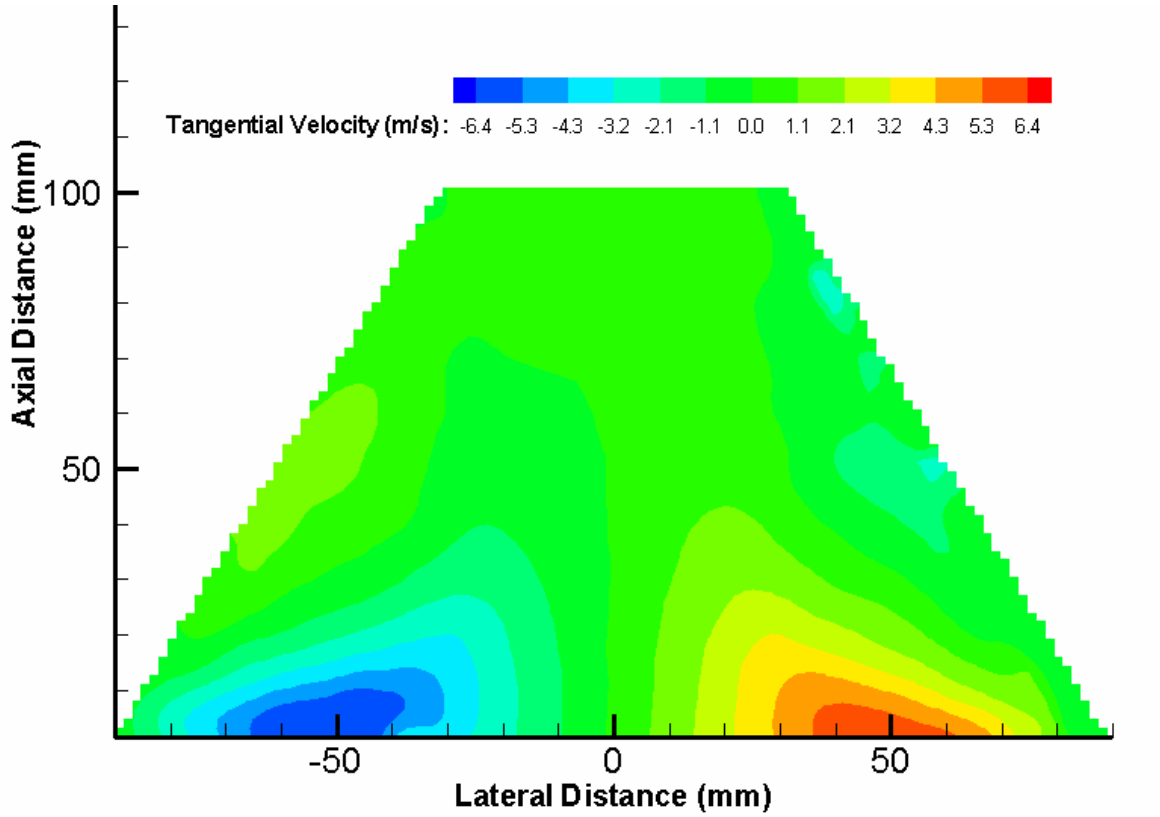

Figure 5.9: Full-field of view contour plot for tangential velocity at Re: 41800 for 27 mm monolith

5.5.2 Half-field of view plots for 27 mm monolith

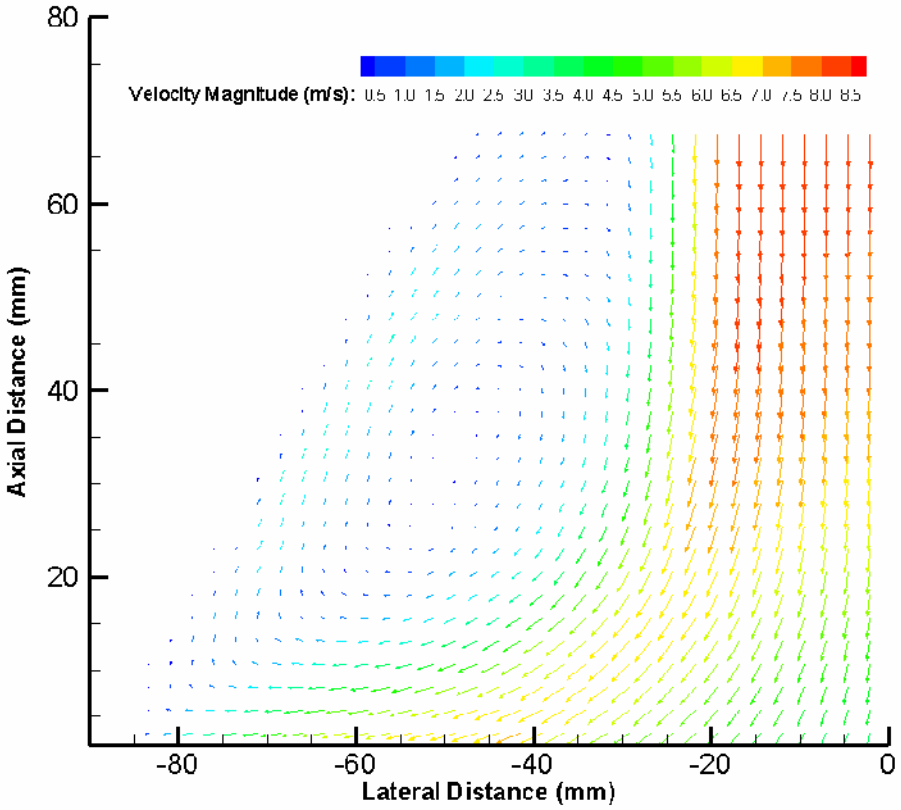

Figure 5.10: Half-field of view vector plot for velocity magnitude at Re: 41800 for 27 mm monolith

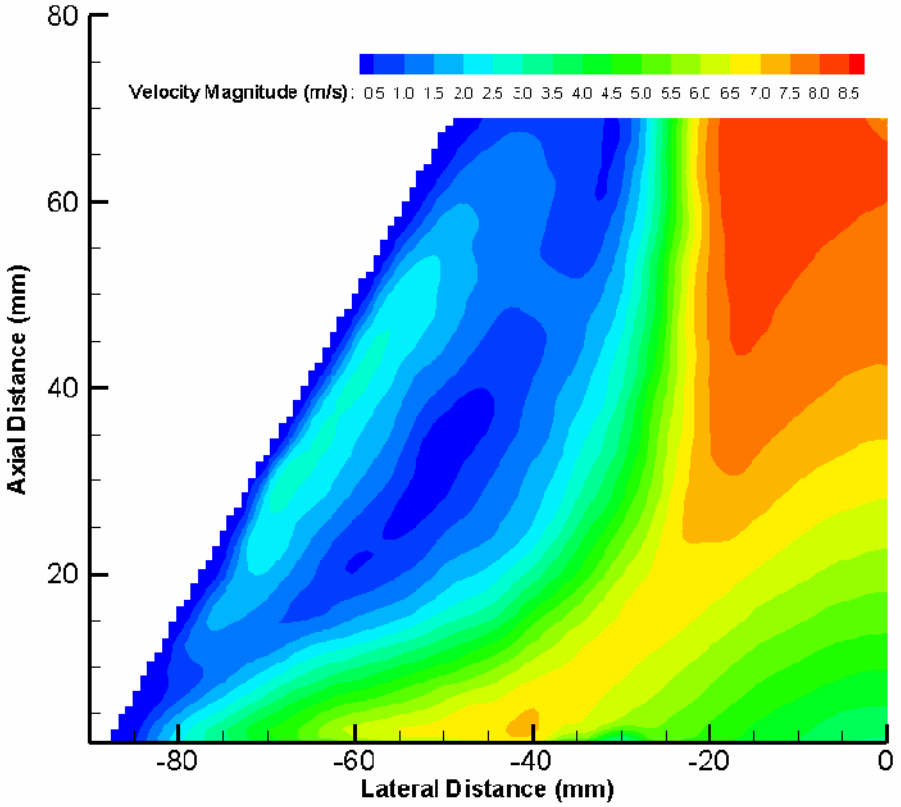

Figure 5.11: Half-field of view contour plot for velocity magnitude at Re: 41800 for 27 mm monolith

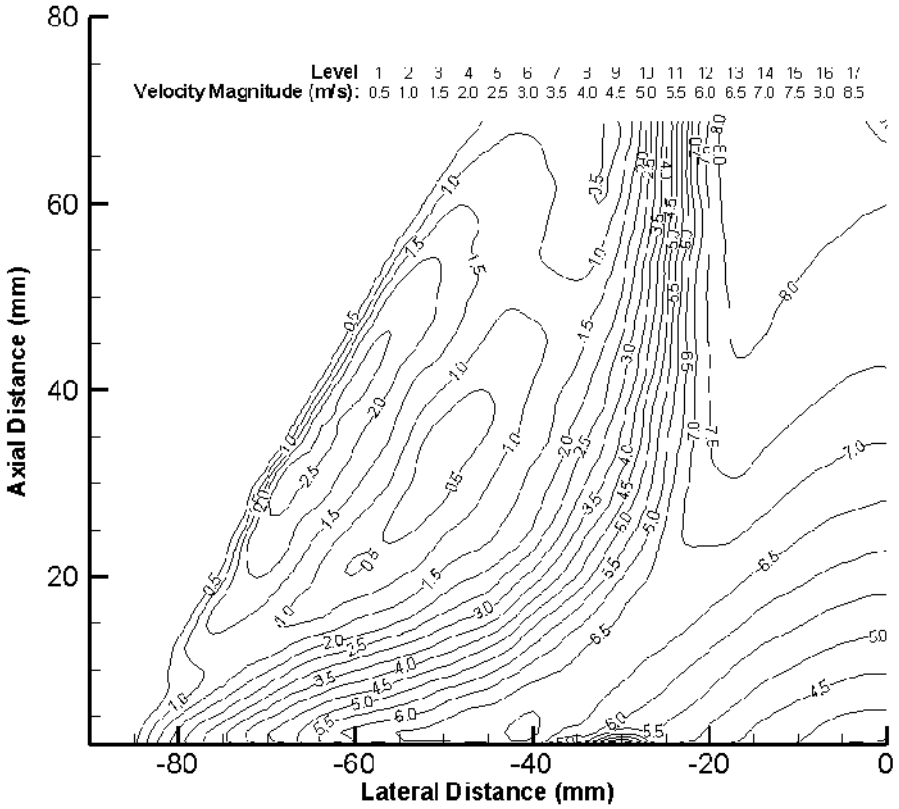

Figure 5.12: Half-field of view line-contour plot for velocity magnitude at Re: 41800 for 27 mm monolith

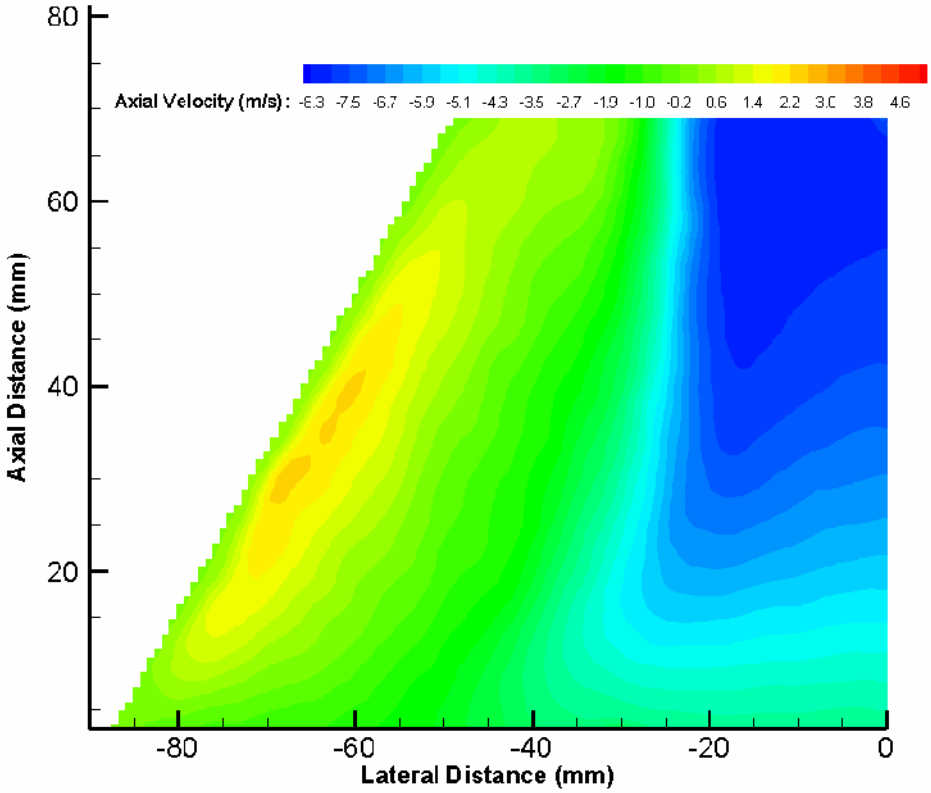

Figure 5.13: Half-field of view contour plot of axial velocity at Re: 41800 for 27 mm monolith

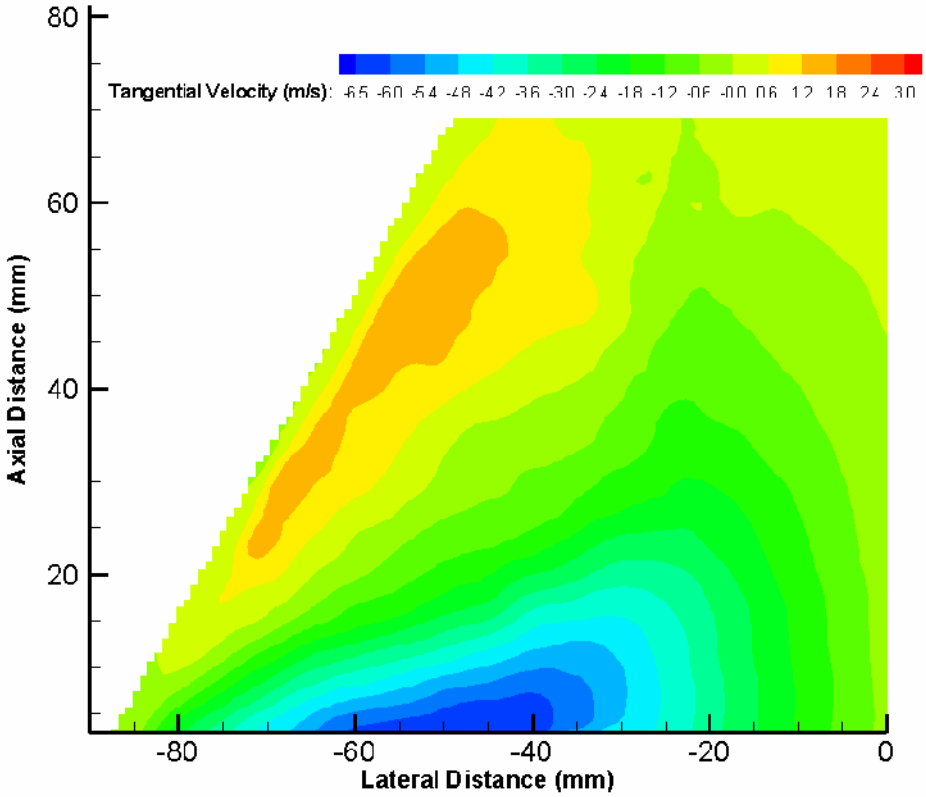

Figure 5.14: Half-field of view contour plot of tangential velocity at Re: 41800 for 27 mm monolith

5.5.3 Near-wall field of view plots for 27 mm monolith

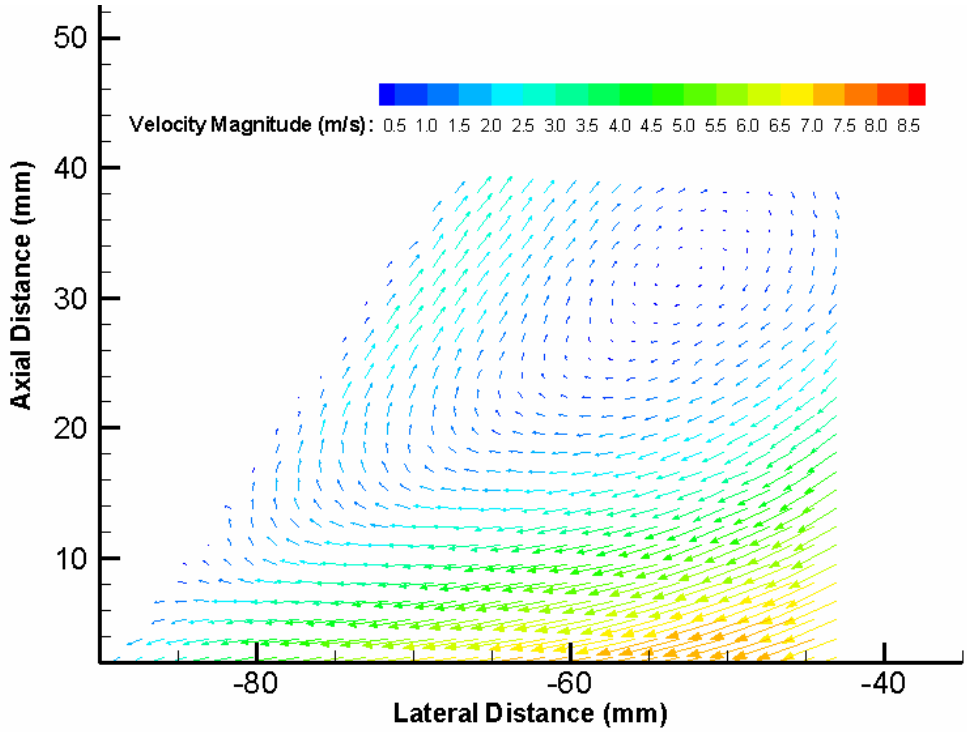

Figure 5.15: Near-wall field of view vector plot at Re: 41800 for 27 mm monolith

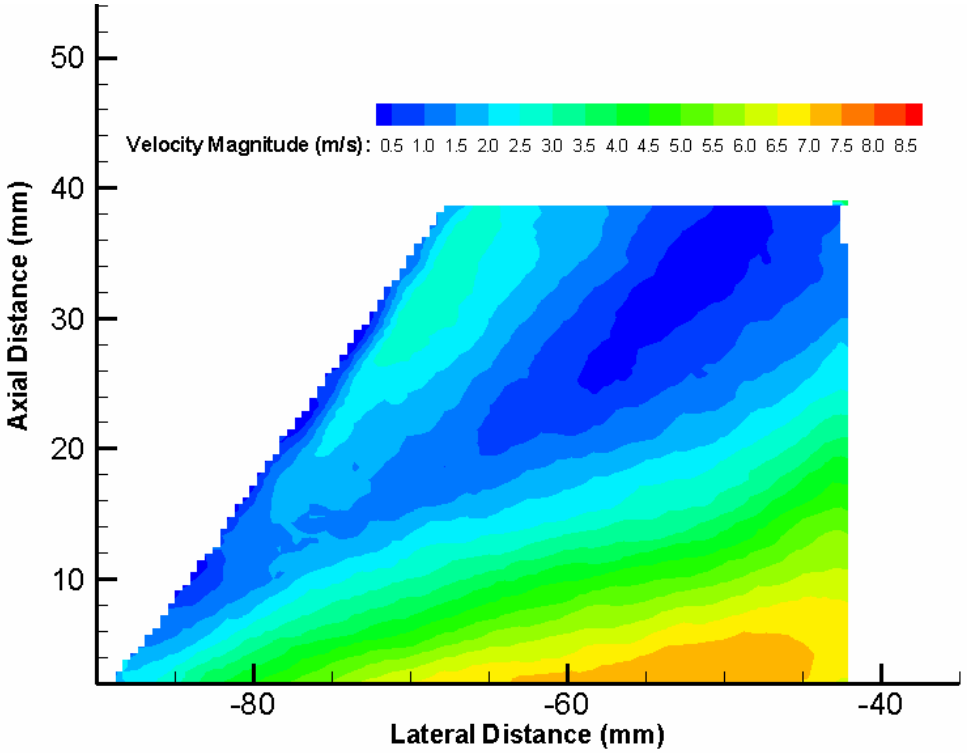

Figure 5.16: Near-wall field of view contour plot of velocity magnitude at Re: 41800 for 27 mm monolith

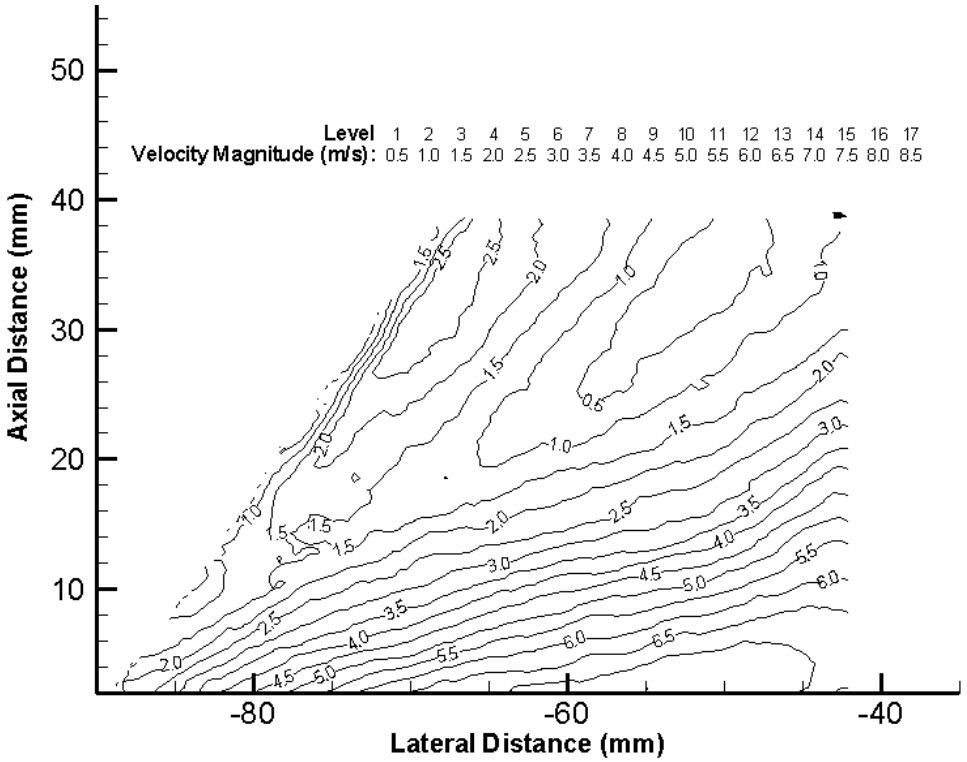

Figure 5.17: Near-wall field of view line-contour plot for velocity magnitude at Re: 41800 for 27 mm monolith

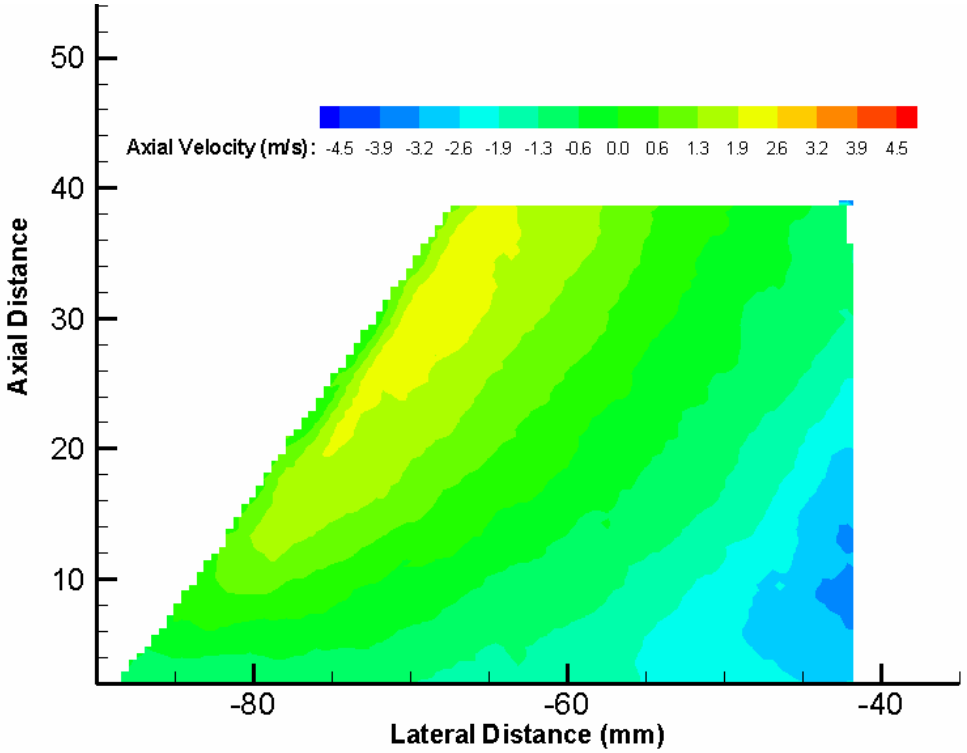

Figure 5.18: Near-wall field of view contour plot of axial velocity at Re: 41800 for 27 mm monolith

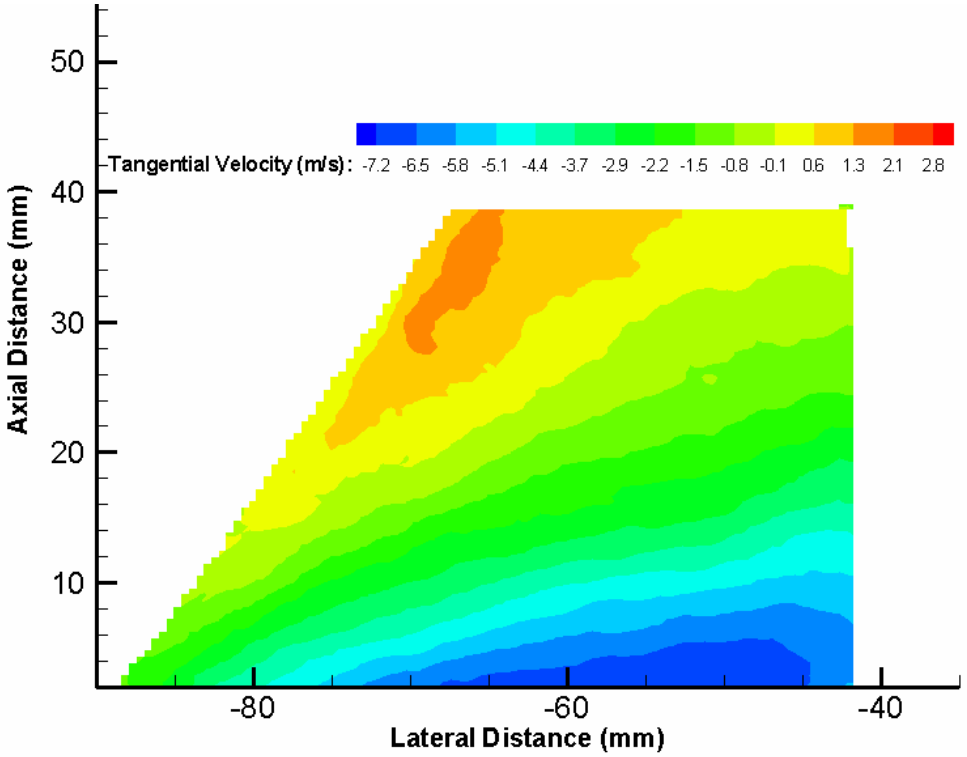

Figure 5.19: Near-wall field of view contour plot of tangential velocity at Re: 41800 for 27 mm monolith

5.5.4 Non-dimensional axial velocity profiles for 27 mm monolith

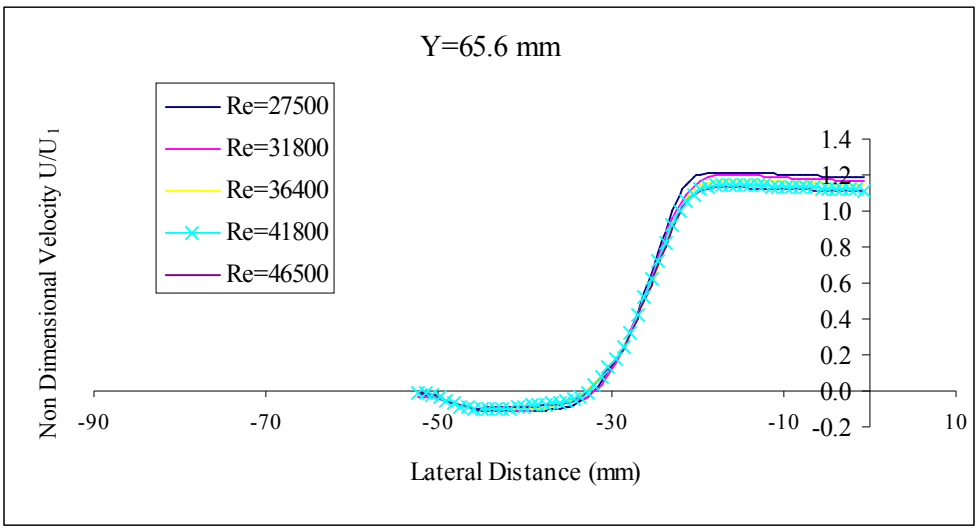

Figure 5.20: Non-dimensional axial velocity profiles at an axial distance of 65.6 mm

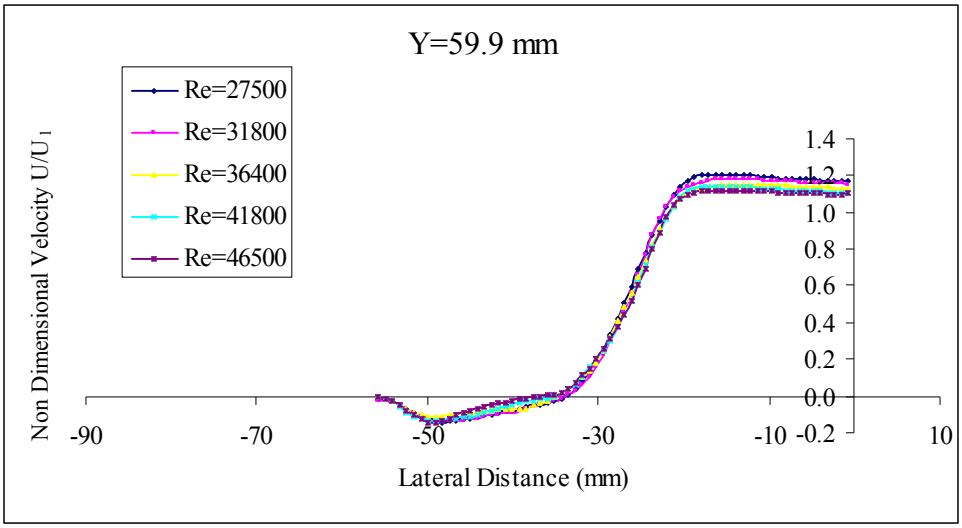

Figure 5.21: Non-dimensional axial velocity profiles at an axial distance of 59.9 mm

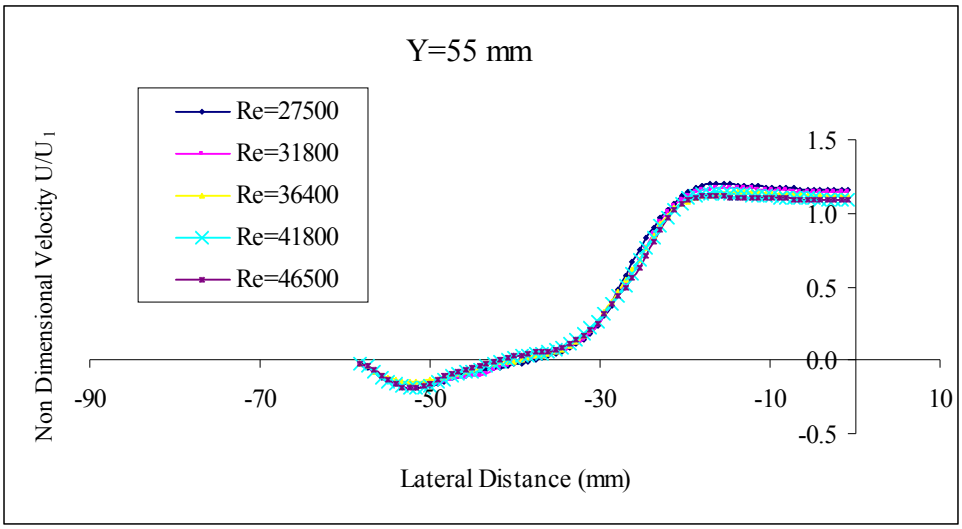

Figure 5.22: Non-dimensional axial velocity profiles at an axial distance of 55 mm

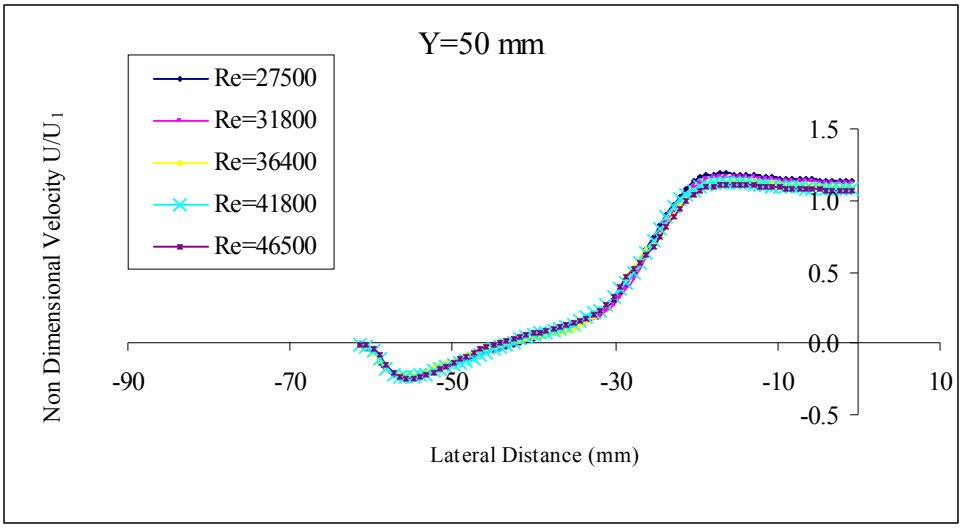

Figure 5.23: Non-dimensional axial velocity profiles at an axial distance of 50 mm

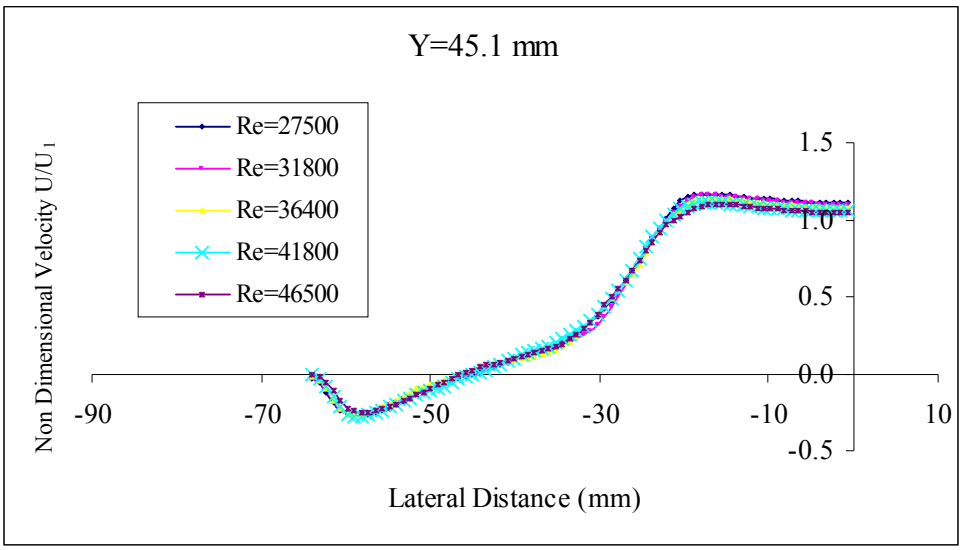

Figure 5.24: Non-dimensional axial velocity profiles at an axial distance of 45.1 mm

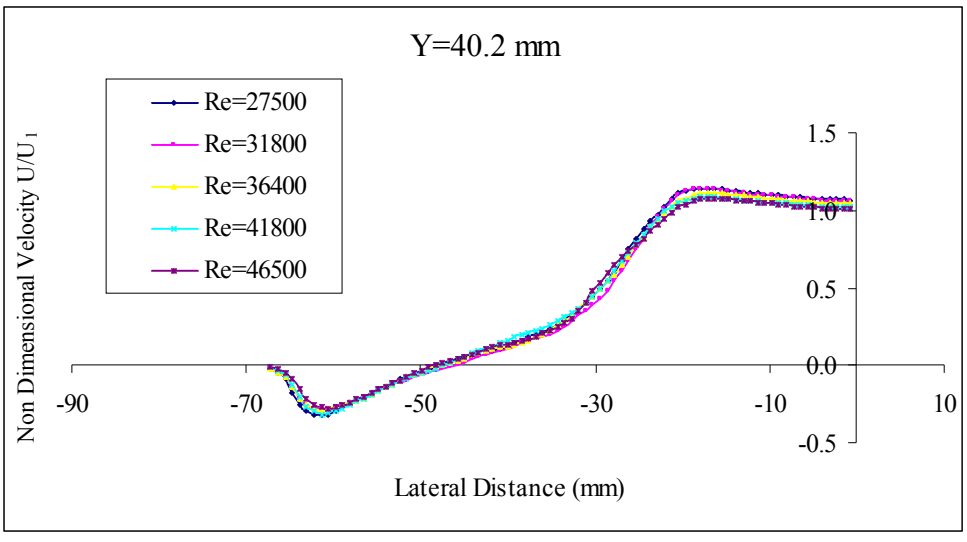

Figure 5.25: Non-dimensional axial velocity profiles at an axial distance of 40.2 mm

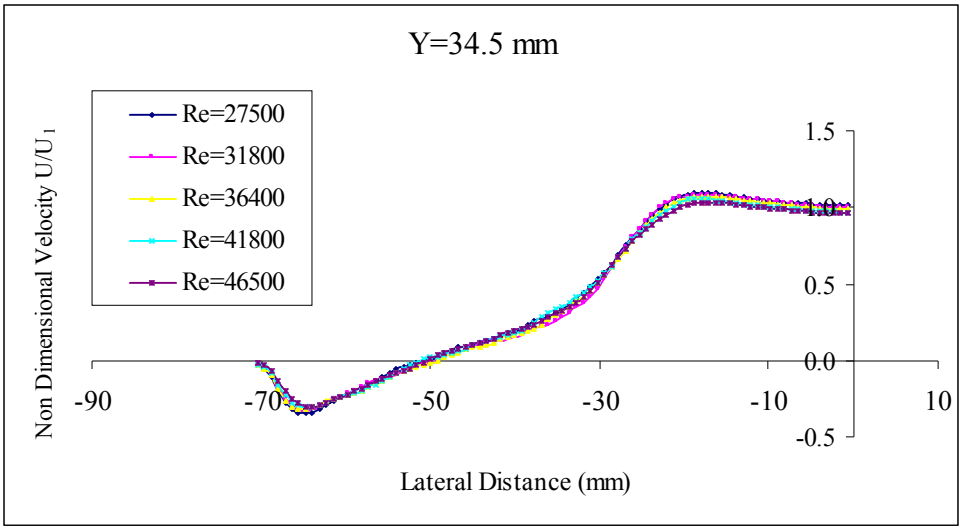

Figure 5.26: Non-dimensional axial velocity profiles at an axial distance of 34.5 mm

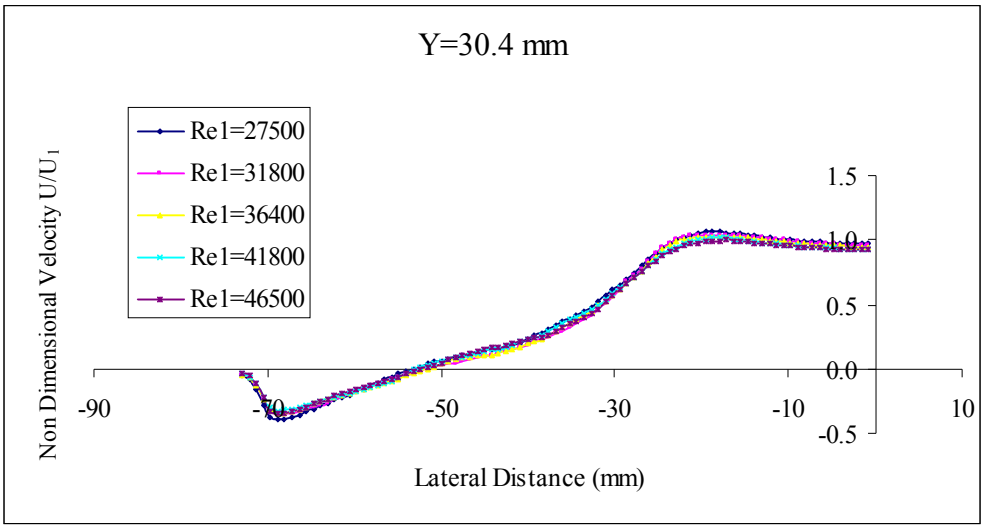

Figure 5.27: Non-dimensional axial velocity profiles at an axial distance of 30.4 mm

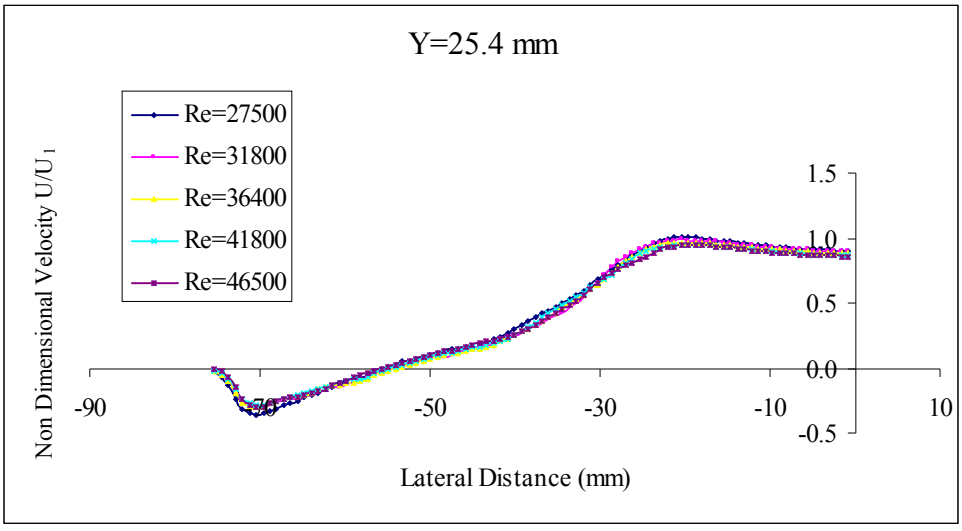

Figure 5.28: Non-dimensional axial velocity profiles at an axial distance of 25.4 mm

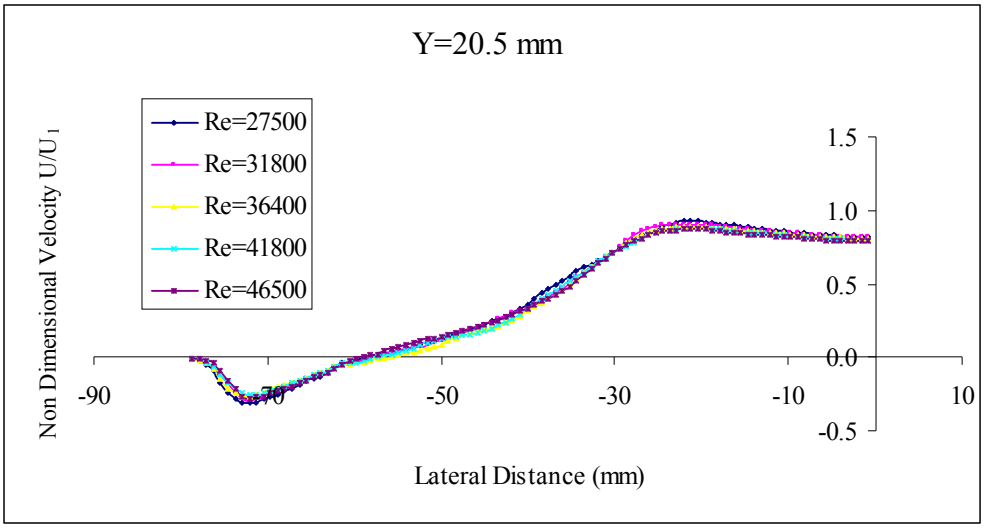

Figure 5.29: Non-dimensional axial velocity profiles at an axial distance of 20.5 mm

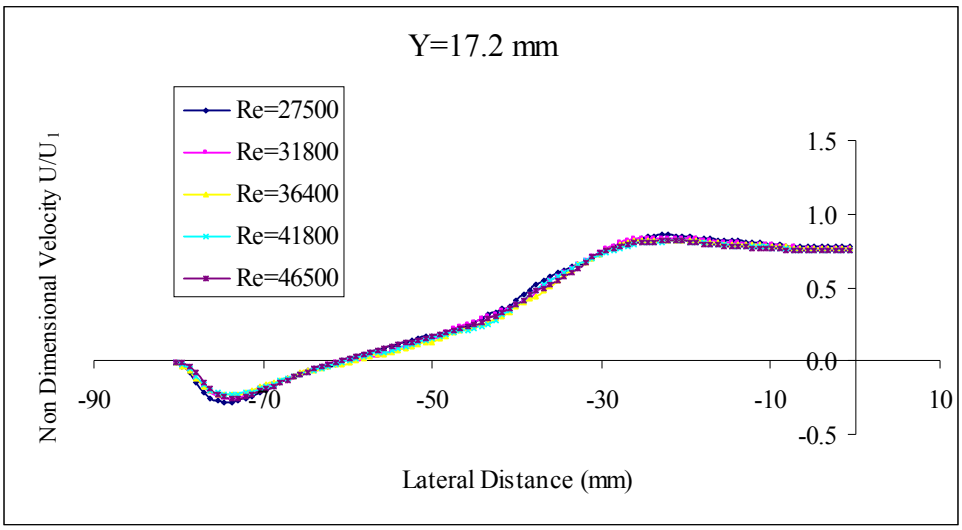

Figure 5.30: Non-dimensional axial velocity profiles at an axial distance of 17.2 mm

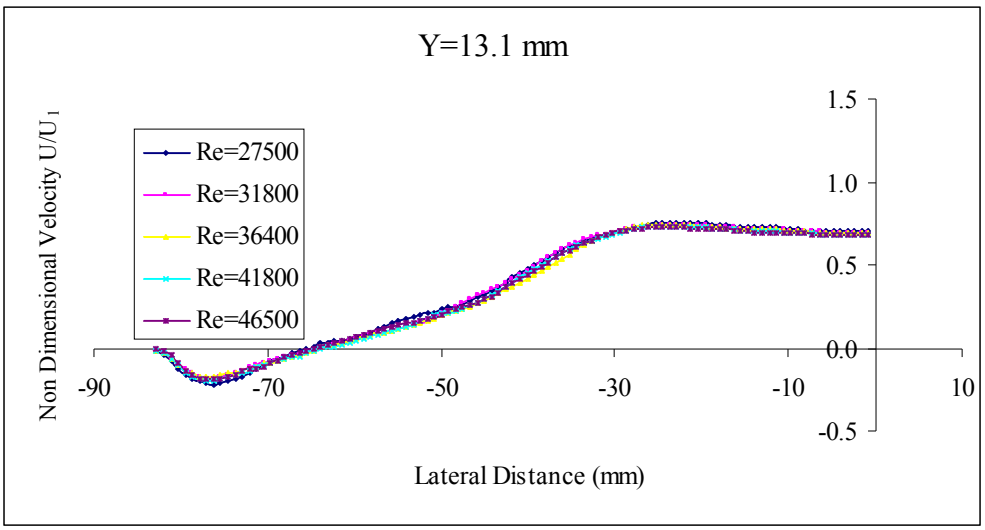

Figure 5.31: Non-dimensional axial velocity profiles at an axial distance of 13.1 mm

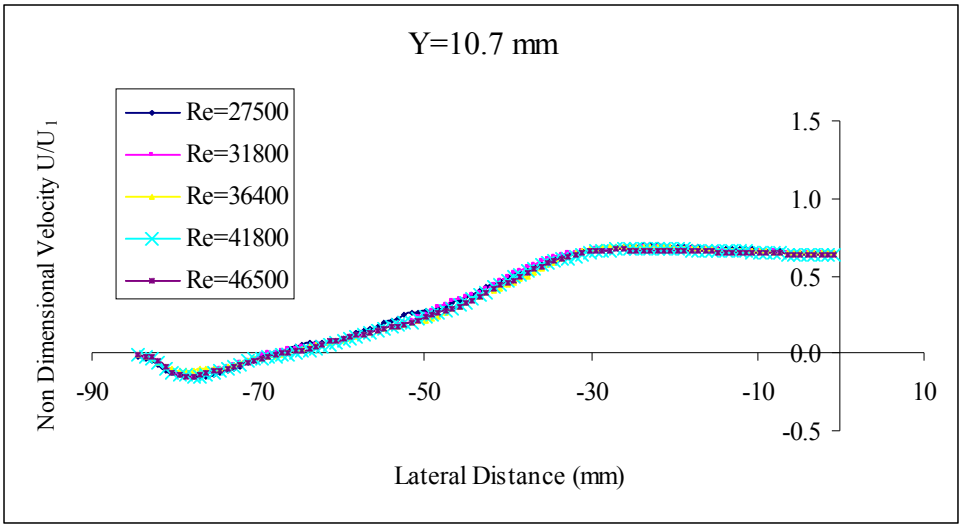

Figure 5.32: Non-dimensional axial velocity profiles at an axial distance of 10.7 mm

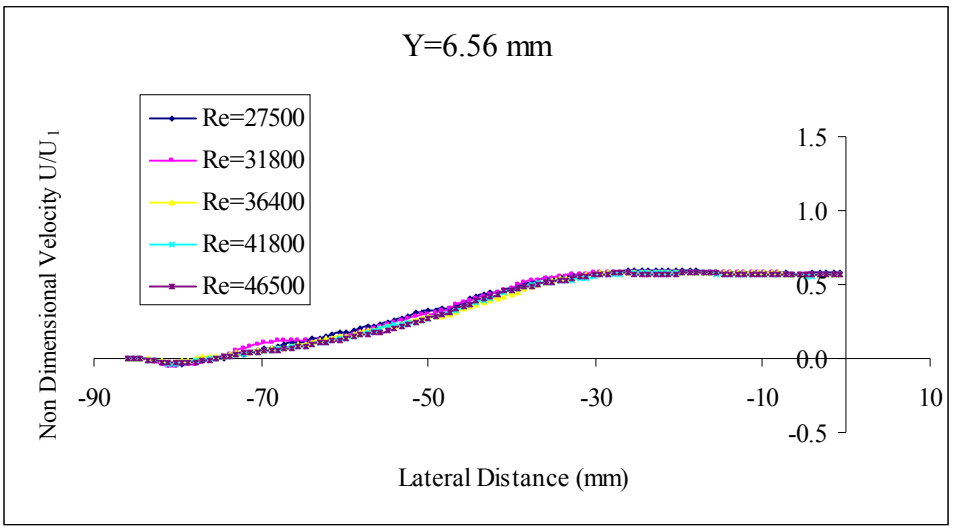

Figure 5.33: Non-dimensional axial velocity profiles at an axial distance of 6.56 mm

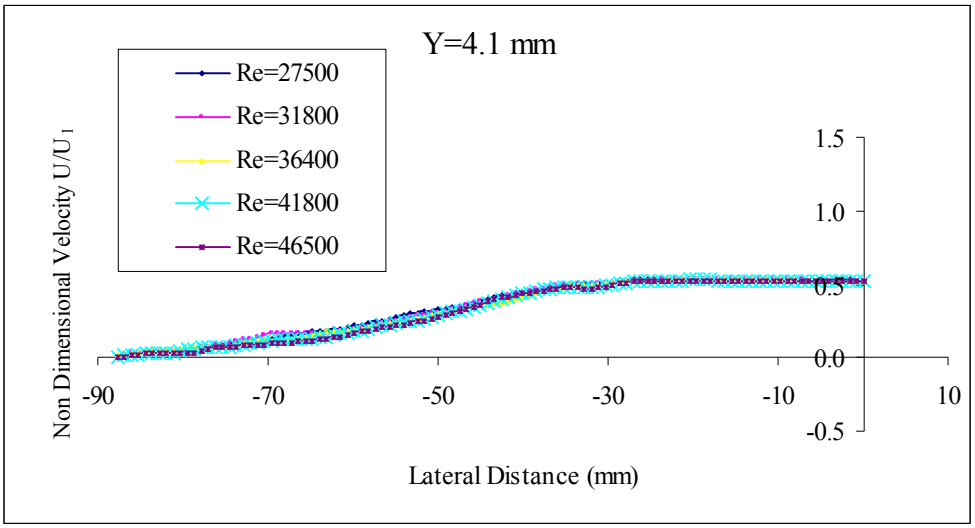

Figure 5.34: Non-dimensional axial velocity profiles at an axial distance of 4.1 mm

5.5.5 Plot of angle of attack close to the substrate

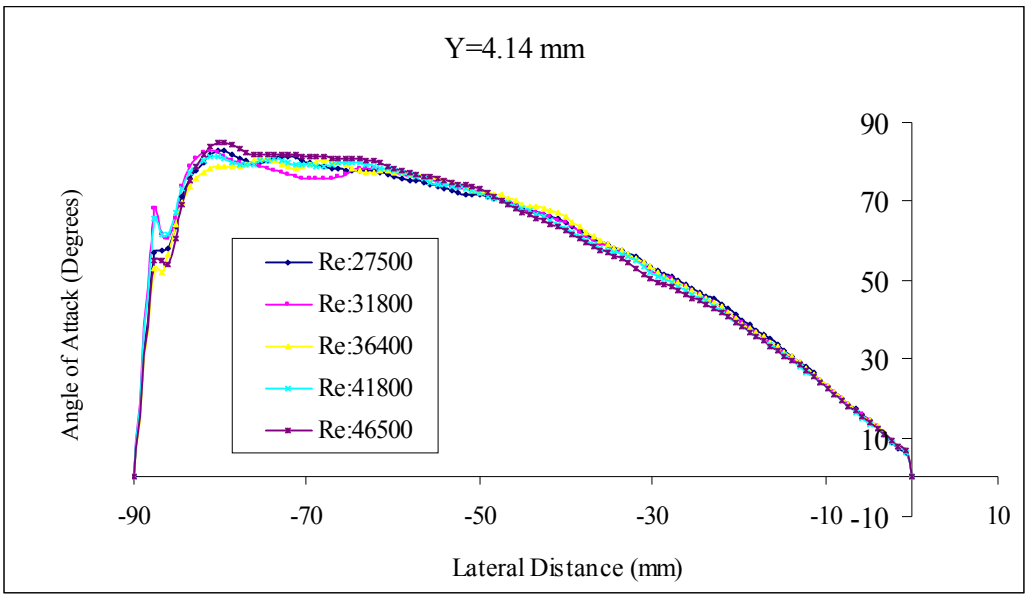

Figure 5.35: Plot of angle of attack against lateral distance at an axial distance of 4.14 mm

5.6 PIV plots for 100 mm monolith

The units for the contour plots in this section are in m/s

5.6.1 Full-field of view plots for 100 mm monolith

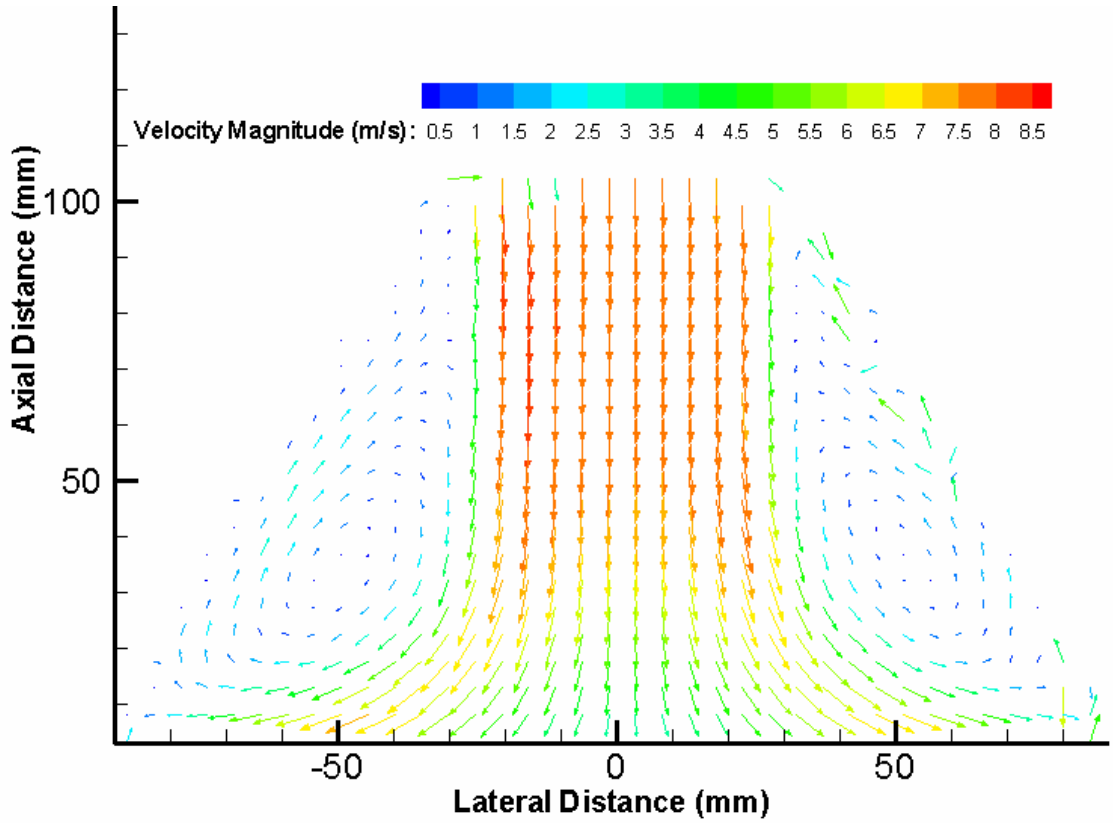

Figure 5.36: Full-field of view vector plot at Re: 41800 for 100 mm monolith

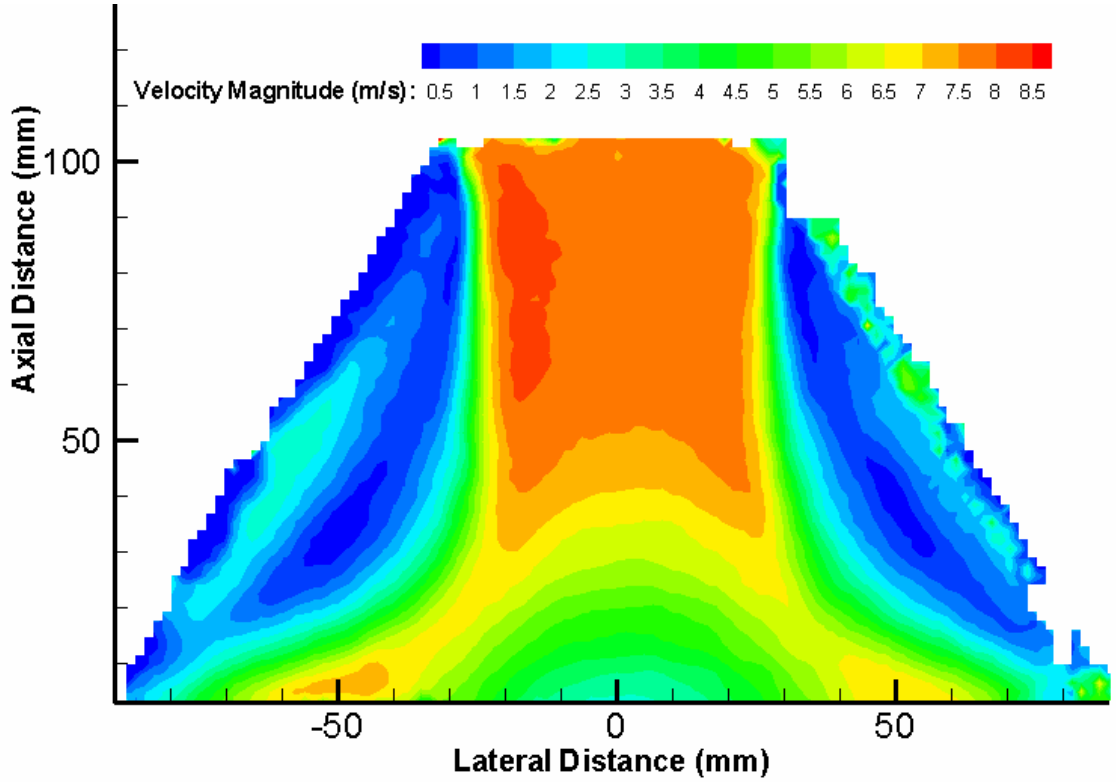

Figure 5.37: Full-field of view contour plot of velocity magnitude at Re: 41800 for 100 mm monolith

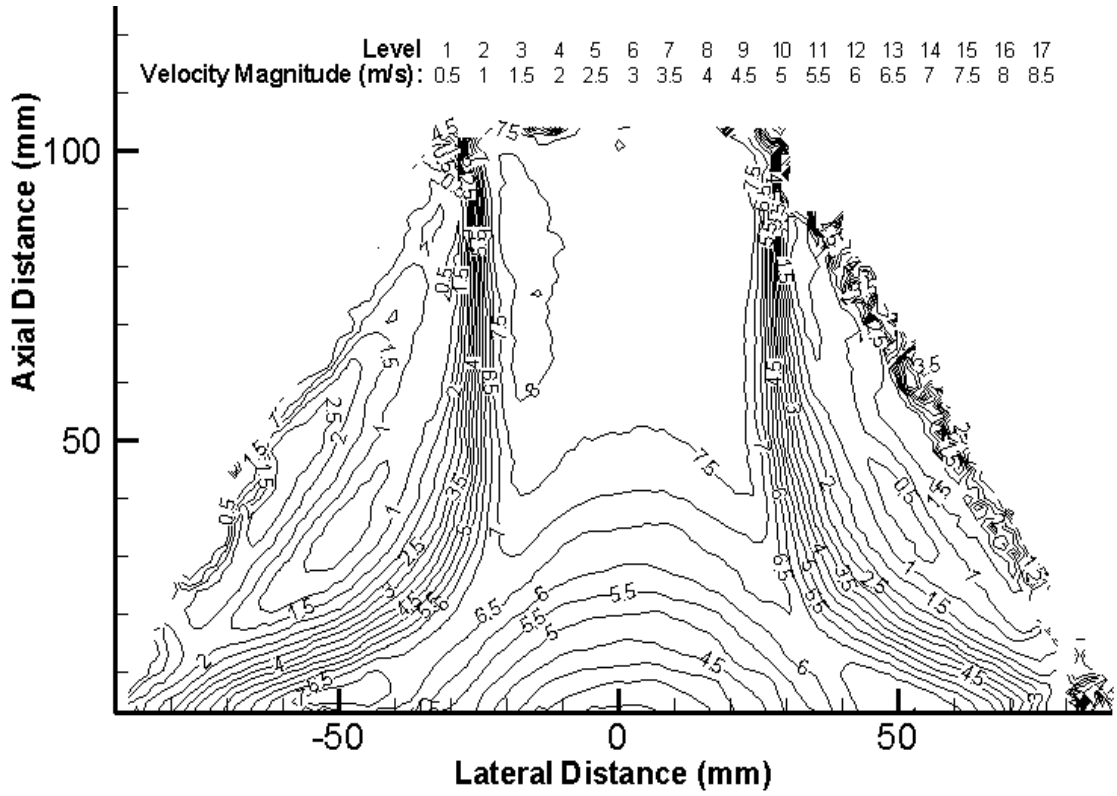

Figure 5.38: Full-field of view line-contour plot at Re: 41800 for 100 mm monolith

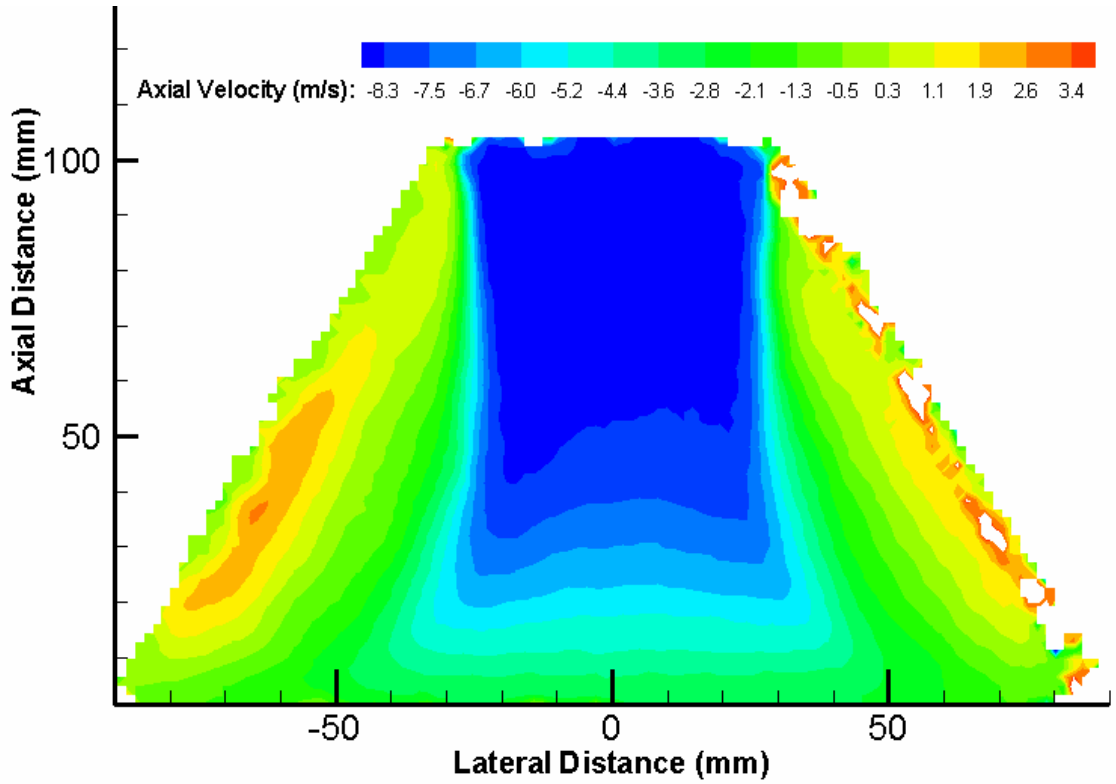

Figure 5.39: Full-field of view contour plot of axial velocity at Re: 41800 for 100 mm monolith

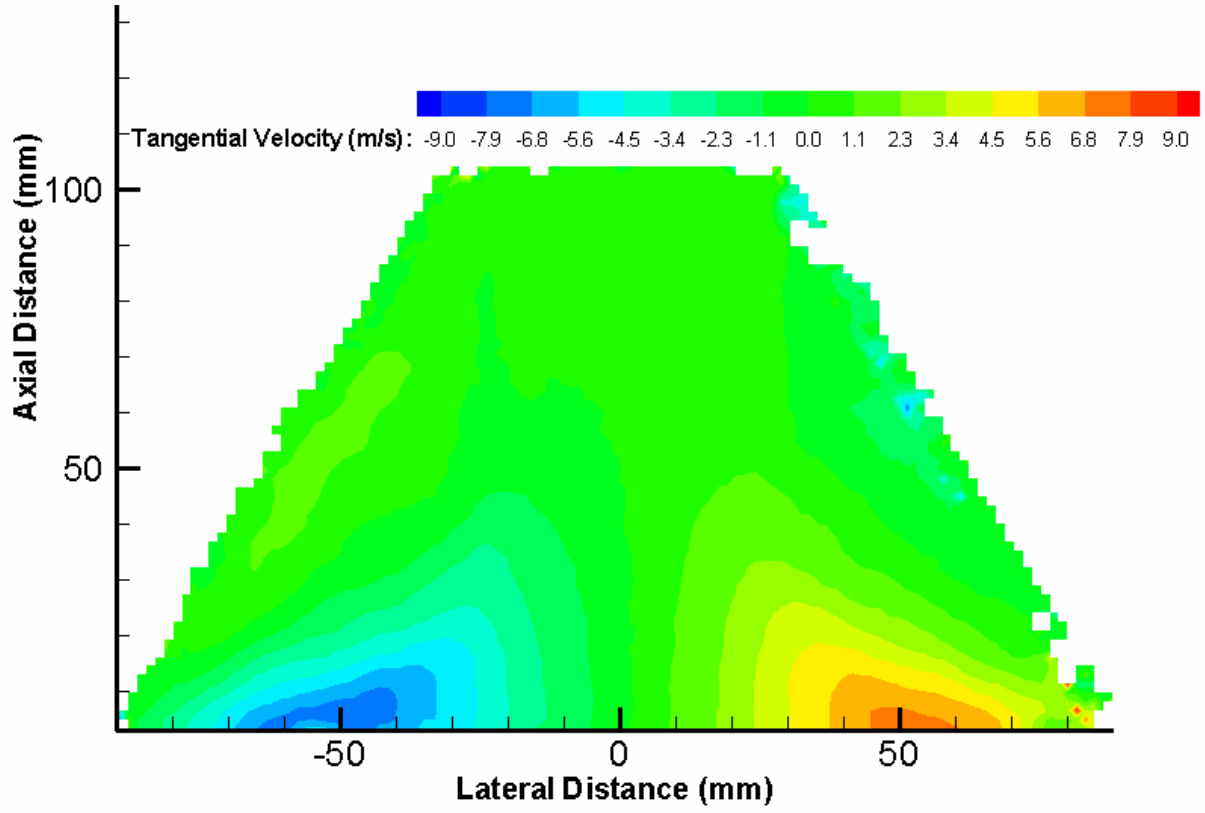

Figure 5.40: Full-field of view contour plot of tangential velocity at Re: 41800 for 100 mm monolith

5.6.2 Half-field of view plots for 100 mm monolith

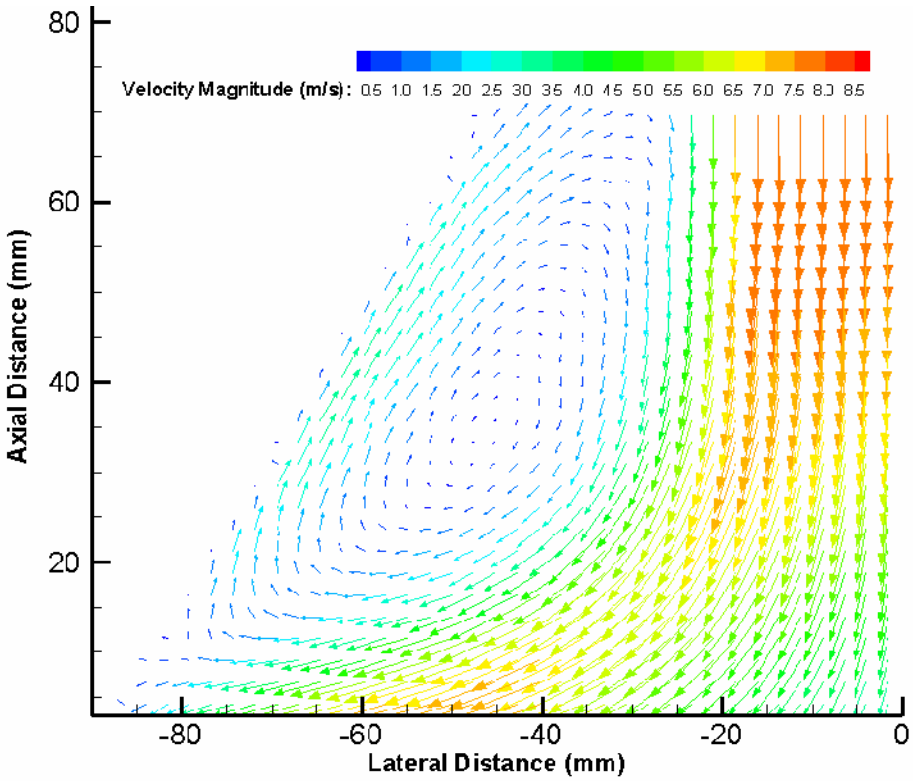

Figure 5.41: Half-field of view vector plot of axial velocity at Re: 41800 for 100 mm monolith

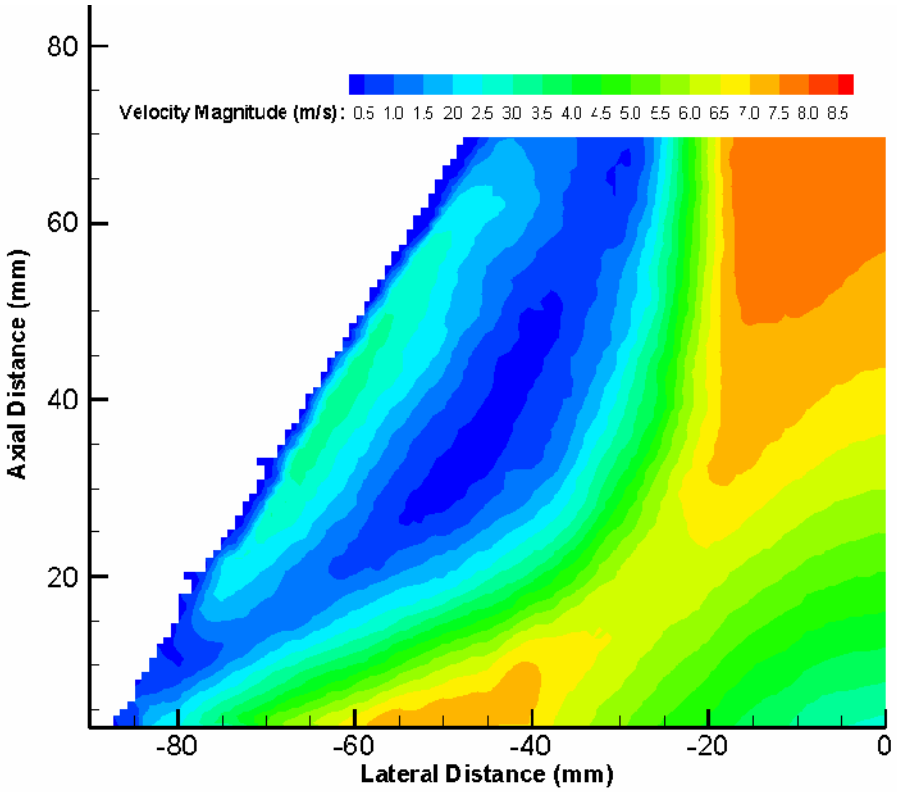

Figure 5.42: Half-field of view contour plot of tangential velocity at Re: 41800 for 100 mm monolith

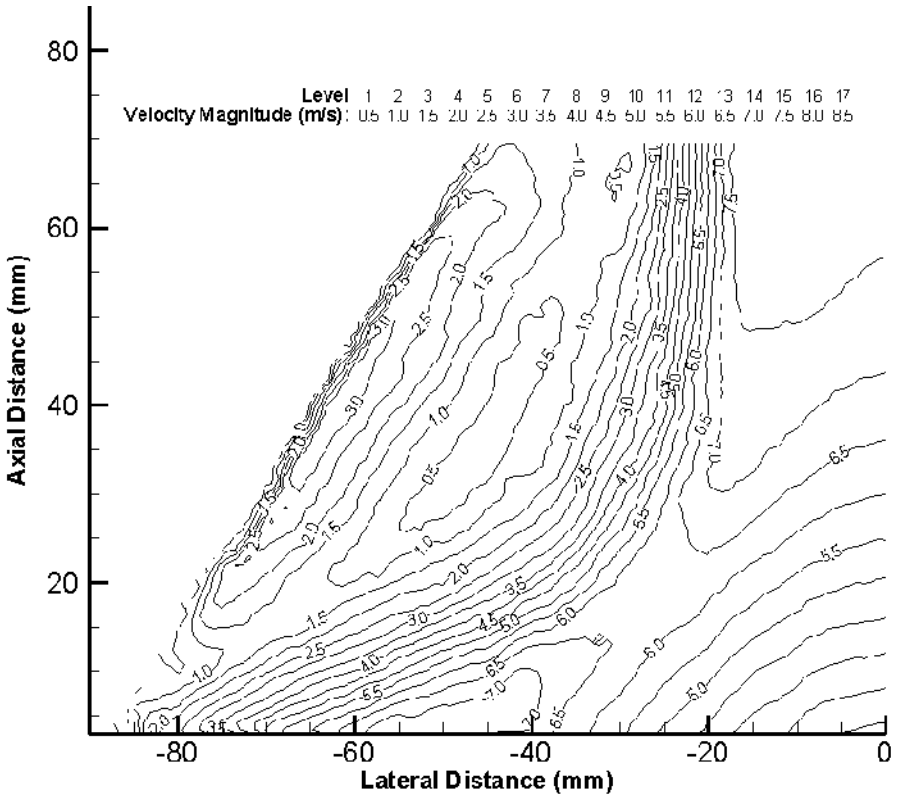

Figure 5.43: Half-field of view line-contour plot at Re: 41800 for 100 mm monolith

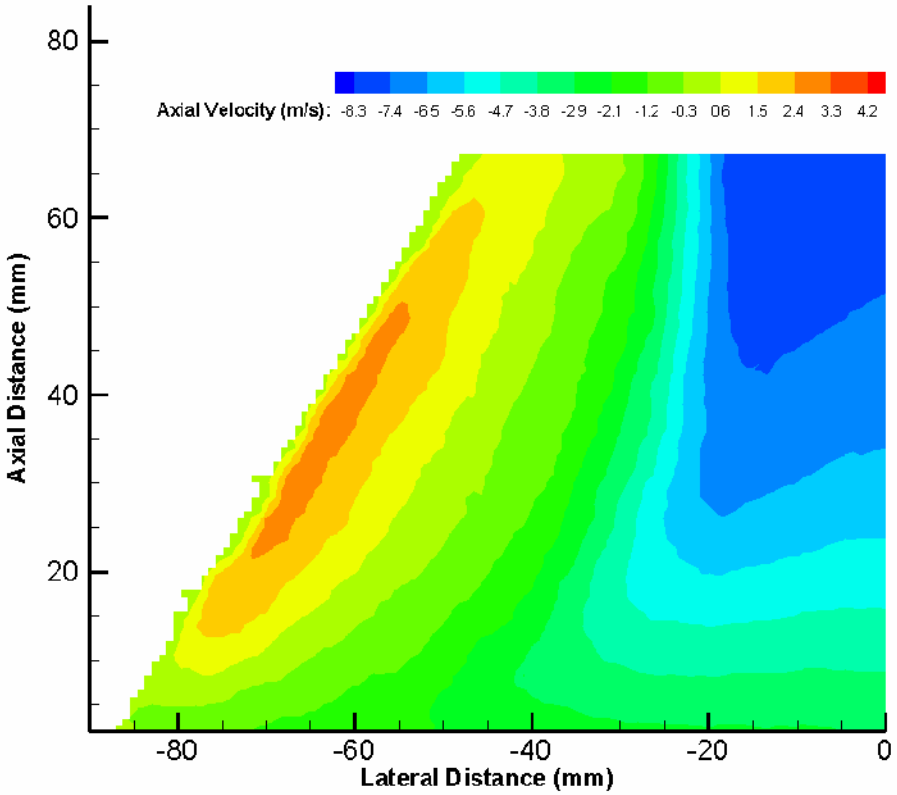

Figure 5.44: Half-field of view contour plot of axial velocity at Re: 41800 for 100 mm monolith

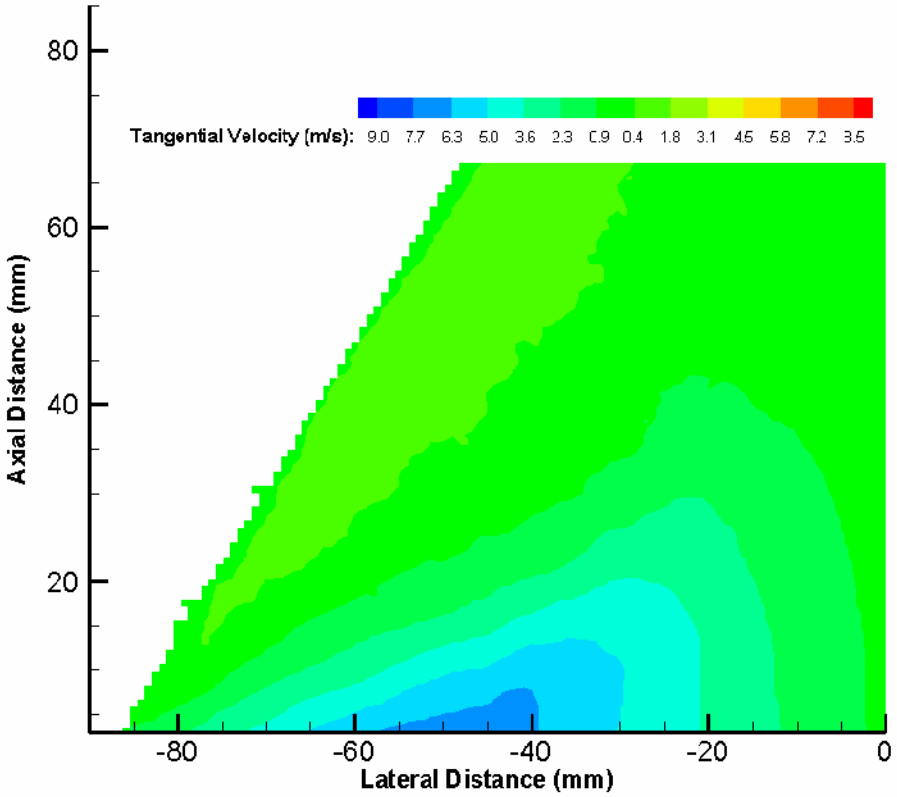

Figure 5.45: Half-field of view contour plot of tangential velocity at Re: 41800 for 100 mm monolith

5.6.3 Near-wall field of view plots for 27 mm monolith

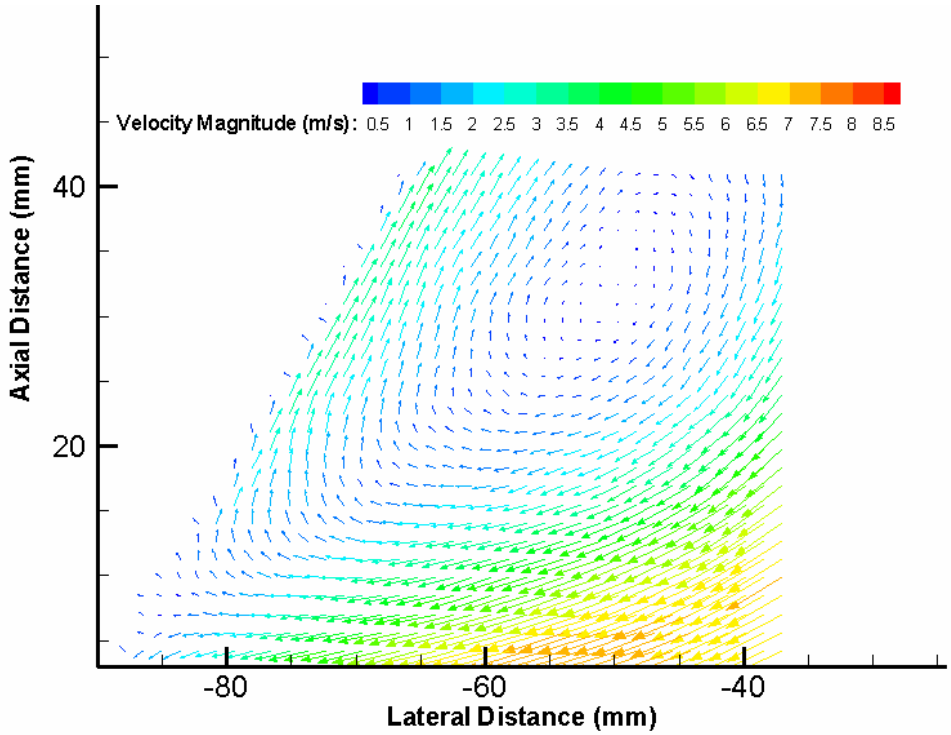

Figure 5.46: Near-wall field of view vector plot at Re: 41800 for 100 mm monolith

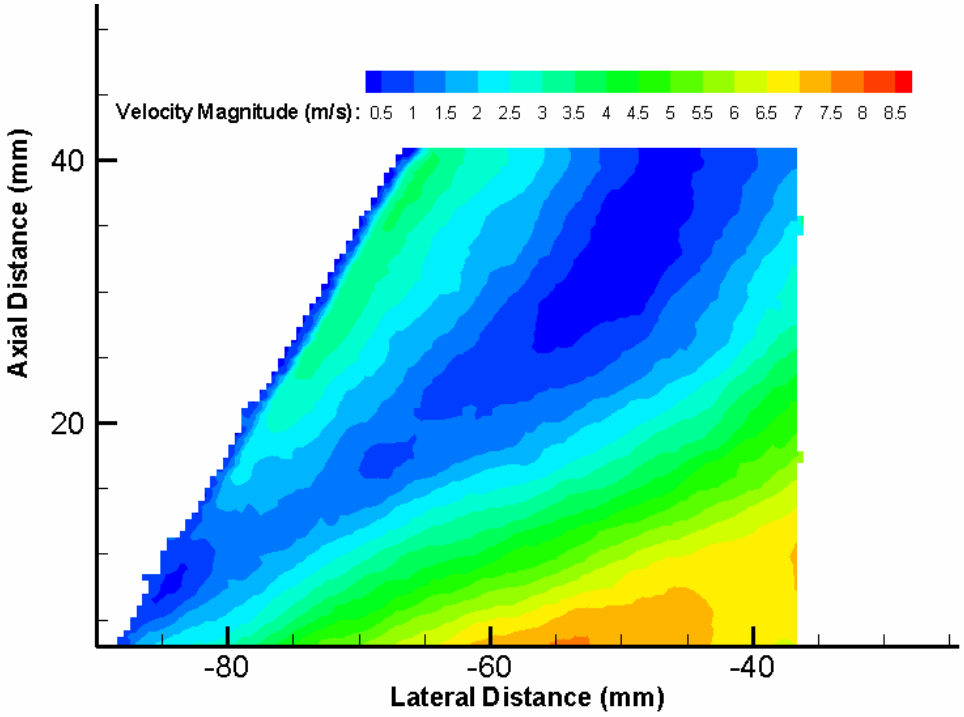

Figure 5.47: Near-wall field of view contour plot of velocity magnitude at Re: 41800 for 100 mm monolith

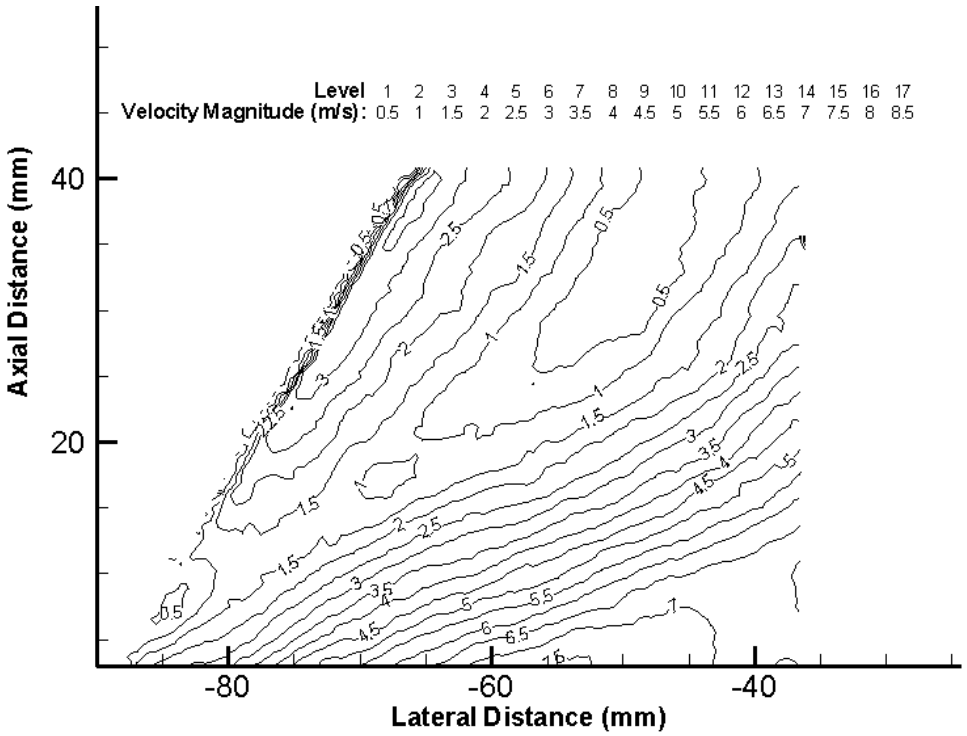

Figure 5.48: Near-wall field of view line-contour plot of velocity magnitude at Re: 41800 for 100 mm monolith

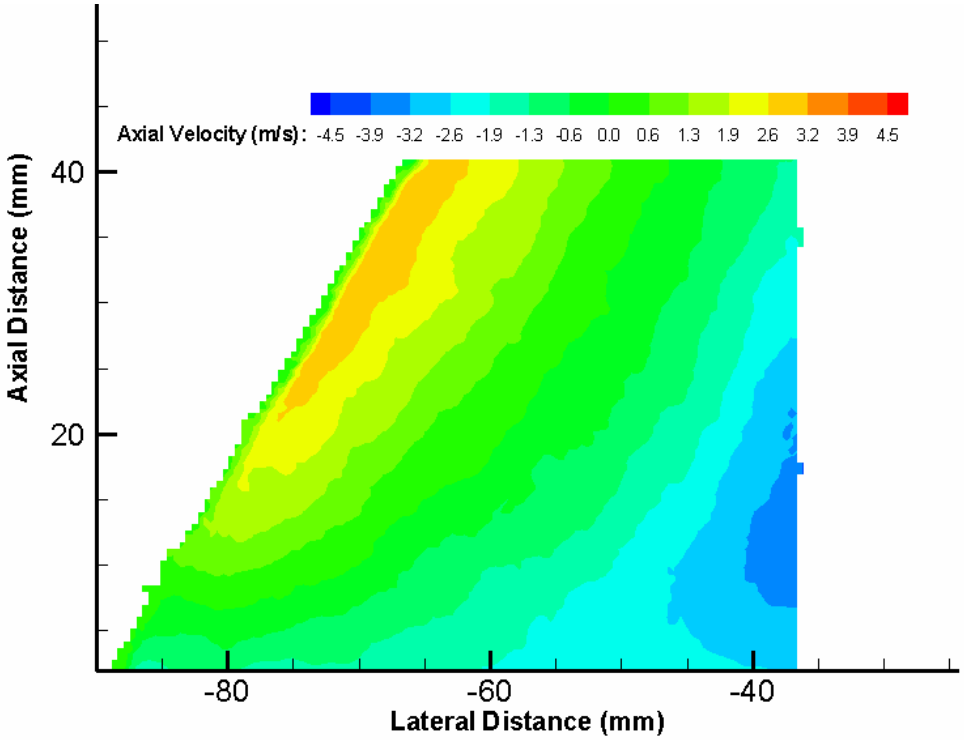

Figure 5.49: Near-wall field of view contour plot of axial velocity at Re: 41800 for 100 mm monolith

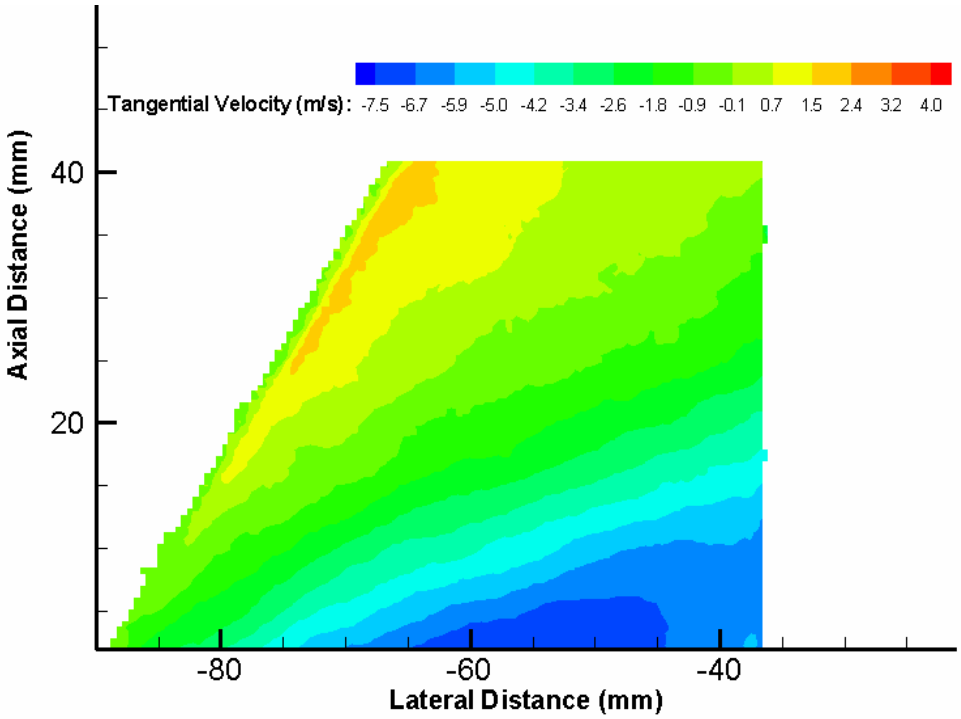

Figure 5.50: Near-wall field of view contour plot of tangential velocity at Re: 41800 for 100 mm monolith

5.6.4 Non-dimensional axial velocity profiles for 100 mm monolith

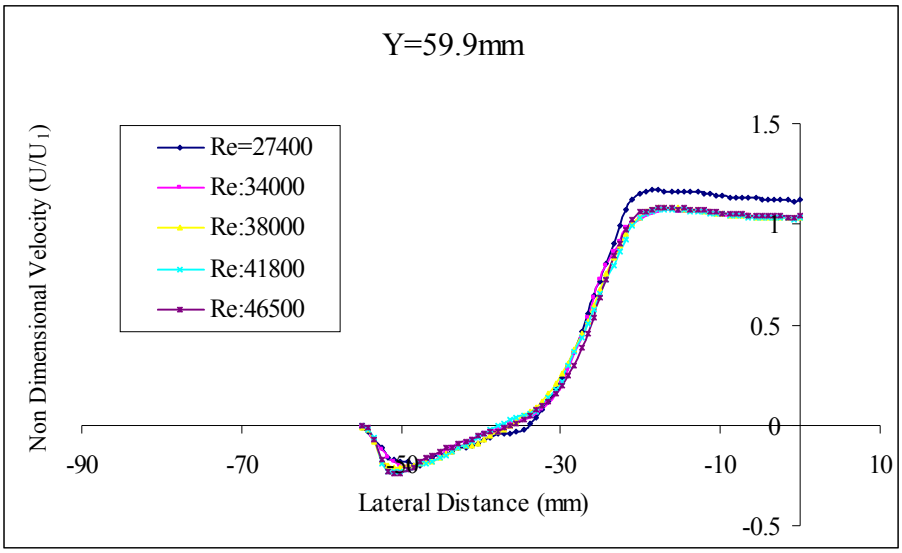

Figure 5.51: Non-dimensional axial velocity profiles at an axial distance of 59.9 mm for 100 mm monolith

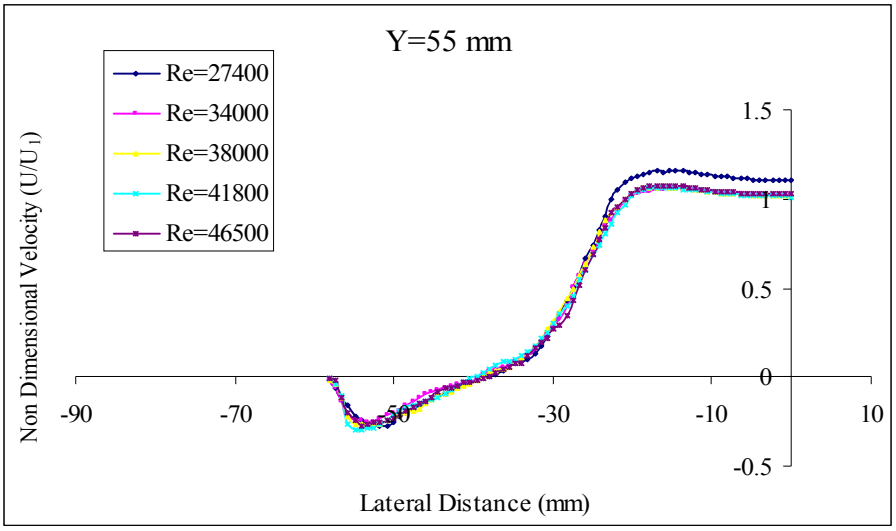

Figure 5.52: Non-dimensional axial velocity profiles at an axial distance of 55 mm for 100 mm monolith

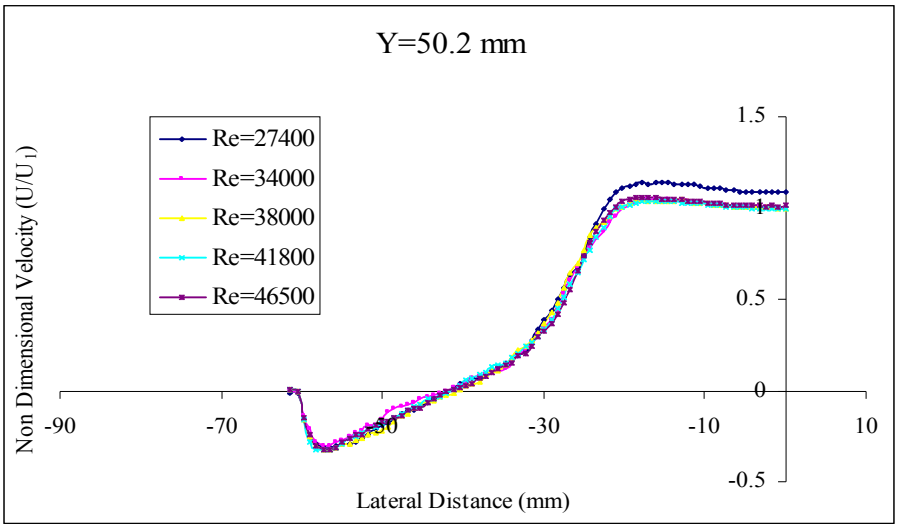

Figure 5.53: Non-dimensional axial velocity profiles at an axial distance of 50.2 mm for 100 mm monolith

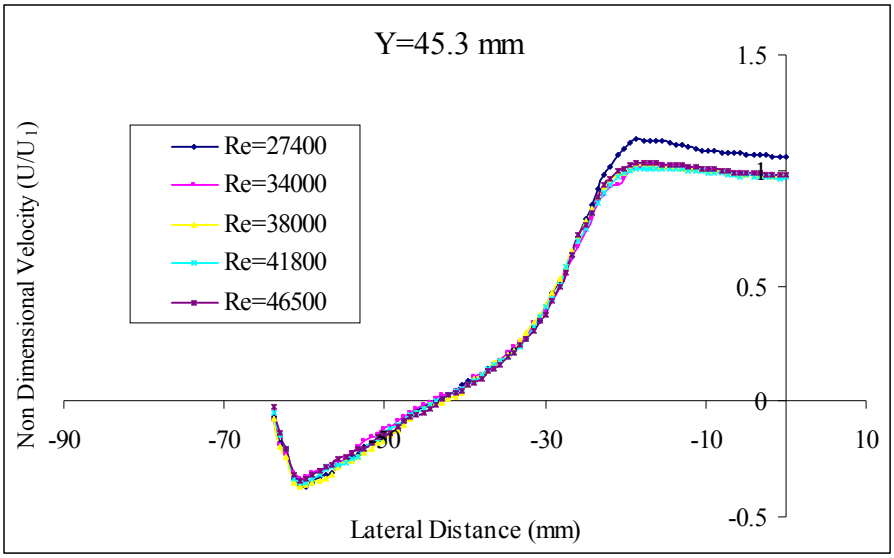

Figure 5.54: Non-dimensional axial velocity profiles at an axial distance of 45.3 mm for 100 mm monolith

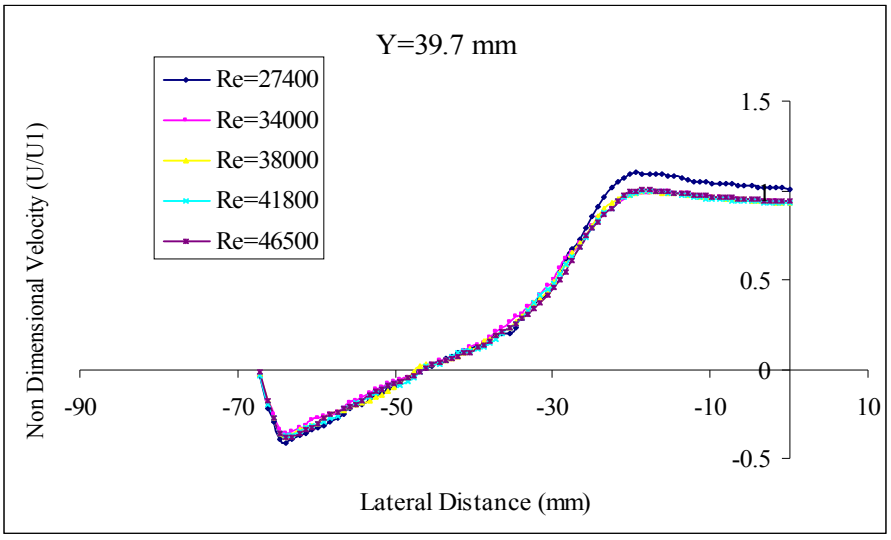

Figure 5.55: Non-dimensional axial velocity profiles at an axial distance of 39.7 mm for 100 mm monolith

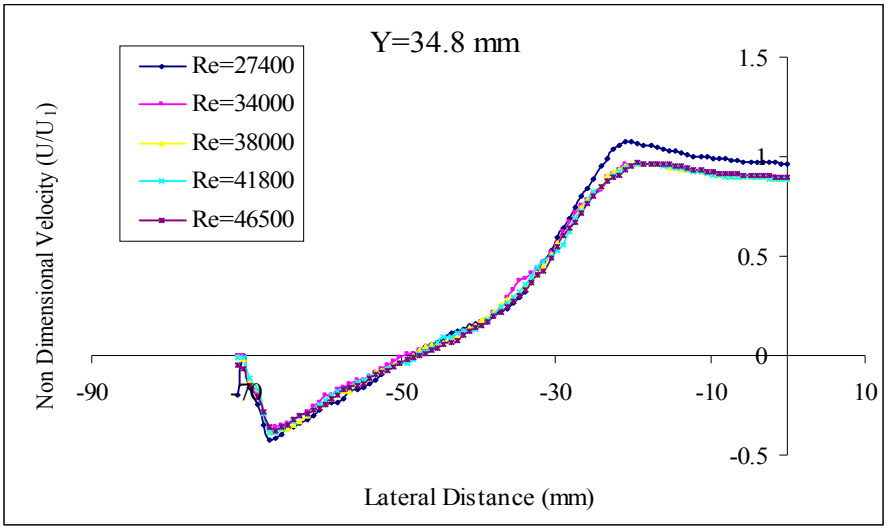

Figure 5.56: Non-dimensional axial velocity profiles at an axial distance of 34.8mm for 100 mm monolith

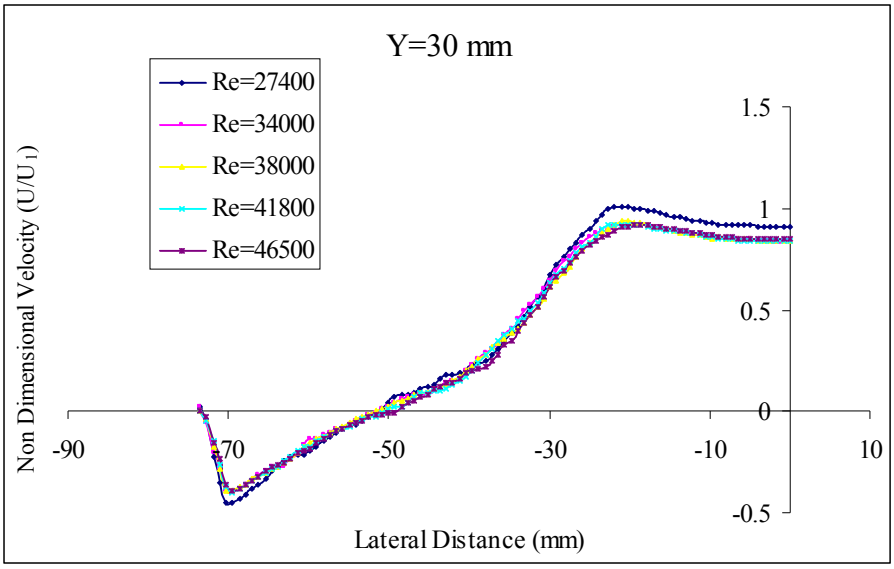

Figure 5.57: Non-dimensional axial velocity profiles at an axial distance of 30 mm for 100 mm monolith

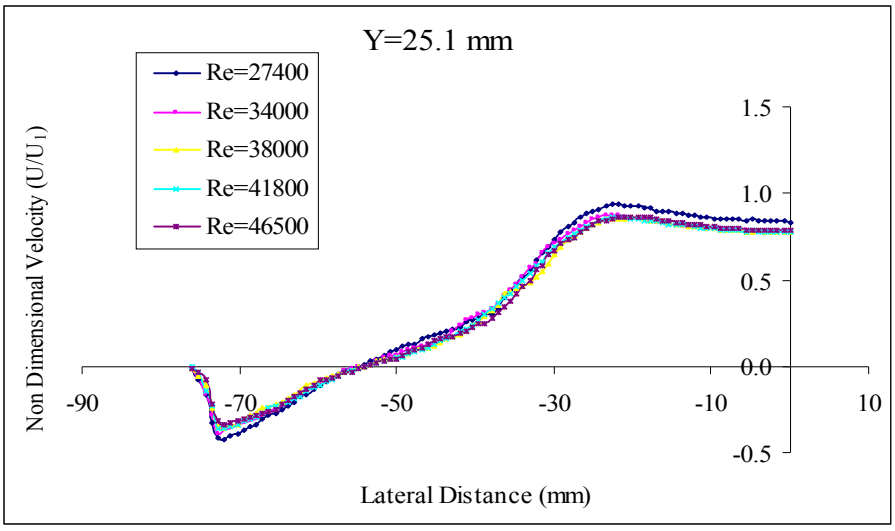

Figure 5.58: Non-dimensional axial velocity profiles at an axial distance of 25.1 mm for 100 mm monolith

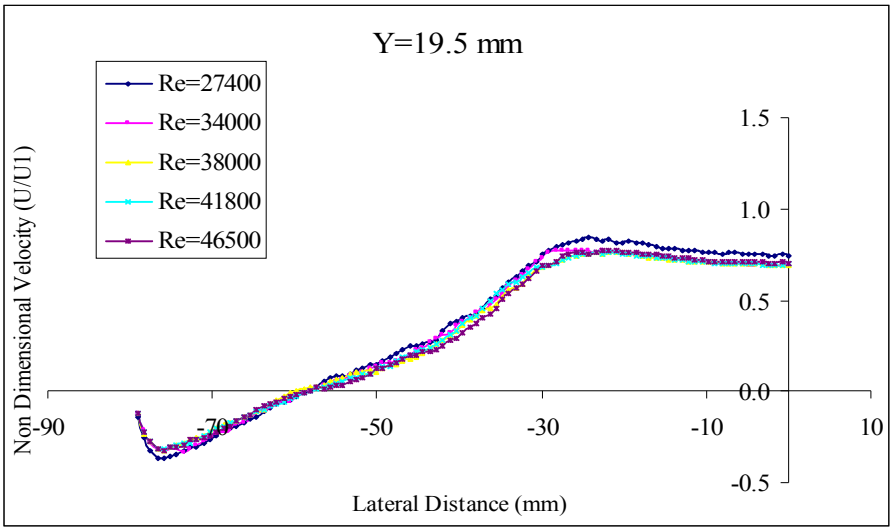

Figure 5.59: Non-dimensional axial velocity profiles at an axial distance of 19.5 mm for 100 mm monolith

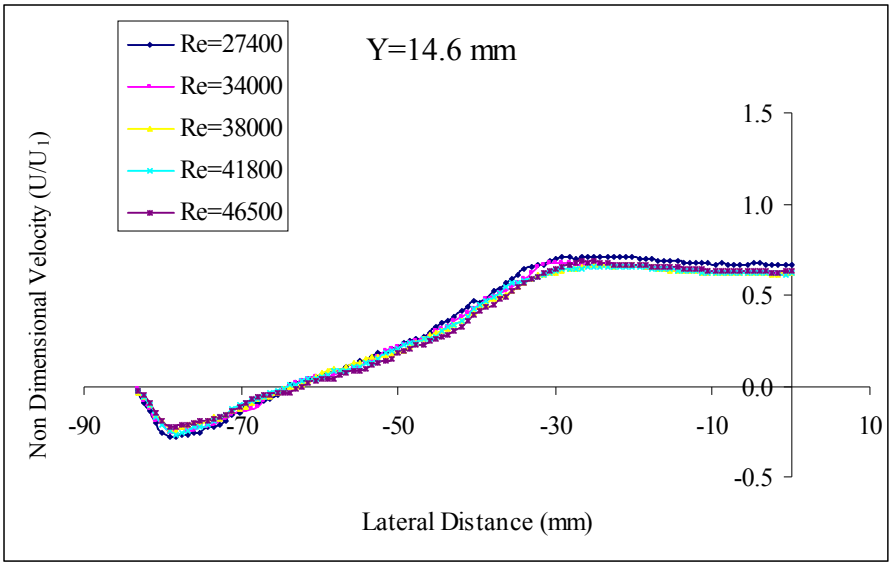

Figure 5.60: Non-dimensional axial velocity profiles at an axial distance of 14.6 mm for 100 mm monolith

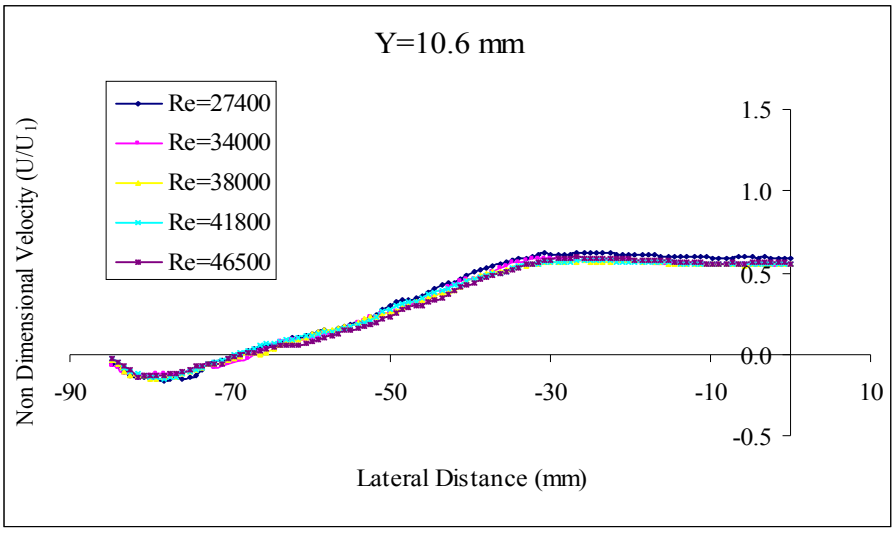

Figure 5.61: Non-dimensional axial velocity profiles at an axial distance of 10.6 mm for 100 mm monolith

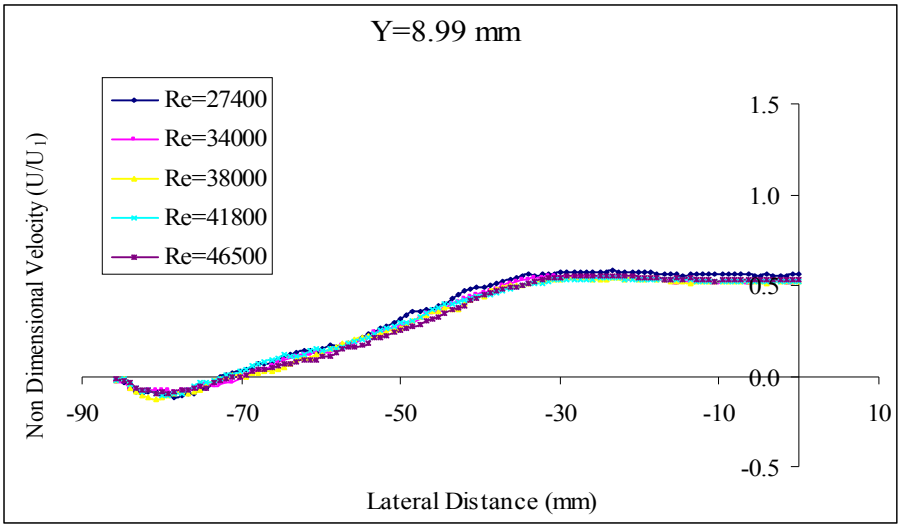

Figure 5.62: Non-dimensional axial velocity profiles at an axial distance of 8.99 mm for 100 mm monolith

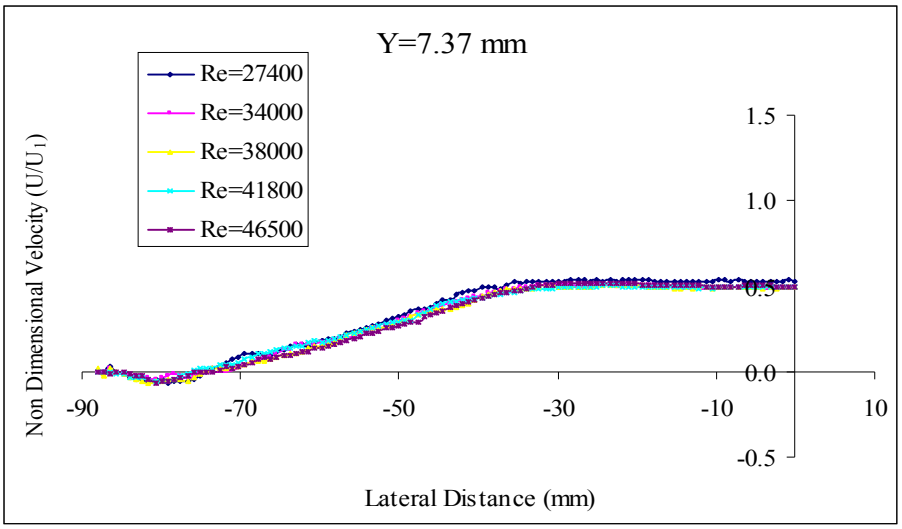

Figure 5.63: Non-dimensional axial velocity profiles at an axial distance of 7.37 mm for 100 mm monolith

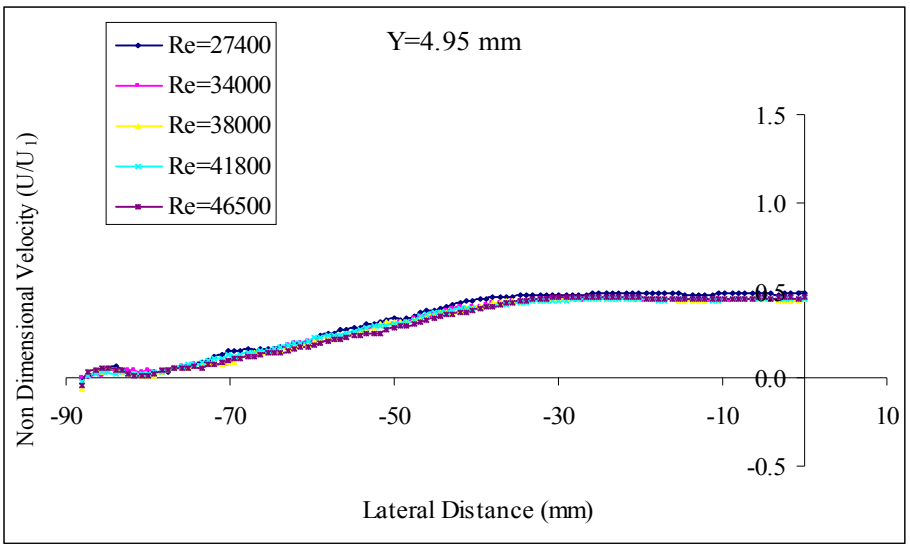

Figure 5.64: Non-dimensional axial velocity profiles at an axial distance of 4.95 mm for 100 mm monolith

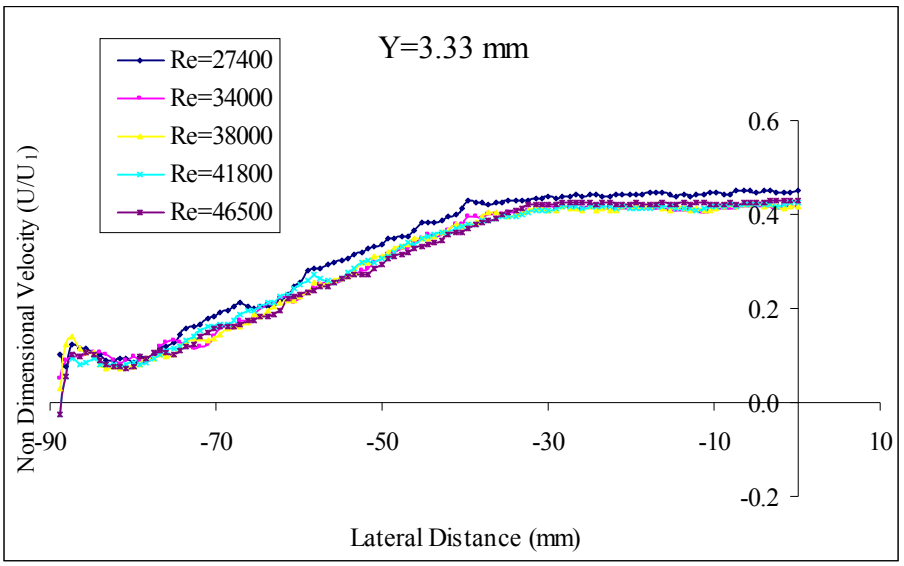

Figure 5.65: Non-dimensional axial velocity profiles at an axial distance of 3.33 mm for 100 mm monolith

5.6.5 Non-dimensional tangential velocity profiles for 100 mm monolith

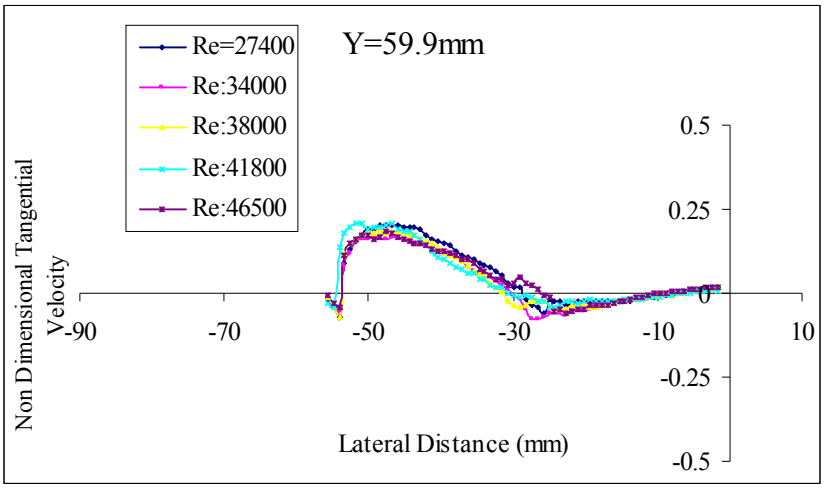

Figure 5.66: Non-dimensional tangential velocity profiles at an axial distance of 59.9 mm for 100 mm monolith

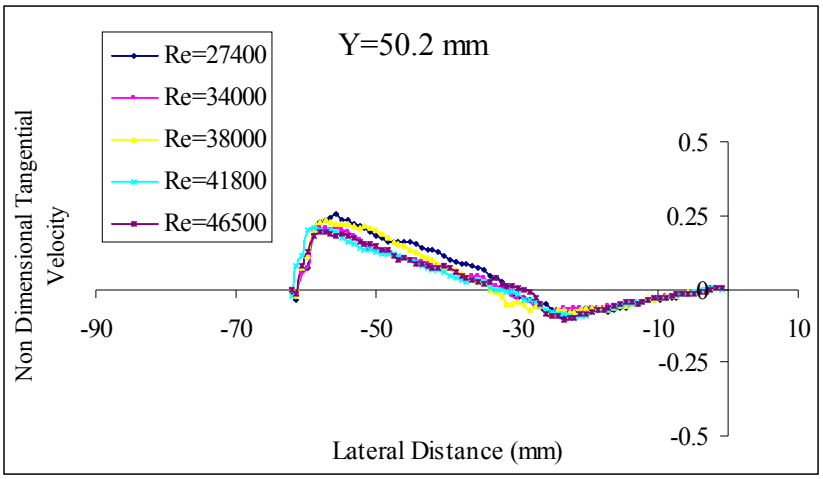

Figure 5.67: Non-dimensional tangential velocity profiles at an axial distance of 50.2 mm for 100 mm monolith

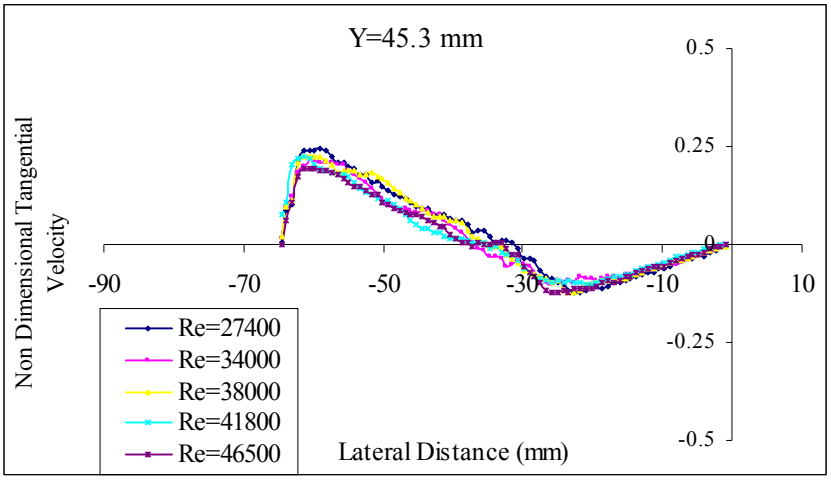

Figure 5.68: Non-dimensional tangential velocity profiles at an axial distance of 45.3 mm for 100 mm monolith

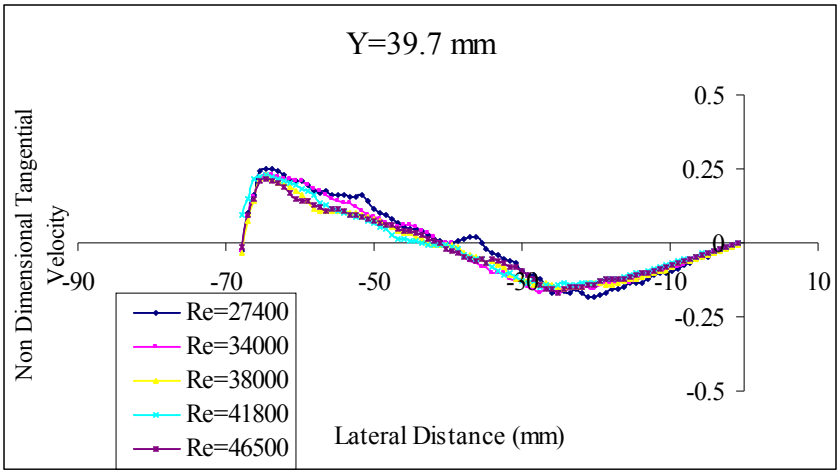

Figure 5.69: Non-dimensional tangential velocity profiles at an axial distance of 39.7 mm for 100 mm monolith

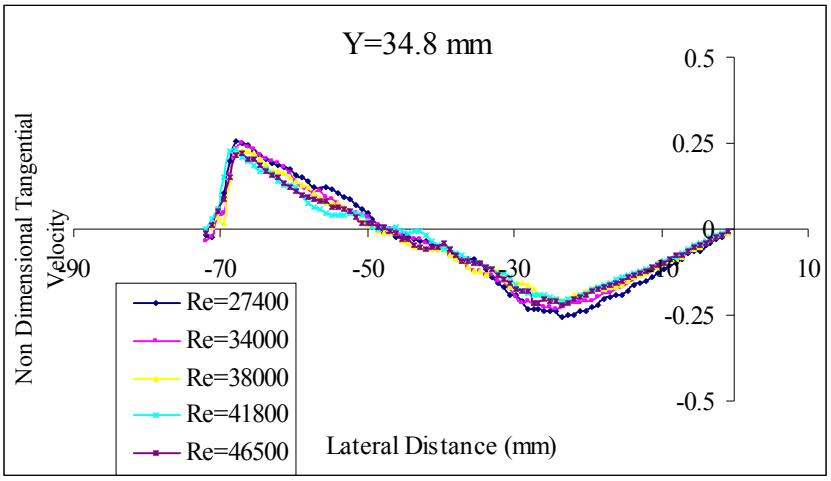

Figure 5.70: Non-dimensional tangential velocity profiles at an axial distance of 34.8 mm for 100 mm monolith

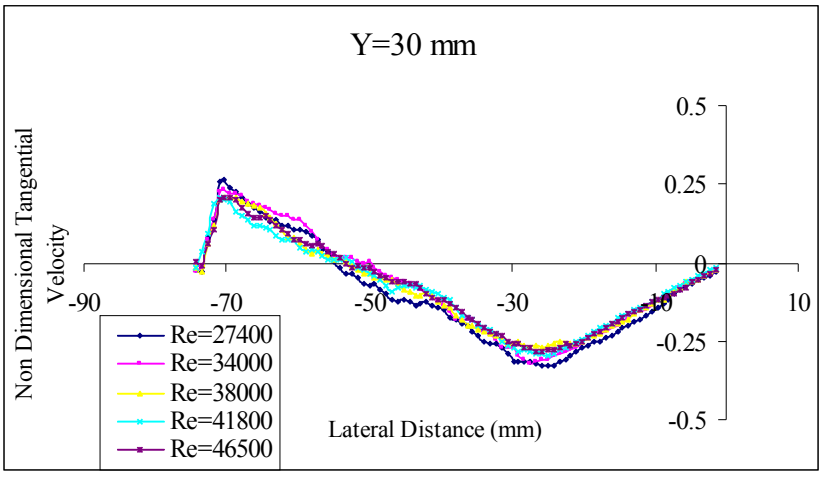

Figure 5.71: Non-dimensional tangential velocity profiles at an axial distance of 30 mm for 100 mm monolith

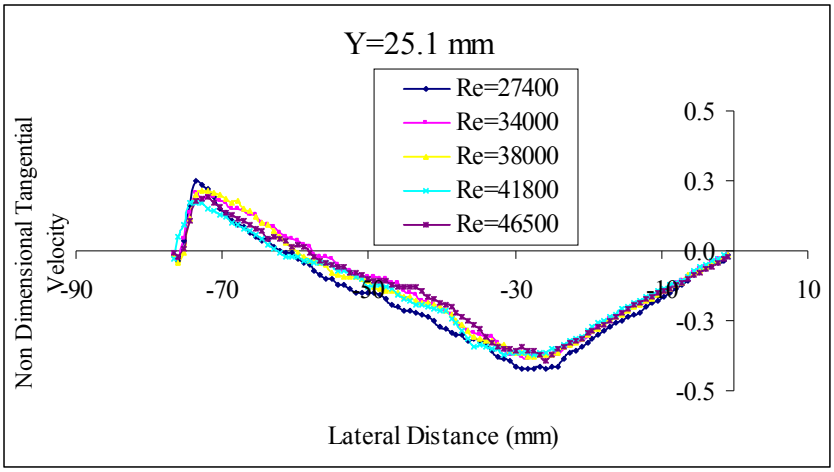

Figure 5.72: Non-dimensional tangential velocity profiles at an axial distance of 25.1 mm for 100 mm monolith

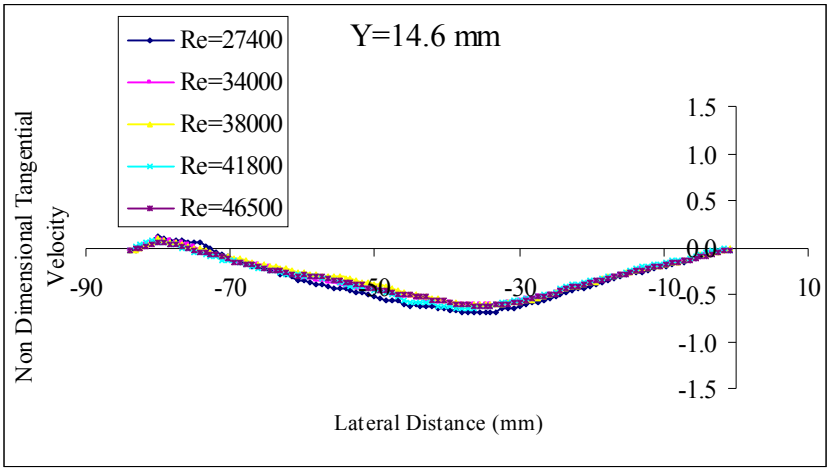

Figure 5.73: Non-dimensional tangential velocity profiles at an axial distance of 14.6 mm for 100 mm monolith

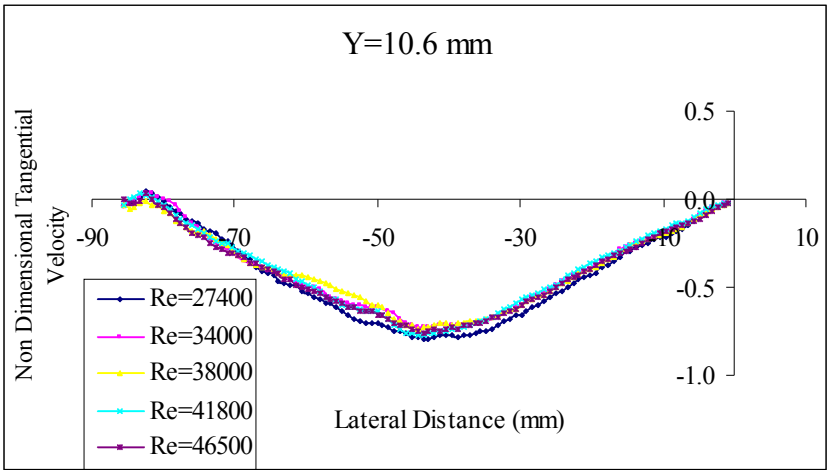

Figure 5.74: Non-dimensional tangential velocity profiles at an axial distance of 10.6 mm for 100 mm monolith

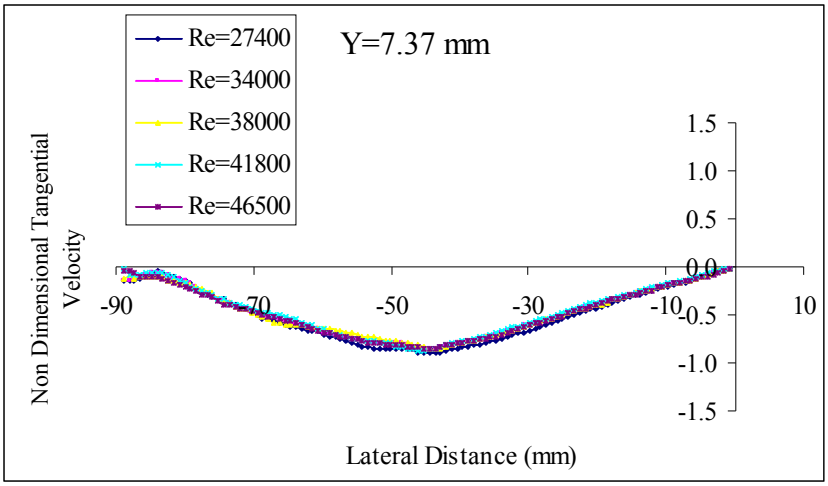

Figure 5.75: Non-dimensional tangential velocity profiles at an axial distance of 7.37 mm for 100 mm monolith

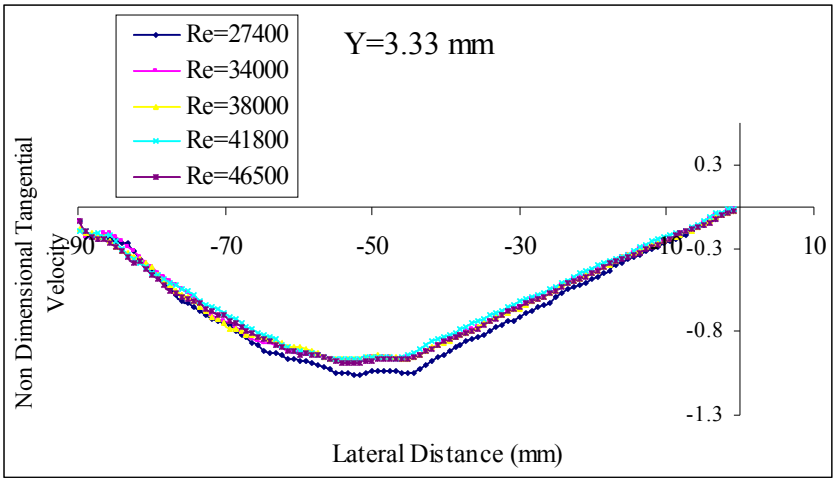

Figure 5.76: Non-dimensional tangential velocity profiles at an axial distance of 3.33 mm for 100 mm monolith

5.6.6 Plot of angle of attack close to the substrate

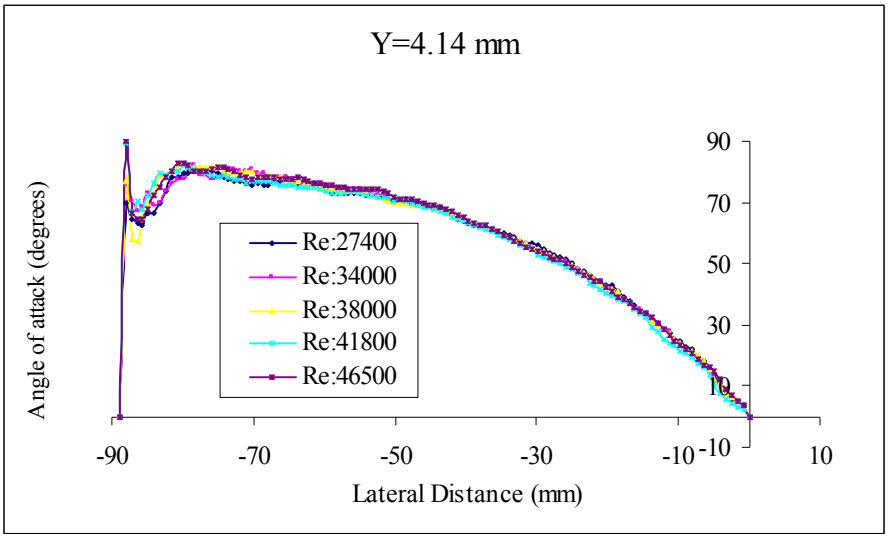

Figure 5.77: Plot of angle of attack against lateral distance at an axial distance of 4.14 mm

5.7 Comparison of axial velocity profiles for 100 mm and 27 mm monoliths

(Legend in Figs. (5.78-5.89) show the axial distance from the diffuser-substrate interface)

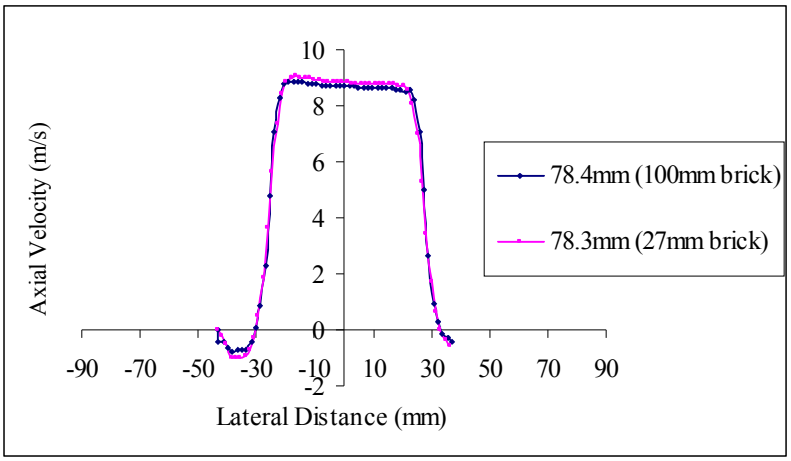

Figure 5.78: Comparison of axial velocity profiles for 27 and 100 mm monolith at Re: 46500

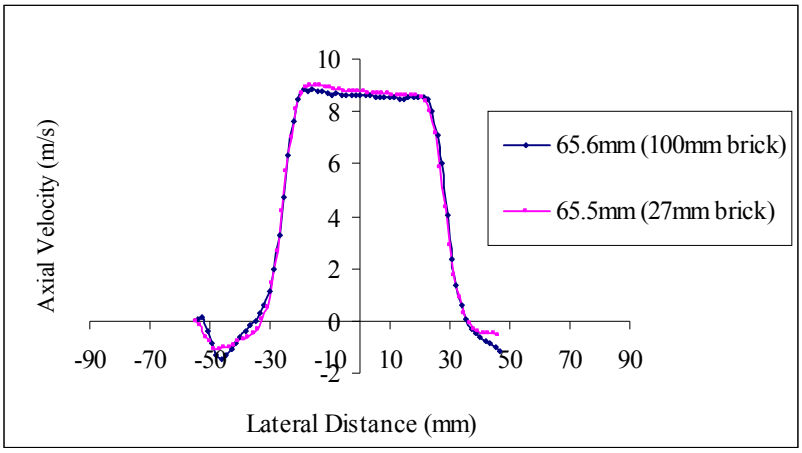

Figure 5.79: Comparison of axial velocity profiles for 27 and 100 mm monolith at Re: 46500

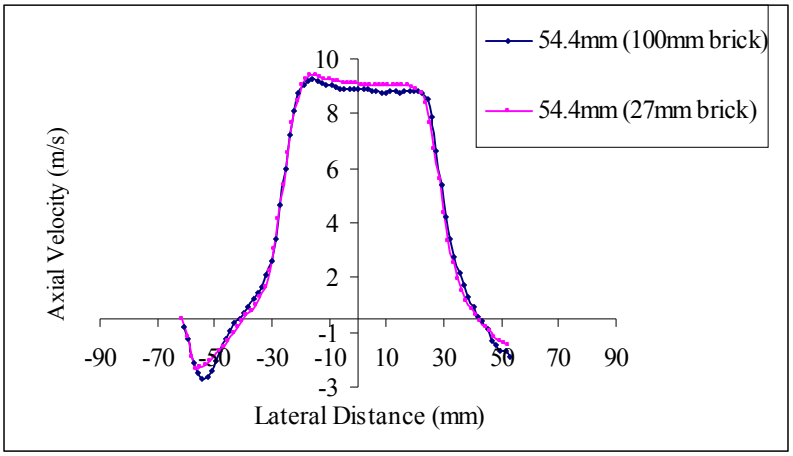

Figure 5.80: Comparison of axial velocity profiles for 27 and 100 mm monolith at Re: 46500

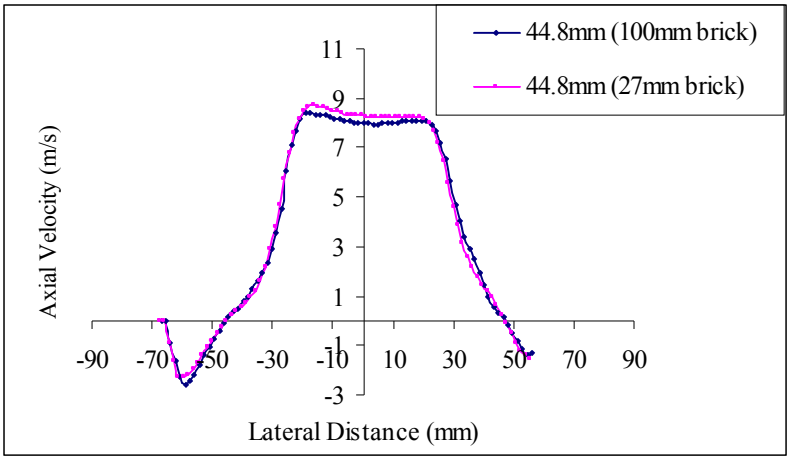

Figure 5.81: Comparison of axial velocity profiles for 27 and 100 mm monolith at Re: 46500

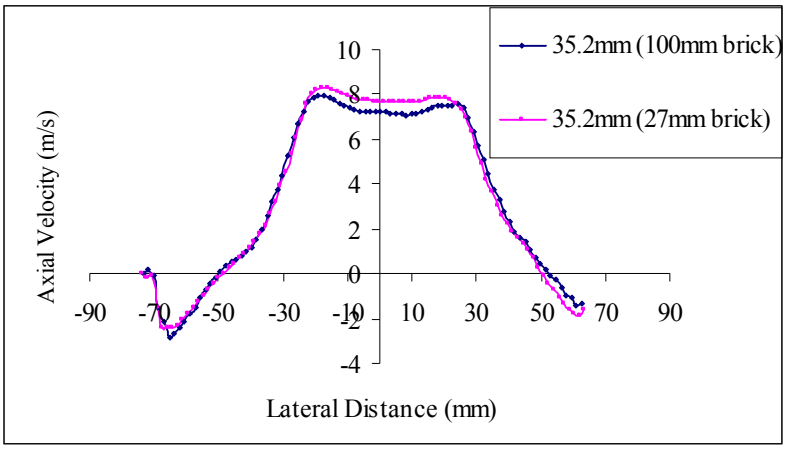

Figure 5.82: Comparison of axial velocity profiles for 27 and 100 mm monolith at Re: 46500

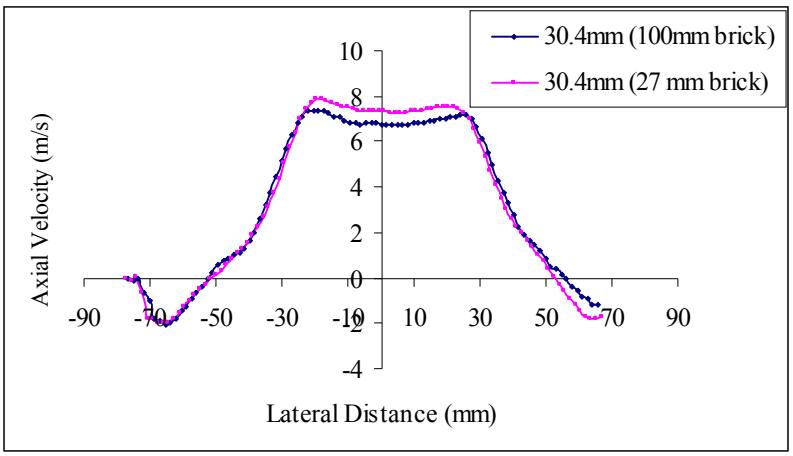

Figure 5.83: Comparison of axial velocity profiles for 27 and 100 mm monolith at Re: 46500

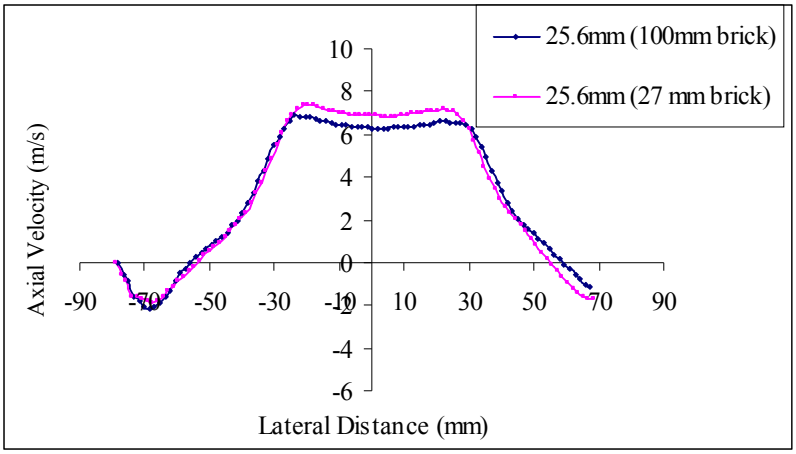

Figure 5.84: Comparison of axial velocity profiles for 27 and 100 mm monolith at Re: 46500

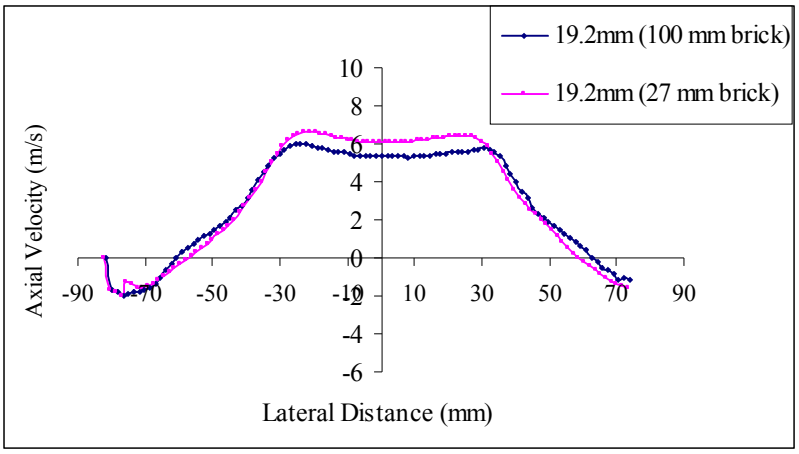

Figure 5.85: Comparison of axial velocity profiles for 27 and 100 mm monolith at Re: 46500

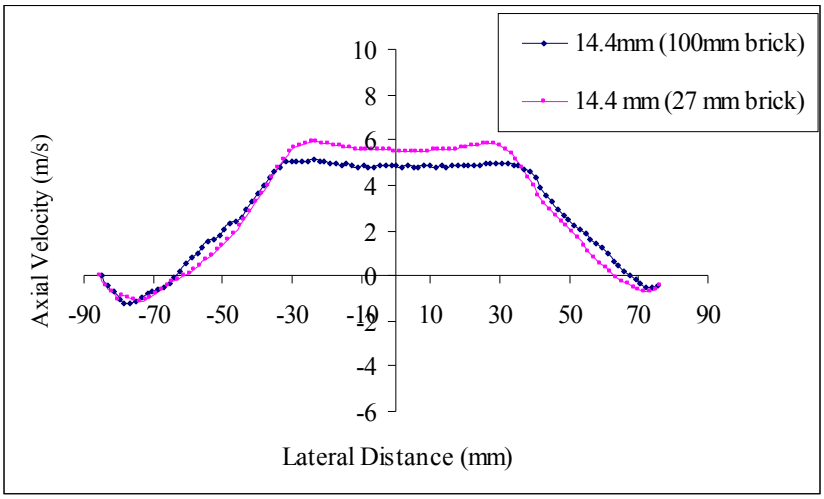

Figure 5.86: Comparison of axial velocity profiles for 27 and 100 mm monolith at Re: 46500

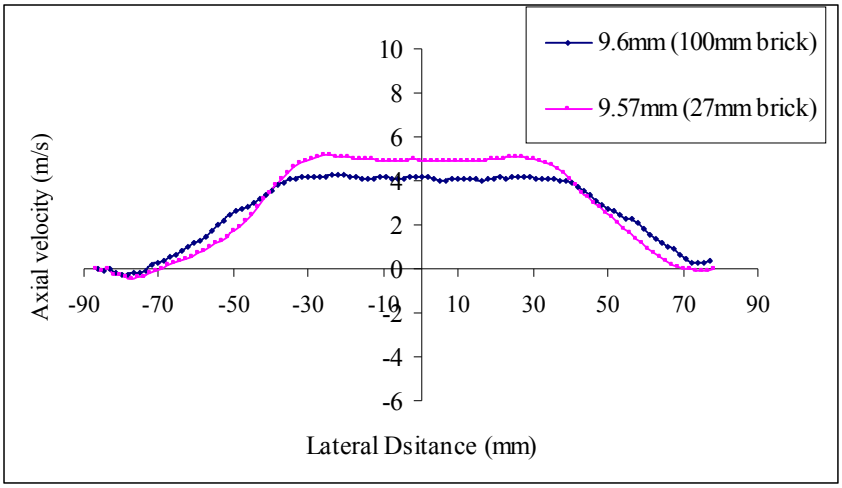

Figure 5.87: Comparison of axial velocity profiles for 27 and 100 mm monolith at Re: 46500

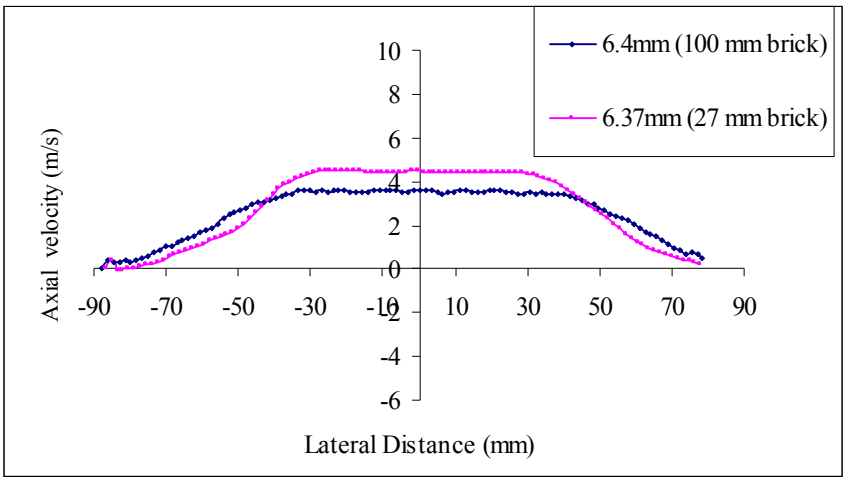

Figure 5.88: Comparison of axial velocity profiles for 27 and 100 mm monolith at Re: 46500

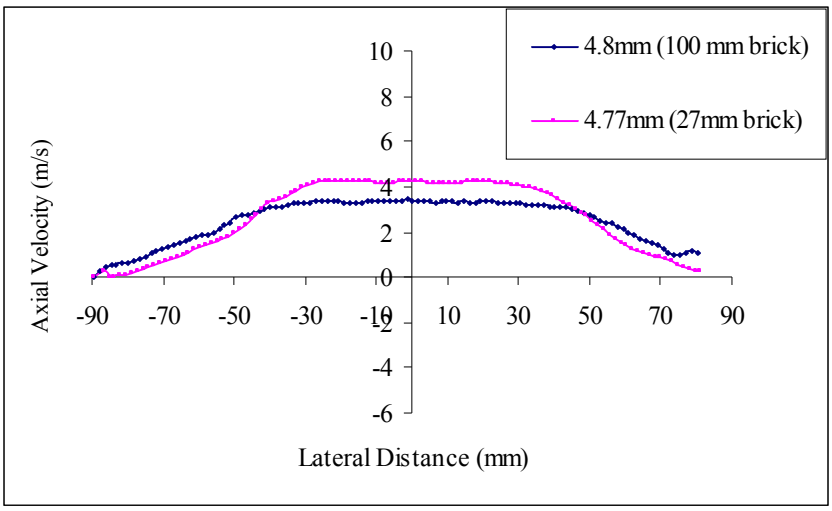

Figure 5.89: Comparison of axial velocity profiles for 27 and 100 mm monolith at Re: 46500

5.8 Summary

PIV experiments for flow in a diffuser in the presence of downstream substrates have been successfully performed. The PIV results showed that the flow in a wide angle diffuser consists of a central core region, free shear layer region and recirculation region. The characteristics of flow in the central core region are similar to that of plane rectangular jets in their near field region. There is an occurrence of saddle shape profiles downstream of the diffuser. The free shear layer region grows downstream of the diffuser and separates the central core region and the recirculation region. The recirculation region consists of vortices and is dependent on the angle of the diffuser. The flow at the periphery reaches a stagnation point at approximately 7 mm from the diffuser-substrate interface. The non-dimensional axial velocity profiles show the point of crossover where the flow has changed its initial direction. The axial velocity profiles showed that there is no Reynolds number effect on the flow field. For two substrate lengths, the results showed a flattening of the axial profile upstream of the substrate with the higher resistance monolith.

Such information and the quality of the data from the experiments will be used to compare with CFD predictions. In order for the CFD to predict the flow in the diffuser accurately, its ability to predict the recirculation bubble and point of cross over is extremely important. The comparison of the CFD predictions for a 2-D model using various turbulence models will be discussed in Chapter 6.

Chapter 6: CFD Simulations

6.1 Introduction

The aim of this study is to incorporate the entrance effect relationship obtained from the one-dimensional oblique angle flow measurements in Chapter 2 into the CFD code and compare with experimental data. The CFD predictions have been performed for an axisymmetric and 2-D catalyst model. For the axisymmetric catalyst model, experimental data of the velocity profiles on an axisymmetric catalyst flow rig from a previous study (Wollin, 2001) have been used for comparison. The 2-D predictions have been compared with the experimental measurements from PIV and HWA performed in Chapter 4 and 5. The CFD predictions for both models have been performed using STAR-CD.

STAR-CD is a general purpose computational fluid dynamics (CFD) code which predicts fluid flow, heat transfer, chemical behaviour and other related phenomena using the finite volume method. It consists of a pre-processor (PROSTAR), main processor (STAR) and a post-processor (PROSTAR). PROSTAR as a pre-processor is used to specify the fluid flow problems like the geometry, meshing, thermo-physical properties, boundary conditions etc using a graphical user interface. The main processor STAR discretizes the Navier-Stokes equation and then solves them numerically. There are three algorithms available in STAR, SIMPLE, PISO and SIMPISO. The output data obtained from STAR are plotted and extracted using PROSTAR. STAR-CD Version 3.26 is used for CFD simulations in this study.

6.2 Porous Medium Approach

An automotive monolith consists of thousands of channels and it requires considerable computational resources in order to simulate the flow behaviour in each of the channels. A widely popular approach is the equivalent continuum method, also called the porous medium approach, wherein the entire substrate is treated as a porous medium with a distributed resistance applied to the entire region. In STAR-CD the distributed resistance is correlated to the pressure drop by Equation 6.1.

$$\frac{\partial p}{\partial \xi i} = -K_i U_{s,i} \qquad 6.1$$

Where ξ_i (i=1, 2, 3) represent the three mutually perpendicular directions and K_i and $U_{s,i}$ are the permeability and superficial velocity in the direction ξ_i. The superficial velocity is defined as the volume flow rate divided by cross-sectional area. If U_c is the actual velocity in the channels and ε is the porosity, then the superficial velocity is defined as $\varepsilon.U_c$.

The permeability is a quasilinear function of the superficial velocity magnitude $|\vec{v}|$ and is given by (CD-Adapco, 2004)

$$K_i=\alpha_i|\vec{v}|+\beta_i \qquad 6.2$$

Where α_i and β_i are the user defined permeability coefficients which may be constant or spatially varying. Hence Equation 6.1 can be rewritten as

$$\frac{\partial p}{\partial \xi i} = -\alpha_i U_{s,i}^{\ 2} - \beta_i U_{s,i} \qquad 6.3$$

If the flow in the channels is considered fully developed and laminar, then the pressure drop is given by the Darcy or Hagen-Poiseuille equation.

$$\frac{\Delta P}{L} = \frac{2f\,Re_c\,\mu U_s}{\varepsilon d_h^{\ 2}} \qquad 6.4$$

fRe_c is a constant and is dependent on the cross-sectional shape of the monolith, Re_c is the channel Reynolds number, μ is the dynamic viscosity of the fluid, d_h is the channel hydraulic diameter and ε is the porosity of the substrate.

The flow in the monolith channels is unidirectional and therefore α and β values in the directions perpendicular to the flow are set to very large values (10^6) to ensure a very high resistance to flow in those directions. Also equating 6.3 and 6.4, α in the direction of the flow is set to a very small value and then β is calculated from Darcy's equation.

$$\beta = \frac{2f\,Re_c\,\mu}{\varepsilon d_h^{\ 2}} \qquad 6.5$$

A study by Benjamin et al (1996) showed that the CFD predictions using Darcy's equation (Equation 6.4) under predict the maximum velocity by 17.5%.

An overview of the different approaches used in this study and previous studies to predict the pressure drop in the monolith and the oblique flow entrance effect has been described in Table 6.1. The total pressure drop in the monolith ignoring the contraction and expansion channel losses is given by

$$\Delta P = \Delta P_{Monolith} + P_{Obl} \qquad 6.6$$

Scheme	**$\Delta P_{Monolith}$ (Pa)**		**Entrance Effect (P_{Obl}) (Pa)**
	α	**β**	
Benjamin et.al (1996)	0.0001	Darcy	N/A
Benjamin et.al (1996)	0.0001	Shah	N/A
Kuchemann and Weber (1953) (Theoretical Entrance Effect)	N/A	N/A	$P_{Obl} = \frac{1}{2}\rho V^2$ (Heat Exchanger Loss)
Wollin (2001)	0.0001	Darcy	$\frac{1}{2}\rho V^2$
Liu (2003)	0.0001	Darcy	$P_{Obl} = \frac{1}{2}\rho V^2$, if $(\frac{1}{2}\rho V^2 \leq$ Monolith Loss) $P_{Obl} =$ Monolith Loss, if $(\frac{1}{2}\rho V^2 >$ Monolith Loss)
Present (Axisymmetric)	0.0001	Darcy	Liu
Present (Axisymmetric)	0.0001	Darcy	$P_{Obl} = (\frac{1}{2}\rho U_1^2)A(\sin^2\alpha)^B(Re_c)^C(\frac{L}{d_h})^D$ if $(\alpha \leq \alpha_{c,F})$ $P_{Obl} = (\frac{1}{2}\rho U_1^2)A(\sin^2\alpha_{c,F})^B(Re_c)^C(\frac{L}{d_h})^D$ if $(\alpha > \alpha_{c,F})$ where A=0.447, B=1.233, C=0.0756 and D=0.1287
Present (2-D Planar) 100 mm Monolith	0.0001	Darcy	
Present (2-D Planar) 27 mm Monolith	Value obtained from polynomial (Fig. 2.21)	Value obtained from polynomial (Fig. 2.21)	

Table 6.1 Overview of the approaches to predict entrance effect

6.3 Oblique entry pressure loss formulations

Wollin et.al (2001) incorporated Kuchemann and Weber's suggestion of $\frac{1}{2}\rho V^2$ for oblique entry pressure loss with Darcy's equation using user subroutines poros1.f and postdat.f within STAR-CD. The pressure drop and permeability coefficient, β, were

$$\Delta P = \frac{(2f\,Re_c)\mu L}{\varepsilon d_h^2} U_s + \frac{1}{2}\rho V^2 \qquad 6.7$$

$$\beta = \frac{(2f\,Re_c)\mu}{\varepsilon d_h^2} + \frac{\frac{1}{2}\rho V^2}{LU_s} \qquad 6.8$$

The predictions were compared with HWA profiles obtained at the rear of axisymmetric catalysts. Incorporating the additional pressure loss term due to oblique entrance considerably improved the predicted velocity profile and the peak velocities at the centre were close to the experimentally determined values. However, the predictions at high angles of attack corresponding to a region of ≈ 30 mm from the wall (Fig. 6.1) and also the flow distribution near the walls did not compare well with the experimental results.

Liu (2003) used the critical angle of attack approach ($\alpha_{c,V}$) with the theoretical entrance effect and compared his results against Wollin's (2001) measurements. If ($\alpha \leq \alpha_{c,V}$), the critical angle of attack, then the pressure drop and the permeability coefficient in the flow direction were given by Equation 6.7 and Equation 6.8.

If the angle of attack was greater than the critical angle ($\alpha > \alpha_{c,V}$), then the pressure loss due to entrance effect cannot exceed the pressure drop in the monolith. The pressure drop and permeability coefficient, β are given in Equation 6.9 & 6.10

If $\alpha > \alpha_{c,V}$ then,

$$\Delta P = \frac{(2f\,Re_c)\mu L}{\varepsilon d_h^2} U_s + \frac{1}{2}\rho(U_o \tan\alpha_{c,V})^2 \qquad 6.9$$

$$\beta = \frac{(2f\,Re_c)\mu}{\varepsilon d_h^2} + \frac{\frac{1}{2}\rho(U_o \tan\alpha_{c,V})^2}{LU_s} \qquad 6.10$$

where the critical angle of attack is given by $\alpha_{c,V} = \tan^{-1}\sqrt{\frac{(4f\,Re_c)\mu L}{\rho\varepsilon d_h^2}\frac{U_s}{U_o^2}}$

Figure 6.2: CFD predictions with entrance effect using critical angle approach (Liu, 2003)

(The legend CFD-with entrance effect, is based on critical angle ($\alpha_{c,V}$) approach)

The predictions using the critical angle approach improved considerably as shown in Fig. 6.2. In this chapter, the work of Wollin (2001) and Liu (2003) is extended by incorporating the entrance effect measurements obtained in Chapter 2. Comparisons are made with the measurements obtained by Wollin (2001) and also those obtained from the 2-D planar measurements of the present study.

The pressure drop and permeability coefficient by incorporating the measured entrance effect correlation in Chapter 2 with the Darcy's equation were

for $\alpha \leq \alpha_{c,F}$

$$\Delta P = \frac{(2f\,Re_c)\mu L}{\varepsilon d_h^2} U_s + (\frac{1}{2}\rho U_1^{\,2}) A(\sin^2\alpha)^B (Re_c)^C (\frac{L}{d_h})^D \qquad 6.12$$

$$\beta = \frac{(2f\,Re_c)\mu}{\varepsilon d_h^2} + \frac{(\frac{1}{2}\rho U_1^{\,2}) A(\sin^2\alpha)^B (Re_c)^C (\frac{L}{d_h})^D}{LU_s} \qquad 6.13$$

where α=angle of attack for $\alpha \leq \alpha_{c,F}$

and $\alpha=\alpha_{c,F}$ for $\alpha>\alpha_{c,F}$, $\alpha_{c,F} = \tan^{-1}\frac{V_F}{U_o}$ is the fixed critical angle of attack.

A=0.447, B=1.233, C=0.0756 and D=0.1287.

The results from the oblique angle flow measurements showed that the rate of increase in the magnitude of the entrance effect decreased as the angle of attack increased indicating a critical angle effect. Due to rig limitations, the oblique angle flow measurements could not be measured at high angles of attack greater than 80^0 and so it was not possible to determine $\alpha_{c,F}$. However for the axisymmetric study, $\alpha_{c,F}$ was varied and from these a value was deduced. This is described in the next section. An example of the coding for the poros1.f user-subroutine by incorporating the entrance effect correlation is shown in Appendix F.

6.4 Axisymmetric CFD study

6.4.1 Axisymmetric CFD model

Velocity profiles obtained from an axisymmetric catalyst flow rig from a previous study (Wollin 2001) have been used for comparison with CFD predictions**.** A

previous axisymmetric CFD model set up (Wollin, 2001) was selected as a starting point in this project and a brief description of the model is given below. The flow rig was axisymmetric and hence a full 3D CFD model is not necessary. Therefore a 5^0 degree wedge was modelled. As shown in Fig. 6.3, a multi-block approach was used to set up the mesh for application of the two-layer turbulence model, with the X, Y, Z axes being the radial, circumferential and axial directions respectively. The two side faces of the wedge were defined as symmetry planes. The mesh consisted of 96 mm long inlet pipe with a half radius of 24 mm (blocks 1, 2, 6 and 7) leading into a 60^0 total angled diffuser 60 mm in length (blocks 3 and 8). A 152 mm unwashcoated substrate (400 cpsi) of diameter of 118 mm (blocks 4 and 9) is located downstream of the diffuser followed by a 30 mm long outlet sleeve (blocks 5 and 10). The mesh has 28314 cells in total and comprises 363 in the Z-direction, 58 cells in the X-direction for high Reynolds number region (blocks 1-5) and 20 cells in the X-direction for the 9 mm near wall region. A higher density of cells in the Z-direction was used in the diffuser and the short inlet section (blocks 2 and 7). This was done to ensure that important flow features such as flow separation, recirculation and reattachment in the diffuser could be captured. A mesh independence study was performed by Wollin (2001) which showed that the current grid resolution is sufficient. Wollin (2001) also performed CFD simulations for a 102 mm unwashcoated substrate (400 cpsi) of diameter 118 mm (Figure 6.4) and compared it with the experimental results.

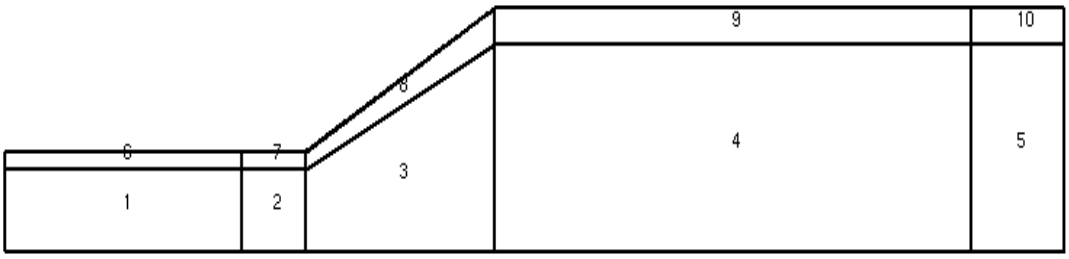

Figure 6.3: Computational grid represented by blocks, 152 mm substrate

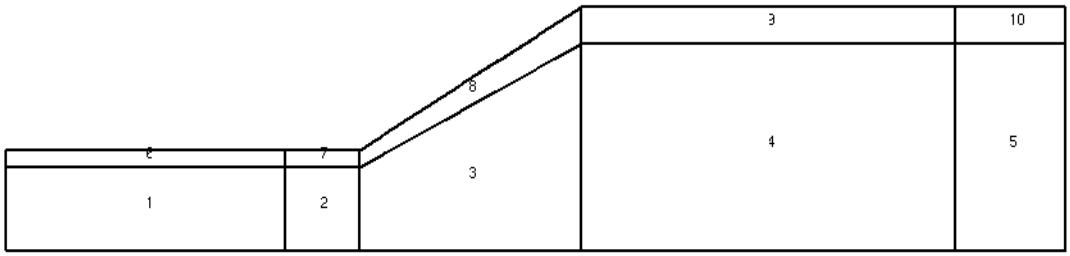

Figure 6.4: Computational grid represented by blocks, 102 mm substrate

Wollin (2001) found that the k-ε quadratic high Reynolds turbulence model together with a Norris Reynolds near wall model provided the best predictions. When using the k-ε quadratic high Reynolds model with the near wall model, the y^+ value was less than 1 with 20 cells in the near wall region. Wollin (2001) showed that the best predictions were obtained using a MARS differencing scheme for U, V, W momentum equations and upwind differencing scheme for turbulent kinetic energy and dissipation. The SIMPLE algorithm available in STAR was used to perform steady state simulations.

CFD simulations performed by Iaccaraino (2001) showed that the k-ε turbulence model failed to predict the flow separation and reattachment in a diffuser accurately. Iaccaraino (2001) performed CFD simulations using various turbulence models and found that V2F turbulence model best predicted the flow separation and recirculation in the diffuser. A CFD study was undertaken (discussed later in Section 6.5.3.2) to compare the flow predictions in the diffuser using various turbulence models and it was found that the V2F turbulence model best predicts the flow in the diffuser. Hence V2F turbulence model has been used throughout this study.

Simulations were performed for both the models (152 & 102 mm substrate) without the entrance effect. Simulations were also performed by incorporating the theoretical entrance effect of $\frac{1}{2}\rho V^2$ and the entrance effect formulae obtained from oblique angle flow measurements with the fixed critical angle ($\alpha_{c,F}$) approach.

6.4.2 Axisymmetric CFD Results

The experimental data in this section is obtained from Wollin (2001). Wollin (2001) obtained the hot-wire velocity profiles 30 mm from the exit of 152 mm and 102 mm substrate for a range of Reynolds number. The hot-wire velocity profiles gave a measure of maldistribution in the flow across the substrate. CFD simulations were performed to predict the maldistribution in the flow with and without entrance effect. Figs. 6.5-6.14 show the CFD predictions of maldistribution in the flow across the substrate by incorporating the measured entrance effect and theoretical entrance effect to the Darcy's equation. The zero degree angle of attack measurements for 100 mm

substrate in Chapter 2 showed that for low channel velocities (U_c<13 m/s), the pressure drop in the substrate using Darcy's equation compared well with the experimental data. Also the experimental investigations in Chapter 2 showed that the prediction of pressure drop in the substrate using Darcy's equation at higher channel velocities improved as the length of the substrate increased. In all the CFD cases considered in this study, the channel velocities were 13 m/s or less and the substrate lengths were 152 mm and 102 mm. Hence, in this study Darcy's equation has been considered adequate to predict the pressure drop in the monolith. It can be seen that Darcy's equation without the entrance effect under predicts the flow maldistribution (Figs. 6.5, 6.8, 6.11, 6.12, 6.13). Incorporating the measured entrance effect without the fixed critical angle approach ($\alpha_{c,F}$) improved the prediction of the velocities in the central region of the substrate (Figs. 6.5, 6.8, 6.11, 6.12, and 6.13), but the predictions worsened in the region of 10-30 mm from the substrate wall. The flow is incident at high angles of attack to substrate channels in this region and incorporating the entrance effect without critical angle results in high resistance to flow. This high resistance prevents the flow entering the substrate channels and hence results in a local high resistance region at the front face of the monolith and steers the flow towards the wall. Hence the velocities near the wall are over predicted when entrance effect without critical angle was used.

The over prediction of the velocities in the region of 10-30 mm from the wall was improved by incorporating the entrance effect with the fixed critical angle approach ($\alpha_{c,F}$). From the experimentally obtained relationship for entrance effect, it was found that the pressure loss increases as the angle of attack increases and was almost constant at high angles of attack. Unfortunately the experimental study described in Chapter 2 was not able to explore the entrance effect at high angles of attack greater than 75^0 due to rig limitations. Hence a CFD study was undertaken incorporating the entrance effect with the fixed critical angle approach and limiting the fixed critical angle ($\alpha_{c,F}$) to 75^0,79^0,81^0,85^0 (Figs. 6.6, 6.9, 6.14). The CFD predictions showed that limiting the fixed critical angle ($\alpha_{c,F}$) to 75^0 under predicted the maximum velocities at the centre and over predicted the velocities in the 10- 30 mm region from the wall. This suggested that the fixed critical angle ($\alpha_{c,F}$) was higher than 75^0. By limiting the fixed critical angle ($\alpha_{c,F}$) to 85^0 the predictions over predicted the central velocities and under predicted the velocities in the 10-30 mm region from the wall. When the

fixed critical angle ($\alpha_{c,F}$) was limited to 79^0 the predictions improved and it was found that the fixed critical angle ($\alpha_{c,F}$) of 81^0 provided the best results. Hence from the CFD predictions, the fixed critical angle ($\alpha_{c,F}$) was found to be approximately around 81^0. Above the fixed critical angle of attack ($\alpha_{c,F}$), the entrance effect is *assumed constant*.

CFD predictions were also performed to compare the difference between predictions made using the measured entrance effect and the theoretical entrance effect ($\frac{1}{2}\rho V^2$) suggested by Kuchemann and Weber (1953). The theoretical entrance effect predictions with the critical angle of attack approach ($\alpha_{c,V}$) compared well with the measured entrance effect with the fixed critical angle of attack ($\alpha_{c,F}$) approach predictions. (Figs. 6.7, 6.10).There was a slight under prediction of the velocity in the central core region using the theoretical entrance effect with the critical angle method ($\alpha_{c,V}$). In all the CFD cases considered, the channel velocities were 13 m/s or less and hence the difference between predictions made using the measured entrance effect and theoretical entrance effect at high channel velocities (U_c>13 m/s) as observed in experimental study described in Chapter 2 have not been explored.

Although it appears that $\alpha_{c,F}$ of 81^0 provides the best fit for the measured profiles at the substrate exit, there is an implicit assumption that the predicted flow in the diffuser is correct. This cannot be verified at present. It may well be that the optimum value of $\alpha_{c,F}=81^0$ compensates for inadequacies in the modelling of diffuser flow. However, for the case of the 2D planar diffuser, measurements in the diffuser can be directly compared with predictions and the validity of the oblique flow loss formulation further assessed. This is the subject of the next section.

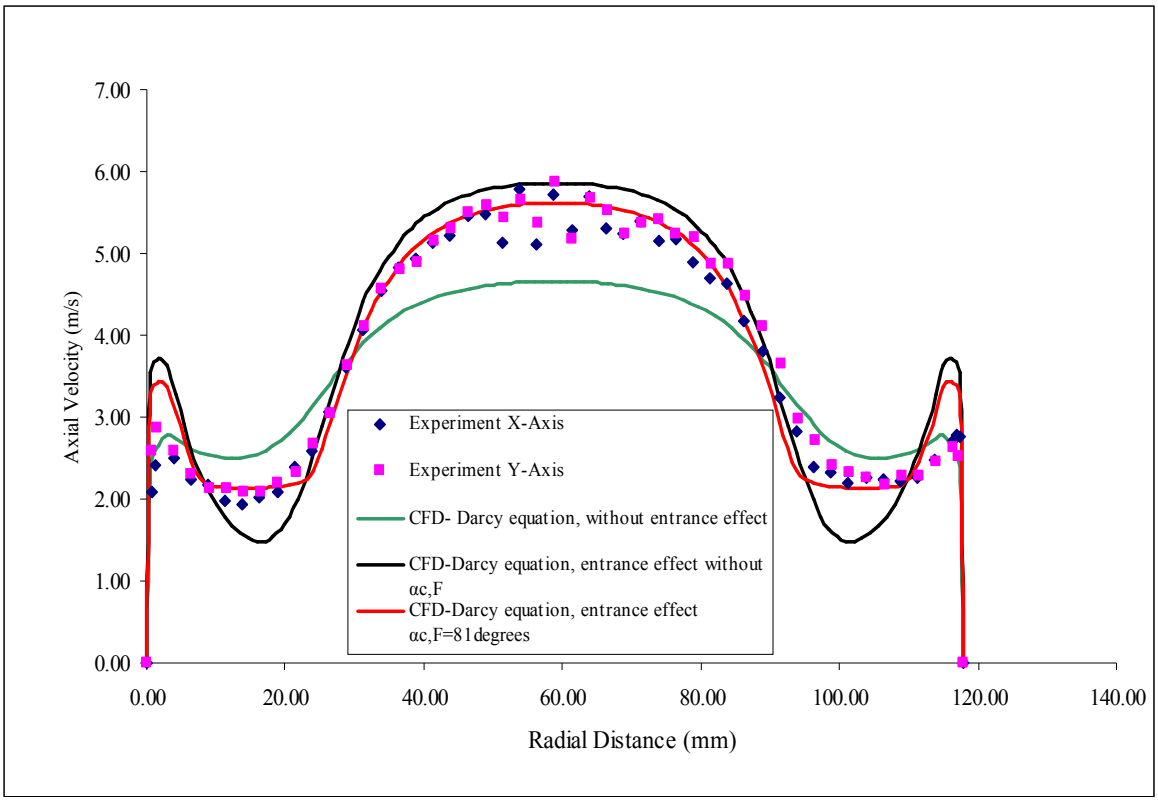

Figure 6.5: Comparison between experiment and CFD predictions by incorporating entrance effect (152 mm substrate Re: 58300)

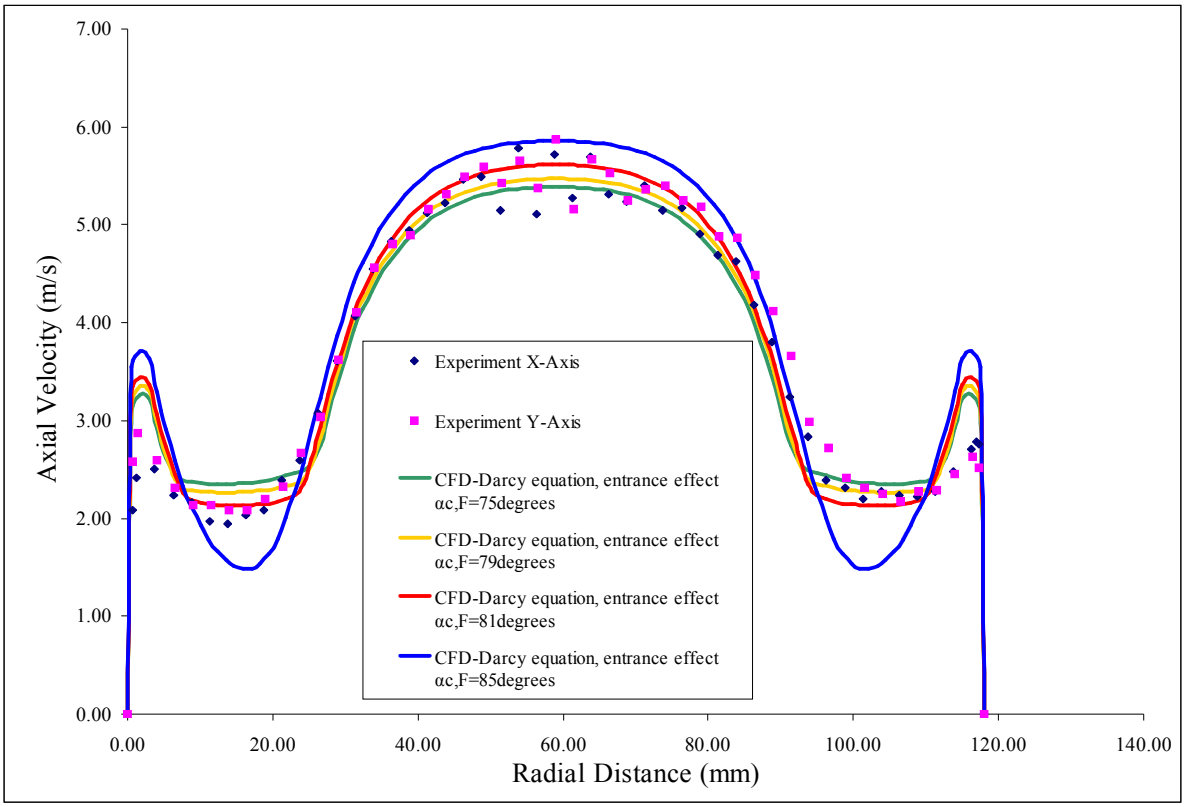

Figure 6.6: Comparison between experiment and CFD predictions at various critical angles of attack (152 mm substrate Re: 58300)

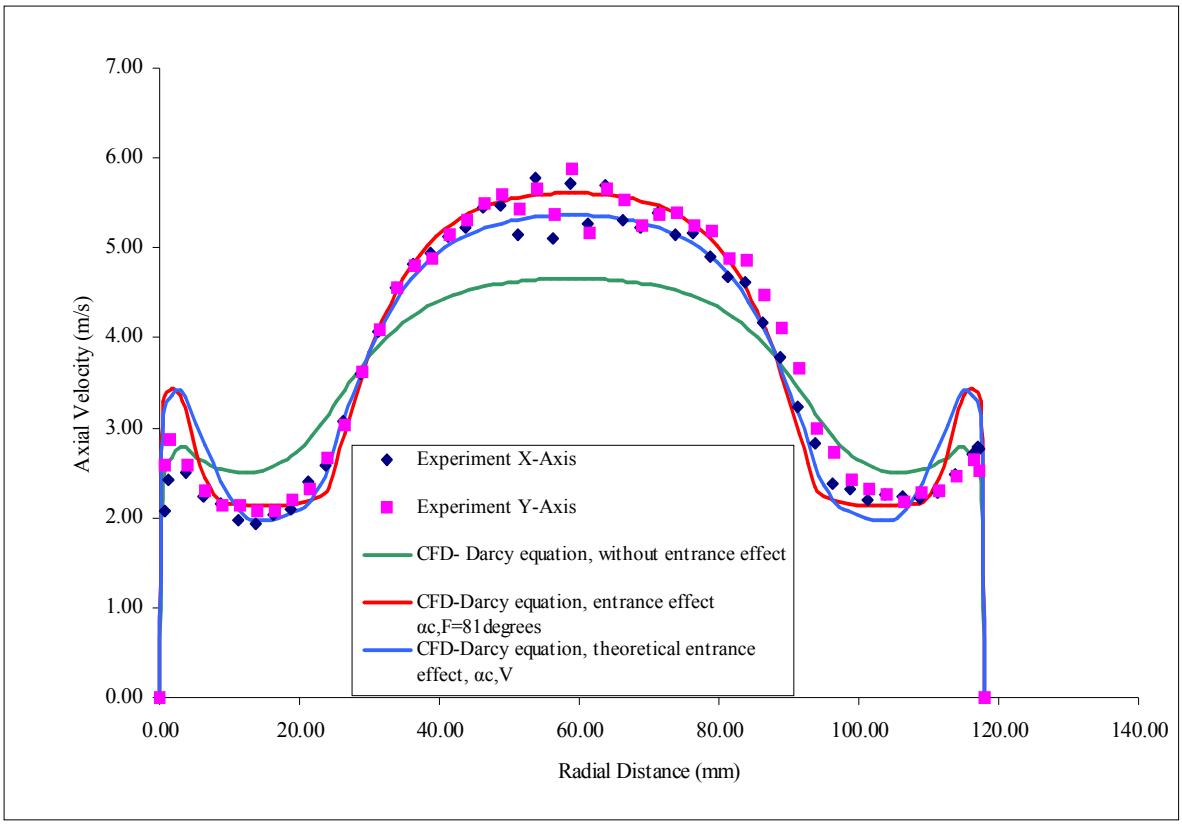

Figure 6.7: Comparison between experiment and CFD predictions by incorporating entrance effect and theoretical entrance effect (152 mm substrate Re: 58300)

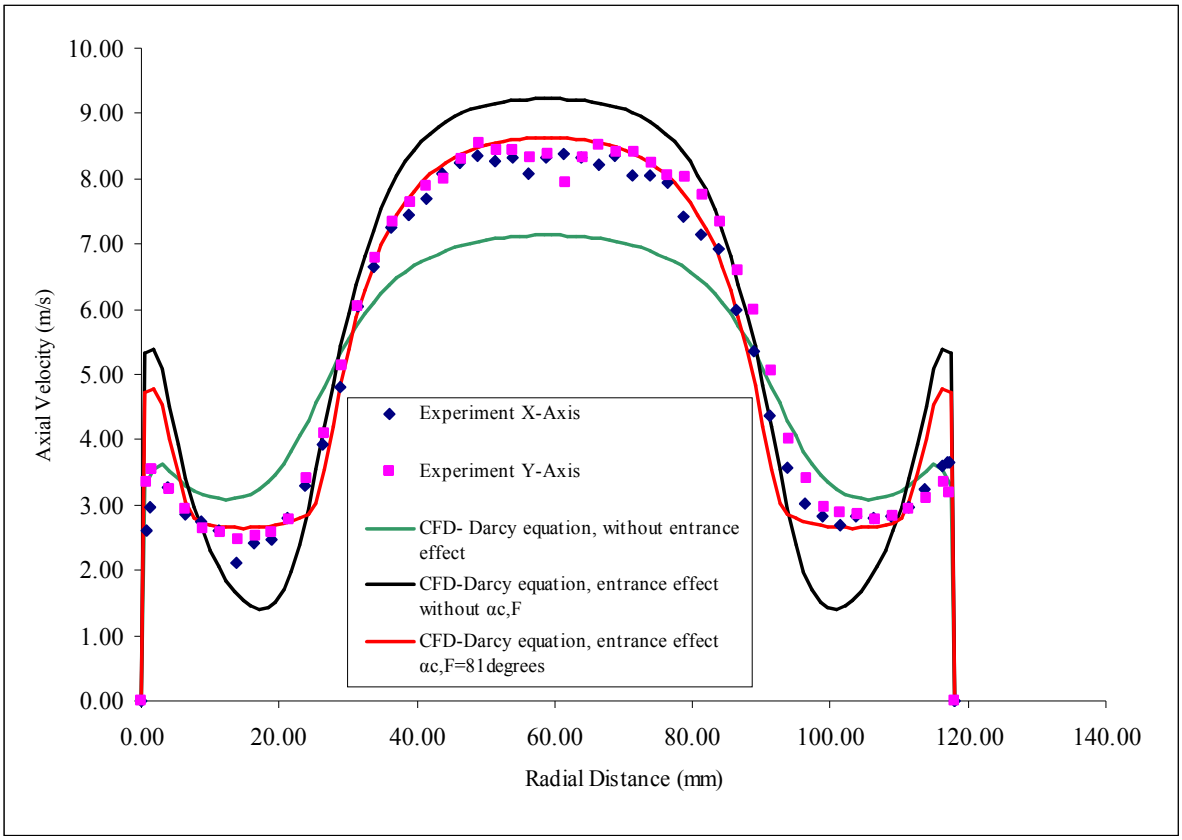

Figure 6.8: Comparison between experiment and CFD predictions by incorporating entrance effect (152 mm substrate Re: 79900)

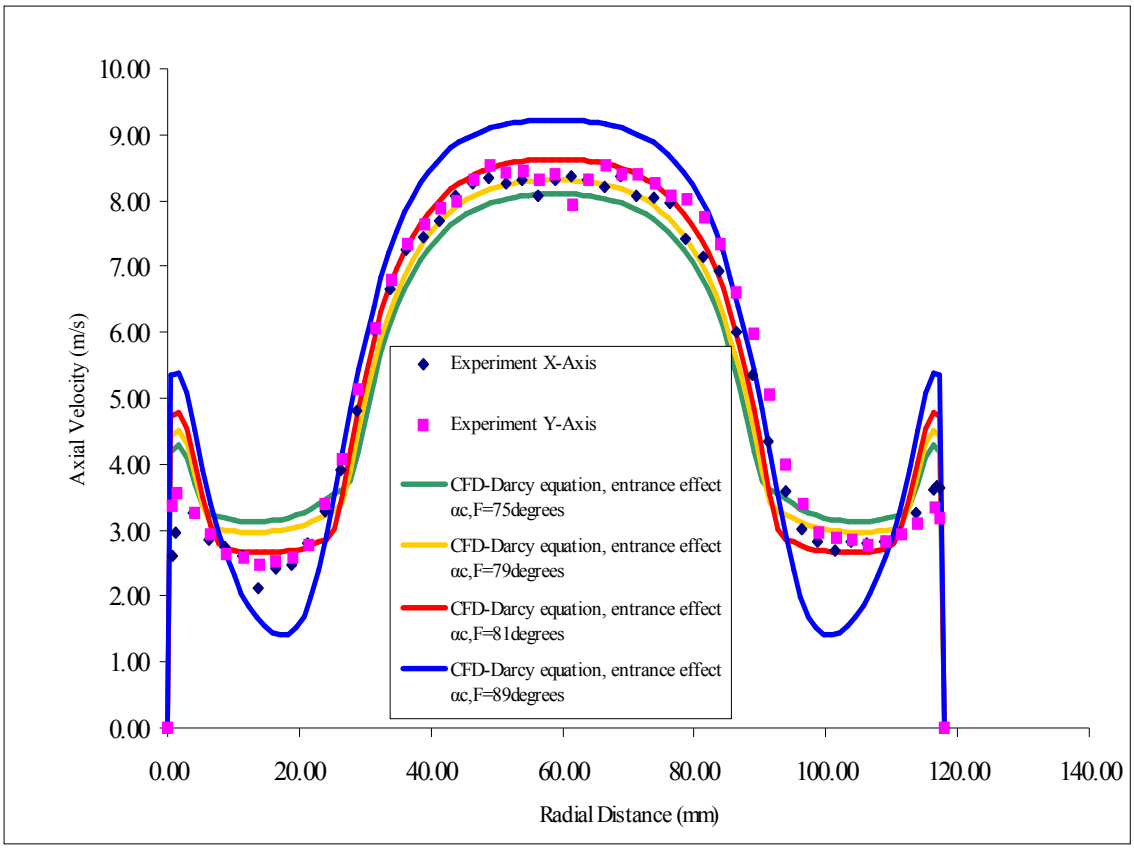

Figure 6.9: Comparison between experiment and CFD predictions at various critical angles of attack (152 mm substrate Re: 79900)

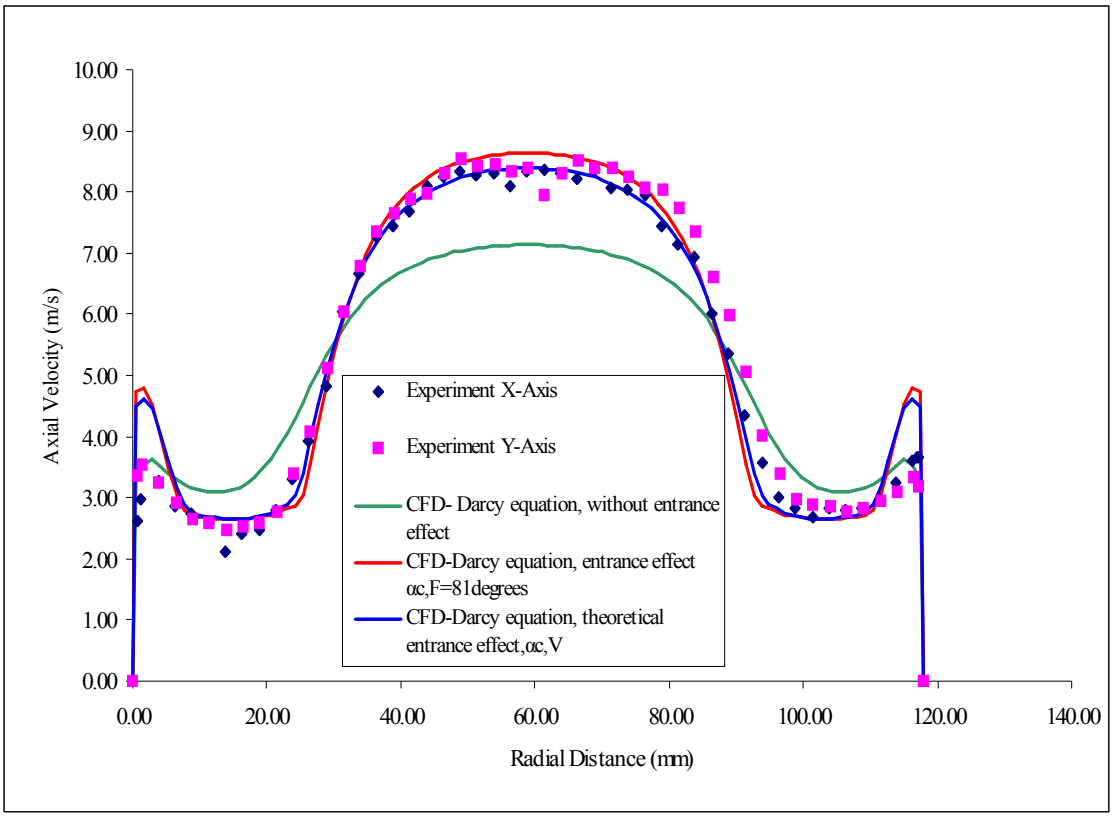

Figure 6.10: Comparison between experiment and CFD predictions by incorporating entrance effect and theoretical entrance effect (152 mm substrate Re: 79900)

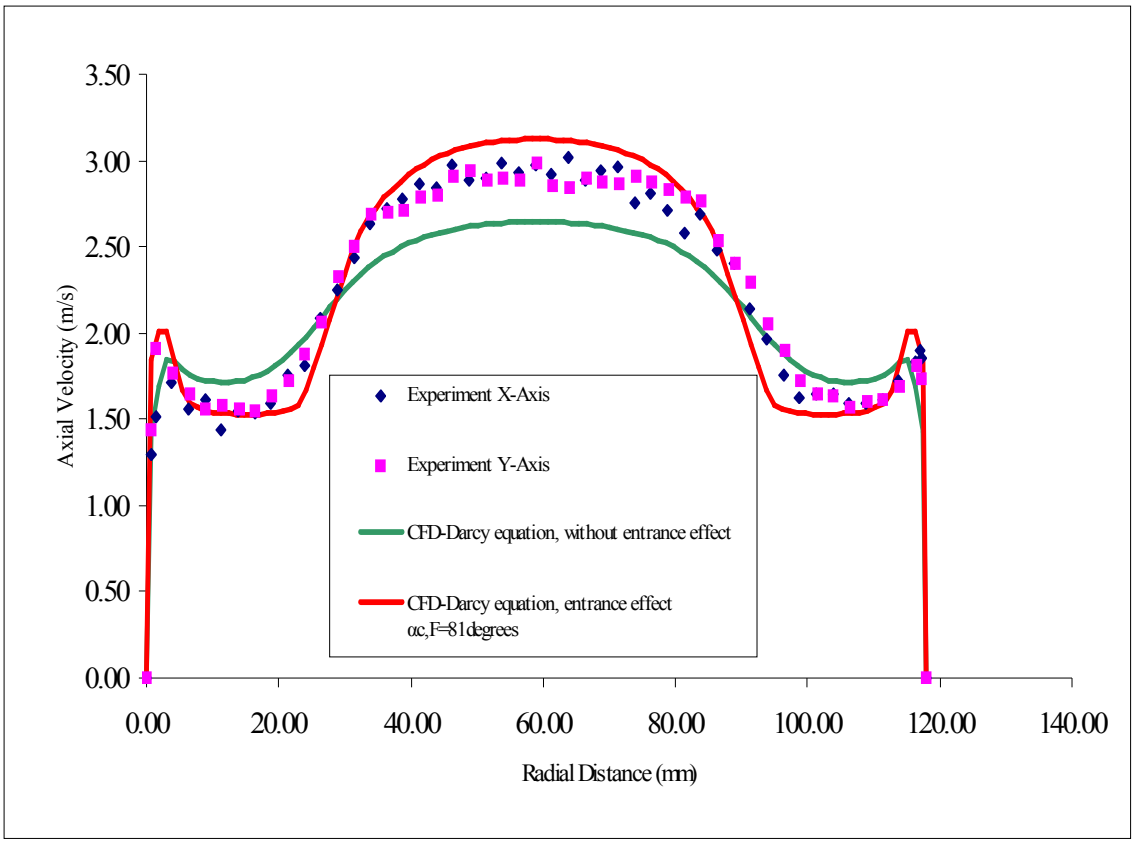

Figure 6.11: Comparison between experiment and CFD predictions by incorporating entrance effect (152 mm substrate Re: 37600)

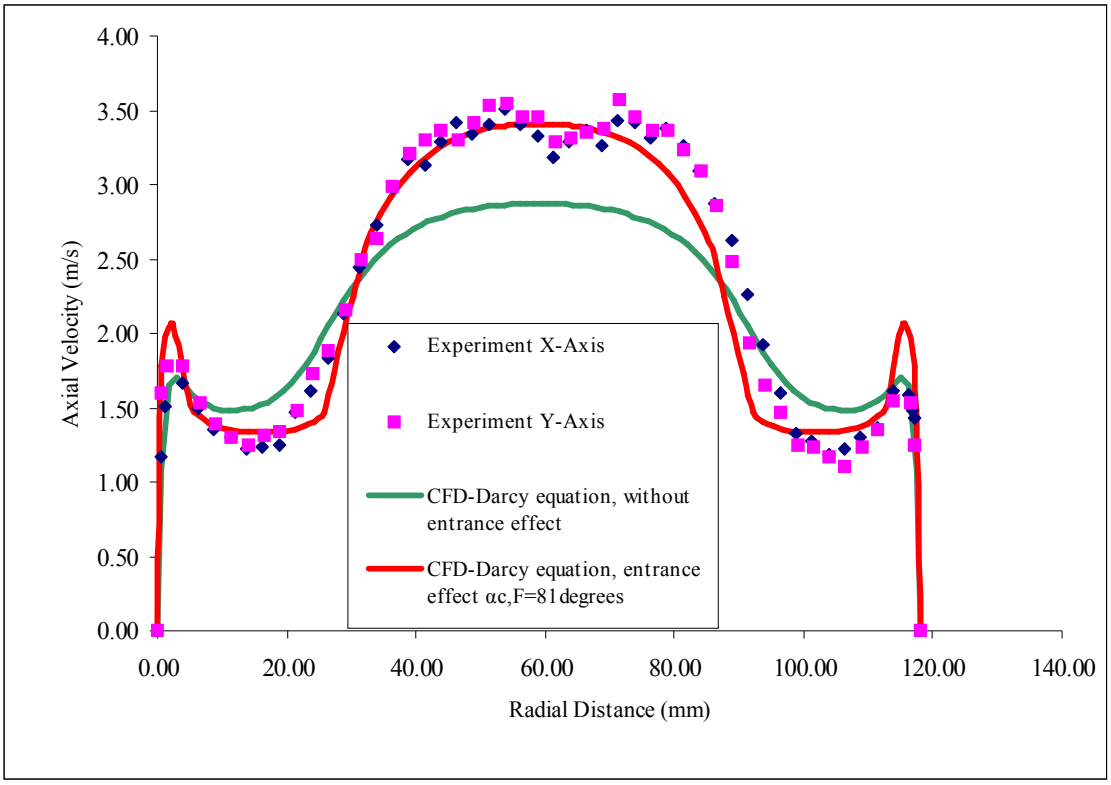

Figure 6.12: Comparison between experiment and CFD predictions by incorporating entrance effect (102 mm substrate Re: 35900)

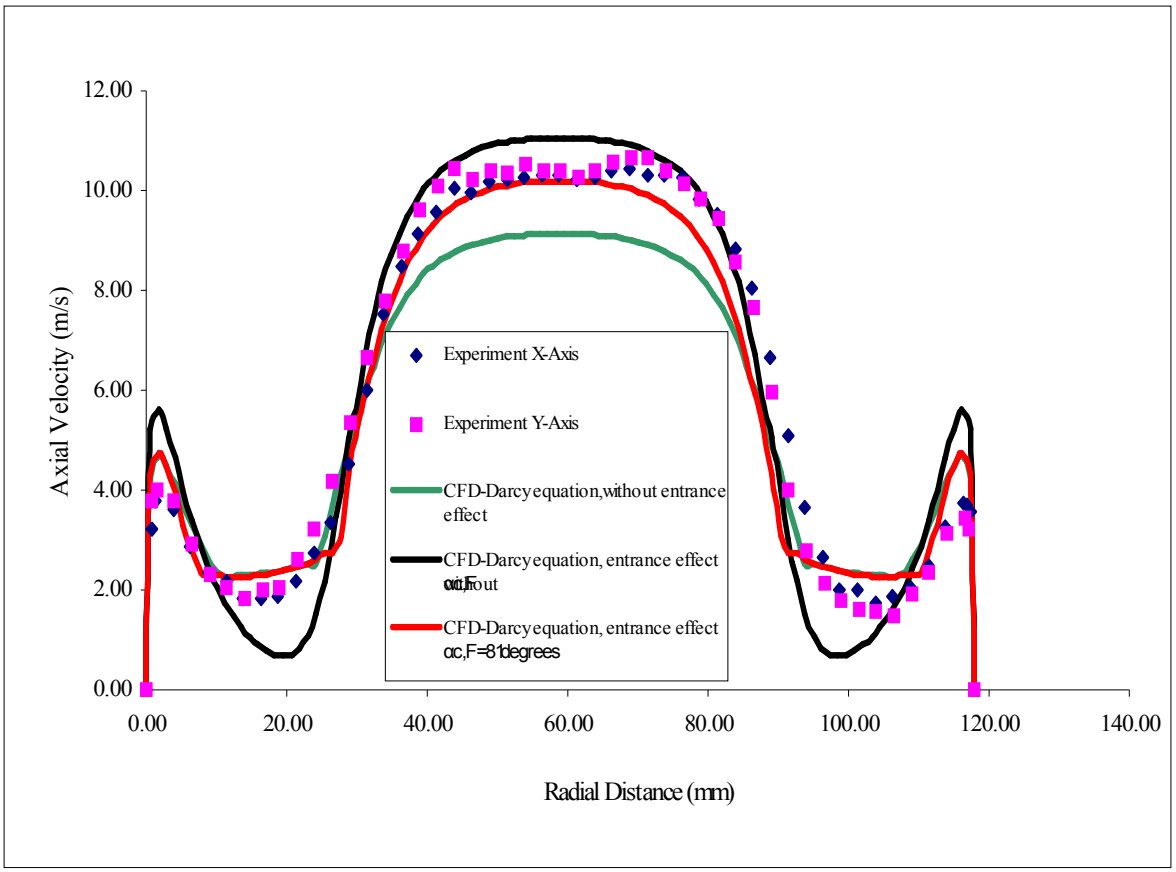

Figure 6.13: Comparison between experiment and CFD predictions by incorporating entrance effect (102 mm substrate Re: 83200)

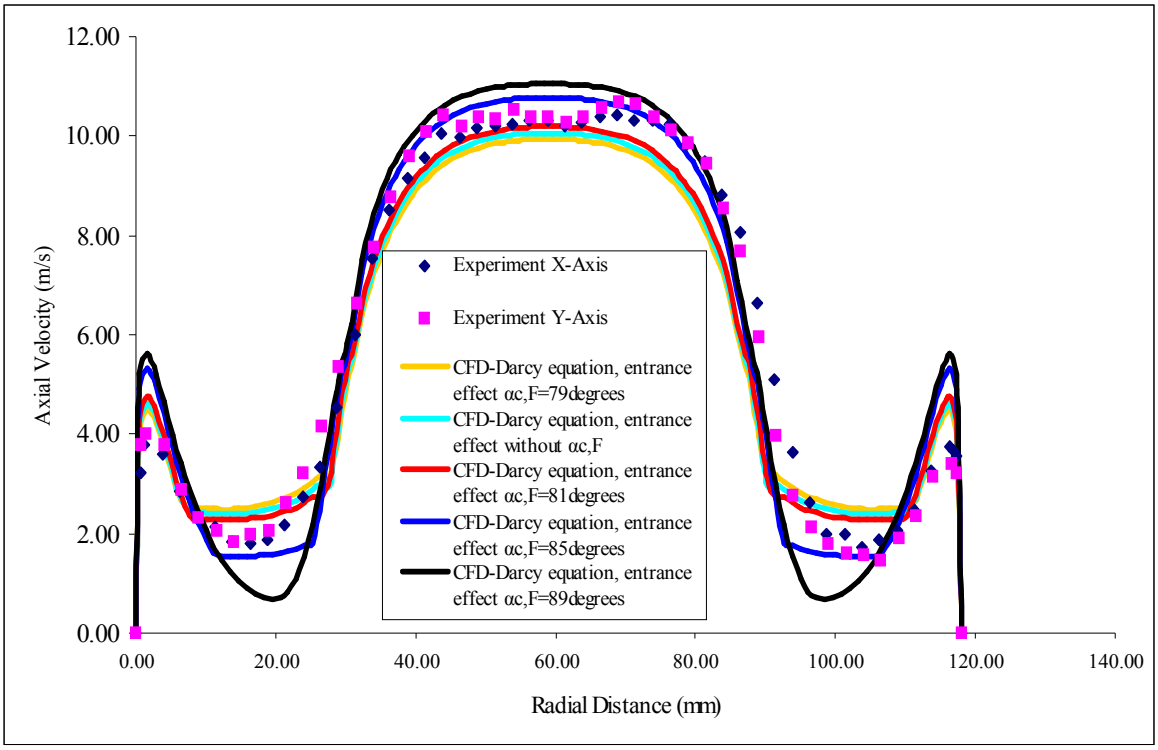

Figure 6.14: Comparison between experiment and CFD predictions at various critical angles of attack (102 mm substrate Re: 83200)

6.5 Two-Dimensional CFD study

6.5.1 Two-Dimensional CFD model

CFD simulations were performed with and without the entrance effect ($\alpha_{c,F}$ approach) to compare with the flow profiles in the 2-D diffuser obtained from the PIV measurements and also the hot wire velocity measurements at the exit of the substrate. Substrate lengths of 27 mm and 100 mm were used for comparison. The mesh for the 2-D model was based on the 2-D rig designed in Chapter 4. The mesh consists of a 40 mm long rectangular duct with a half height of 27.5 mm, a 30^0 half angled plane walled diffuser 108.2 mm long, a 100 mm long 2-D substrate with a half height of 90 mm and a 30 mm long outlet sleeve downstream of the substrate. The flow direction was along the X-axis and the lateral ordinates were described by the Y-axis. A multi block approach was used to create the mesh as shown in Figs. 6.15 and 6.16

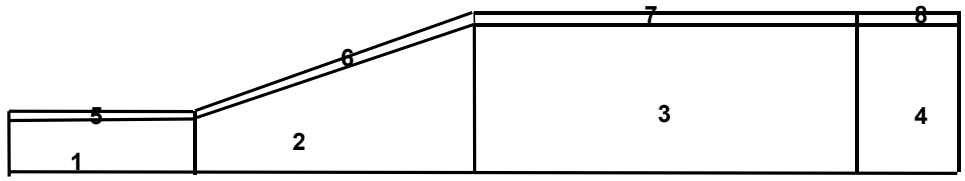

Figure 6.15: Grid created using multi-block approach

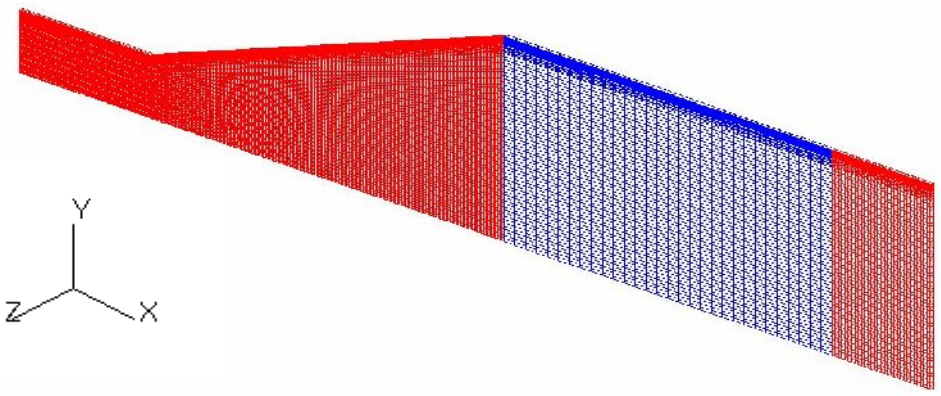

Figure 6.16: Mesh of the 2-D CFD model (100mm substrate)

The flow was assumed to be isothermal and incompressible. The V2F turbulence model available in STAR V3.26 was used. It is inherently a low-Re model with the y^+ value in the near wall region <1. This was achieved by having 20 cells in the near wall region graded so that the cells were gradually denser, close to the wall. A uniform axial velocity was applied as the inlet boundary condition and the exit plane was defined as a pressure boundary. The two side faces of the model were defined as symmetry planes. The cells in the z-direction were 2 mm thick. The axisymmetric studies by Wollin (2001) showed that the best predictions were obtained using a MARS differencing scheme for U, V, W momentum equations and upwind differencing scheme for turbulent kinetic energy and dissipation. This mixed blend of scheme was therefore used to perform the simulations. The SIMPLE algorithm available in STAR was used to perform steady state simulations. A similar model was also created for the 27 mm substrate.

6.5.2 Mesh Independence

A mesh independence study was conducted at Re 41800 and the different cell sizes used were as shown in Table 6.2. Default values for under relaxation factors, number of sweeps and residual tolerances were used in this study. The results obtained from all the three different mesh sizes showed good agreement (Fig. 6.16) and mesh 2 was used for the rest of this study.

Block Numbers (Direction)	**Mesh1 (No. of cells)**	**Mesh2 (No. of cells)**	**Mesh3 (No. of cells)**
Blocks (5-8) (Lateral)	20	20	20
Blocks (1-4) (Lateral)	60	60	70
Block 1 & 5 (Axial)	60	60	60
Block 2 & 6 (Axial)	150	175	200
Block 3 & 7 (Axial)	30	30	30
Block 4 & 8 (Axial)	30	30	30
Total pressure drop [Pa]	**144.3**	**144.5**	**144.4**

Table 6.2: Number of cells for the different meshes

6.5.3 Results & Discussion

6.5.3.1 Comparison of flow profiles upstream of the substrate using different turbulence models

The flow profiles in the diffuser from the CFD predictions without entrance effect were compared with the experimental measurements from the PIV obtained in Chapter 5. Fig. 6.17 shows the comparison of line contour velocity magnitude profiles without the entrance effect using different turbulence models at Re: 41800 for the flow in the diffuser upstream of the 100 mm substrate. Figs. 6.18-6.27 show the comparison of axial velocity profiles for various turbulence models with experimental results. All the three turbulence models without entrance effect under predict the velocity magnitude in the central core region of the diffuser. At distances far from the substrate (Y>15mm) the predictions for the velocity in the central core region and recirculation bubble were worse for the two layer k-ε high Reynolds turbulence model (Fig. 6.18-6.24). Also the prediction of the point of cross-over was inaccurate for the two layer k-ε high Reynolds turbulence model. The point of cross-over is defined as the point wherein the axial velocity is zero, i.e., where the axial velocity magnitude changes sign. The predictions both in terms of velocity in the central core region and recirculation bubble are improved and similar using the k-ε quadratic high Reynolds and V2F turbulence model (Fig. 6.17 & Figs. 6.18-6.27). The V2F turbulence model best predicts the recirculation bubble and the point of cross-over (Figs. 6.18-6.24). However, width of the free shear layer region was relatively thin for the V2F turbulence model as compared to the k-ε quadratic high Reynolds and experimental results as shown by the steep gradient in axial profiles around 30 mm (Figs. 6.18-6.22). As the flow proceeds further downstream the difference in predictions for turbulence models reduces and for flow profiles close to the substrate (Y<15 mm), the turbulence model selection hardly makes a difference (Figs. 6.25-6.27). This appears to be due to the influence of substrate resistance on the flow as the flow redistributes itself. Also interestingly, the k-ε models show higher velocity at the periphery whilst this is not the case for the V2F model which is similar to PIV results. Hence selection of turbulence model is important for the prediction of flow features such as flow separation and recirculation region, width of the free shear layer and the point of cross-over. But the selection of turbulence model made a very small difference for the

flow entering the substrate channels. Hence, the V2F turbulence model was used throughout this study for the CFD predictions.

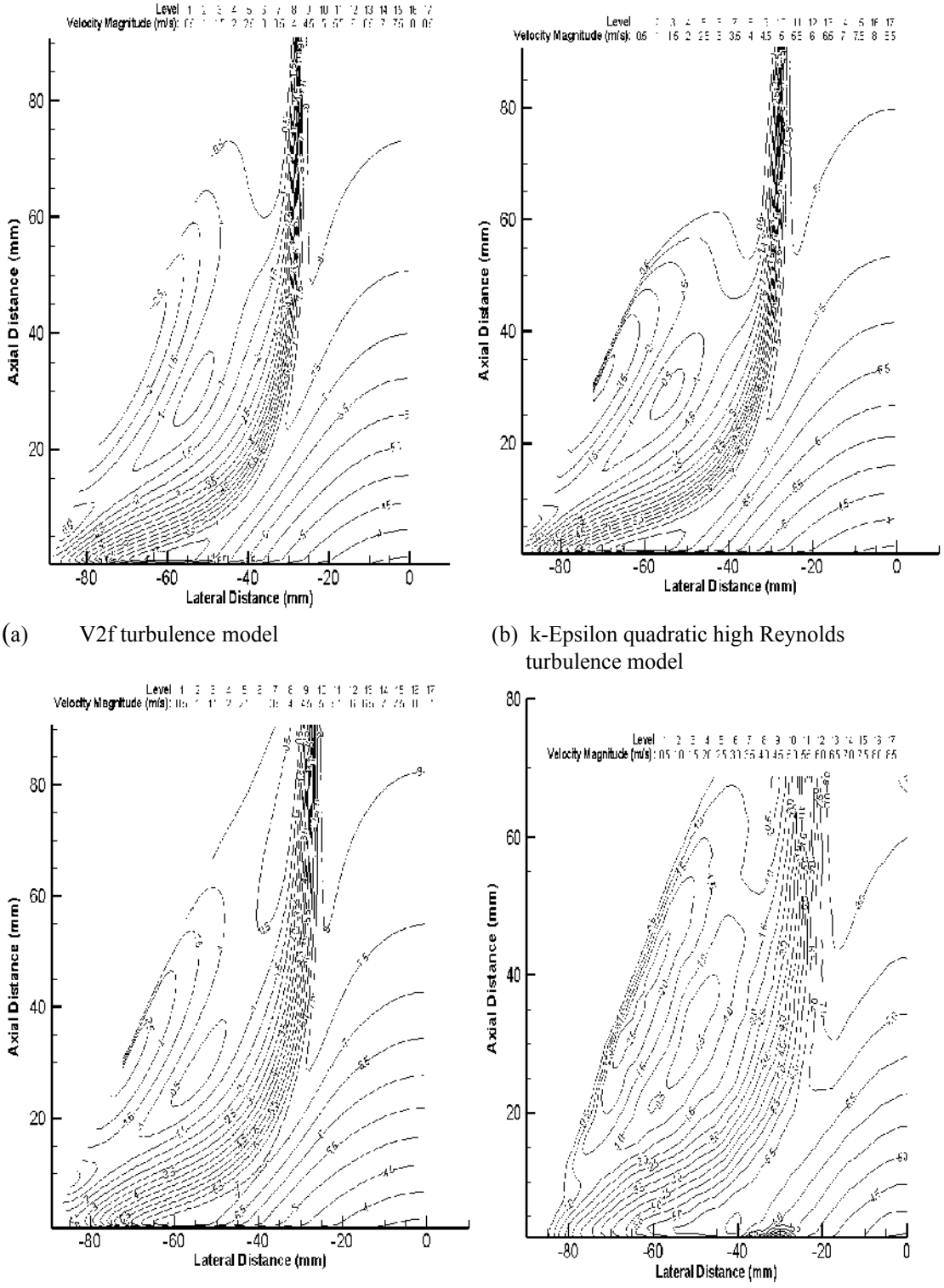

(a) V2f turbulence model

(b) k-Epsilon quadratic high Reynolds turbulence model

(c) k-Epsilon high Reynolds turbulence model

(d) Experimental results from PIV

Figure 6.17: Comparison of line contour velocity magnitude profiles in the diffuser using different turbulence models and experimental results without entrance effect. (100 mm substrate Re: 41800): (a) V2F turbulence model, (b) k-Epsilon quadratic high Reynolds turbulence model, (c) k-Epsilon high Reynolds turbulence model, (d) Experimental results from PIV

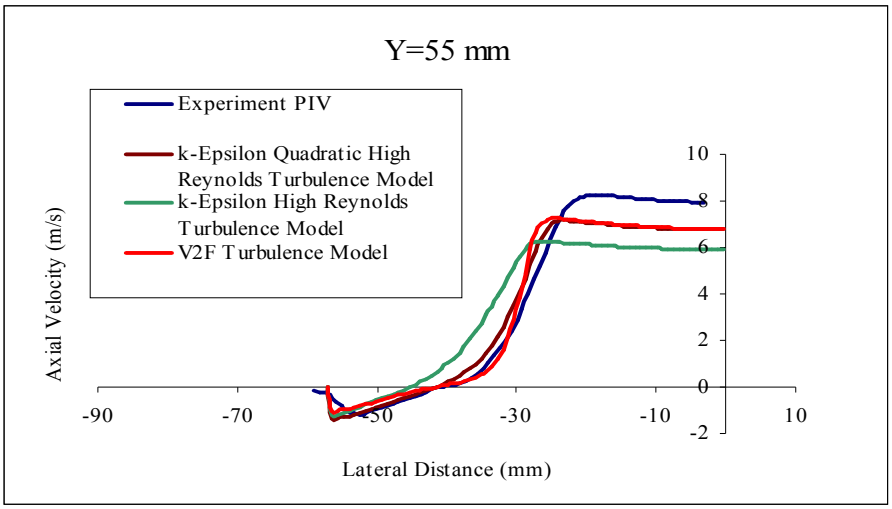

Figure 6.18: Comparison of CFD predictions using different turbulence models with experimental results (100 mm substrate, Re: 41800 & Y=55 mm)

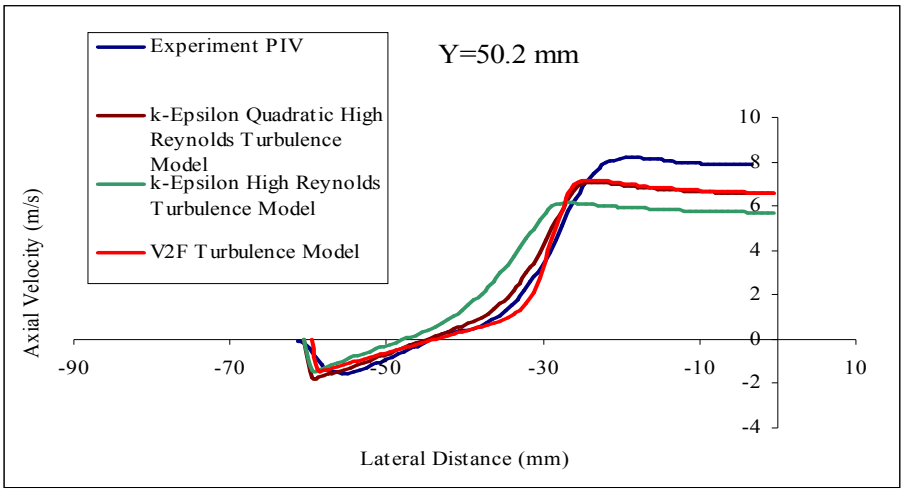

Figure 6.19: Comparison of CFD predictions using different turbulence models with experimental results (100 mm substrate, Re: 41800 & Y=50.2 mm)

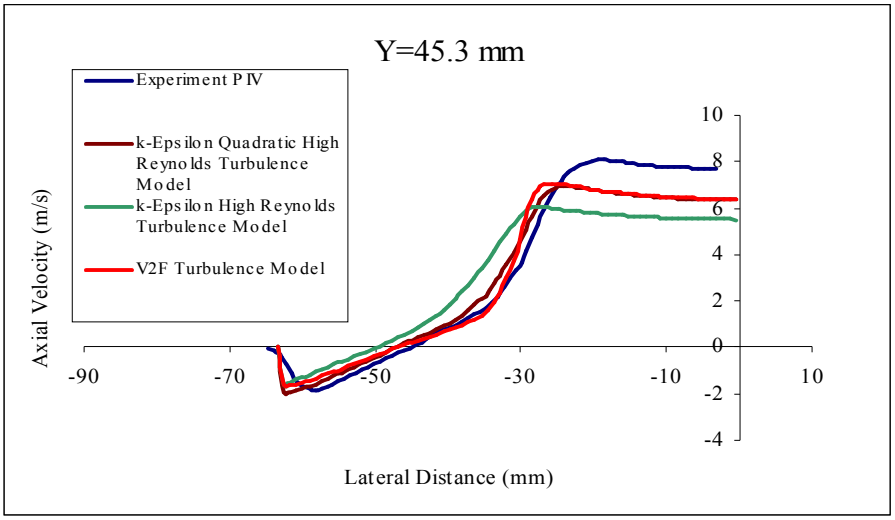

Figure 6.20: Comparison of CFD predictions using different turbulence models with experimental results (100 mm substrate, Re: 41800 & Y=45.3 mm)

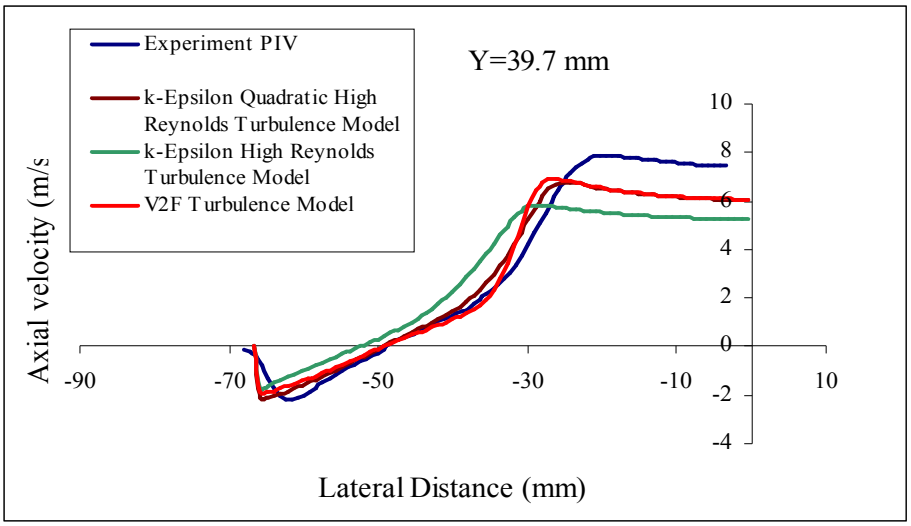

Figure 6.21: Comparison of CFD predictions using different turbulence models with experimental results (100 mm substrate, Re: 41800 & Y=39.7 mm)

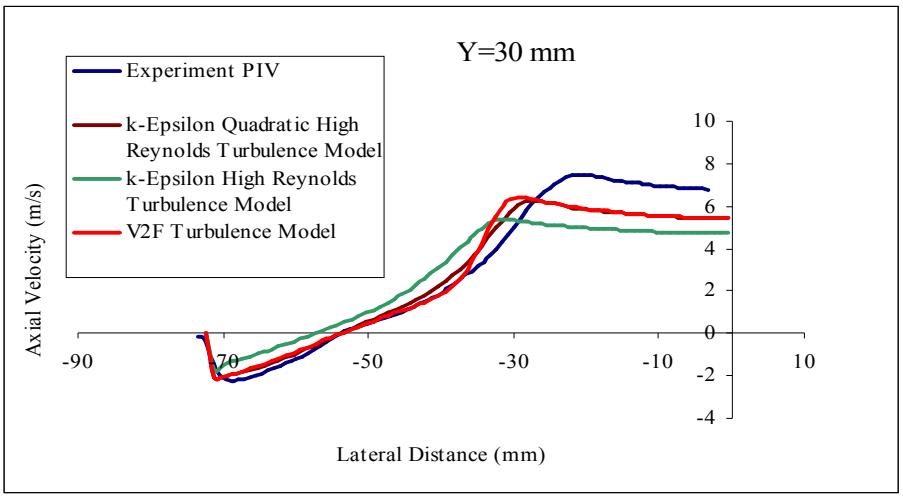

Figure 6.22: Comparison of CFD predictions using different turbulence models with experimental results (100 mm substrate, Re: 41800 & Y=30 mm)

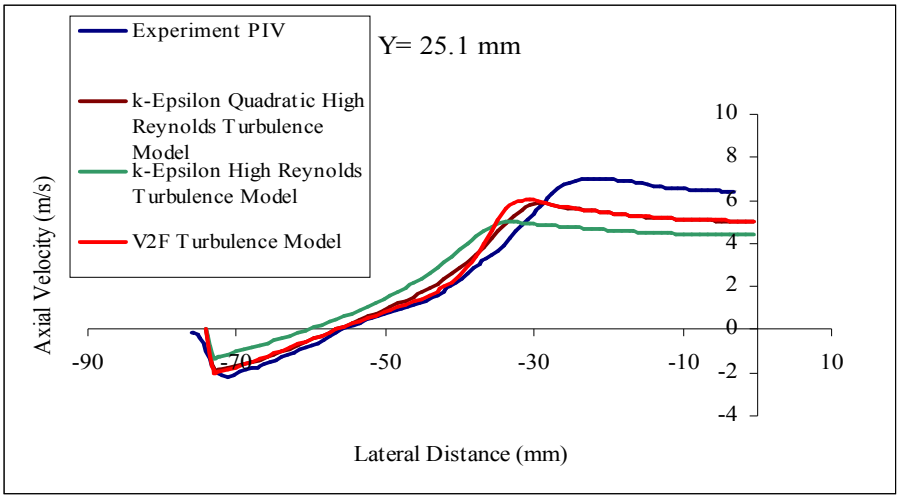

Figure 6.23: Comparison of CFD predictions using different turbulence models with experimental results (100 mm substrate, Re: 41800 & Y=25.1 mm)

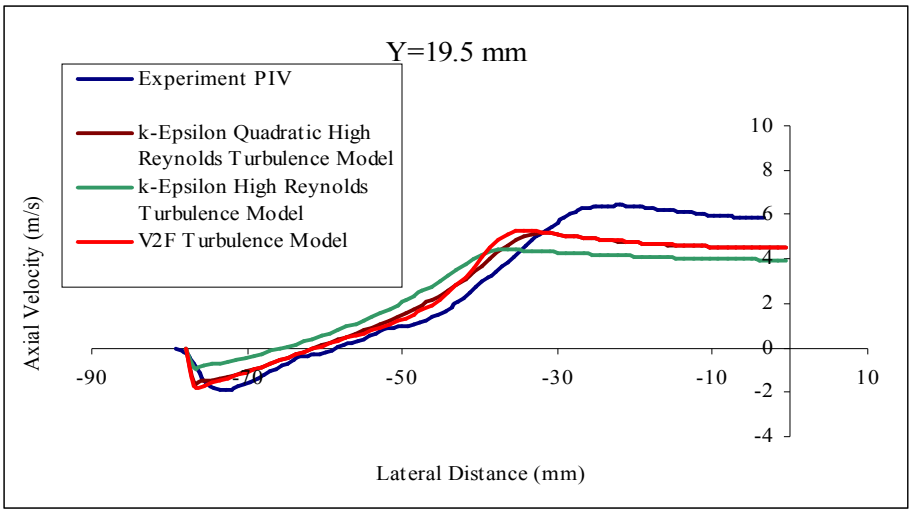

Figure 6.24: Comparison of CFD predictions using different turbulence models with experimental results (100 mm substrate, Re: 41800 & Y=19.5 mm)

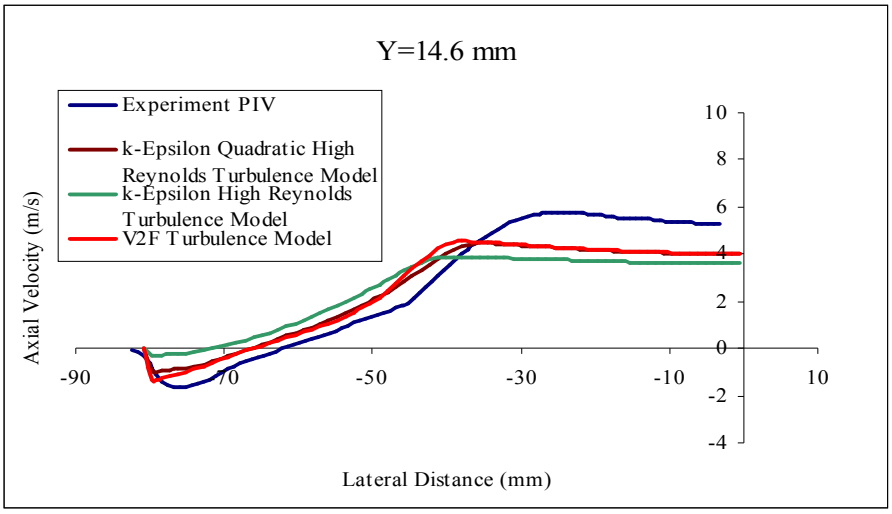

Figure 6.25: Comparison of CFD predictions using different turbulence models with experimental results (100 mm substrate, Re: 41800 & Y=14.6 mm)

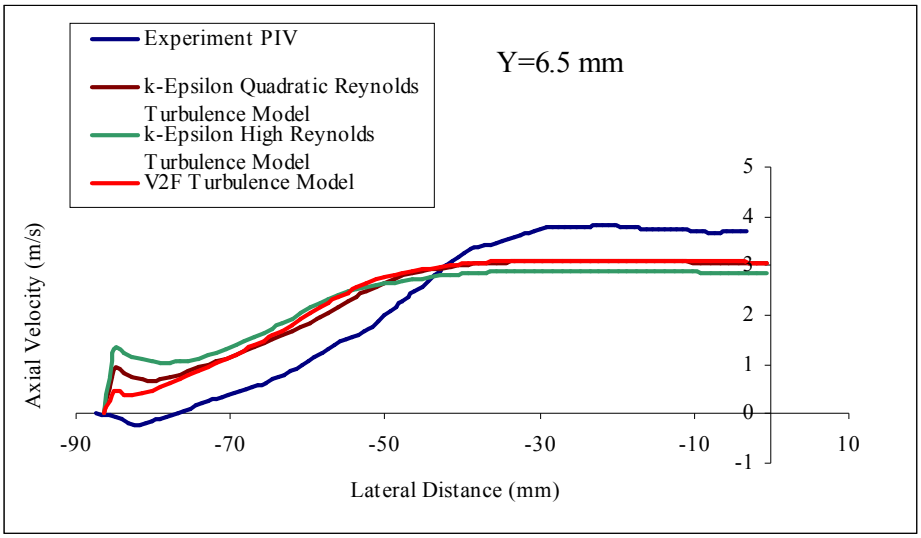

Figure 6.26: Comparison of CFD predictions using different turbulence models with experimental results (100 mm substrate, Re: 41800 & Y=6.5 mm)

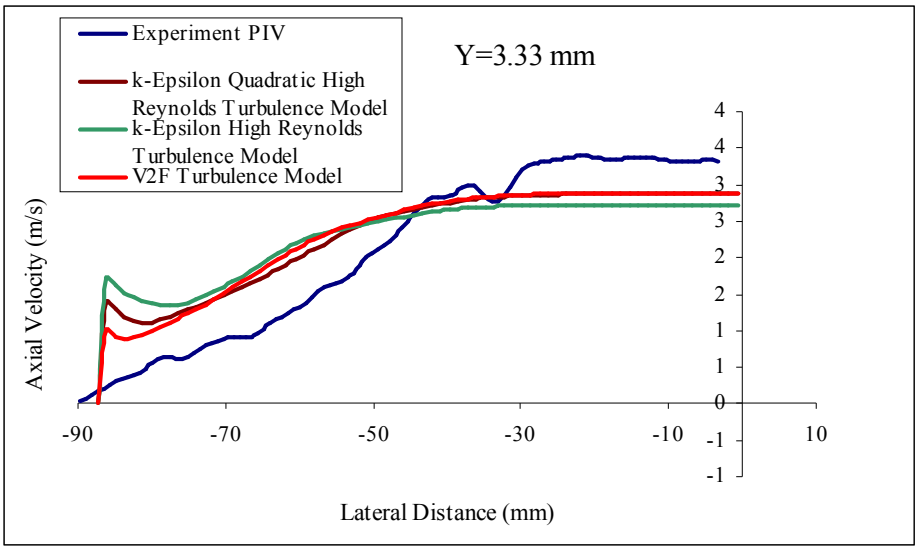

Figure 6.27: Comparison of CFD predictions using different turbulence models with experimental results (100 mm substrate, Re: 41800 & Y=3.33 mm)

6.5.3.2 Comparison of flow profiles upstream of the 100 mm substrate with and without entrance effect ($\alpha_{c,F}= 81^0$)

The axisymmetric CFD studies in Chapter 6 showed that incorporating the entrance effect with a fixed critical angle ($\alpha_{c,F}= 81^0$) gave the best predictions of maldistribution in the flow across the substrate. Hence an entrance effect with a fixed critical angle ($\alpha_{c,F}$) of 81 degrees has been used in this study. Fig. 6.28 shows the comparison of line contour velocity magnitude profiles with and without entrance effect ($\alpha_{c,F}=81^0$) Figs. 6.29-6.40 show the comparison of axial magnitude profiles with and without entrance effect ($\alpha_{c,F}= 81^0$) at Re:41800. Incorporating the entrance effect ($\alpha_{c,F}=81^0$) increased the porous medium resistance. This had a small effect on the flow profiles far from the substrate (Y>20 mm) where the velocity magnitude increase in the central core region is very small (Figs. 6.29-6.36). As the flow proceeds further downstream, the flow is under the influence of the comparatively higher resistance of the substrate due to the entrance effect. As a result, prediction of axial velocity in the central core region was higher. This can be seen from Figs. (6.37-6.40) and is most evident very close to the substrate at Y=3.33 mm (Fig. 6.40). Fig. 6.41 shows the comparison of angle of attack by incorporating the entrance effect with experimental results. The results show that as the flow approaches the substrate, the angle of attack in the near-wall reduces and is in good agreement with PIV measurements. Incorporating the entrance effect ($\alpha_{c,F}=81^0$) improved the predictions close to the

substrate and the velocity in the central core region is similar to the experimental results from PIV.

(Legend αcF in Figs. 6.29-6.40 corresponds to the fixed critical angle, $\alpha_{c,F}$)

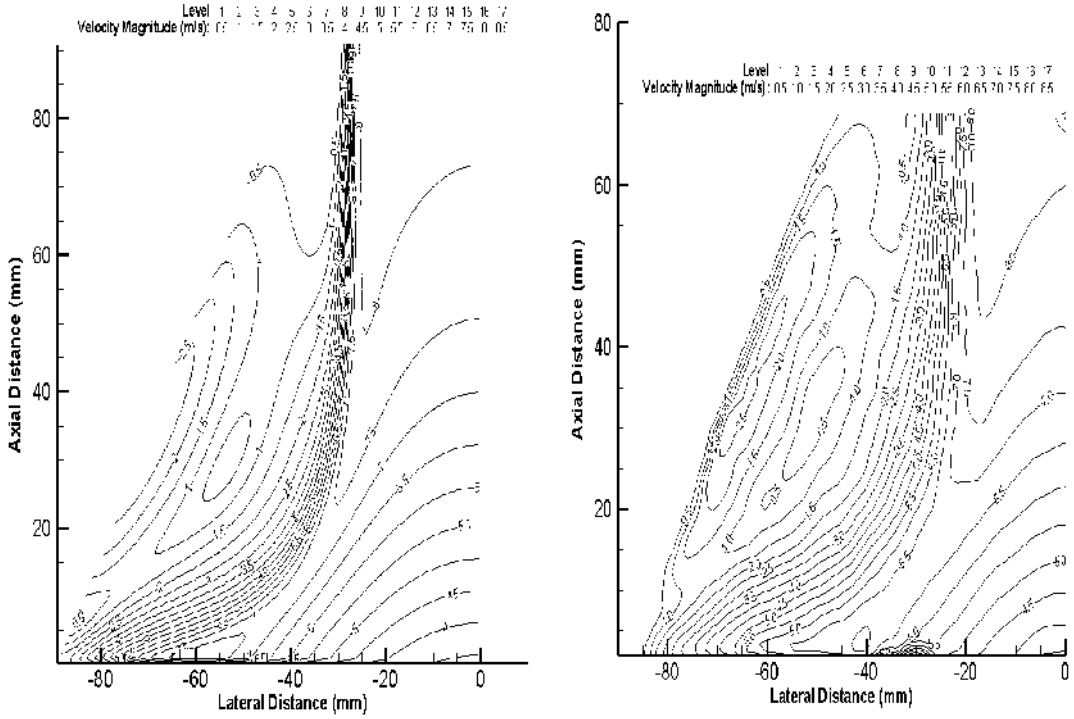

(a) V2f turbulence model (b) Experimental results from PIV

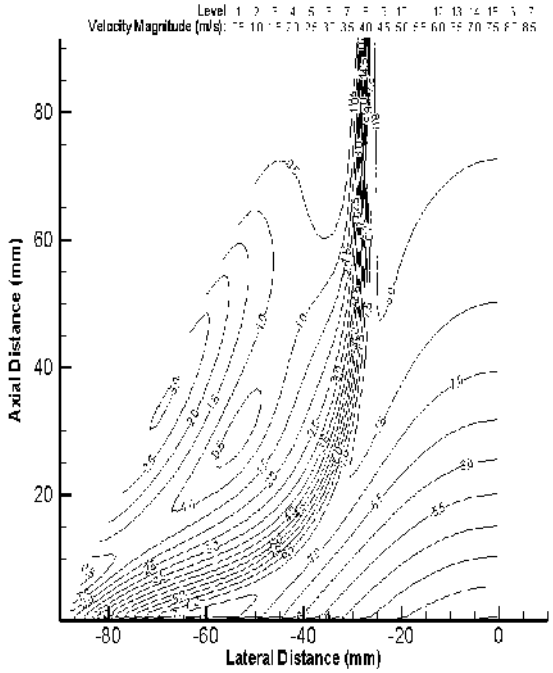

(c) V2F turbulence model with entrance effect

Figure 6.28: Comparison of line contour velocity magnitude profiles in the diffuser and experimental results with and without entrance effect. (100 mm substrate Re: 41800): (a) V2F turbulence model, (b) Experimental results from PIV, (c) V2F turbulence model with entrance effect and fixed critical angle ($\alpha_{c,F}$) of 81^0.

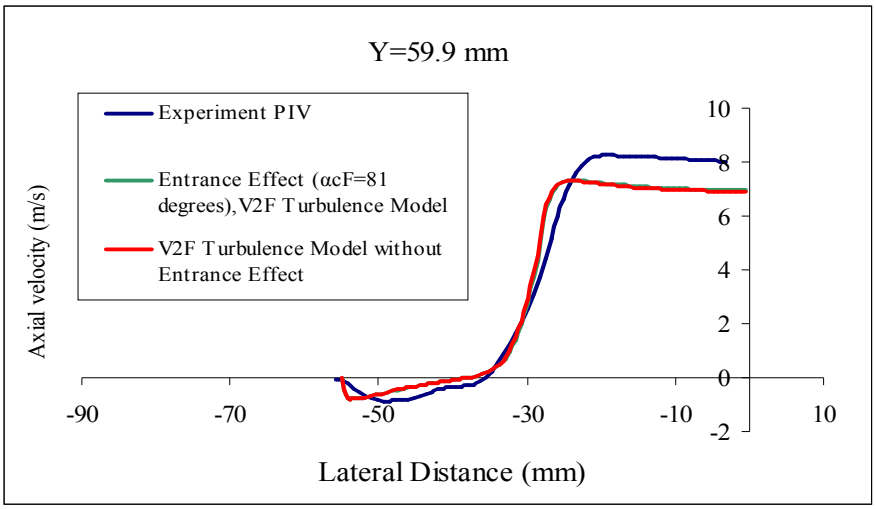

Figure 6.29: Comparison of CFD predictions with and without entrance effect and experimental results (100 mm substrate, Re: 41800 & Y=59.9 mm)

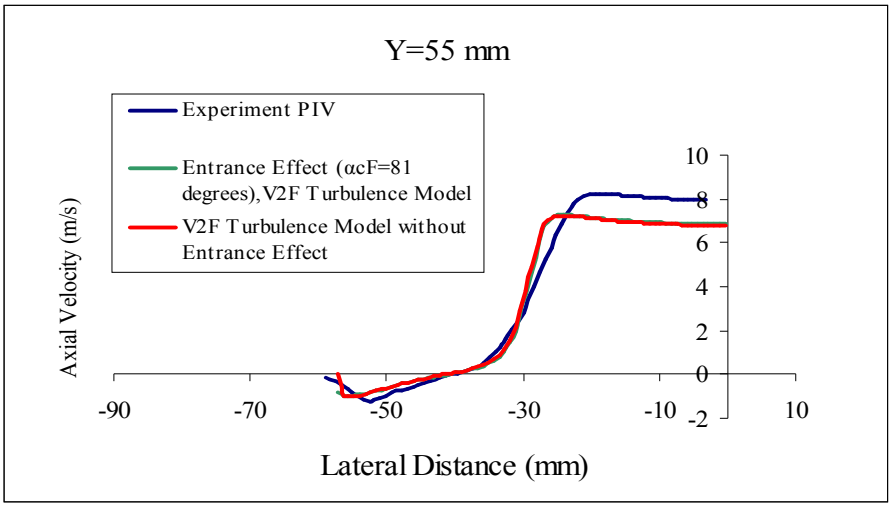

Figure 6.30: Comparison of CFD predictions with and without entrance effect and experimental results (100 mm substrate, Re: 41800 & Y=55 mm)

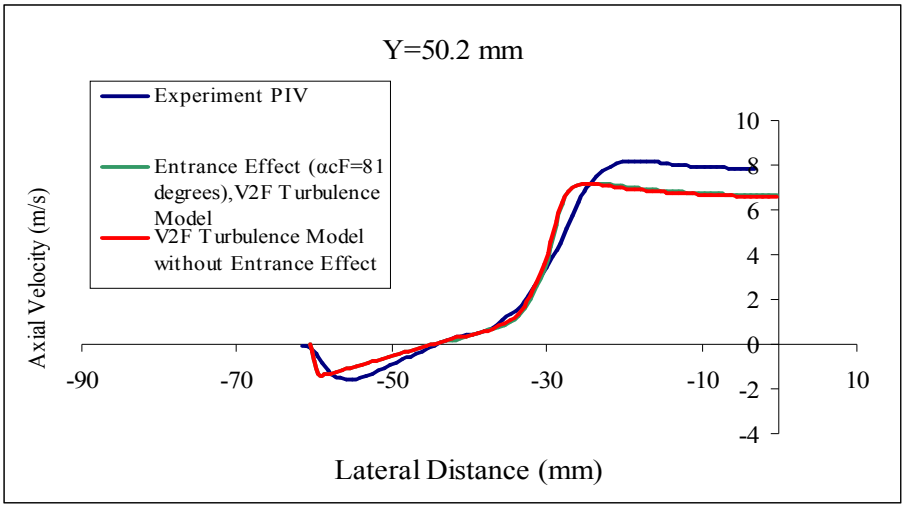

Figure 6.31: Comparison of CFD predictions with and without entrance effect and experimental results (100 mm substrate, Re: 41800 & Y=50.2 mm)

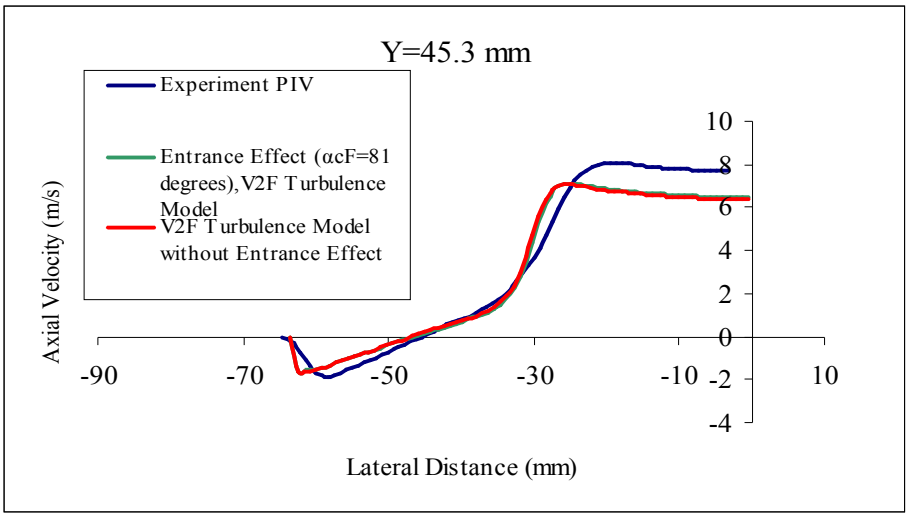

Figure 6.32: Comparison of CFD predictions with and without entrance effect and experimental results (100 mm substrate, Re: 41800 & Y=45.3 mm)

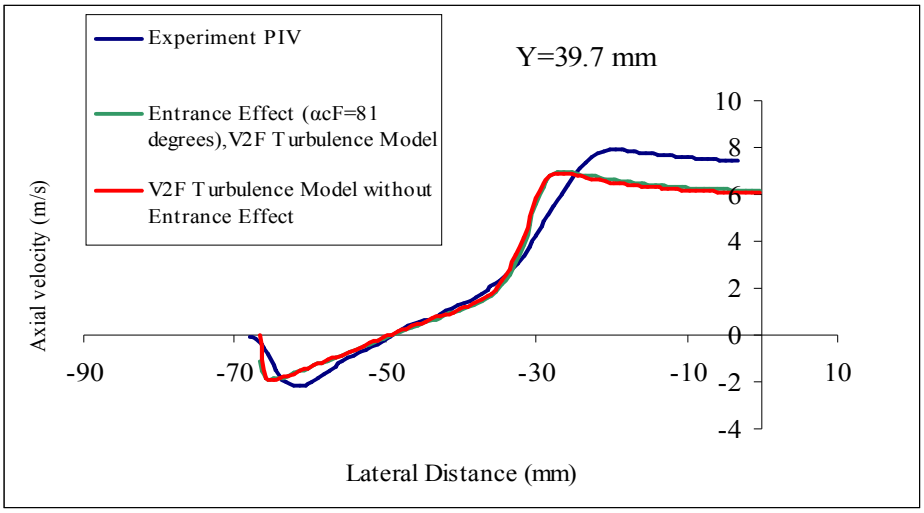

Figure 6.33: Comparison of CFD predictions with and without entrance effect and experimental results (100 mm substrate, Re: 41800 & Y=39.7 mm)

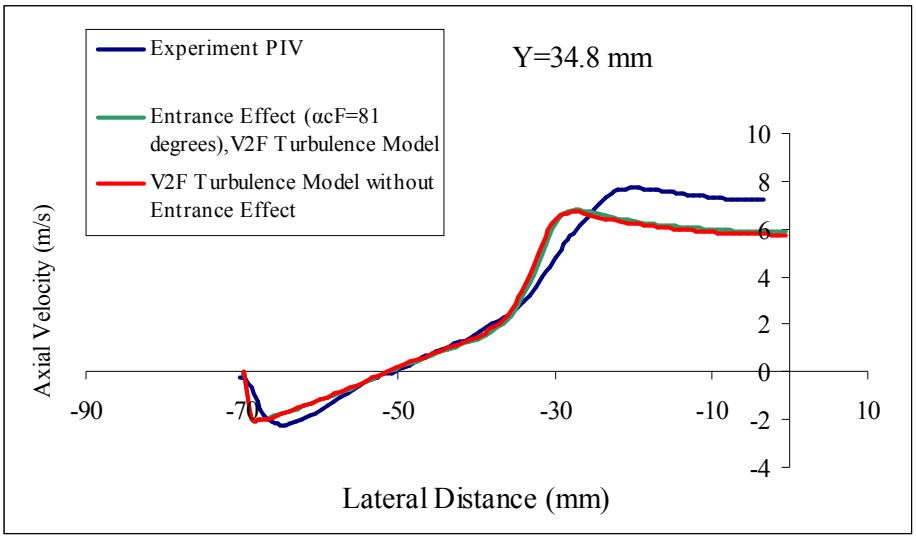

Figure 6.34: Comparison of CFD predictions with and without entrance effect and experimental results (100 mm substrate, Re: 41800 & Y=34.8 mm)

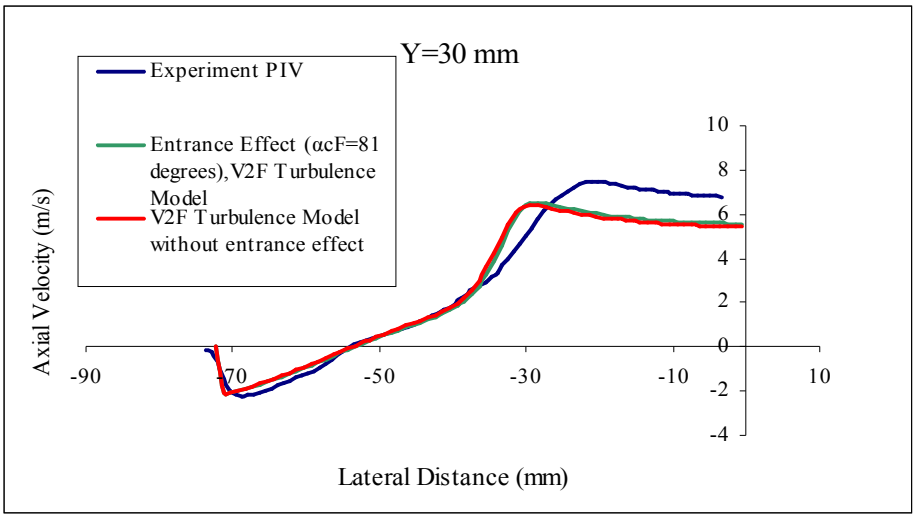

Figure 6.35: Comparison of CFD predictions with and without entrance effect and experimental results (Re: 41800 & Y=30 mm)

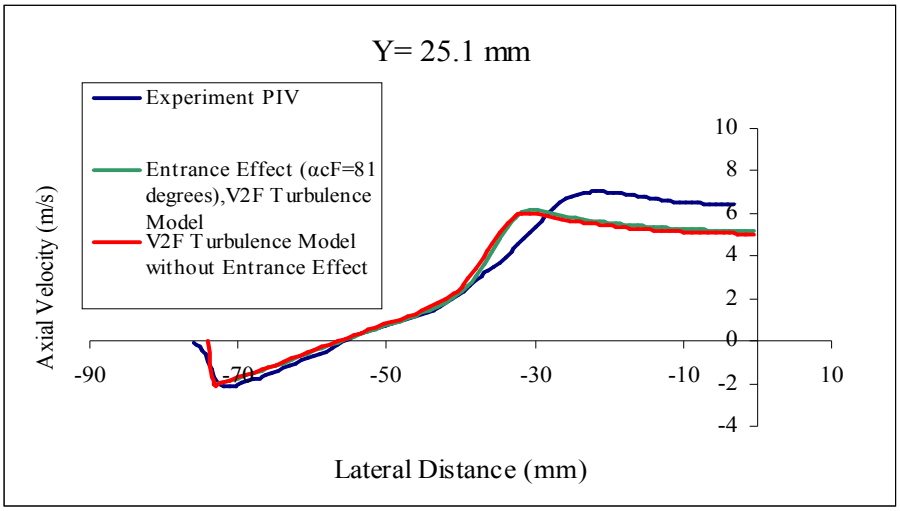

Figure 6.36: Comparison of CFD predictions with and without entrance effect and experimental results (Re: 41800 & Y=25.1 mm)

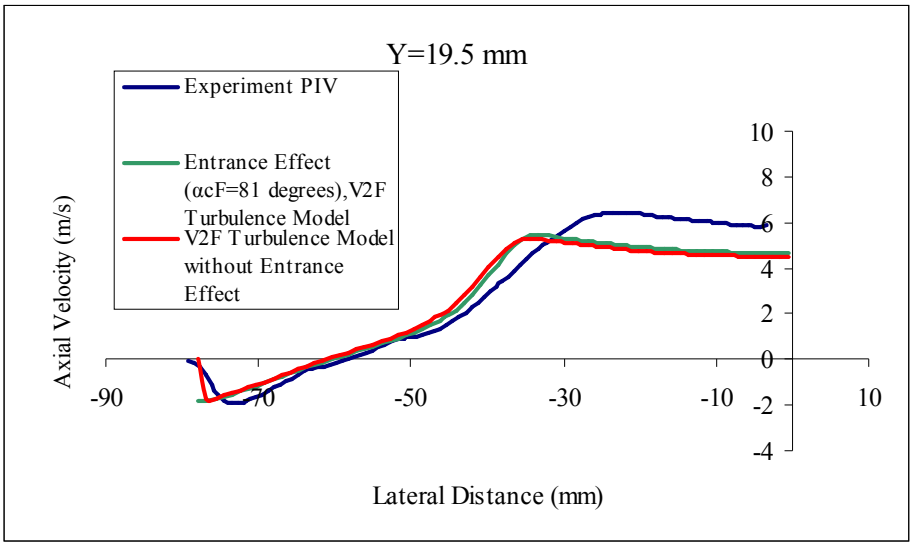

Figure 6.37: Comparison of CFD predictions with and without entrance effect and experimental results (Re: 41800 & Y=19.5 mm)

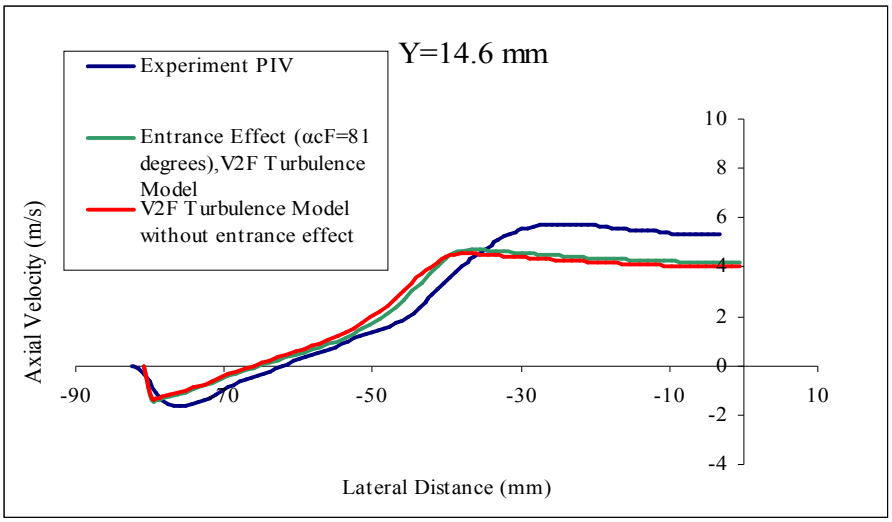

Figure 6.38: Comparison of CFD predictions with and without entrance effect and experimental results (Re: 41800 & Y=14.6 mm)

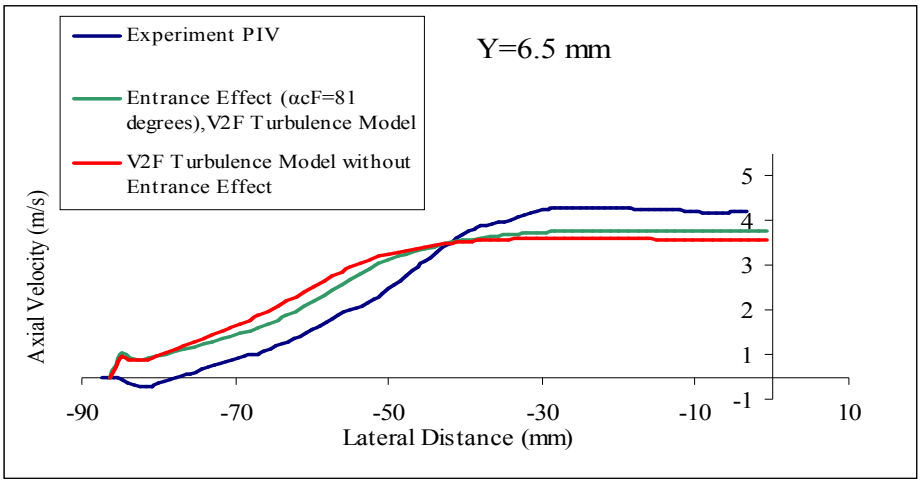

Figure 6.39: Comparison of CFD predictions with and without entrance effect and experimental results (Re: 41800 & Y=6.5 mm)

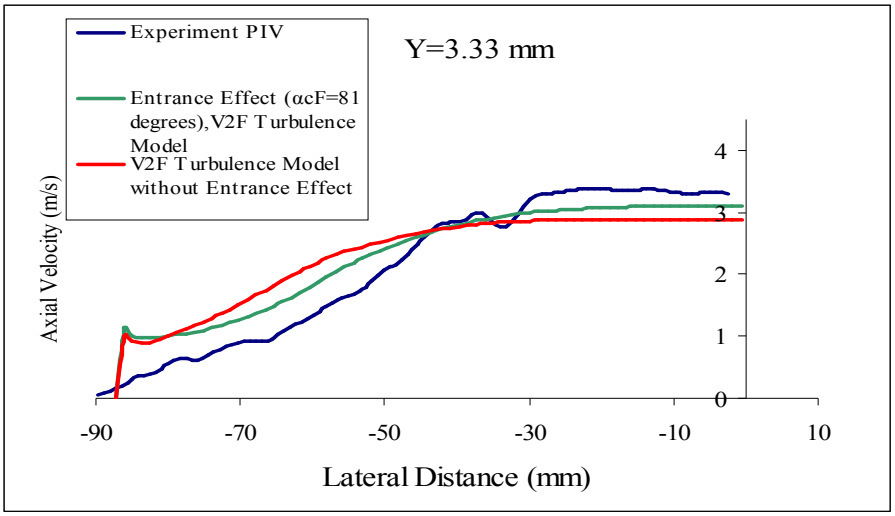

Figure 6.40: Comparison of CFD predictions with and without entrance effect and experimental results (Re: 41800 & Y=3.33 mm)

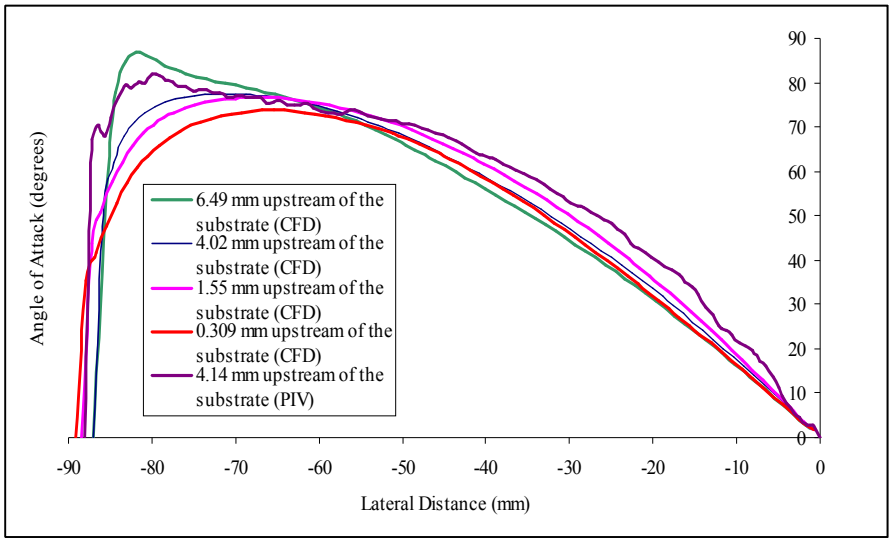

Figure 6.41: Comparison of CFD predictions of angle of attack with entrance effect and experimental results (Re: 41800)

6.5.3.3 Comparison of flow profiles upstream of the 27 mm substrate with and without entrance effect ($\alpha_{c,F}= 81^0$)

CFD predictions for flow in the diffuser upstream of 27 mm substrate with and without entrance effect ($\alpha_{c,F=}81^0$) were compared with the experimental results from PIV. Due to the short length of the 27 mm substrate, the flow was still developing as it exits the substrate channels. As discussed in Chapter 2, the Darcy's equation would therefore give an inaccurate account of pressure drop in the substrate as it ignores the pressure drop due to developing flow. As a result for the 27 mm substrate, both α and β permeability coefficients obtained from the zero degree angle of attack measurements from Chapter 2 have been used. Fig. 6.42 shows the comparison of line contour velocity magnitude plot with and without entrance effect ($\alpha_{c,F}= 81^0$) with experimental results from PIV. Incorporating the entrance effect ($\alpha_{c,F}= 81^0$) had a very small effect on the flow profiles far from the substrate (Y>20 mm) where the velocity magnitude increase in the central core region is very small (Figs. 6.43-6.50). As the flow proceeds further downstream the flow is under the influence of the comparatively higher resistance of the substrate due to entrance effect. As a result, prediction of axial velocity with entrance effect is comparatively higher. This can be seen from Figs. (6.52-6.54) and at Y=3.28 mm very close to the substrate (Fig. 6.54). The angle of attack predictions with entrance effect show that as the flow approaches the substrate, the angle of attack in the near-wall reduces and is in good agreement

with PIV measurements (Fig. 6.55). Hence incorporating the entrance effect improved the predictions close to the substrate.

(Legend αcF in Figs. 6.43-6.54 corresponds to the fixed critical angle, $\alpha_{c,F}$)

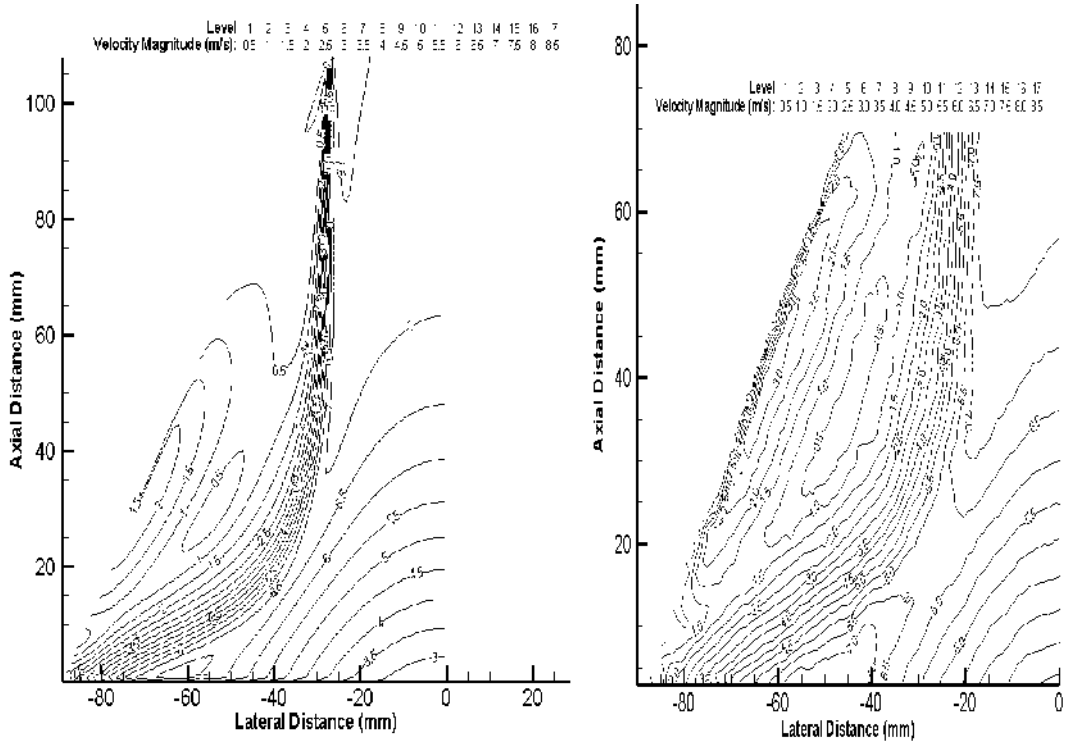

(a) V2f turbulence model (b) Experimental results from PIV

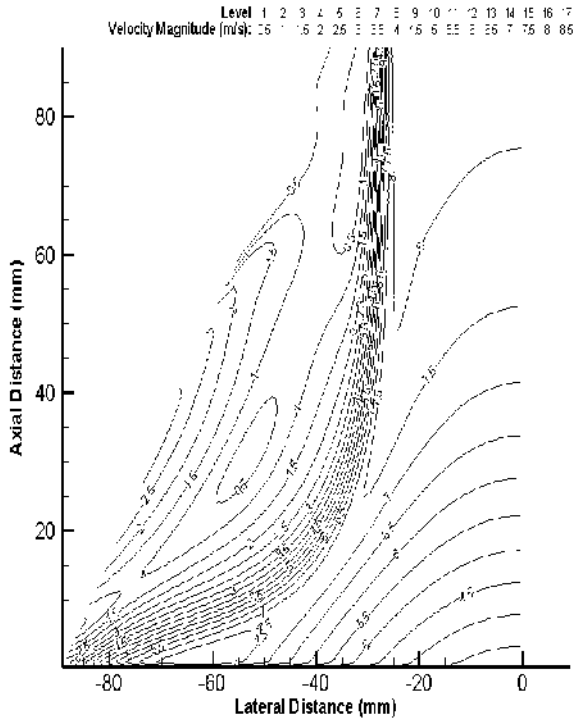

(c) V2f turbulence model with entrance effect

Figure 6.42: Comparison of predictions of line contour velocity magnitude profiles in the diffuser with experimental results (27 mm substrate Re: 41800): (a) V2F turbulence model, (b) Experimental results from PIV, (c) V2F turbulence model with entrance effect and fixed critical angle ($\alpha_{c,F}$) of 81^0.

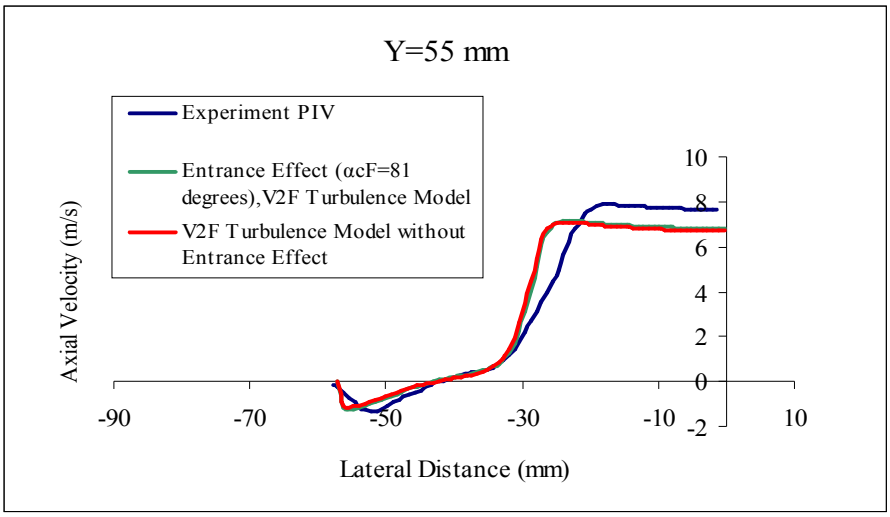

Figure 6.43: Comparison of CFD predictions with and without entrance effect ($\alpha_{c,F}$= 81^0) and experimental results (27 mm substrate, Re: 41800 & Y=55 mm)

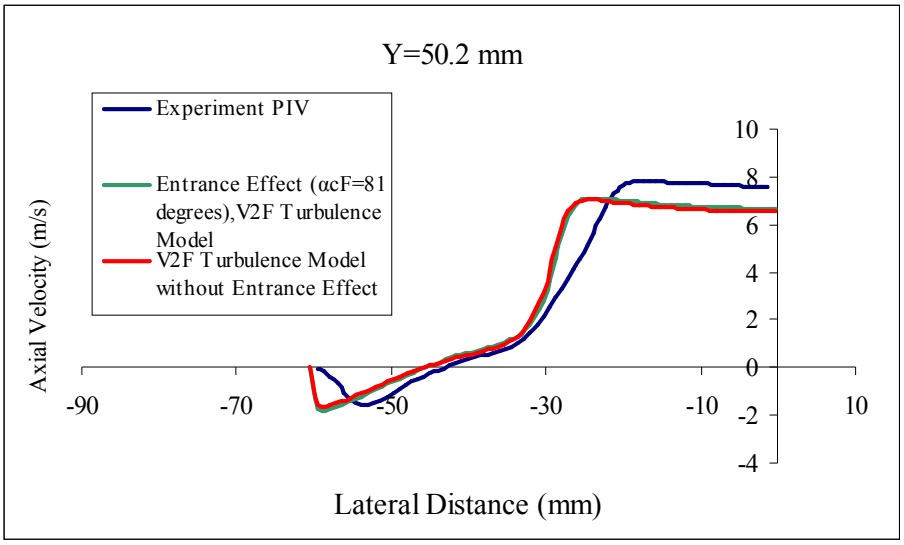

Figure 6.44: Comparison of CFD predictions with and without entrance effect ($\alpha_{c,F}$= 81^0) and experimental results (27 mm substrate, Re: 41800 & Y=50.2 mm)

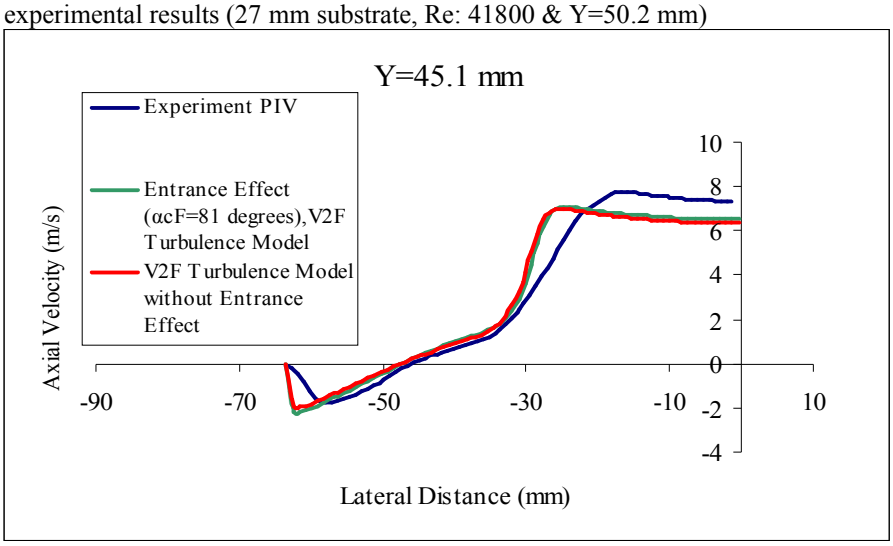

Figure 6.45: Comparison of CFD predictions with and without entrance effect ($\alpha_{c,F}$= 81^0) and experimental results (27 mm substrate, Re: 41800 & Y=45.1 mm)

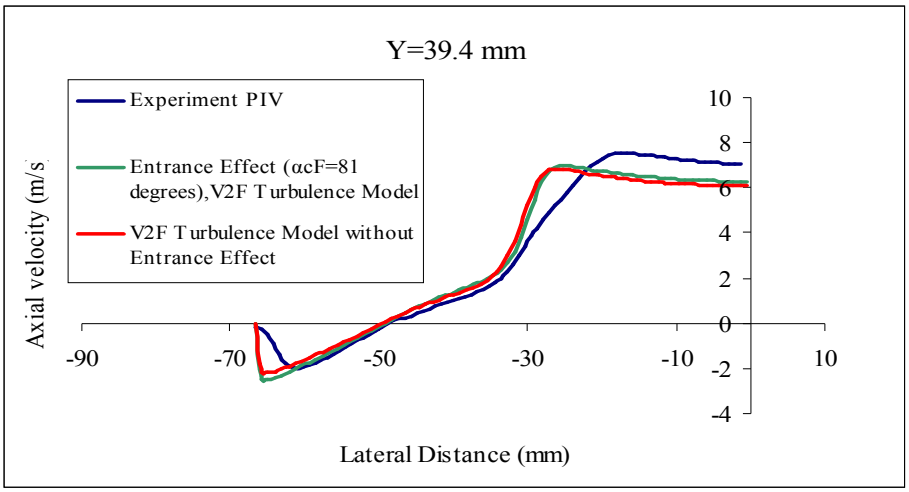

Figure 6.46: Comparison of CFD predictions with and without entrance effect ($\alpha_{c,F}$= 81^0) and experimental results (27 mm substrate, Re: 41800 & Y=39.4 mm)

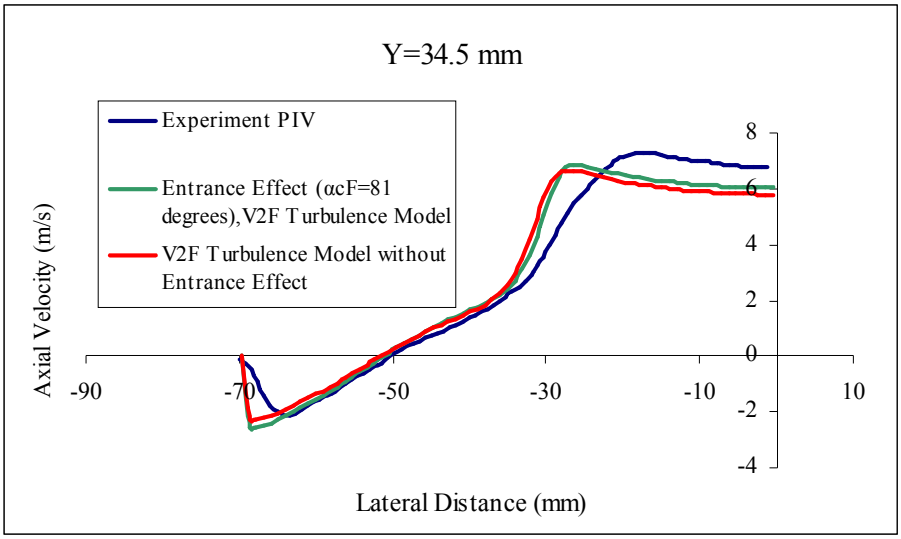

Figure 6.47: Comparison of CFD predictions with and without entrance effect ($\alpha_{c,F}$= 81^0) and experimental results (27 mm substrate, Re: 41800 & Y=34.5 mm)

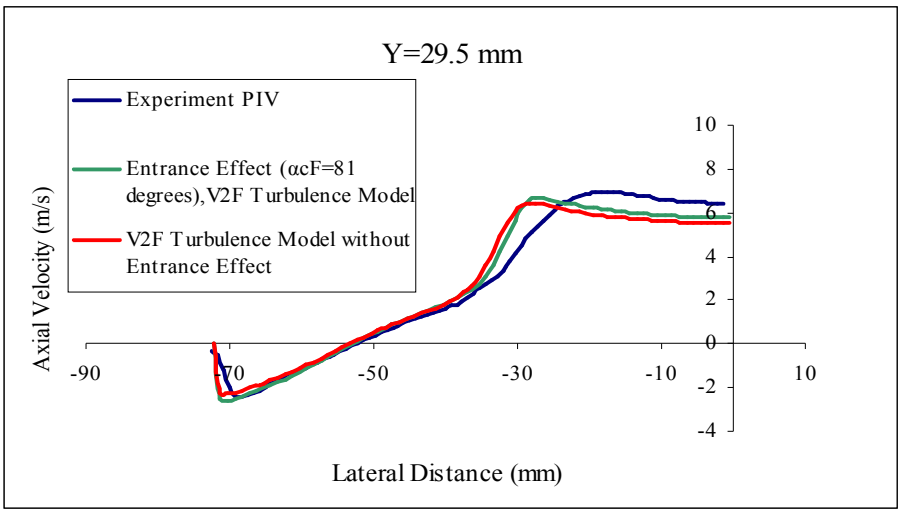

Figure 6.48: Comparison of CFD predictions with and without entrance effect ($\alpha_{c,F}$= 81^0) and experimental results (27 mm substrate, Re: 41800 & Y=29.5 mm)

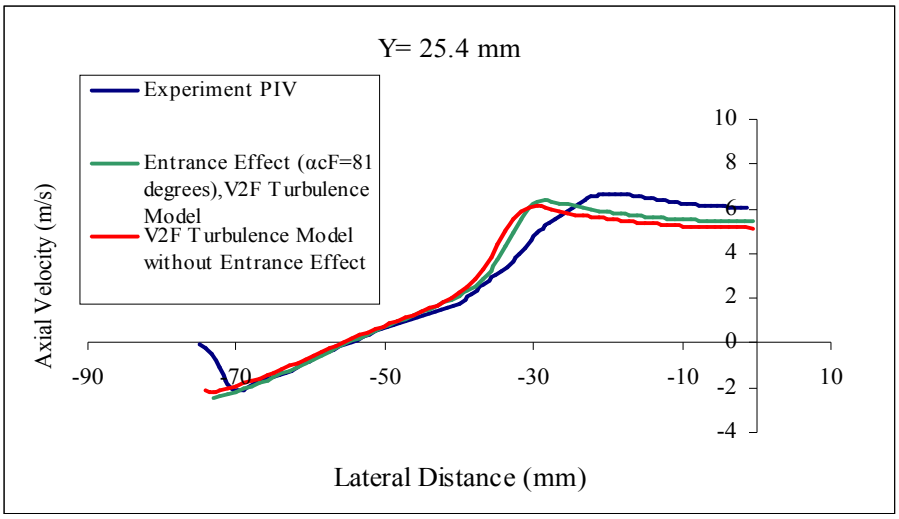

Figure 6.49: Comparison of CFD predictions with and without entrance effect ($\alpha_{c,F}$= 81^0) and experimental results (27 mm substrate, Re: 41800 & Y=25.4 mm)

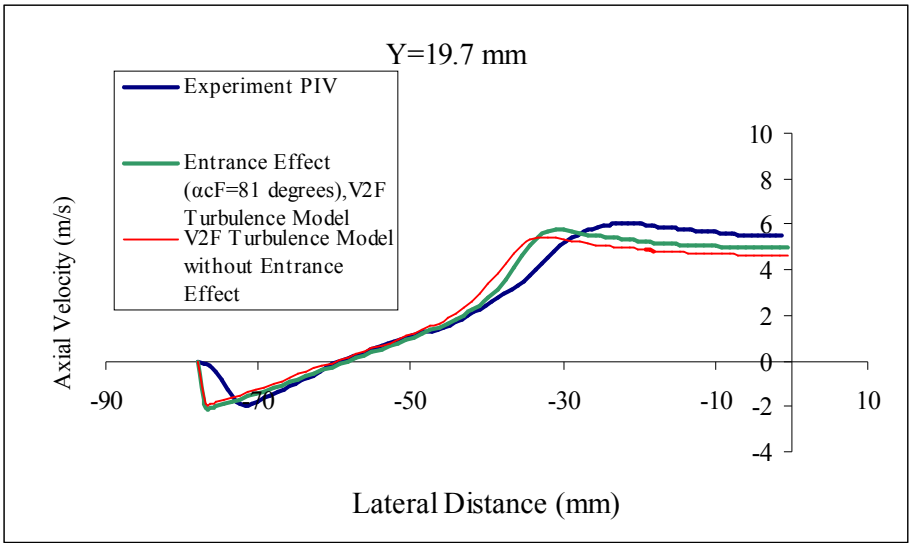

Figure 6.50: Comparison of CFD predictions with and without entrance effect ($\alpha_{c,F}$= 81^0) and experimental results (27 mm substrate, Re: 41800 & Y=19.7 mm)

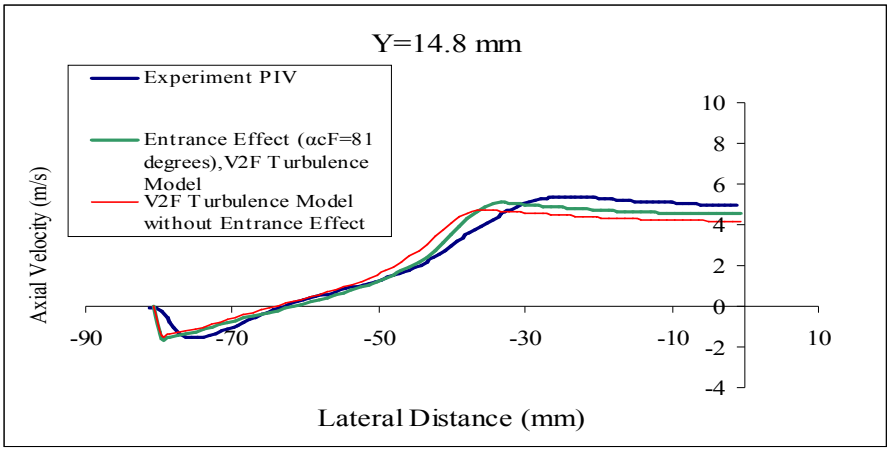

Figure 6.51: Comparison of CFD predictions with and without entrance effect ($\alpha_{c,F}$= 81^0) and experimental results (27 mm substrate, Re: 41800 & Y=14.8 mm)

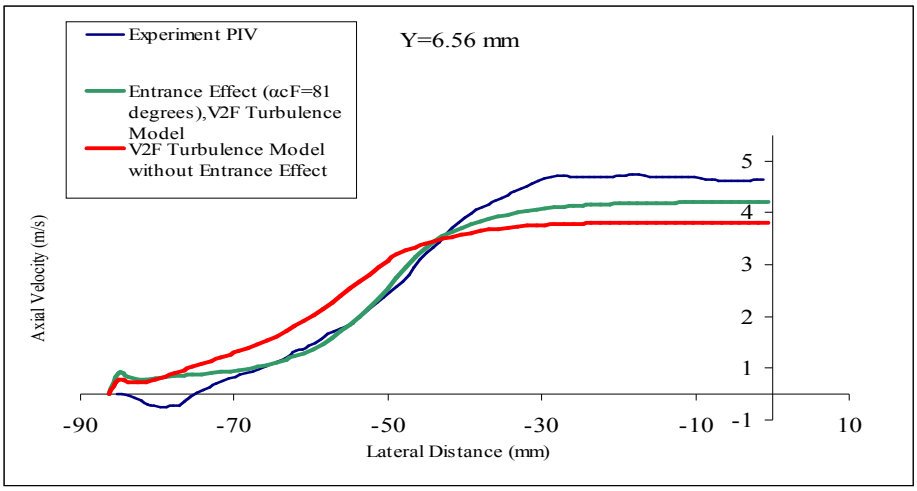

Figure 6.52: Comparison of CFD predictions with and without entrance effect ($\alpha_{c,F}$= 81^0) and experimental results (27 mm substrate, Re: 41800 & Y=6.56 mm)

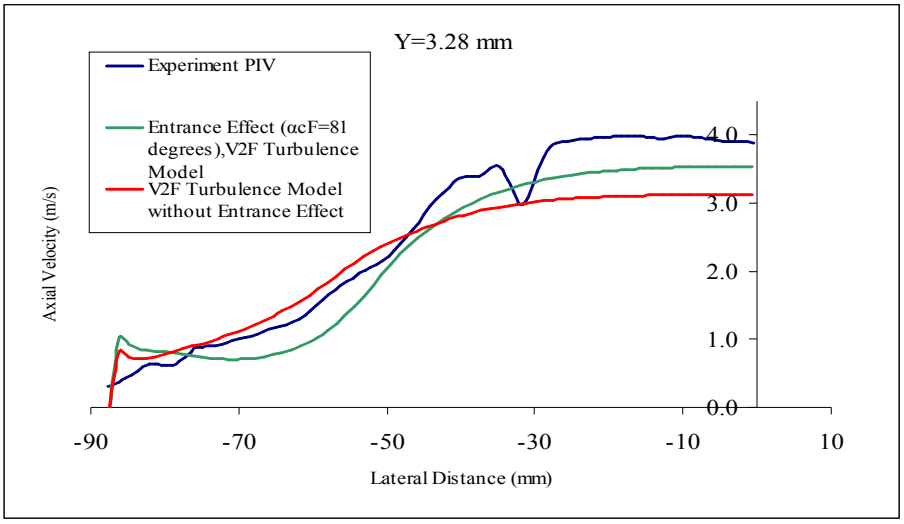

Figure 6.53: Comparison of CFD predictions with and without entrance effect ($\alpha_{c,F}$= 81^0) and experimental results (27 mm substrate, Re: 41800 & Y=3.28 mm)

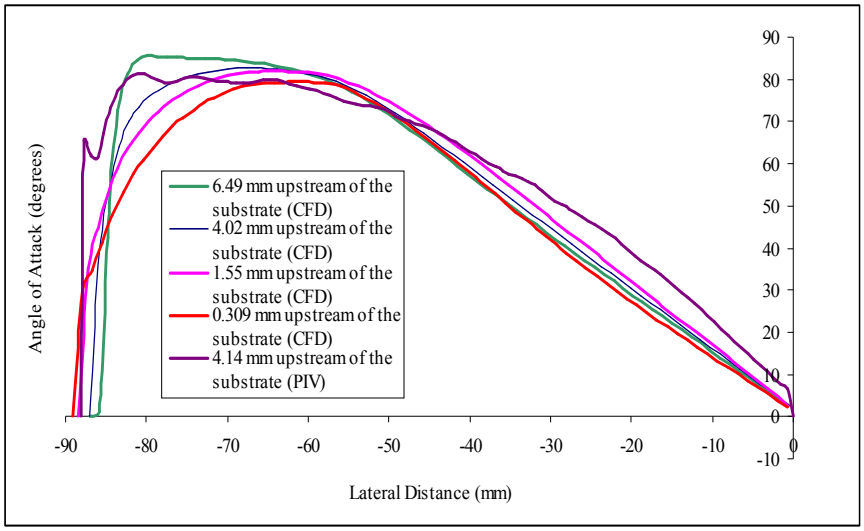

Figure 6.54: Comparison of CFD predictions of angle of attack with entrance effect and experimental results (Re: 41800)

6.5.3.4 CFD comparison of hot-wire velocity profiles at the exit of the substrate

Figs. 6.55-6.60 show the CFD predictions performed with and without the entrance effect ($\alpha_{c,F}$=81^0) for the 27 mm and 100 mm substrate. The hot-wire velocity profiles 30 mm from the exit of 27 and 100 mm substrates have been used for comparison with the CFD predictions. Incorporating the entrance effect improved the predictions for both the lengths of the substrate and the velocity in the central core region was similar to the experimental results.

(Legend αcF in Figs. 7.41-7.48 corresponds to the fixed critical angle, $\alpha_{c,F}$)

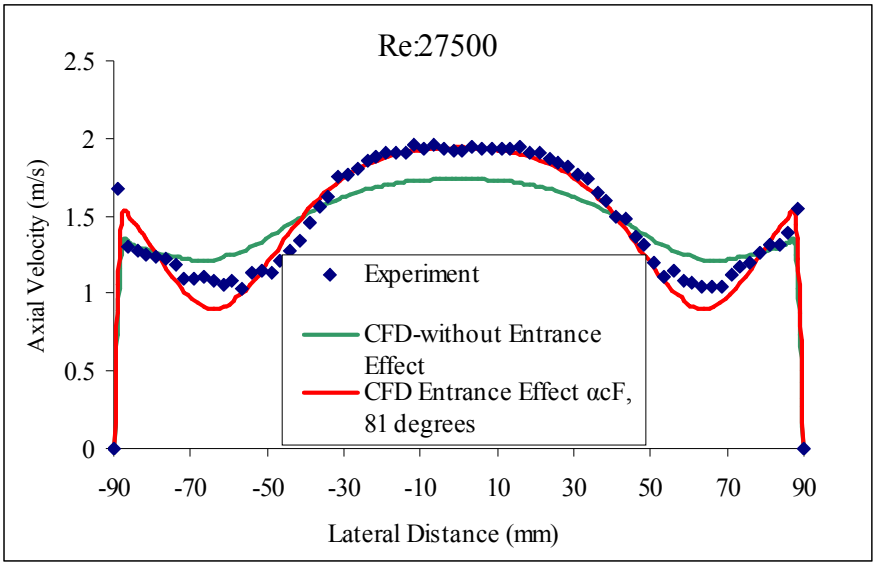

Figure 6.55: Comparison between HWA experiment and CFD predictions V2F model with and without entrance effect ($\alpha_{c,F}$= 81^0) for 2-D model (27 mm substrate Re: 27500)

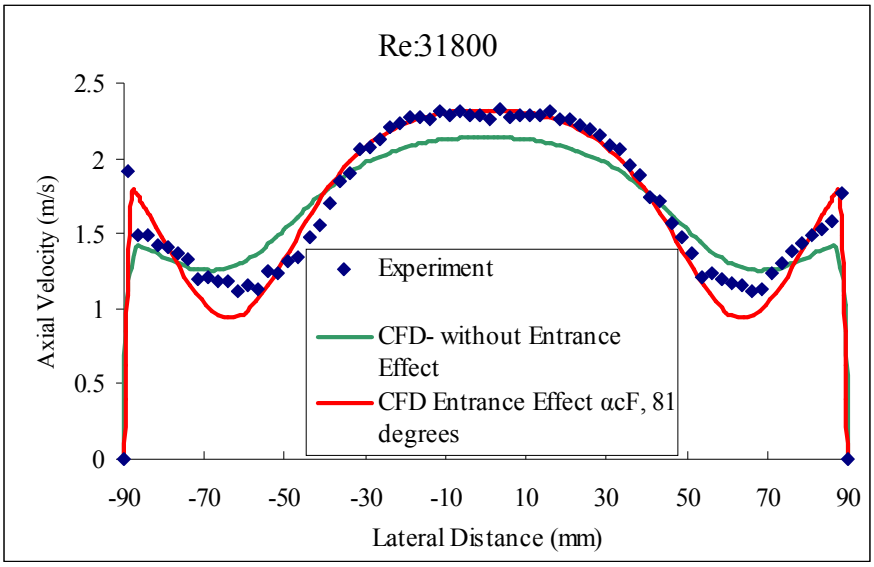

Figure 6.56: Comparison between HWA experiment and CFD predictions V2F model with and without entrance effect ($\alpha_{c,F}$= 81^0) for 2-D model (27 mm substrate Re: 31800)

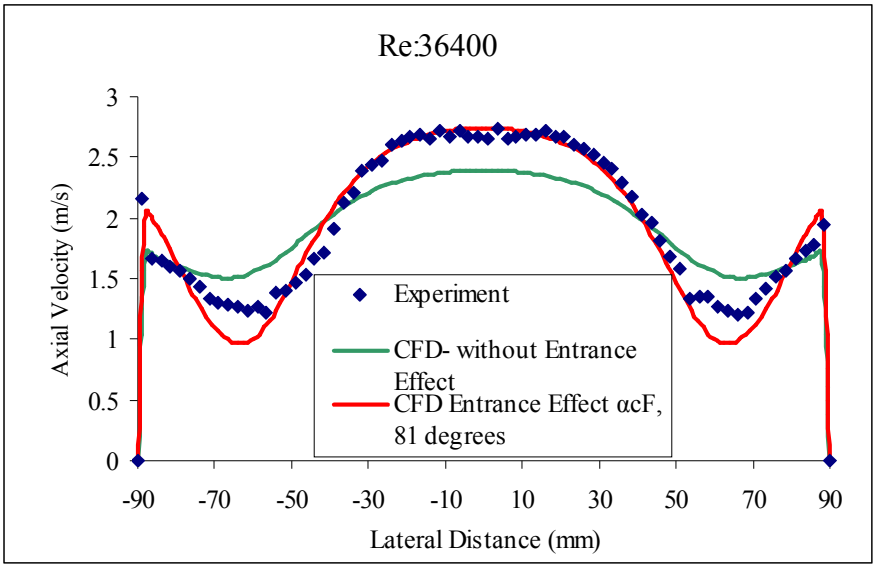

Figure 6.57: Comparison between HWA experiment and CFD predictions V2F model with and without entrance effect ($\alpha_{c,F}$= 81^0) for 2-D model (27 mm substrate Re: 36400)

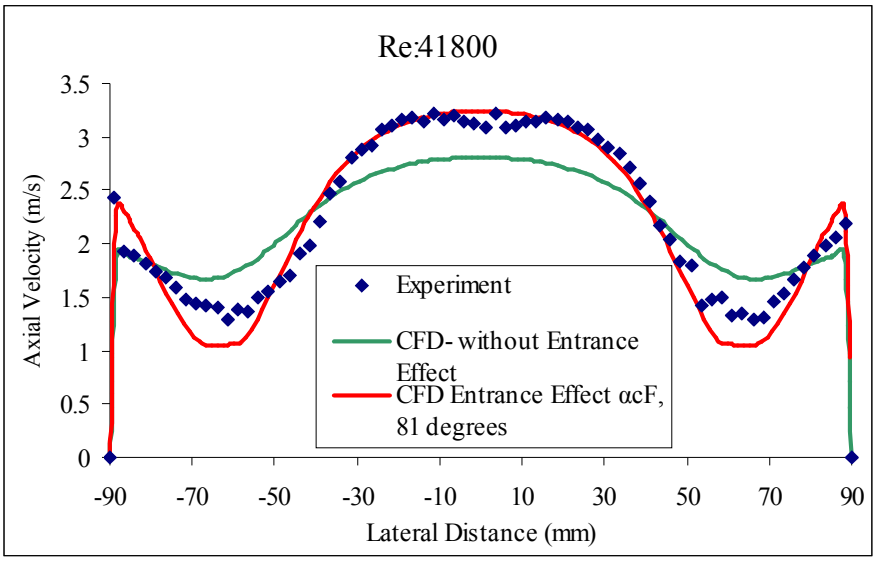

Figure 6.58: Comparison between HWA experiment and CFD predictions V2F model with and without entrance effect ($\alpha_{c,F}$= 81^0) for 2-D model (27 mm substrate Re: 41800)

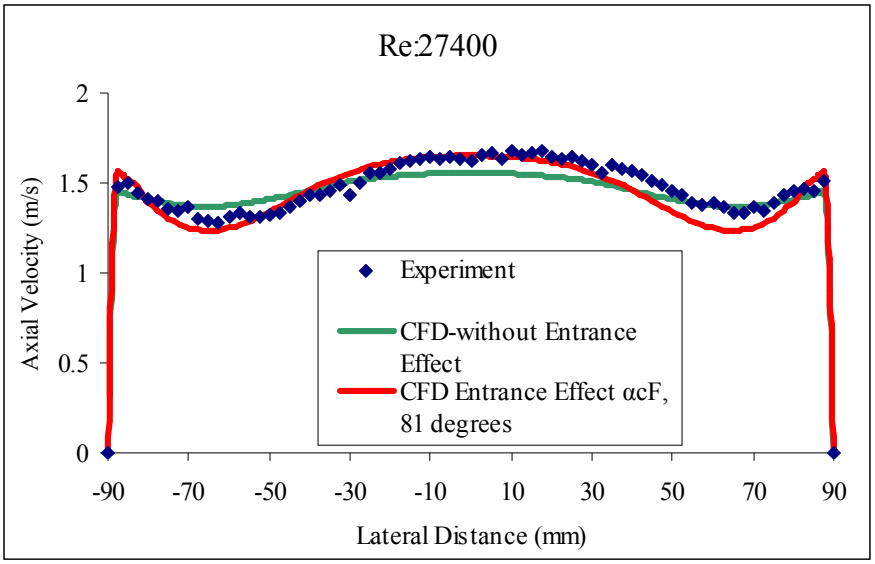

Figure 6.59: Comparison between HWA experiment and CFD predictions V2F model with and without entrance effect ($\alpha_{c,F}$= 81^0) for 2-D model (100 mm substrate Re: 27400)

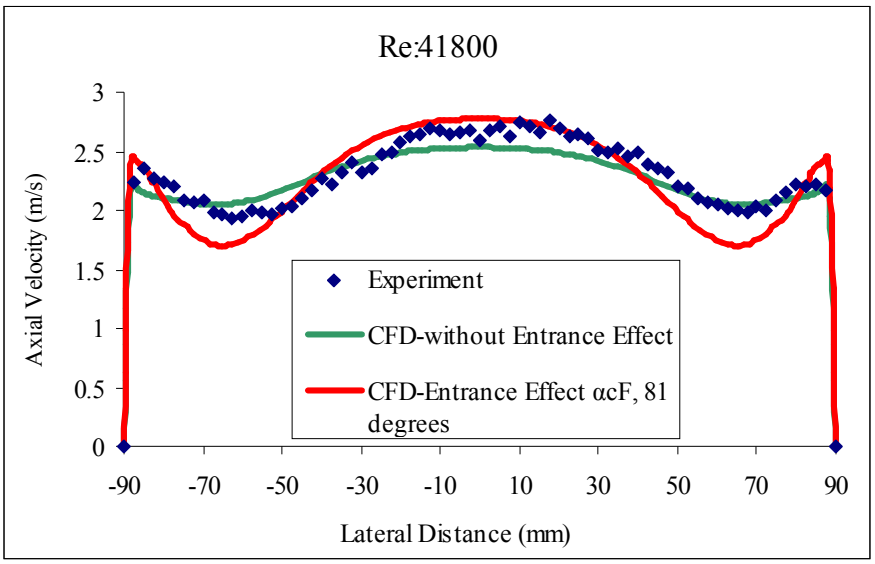

Figure 6.60: Comparison between HWA experiment and CFD predictions V2F model with and without entrance effect ($\alpha_{c,F}$= 81^0) for 2-D model (100 mm substrate Re: 41800)

6.5.3.5 Comparison of profiles upstream and downstream of the substrate

Figs. 6.61 and 6.63 show the comparison of axial velocity profiles upstream and downstream of the substrate using PIV and HWA. As discussed in Chapter 5, due to reflection from the surface close to the diffuser-substrate interface accurate measurements using PIV were not possible close to the diffuser-substrate interface (approximately 2 mm). Hence CFD predictions upstream and downstream of the substrate give a good measure of the flattening of the velocity profiles close to the

diffuser-substrate interface (Figs. 6.62 & 6.64). The CFD predictions in Figs. 6.62 and 6.64 are obtained using the entrance effect, fixed critical angle ($\alpha_{c,F}=81^0$) approach. Figs. 6.64 & 6.66 show that most of the flattening of profile happens close to the substrate. The flattening of the profiles increases as the length of the substrate increases. The hot-wire velocity profiles downstream of the substrate show that more flow is entering the substrate channels near the wall as compared to the 10-30 mm region from the periphery of the substrate. The CFD predictions show that this phenomenon occurs very close to the substrate approximately 2mm upstream of the substrate.

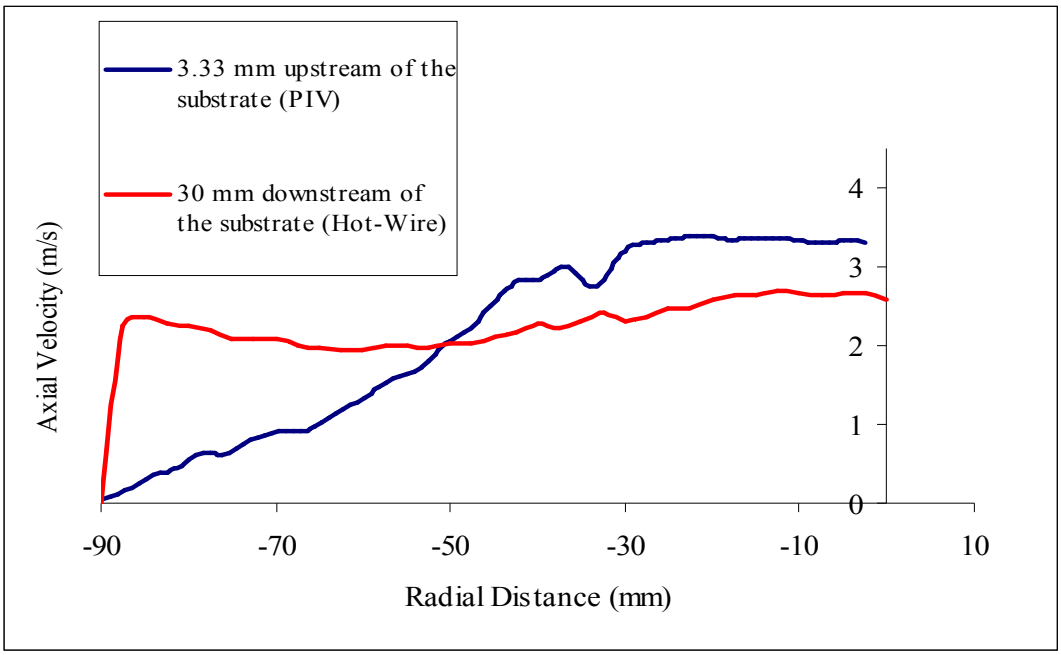

Figure 6.61: Comparison of axial velocity profiles upstream and downstream of the 100 mm substrate at Re: 41800 using PIV and Hot-Wire Anemometry

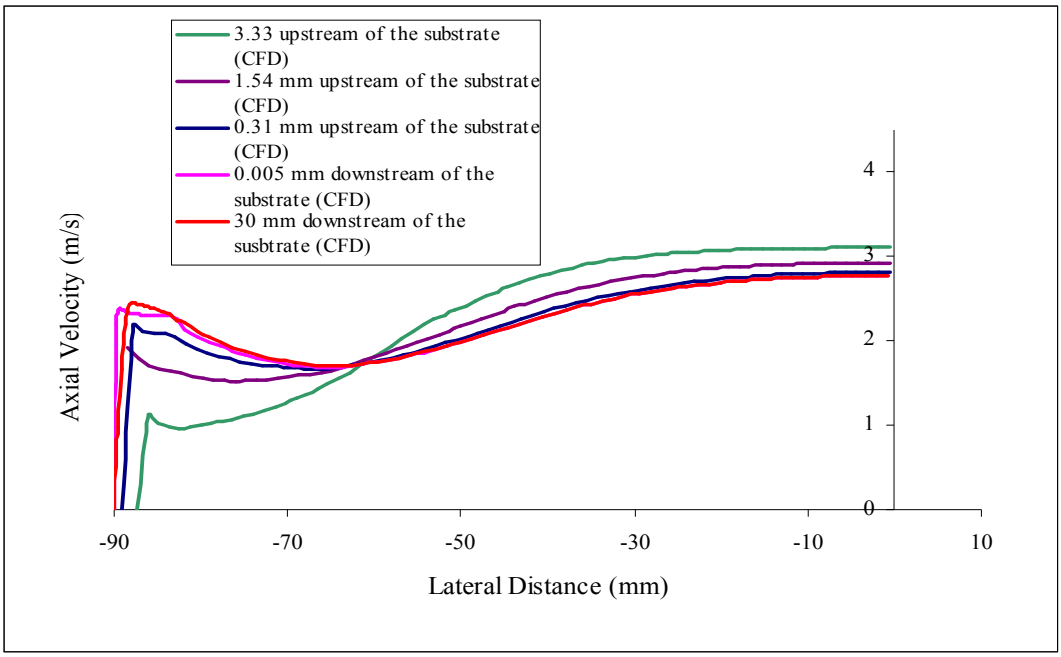

Figure 6.62: Comparison of axial velocity profiles upstream and downstream of the 100 mm substrate at Re: 41800 using CFD

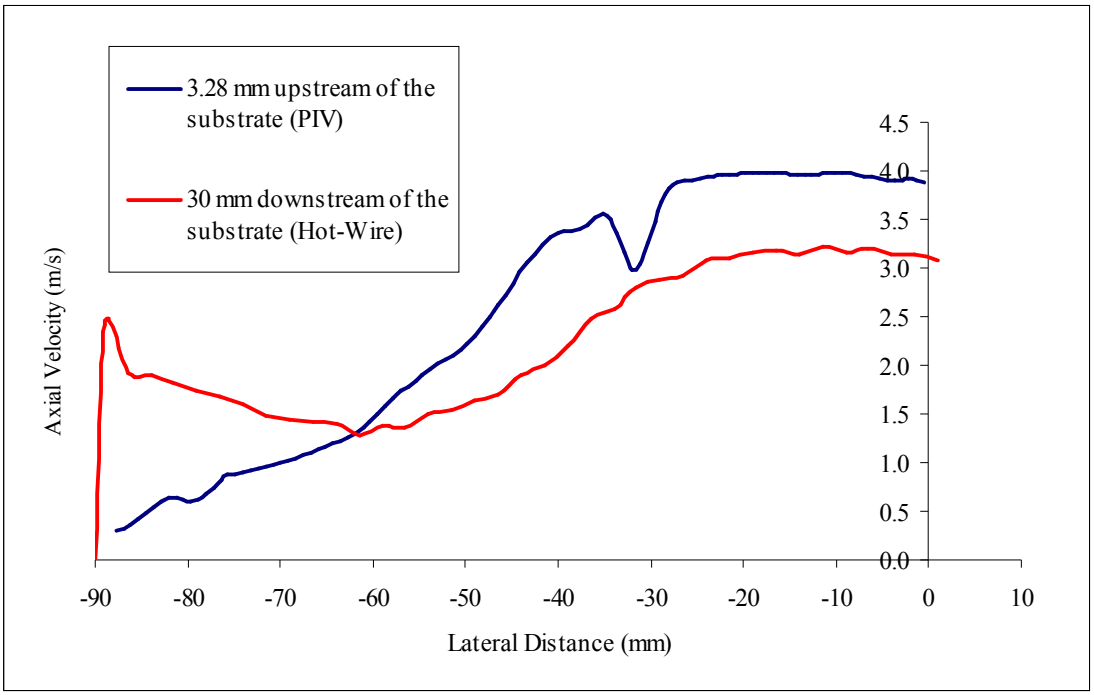

Figure 6.63: Comparison of axial velocity profiles upstream and downstream of the 27 mm substrate at Re: 41800 using PIV and Hot-Wire Anemometry

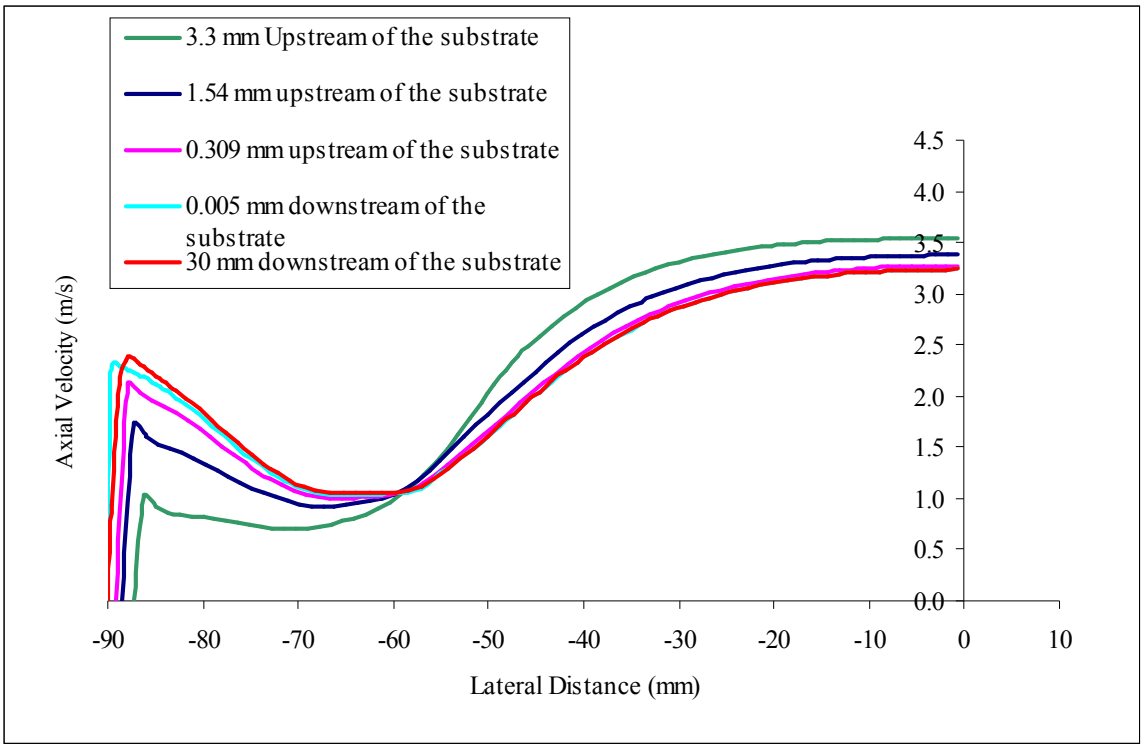

Figure 6.64: Comparison of axial velocity profiles upstream and downstream of the 27 mm substrate at Re: 41800 using CFD

6.6 Summary

An axisymmetric CFD study was undertaken to predict the flow distribution at the exit of a substrate. The predictions showed that using Darcy's equation alone under predicted the maldistribution in the flow. Incorporating the entrance effect without the critical angle approach improved the predictions in the central core region but under predicted the velocity in the region of 10-30 mm from the wall. Using a critical angle approach with a critical angle of 81^0 predicted the maldistribution in the flow across the substrate accurately. This has been verified in cases with channel velocities up to 13 m/s.

A 2-D CFD study was also undertaken to predict the flow distribution upstream and downstream of a substrate. A comparison of the CFD predictions in the diffuser using different turbulence models showed that the selection of the turbulence model had a small influence on the flow predictions close to the substrate. In terms of the flow features in the diffuser such as the recirculation bubble and the point of cross-over, the V2F turbulence model compared best with experimental results. Without the

entrance effect the velocity in the central core region of the diffuser was under predicted. Incorporating the entrance effect ($\alpha_{c,F}= 81^0$) improved the predictions close to the substrate and had a small influence far from the substrate (Y>20 mm). It also improved the flow predictions downstream of the substrate.

In order to further improve the predictions in the diffuser, improved turbulence models are needed. CFD studies have shown that the use of LES (Kaltenbach et.al, 1999) improves the CFD predictions for flow in the diffuser. The use of such techniques would require large computational resources. This 2D study has shown that using the entrance effect methodology ($\alpha_{c,F}= 81^0$) and the V2F turbulence model does give good predictions of flow entering the substrate even though the predictions in the diffuser need improvement.

Chapter 7: Conclusions and Future Work

7.1 Introduction

This thesis aims to improve CFD predictions of flow maldistribution across a catalyst substrate where the flow is from an upstream conical or 2-D diffuser. Previous studies by Haimad (1997), Wollin (2001) and Liu (2003) showed that modelling monolith flow resistance using the Hagen-Poiseuille formulation under predicted flow maldistribution. The predictions were improved by incorporating an additional pressure loss term for oblique entry of the flow into the monolith. This was termed the entrance effect. Further improvement was obtained by Liu (2003) by incorporating the critical angle of attack method ($\alpha_{c,V}$). However, there was no experimental evidence to support these oblique entry losses formulations. There also remained the possibility that under prediction of flow maldistribution might be due to the failure to predict flow in the diffuser accurately. Hence in order to understand and improve predictions this thesis has investigated the following:

- Measurements of oblique entry losses across a monolith as a function of angle of attack, monolith length and Reynolds number.
- CFD predictions of flow maldistribution across an axisymmetric catalyst monolith incorporating the correlation for oblique flow entrance losses from measurements
- Visualisation and measurement of the flow field in a 2-D diffuser upstream of monoliths using particle image velocimetry (PIV)
- CFD predictions of flow in a 2-D diffuser using various turbulence models and comparison with PIV measurements.
- CFD predictions of maldistribution in the flow profiles across 2-D catalyst substrates by incorporating the correlation for oblique flow entrance losses obtained from measurements.

The conclusions of this study are reported in the following sections.

7.2 One-dimensional oblique angle flow rig

A one-dimensional oblique angle flow rig has been designed and developed to measure the effect of oblique entry flow losses in monoliths. Experiments were performed at different angles of attack using different lengths of substrate and a methodology was developed to obtain the oblique flow entrance losses also known as entrance effect.

The results for the zero degree angle of attack experiments showed that for short substrates (17 & 27 mm monolith), the flow is still developing when it exits the substrate channels. Darcy's equation (H-P) ignores the pressure drop due to developing flow and looses its validity, even at low velocities, for short length substrates. As the length of the substrate increases, the predictions using Darcy's equation are improved at low velocities. Shah's correlation (1978) better predicts the pressure drop for long length substrates at high channel velocities. This was in good agreement with a similar study performed by Benjamin et al (1996). The results from the oblique angle of attack measurements showed that as the angle of attack increases, the entrance effect also increases. The entrance effect was also found to be dependent on channel Reynolds number and substrate length. The theoretical assumption of $\frac{1}{2}\rho V^2$ for the entrance effect, postulated by Kuchemann and Weber (1953), predicts accurately at low flow rates but looses validity at high Reynolds number.

From the experimental studies, an improved correlation for the entrance effect has been found by taking into consideration the major controlling variables, angle of attack, length of the substrates and Reynolds number. The obtained correlation for entrance effect is

$$P_{Obl} = (\frac{1}{2}\rho U_1^{\,2})A(\mathrm{Sin}^2\alpha)^B(\mathrm{Re})^C(\frac{L}{d_h})^D$$

where A=0.447, B=1.233, C=0.0756 and D=0.1287.

This correlation would be useful for design engineers when developing similar types of catalyst system and could readily be incorporated into CFD codes.

7.3 Flow in a two-dimensional diffuser using PIV

A two-dimensional rig has been designed and a PIV system commissioned to investigate the flow in a 2-D diffuser upstream of a substrate. The PIV results showed that the flow in a wide angle diffuser consisted of a central core region, free shear layer region and recirculation regions. The characteristics of flow in the central core region were similar to that of plane rectangular jets in their near field region. There was an occurrence of saddle shape profiles downstream of the diffuser. The free shear layer region developed downstream of the diffuser and separated the central core region and the recirculation region. The flow at the periphery reached a stagnation point at approximately 7 mm from the diffuser-substrate interface. There was no Reynolds number effect on the flow field. Flow comparisons were made for two substrate lengths, 27 and 100 mm. The flow field is largely unaffected by increased resistance up to about 68 mm from the diffuser inlet. The results showed that due to the higher resistance of the longer substrate more flow is forced towards the periphery of the diffuser.

The results from the PIV provide a very useful set of data for comparison with CFD predictions.

7.4 Axisymmetric CFD simulations

A CFD study was undertaken to predict maldistributed flow at the exit of the substrate for an axisymmetric catalyst model by incorporating the measured entrance effect correlation. The CFD predictions showed that Darcy's equation under predicted maldistributed flow. A fixed critical angle of attack ($\alpha_{c,F}$) approach wherein the entrance effect is assumed constant above the fixed critical angle has been used. Incorporating the entrance effect with a fixed critical angle ($\alpha_{c,F}$) of 81^0 best predicted the experimental results.

7.5 2-D CFD study and comparison with PIV measurements

A 2-D CFD study was undertaken to predict the flow distribution in the diffuser and downstream of the substrate. A comparison of the CFD predictions in the diffuser using different turbulence models showed that the selection of the turbulence model had a small influence on the flow predictions close to the substrate. In terms of the flow features in the diffuser such as flow separation and recirculation, the V2F turbulence model compared best with PIV results. Without the entrance effect the velocity in the central core region of the diffuser was under predicted. Incorporating the entrance effect improved the predictions close to the substrate. The entrance effect had a small influence from about 20 mm from the diffuser-substrate interface. However, far from the substrate the velocity in the central core region was under-predicted as the width of the central core region was over-predicted with the V2F turbulence model. Also the V2F turbulence model had a comparatively thin free shear layer when compared to PIV measurements. In order to improve the predictions in the diffuser, improved turbulence models will be needed.

Downstream of the substrate, predictions of flow maldistribution improved by incorporating the entrance effect.

7.6 Original contributions

The original contributions to knowledge at the end of this study are as follows:

- A one-dimensional oblique angle flow rig has been designed and developed to measure the effect of oblique entry flow losses in monoliths.
- Experimental data for the pressure loss formulation due to the effect of oblique entry of flow on the monolith channels has been obtained.
- An improved correlation to predict oblique entry flow losses, P_{Obl}, as a function of angle of attack, length of the substrate and channel Reynolds number has been developed.

$$P_{Obl} = (\frac{1}{2}\rho U_1^{\,2})A(Sin^2\alpha)^B(Re)^C(\frac{L}{d_h})^D$$

where A=0.447, B=1.233, C=0.0756 and D=0.1287.

- Oblique angle flow measurements showed that the theoretical assumption of $\frac{1}{2}\rho V^2$ for entrance effect predicts well at low flow velocities but looses validity at high Reynolds number.
- High quality velocity vector data of flow in a 2-D diffuser upstream of a substrate has been obtained using PIV.
- An assessment of the accuracy of various turbulence models was made by comparing the CFD predictions in the 2-D diffuser region upstream of the monolith with velocity vector data obtained from PIV. The results showed that the V2F turbulence model best predicted the flow in a 2-D diffuser.
- Improved turbulence models are needed to accurately predict the flow in a 2-D planar diffuser. The models under predict the velocity in the central core region.
- CFD predictions of the flow distribution across a monolith under steady state conditions have been improved by incorporating the new entrance effect correlation for 2-D and axisymmetric catalyst systems.

Hence an improved methodology incorporating entrance effect has been developed to predict maldistributed flow in auto-catalyst monoliths under steady flow conditions.

7.7 Recommendations for future work

Based on the work undertaken in this study, it is recommended that the following areas need further investigation:

7.7.1 One-dimensional oblique angle flow rig

At high angles of attack, there was a flattening of the entrance effect profile indicating the possibility of a critical angle at which there is no additional pressure loss due to oblique entrance. Due to rig limitations, the oblique angle flow measurements were not performed at angles greater than 80^0 as this would have required a monolith with larger diameter than is currently available. CFD simulations, however, were performed on an axisymmetric catalyst model incorporating the entrance effect and it was found that a fixed critical angle ($\alpha_{c,F}$) of 81^0 provided the best predictions. This has not been experimentally verified. In order to perform the oblique angle flow

measurements at high angles of attack would require design of a new nozzle with smaller exit diameter. This would permit the use of the available monolith in performing the experiments at high angles of attack.

7.7.2 PIV studies

7.7.2.1 Steady flow studies

Experiments were performed on a 2-D diffuser using 2D PIV in order to avoid the optical distortion associated with conical diffusers for 3-D flows. Due to rig limitations the experiments were not performed at high flow rates. Further experiments for flow in a 2-D diffuser using PIV should be performed at high flow rates. The present PIV system can also perform 3-D PIV studies using stereoscopic PIV technique. Hence stereoscopic PIV technique could be used to investigate the flow in an axisymmetric diffuser upstream of the substrate, provided that the conical diffuser had thin and optically clear walls.

7.7.2.2 Pulsating flow studies

Experiments could also be performed to investigate the flow in an axisymmetric diffuser using stereoscopic PIV under pulsating flow conditions. The effect of different pulse shapes and frequency on the flow in the diffuser and flow maldistribution across the substrate could be investigated.

7.7.3 CFD studies

In order to improve the predictions in the diffuser, improved turbulence models are needed. CFD studies using LES turbulence models could be investigated to improve predictions for flows in diffusers.

References

1. Abu-Khiran, E., Douglas, R., McCullough, G., Pressure Loss Characteristics in Catalytic Converters, SAE 2003-32-0061, JSAE 20034361, 2003
2. Adrian, R.J., Particle imaging techniques for experimental fluid dynamics, Annual review of Fluid Mechanics 23, 1991 pp261-303.
3. Auckenthaler, T., S., Modelling and Control of Three-Way Catalytic Converters, Ph.D Thesis, Swiss Federal Institute of Technology, Zurich, 2005
4. Bell, J.H., and Mehta, R.D., Boundary-Layer Predictions for small Low-Speed Contractions, AIAA Journal Volume 27, Number 3 Pages 372-374 1989
5. Bella,G., Rocco, V. and Maggiore, M., A study of inlet flow distortion effects on automotive catalytic converters, ASME Journal of Eng. For Gas Turbines and Power, Vol. 113, pp419-426, 1991
6. Benjamin, S.F., Clarkson, R. J., Haimad, N., Girgis, N.S., An Experimental and Predictive study of the Flow field in Axisymmetric Automotive Exhaust Catalyst Systems, SAE Paper 961208, 1996
7. Benjamin, S.F., Roberts, C.A and Woliin, J., A study of the effect of Flow Pulsations on the Flow Distribution within Ceramic Contoured Catalyst Substrates, SAE 2001-01-1996, SAE Spring Fuels and Lubricants conference in Orlando, Florida, USA, 2001 a
8. Benjamin, S.F., Haimad, N., Roberts, C.A. and Wollin J., Modelling the Flow Distribution through Automotive Catalytic Converters, Proc. Instn. Mech. Engrs. Vol. 215 Part C, 2001 b
9. Berkman, M. E. and Katari, A.,Transient CFD: How Valuable is it for Catalyst design?, SAE Paper 2002-01-0064, 2002
10. Buchave P. Particle Image Velocimetry-Status and Trends, Exp,1992, In Thermal and Fluid Science 5, pp 586-604.
11. Burch,S.D., Potter,T.F., Keyser,M.A., Brady, M.J. and Micahels,K.F., Reducing cold-start emissions by Catalytic Converter Thermal Management, SAE Paper 950409, 1995
12. Clarkson, R. J., A Theoretical and Experimetnal Study of Automotive Catalytic Converters, Ph.D thesis, Coventry University, 1995
13. Depcik, C. and Assanis, D., One-dimensional automotive catalyst modelling, Progress in Energy and Combustion Science 31, 308-369,2005

14. Dryden, H.L. (1936), Air flow in the boundary layer near a plate. NACA TR 562
15. ESDU Item Number 76027,Introduction to design and performance data for diffusers
16. Grant, I., 1997. Particle image velocimetry: a review, Proc. Instn. Mech. Engrs. Vol 211, Part C, pp.55-76.
17. Gilbert,R.A.D., Evaluation of FFT based cross-correlation algorithms for particle image Velocimetry,MSc Thesis, University of Waterloo,2002.
18. Guojiang., W. and Song.,T., CFD simulation of the effect of upstream flow distribution on the light-off performance of a catalytic converter, Journal of Energy Conversion and Management 46 2010-2031, 2005
19. Haimad, N., A Theoretical and Experimental Investigation of the Flow Performance of Automotive Catalytic Converters, Ph.D thesis, Coventry University, 1997
20. Heywood, J. B., Internal Combustion Engine Fundamentals, Chap. 11. 567-667, McGraw-Hill, ISBN 0071004998, 1998
21. Holdo, A.E. & Simpson, A.F., Simulation of high-aspect-ratio jets, 2002, International journal for numerical methods in fluids, 39:343-359
22. Huang, H., Fiedler, H and Wang, J., Limitation and improvement of PIV, part II: particle image distortion-a novel technique, Expeiments in Fluids 15, 267-273, 1993
23. Howitt.J.S. and Sekella,T.C., Flow Effects in Monolithic Honeycomb Automotive Catalytic Converters, SAE Paper 740244,1974
24. Iaccarino, G., Predictions of a turbulent separated flow using commercial CFD codes, Journal of Fluids Engineering, ASME, 2001, Vol.123, 819-828.
25. Kaiser, F. W. and Pelters, S., Comparison of metal-supported catalysts with different cell geometries, SAE Paper 910837, 1991
26. Kaltenbach, H.-J., Fatica, M., Mittal, R., Lund, T. S., & Moin, P. ,Study of flow in a planar asymmetric diffuser using large eddy simulation, Journal of fluid mechanics, 1999,390,151-185.
27. Keane, R.D. and Adrian, R. J., Optimization of particle image velocimeters. Part 1: Double pulsed systems, Meas. Sci. Technol. 1, 1990, 1202-1215

28. Kikuchi,S., Hatcho,S., Okayama,T., Inose,S., Ikeshima,K.,High cell density and Thin Wall substrate for higher conversion ratio catalyst, SAE paper 1999-01-0268,1999
29. Kim, J.Y., Lai, M.C., Li, P. and Chu, G., Modeling diffuser-monolith flows and its implications to automotive catalyst converter design, SAE Paper 921093, 1992
30. Kim. J. Y. and Son. S., Improving Flow efficiency of a Catalytic Converter Using the Concept of Radially Variable Cell Density- Part I, SAE Paper 1999-01-0769, 1999
31. Kuchemann, D. and Weber, J., Aerodynamics of Propulsion, McGraw-Hill, New York, 1953
32. Lai, M.C., Kim, J. Y., Cheng, C.Y., Li, P., Chu, G. and Pakko, J.D., Three-dimensional simulations of automotive catalytic converter internal flow, SAE Paper 910200, 1991
33. Lemme, S.J., Givens, W.R., Flow through catalytic converters – An analytical and experimental treatment, SAE Paper 740243,1974
34. Liu, Z., Pulsating flow maldistribution in automotive exhaust catalysts-Numerical modelling and experimental correlation, Ph.D thesis, Coventry University, 2003
35. Lomas, C.G., Fundamentals of Hot wire anemometry, Cambridge University Press 1986
36. Marsters, G.F., Spanwise velocity distributions in jets from rectangular slots, AIAA 1981, 19 (2), 148-152.
37. Martin, A. P., Will, N. S., Bordet, A., Cornet, P., Gondoin, C., Mouton, X., Effect of Flow Distribution on Emissions Performance of Catalytic Converters, SAE Paper 980936, 1998
38. Mehta, R.D. and Bradshaw, P., Design rules for small low speed wind tunnels, The Aeronautical Journal of the Royal Aeronautical Society, November 1979, technical notes
39. Melling, A., Tracer particles and seeding for particle image Velocimetry, Meas. Sci. Technology 8, 1997, 1406-1416.
40. Monroe.D.R. and Krueger H.M., The effect of Pt and Rh loading on the performance of Three-Way Automotive Catalysts, SAE-872130, 1987

41. Morel, T., Comprehensive design of Axisymmetric Wind Tunnel Contractions, Journal of Fluids Engineering, ASME, Pages 225-233, 1975
42. Morel, T., Design of Two-Dimensional Wind Tunnel Contractions, Journal of Fluids Engineering, ASME, Pages 371-378, 1977
43. Prasad, A.K., Adrian, R.J., Landreth, C.C., Offutt, P.W., Effect of resolution on the speed and accuracy of particle image Velocimetry interrogation, Experiment in Fluids, 1992, 13 105-116
44. Pannone,G.M. and Mueller, J.D., A comparison of conversion efficiency and flow restriction performance of ceramic and metallic catalyst substrates, SAE Paper 2001-01-0926, 2001
45. Perny,D.,Gangnet,M., and Coueignoux,Ph., Perspective mapping of planar textures, Computer Graphics, Vol.16-1,1982.
46. Persoons, T., Experimental Flow Dynamics In Automotive Exhaust Systems With Close-Coupled Catalyst, Ph.D Thesis Katholieke Universiteit Leuven, 2006.
47. Pope, S.B., Turbulent Flows, Chapter 5, Pg: 134, Cambridge University Press, ISBN: 0521591252, 2000
48. Quinn, W.R., Passive near-field mixing enhancement in rectangular jet flows, AIAA 1991, 29(4), 515-519
49. Quinn, W.R., Development of a large-aspect-ratio rectangular turbulent free jet, AIAA 1994, 32(3), 547-554.
50. Quinn, W.R., Upstream nozzle shaping effects on near field flow in round turbulent free jets, European journal of mecahncis B/fluids 25, 2006,27-301
51. Raffel.M., Willert.C., Kompenhans.J., Particle Image Velocimetry, A practical guide, 1998, Springer-Verlag, Berlin
52. Rockwell, D.O., Vortex strectching due to shear layer instability, Journal of fluid engineering, Transactions of ASME, March 1977, pp.240-244.
53. Schetz, J.A. and Fuhs, A.E., Fundamentals of Fluid Mechanics, Chapter 5,519-523,John Wiley and Sons, ISBN 0-471-34856-2,1999
54. Schmidtt,J.,Waltner,A., Loose,G., Hirschmann,A., Wirth,A., Mueller,W., Van Den Tillart,J.A.A., Mussmann,L., Lindner,D., Gieshoff,J., Umehara,K., Makino,M., Biehn,K.P., Kunz,A.,The Impact of High Cell density ceramic substrates and washcoat properties on the catalytic activity of three way catalysts, SAE Paper 1999-01-0272,1999

55. Shah, R.K., A correlation for laminar hydrodynamic entry length solutions for circular and noncircular ducts, Transactions of the ASME Journal of Fluids Engineering, June 1978, Vol. 100, 1978
56. Shuai, S. J., Wang, J.X., Dong, Q. L. and Zhuang, R.J., PIV Measurement and Numerical Simulation of Flows in Automotive Catalytic Converters, SAE Paper 2001-01-3494, 2001.
57. Sfeir, A.A., Investigation of three-dimensional turbulent rectangular jets, AIAA 1979, 17(10), 1055-1060.
58. Sforza, P.M., Steiger, M.H and Trentacoste, Studies on three-dimensional viscous jets, AIAA 1965, 4 (5), 800-806.
59. CD-Adapco, STAR-CD V 3.26 Manual, 2004.
60. Trentacoste N, Sforza P. Further experimental results for three dimensional jets, AIAA 1967; 5(5):112–122.
61. TSI Insight 3G Manual
62. Umehara, K.,Yamada,T., Hijakata,T., Ichikawa.,Y, and Katsube, F., Advanced Ceramic Substrate: Catalytic Performance Improvement by high geometric surface area and low heat capacity, SAE paper 971029, 1997
63. Van der Hegge Zijnen, B.G., Measurements of the velocity distribution in a plane turbulent jet of air, Applied Science Research Section A, Vol. 7, 1958, pp. 256-276.
64. Williamson, W.B., Stepien, H.K., Watkins, W.L.H., Gandhi, H.S., Poisoning of Platinum-Rhodium Automotive Three-way Catalysts, American Chemical Society Volume 13, Number 9, September 1979
65. Wendland, D.W. and Matthes, W.R., Visualisation of automotive catalytic converter internal flows, SAE Paper 861554, 1986
66. Wendland, D.W., Sorell, P.L. and Kreucher, J.E., Sources of monolith catalytic converter pressure loss, SAE Paper 912372, 1991
67. Wendland, D.W., Matthes, W.R. and Sorell, P.L., Effect of header truncation on monolith converter emission-control performance, SAE Paper 922340, 1992
68. Westerweel, J., Digital particle image velocimtery, theory and application, Ph.D thesis, Technische Universiteit Delft , Netherlands, 1993, ISBN 90-6275-881-9.

69. Will,N.S., Bennett, C.J., The use of CFD as an aid to catalytic converter design, ATA Proc. 4th International Conference Vol.1 387-393 (1994)
70. Wollin, J., Benjamin, S.F., A Study of the Flow Performance of Ceramic Contoured Substrates for Automotive Exhaust Catalyst Systems, SAE Paper 1999-01-3626, 1999
71. Wollin, J., A study of Pulsating Flow in Automotive Exhaust Catalyst Systems, Ph.D thesis, Coventry University, 2001
72. http://europa.eu.int/comm/enterprise/automotive/pagesbackground/pollutant_emission/stakeholder_consultation/euro_5_draft_reg.pdf. Date accessed:05-10-2005

Appendix: A

Error Calculations

Error Calculations

From Equation 2.18, the Entrance effect is:

$$P_{Obl} = (P_{s1} - P_{s2}) + \frac{1}{2}\rho(U_1^2 - U_2^2) - P_L$$

The Furness Controls digital manometer has an accuracy of ± 1% of the manometer reading and is used to measure $P_{s1}-P_{s2}$.

U_1 is measured using hot wire anemometry and from the calibration curve has an error of ± 1%

U_2 is calculated from Equation 2.17 and is related to U_1 and also has an error of ± 1%
For 100 mm monolith, the pressure drop due to monolith is given by
$P_L=2.1.573U_2^2+44.822U_2$ where U_2 is the velocity downstream of the substrate.

An error calculation for 30 degree angle of attack, 100 mm monolith at Re: 45900 is shown below

U_1=13.02 m/s (± 1%)
U_2=11.28 m/s (± 1%)
$P_{s1} - P_{s2}$=806 Pa (± 1%)

Substituting the value of U_2, We have
$P_L=2.1573U_2^2+44.8221U_2$
$P_L= (2.1573*(11.28)^2)$ (± 2 %) + (44.822*11.28) (± 1%)
P_L=812 ± 11 Pa

Substituting the values in Equation 2.18, we have
$P_{Obl} = 806(\pm 10) + 0.5 * 1.18 * ((12.86)^2 (\pm 2\%) - (11.28)^2 (\pm 2\%)) - 812 \pm 11$
P_{Obl}=19.30 (±24) Pa

Appendix: B
Number of images and repeatability

Number of images and repeatability

From the statistics point of view better accuracy is obtained if a large number of images are acquired and processed. The selection of the number of images is also dependent on the complexity of the field of view to be investigated, uniformity of the seeding and the quality of the vector obtained. It was decided to look into the velocity profiles obtained from different samples of the images. Three different sample sizes were chosen i.e., N=50,100,150 were selected. It was thought that if a large change in the flow profiles was observed then the number of images can be increased and flow profiles again compared. Also from the velocity profiles obtained it would be possible to see if the flow characteristics have been completely resolved.

The results (Figs. 1-5) showed that a sample size of 50 was adequate to achieve a high quality data. This was largely possible due to the high quality of seeding and a relatively simple flow field. For complex flow fields a general procedure is to use a higher number of images (N=500) in order to resolve the flow field. Hence a sample of 50 has been used for all the PIV measurements in this study.

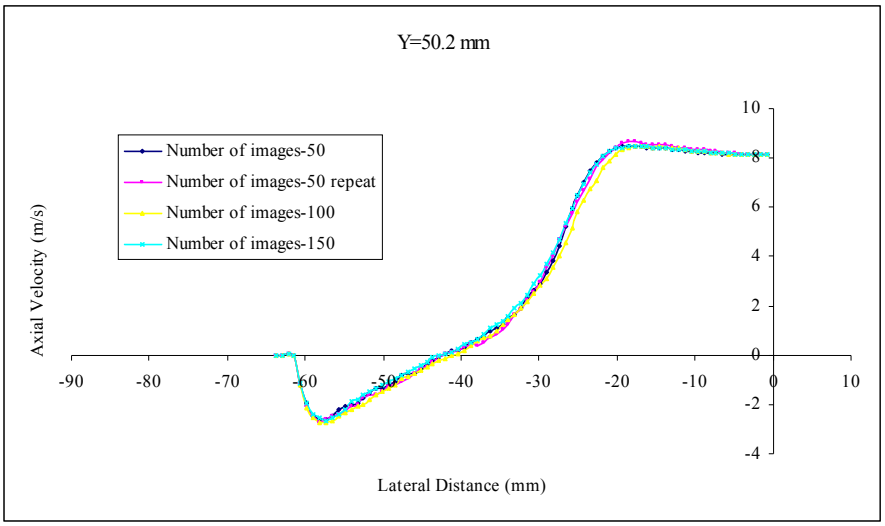

Figure 1: Comparison of axial velocity profiles for 100 mm monolith at Re: 46500 for various image samples

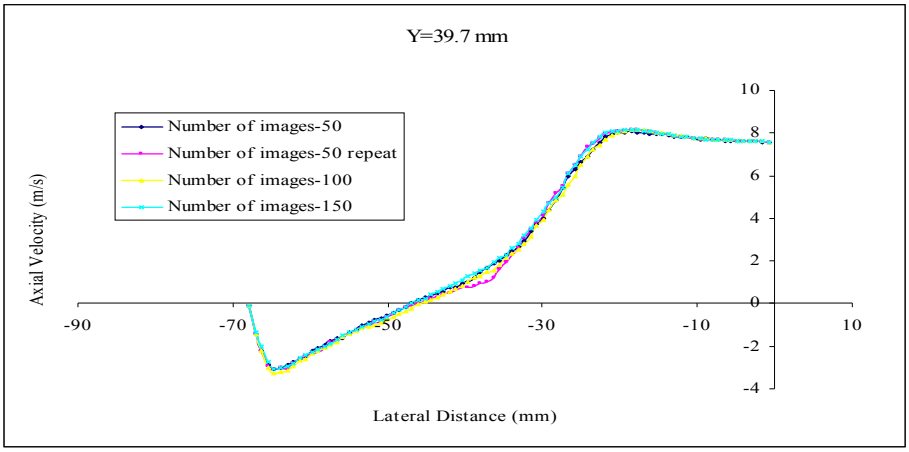

Figure 2: Comparison of axial velocity profiles for 100 mm monolith at Re: 46500 for various image samples

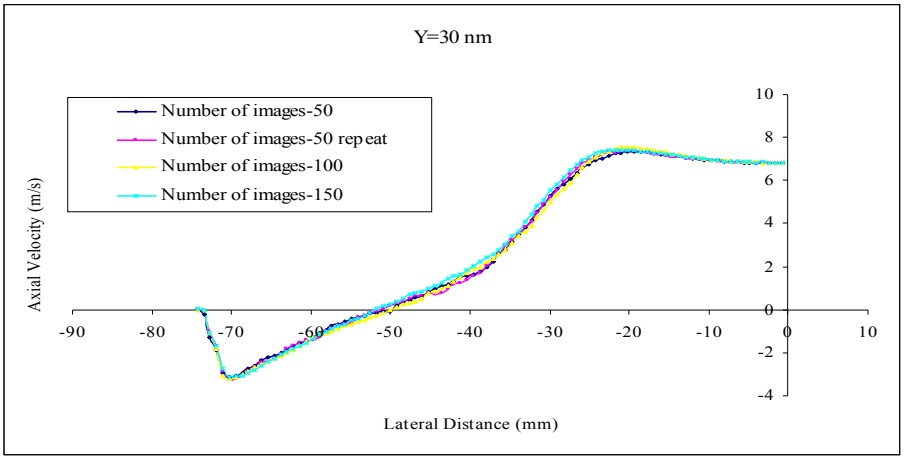

Figure 3: Comparison of axial velocity profiles for 100 mm monolith at Re: 46500 for various image samples

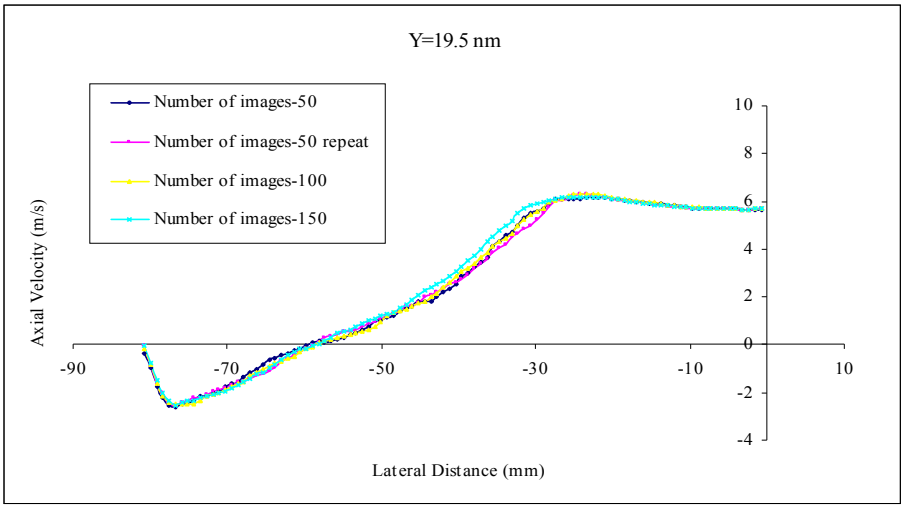

Figure 4: Comparison of axial velocity profiles for 100 mm monolith at Re: 46500 for various image samples

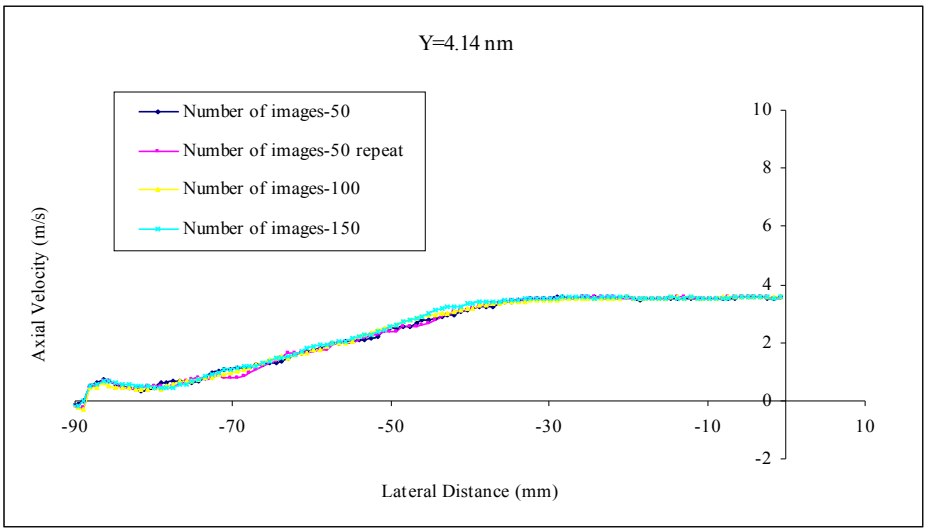

Figure 5: Comparison of axial velocity profiles for 100 mm monolith at Re: 46500 for various image samples

Appendix: C

Design of 2-D contracting nozzle using Morel's method

(Morel's original diagrams and graphs have been removed for copyright reasons)

2.1 Introduction

The contour shape for the 2-D nozzle was designed using Morels method (Morel 1977). A suitable contraction ratio (CR) of 4 was chosen at the start and the design criterion for the nozzle was to have 1% flow non-uniformity at the exit and no boundary layer separation. Figure 2.1 shows the parameters controlling the wall contour of the 2-D nozzle.

Fig 2.1 Wall contour constructed of two matched cubic arcs (Morel, 1977)

The non-uniformity was defined by Morel (1977) as

$$u_2 \equiv \frac{(V_w - U_f)_2}{U_{2,\infty}} \qquad 2.1$$

where V_w was the Wall velocity, U_f was the centreline velocity

$U_{2,\infty}$ was the velocity far downstream.

The wall velocity V_w is the velocity at the outer edge of the boundary layer from the wall and not the wall velocity at the wall. Hence V_w is not zero and is referred to as the wall velocity from now onwards.

Figure 2.2 Wall velocity distributions and the one-dimensional velocity distribution (Morel, 1975)

Some of the symbols used in this study are different to the ones shown in the design charts. The symbols X_i, L_c, V_w, U_f and H_1 corresponds to X, L, V, U_{av} and D_1 respectively in the above design chart respectively. Figure 2.2 shows the velocity along the nozzle centreline (U_f) increases gradually. But the wall velocity initially decreases as the flow anticipates the converging area and reaches a minimum downstream. The point of minimum wall velocity downstream of the nozzle inlet depends on the nozzle contour. The more abrupt the curvature, the further upstream this effect occurs. After reaching a minimum, the flow accelerates but at a faster rate than the centreline velocity. The wall velocity exceeds the centreline velocity at some point inside the nozzle and reaches a maximum just upstream of the nozzle exit. The wall velocity then decreases and is slightly higher than the centreline velocity (Morel, 1975).

Morel (Morel, 1977) showed that the two parameters of the flow required to design the cubic family of wall shapes are the two wall pressure coefficients at the point of maximum and minimum wall velocity. The pressure coefficients were defined as

$$C_{p_e} \equiv 1 - \left(\frac{U_{2,\infty}}{V_{w,e}}\right)^2 \qquad 2.2$$

$$C_{p_i} \equiv 1 - \left(\frac{V_i}{U_{1,\infty}}\right)^2 \qquad 2.3$$

where C_{p_e} was the pressure coefficient at the point of maximum velocity at the wall and the C_{p_i} was the pressure coefficient at the point of minimum velocity at the wall.

The choice of C_{p_i} was made using Stratford's separation criteria as described by Morel (1977). Nozzle length and wall shape were then found from design charts. Also the desired level of non-uniformity acceptable was chosen at the start of the design process.

2.2 Design of the contracting nozzle using Morel's method

The design of the 2-D Nozzle was based on the steps suggested by Morel (1997). The design procedure as described by Morel (1977) is an eight-step process.

Step 1: Selecting the CR

A CR=4 was chosen at the start as a higher CR would result in a large cross-section at the inlet to the nozzle. Keeping into consideration the maximum flow rates achievable on the rig a CR of 4 was found to be suitable. The contraction area ratio is given by

Contraction Area Ratio CR= $A_{inlet}/A_{exit}=H_3*b/H_4*b$
$CR=H_1/H_2$ where H_3 and H_4 were the inlet and exit heights respectively
We have H_4=55 mm (From the inlet of the diffuser) giving,

$$H_2 = \frac{H_4}{2} = 27.5\,\text{mm}$$

A CR=4 was selected for the two-dimensional contraction. We have inlet nozzle height H_3=220 mm

$$H_1 = \frac{H_3}{2} = 110 \text{ mm}$$

Therefore H_1=110 mm H_2=27.5 mm

Step 2: Selecting C_{Pi} & C_{Pe}

a) Selecting C_{Pe}

The main criterion at the exit of the nozzle was the flow non-uniformity. It was desired to have a flow non uniformity of less than 1%, so from eqn (2.1) we have

$$u_2 = 1\%$$

Morel (1977) found that the flow non-uniformity was a function of C_{Pe} and was related by the following equation:

$$C_{Pe} = 5.3 * u_2$$

$$C_{Pe} = 0.053$$

So the C_{Pe} value to be used should be less than 0.053 for 1% flow non-uniformity. Taking into account the manufacturing errors and having a safety margin

C_{Pe} =0.042 was selected.

b) Selecting C_{Pi}

To avoid boundary layer separation and using Stratford's boundary separation criteria, Morel (1977) found that the C_{pi} value should be less than 0.42. At the start of the design process a length to inlet height ratio of 1.25 was selected and in figure 2.3, the symbols L and X stands for L_c and X_i respectively.

Figure 2.3 shows the values of C_{Pi} and C_{Pe} for CR=4 and various L_c/H_1 ratios.

From fig 2.3, for CR=4, C_{Pe}=0.042, L_c/H_1=1.25, gives

C_{pi}=0.22

Figure 2.3 Pressure coefficients C_{pi} and C_{pe} for CR=4 (Morel, 1977)

Step 2: Reading F_i,F_e,G_i from C_{Pi} & C_{Pe} design charts

Four non-dimensional parameters were defined so that the three independent variables m (m=CR), L_c/H_1 and X_i can be grouped as in equation 2.4-2.7. The parameters were based on the assumption that the Cp's due to the wall curvature were related to some characteristic values of that curvature

$$F_i = \frac{m-1}{m} X_i^{-2} \left(\frac{L_c}{H_1}\right)^{-3} \quad 2.4$$

$$F_e = \frac{m-1}{m^3} (1-X_i)^{-2} \left(\frac{L_c}{H_1}\right)^{-3} \quad 2.5$$

$$Gi = \frac{m-1}{m} X_i^{-1} \left(\frac{L_c}{H_1}\right)^{-2} \quad 2.6$$

$$G_e = \frac{m-1}{m^2} (1-X_i)^{-1} \left(\frac{L_c}{H_1}\right)^{-2} \quad 2.7$$

$$m = \frac{H_1}{H_2}, X_i = \frac{x_m}{L_c}$$

The values of non-dimensional parameters F_i, F_e, for the given values of C_{Pi} and C_{Pe} were taken from the design chart fig 2.4 (Morel, 1977) and for G_i were obtained from figure 2.5 (Morel, 1977).

For C_{Pi}=0.22, fig 2.4 gives F_i=1.1
For C_{Pe}=0.042, fig 2.4 gives F_e=0.16

Figure 2.4 Dependence of C_{Pi} and C_{Pe} on the dimensionless parameters F_i and F_e (Morel, 1977), ordinate values in fig 2.4 represent C_{Pi} and C_{Pe}

For C_{Pi} =0.22, fig 2.5 gives G_i=0.8

Figure 2.5 Dependence of C_{Pi} on dimensionless parameter G_i (Morel, 1977)

Step 4: Calculating X_i

For $C_{Pi}>0.15$, X_i was calculated from the equation below (Morel 1977):

$$X_i^{1/2}(1-X_i)^{-2/3} = F_e^{1/3} * G_i^{-1/2} * m^{1/2} * (m-1)^{1/6} \qquad 2.8$$

After obtaining the product term on the right side of the above equation, the expression on the left hand side of Eqn 2.8 is solved graphically for X_i, by using the figure 2.6 in Morel (1975).

Figure 2.6 Graphical aid for evaluation of X_i from equation 2.10 (Morel, 1975)

The value obtained from figure 2.6 was

$$X_i=0.62$$

Step 5: Calculating the length of the contour

The length of the contour shape is calculated using the equation below (Morel 1977):

$$L_c=H_1*((m-1)/(X_i^2*F_i*m))^{1/2}$$

$$L_c=133 \text{ mm}$$

Step 6: Obtaining contour

After obtaining the length, the next step was to find the coordinates for the contour using the equations below (Morel 1977):

$$H=H_2+ ((H_1-H_2)*(1-x/L_c)^3*(1/ (1-X_i)^2)) \quad x/L_c>X_i \qquad 2.9$$

$$H=H_2+ ((H_1-H_2)*(1-(x^3/(X_i^2*L_c^3)))) \quad x/L_c<X_i \qquad 2.10$$

where x is the axial distance along the nozzle contour and H is the height of the nozzle contour at x.

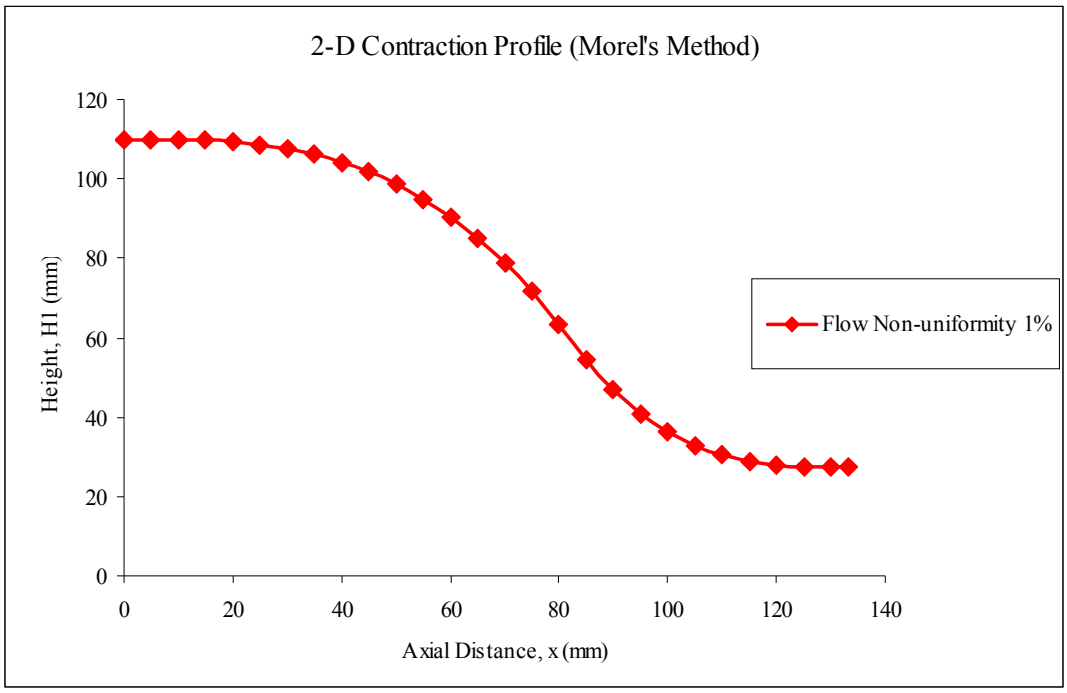

Fig 2.7 Wall shape contour of the 2-D contracting nozzle using Morel's method

The obtained contour is as shown in the figure 2.7.

Step 7: Distance of minimum and maximum velocity from the inlet and exit plane

Again using the design chart shown in fig 2.8 (Morel, 1977)

For CR=4 & $X_iL_c/H_1=0.731$

$$x_i/H_1=0.3$$

x_i=35.2 mm is the distance of the velocity minimum from the inlet plane.

Figure 2.8 Distance from the nozzle beginning to the wall pressure maximum (Morel, 1977)

Figure 2.9 Distance from the nozzle end to the wall pressure minimum (Morel, 1977)

From fig 2.9, for CR=4 & (1-Xi)* Lc/H_2=1.84

$$x_e/H_2=0.38$$

x_e=10.45 mm is the distance of velocity maximum from the exit plane.

Step 8: Total length of the nozzle

The total length of the nozzle as suggested by Morel (1975) is obtained by summing the settling chamber length for the inlet plus the length of contraction plus the settling chamber length of the exit section

Settling chamber length for the inlet=$0.5*H_1$=55 mm

Settling chamber length for the exit=$0.5*H_2$=13.75 mm

Total nozzle length $L_t=L_c+0.5*H_1*0.5*H_2$=202.93 mm

A mean aspect ratio of 4 used in the diffuser design process was used for the 2-D nozzle.

Appendix: D

Calculations for New-Wave, Solo PIV 120, Nd:YAG Laser System

Table of Contents

1. Laser specifications

The pulsed PIV Nd:YAG laser has the following specifications

λ=Wavelength=534 nm

λ=Pulse Width=5 ns

F=Frequency= 15Hz

Q=Energy per pulse =120 mJ

ϕ=Divergence =1-2 mrad

a=Initial beam diameter= $4.5 * 10^{-3}$m

f=focal length of the cylindrical lens=15 mm

α=Angle subtended by an apparent source as viewed at a point in space

α_{min}=Minimum angle subtended by a source=1.5 mrad

α_{max}=Maximum angle subtended by a source=100 mrad

P_p=Peak Power=Q/ t_p=$24*10^6$ W

P_{avg}=Average Power=P_o=Q*F=1.8 W

2. 10 seconds viewing case

2.1 Direct intrabeam viewing without cylindrical lens:

Maximum permissible exposure for ocular hazard calculations:

2.1.1 Single Pulse Assessment:

The exposure from any single-pulse shall not exceed the single-pulse MPE. Thus the radiant exposure for a time period of 5 ns is:

From table 6 in the BS:EN 60825-1:1994 for λ=534 nm and t_p=5ns

$H_{MPE}=5*10^{-3}*C_6$ J/m^2

For point source C_6=1 (From notes to table 1 to 4, page 39 BS:EN 60825-1:1994)

Therefore $H_{MPE}=5*10^{-3}*1=5*10^{-3}$ J/m^2

2.1.2 Average Exposure Assessment:

The average exposure for a pulse train of exposure duration T shall not exceed the MPE for a single pulse of exposure duration T.

The MPE for average exposure duration of 10 seconds

For t=10 seconds

From table 6 in the BS:EN 60825-1:1994

Since $\alpha \leq 1.5$ mrad and T_2=10 s

$H_{MPE}=18t^{0.75}\ C_6$

$H_{MPE}=1.01*10^2$ J/m^2

The number of pulses in exposure duration of 10 seconds is

N=F*t=15*10=150

Therefore $H_{MPE,avg}=1.01*10^2/150$

$H_{MPE,avg}=6.75*10^{-1}$ J/m^2

2.1.3 Multiple Pulse Assessment:

The criterion is the average exposure from pulses within a pulse train shall not exceed the MPE for a single pulse multiplied by a correction factor C_5.

The maximum exposure duration for which this requirement is applied is T_2 in the 400 nm to 1400 nm range
Assuming T_2=10 S for $\alpha \leq \alpha_{min}$

$H_{MPE,\ single}=5*10^{-3}$ J/m^2
$H_{MPE,train}=H_{MPE,\ single}*N^{-0.25}$
Number of pulses=N= (F *T_2)
N=150

$H_{MPE,train}=5*10^{-3}*0.2857$
$H_{MPE,train}=0.001429$ J/m^2

So the most restrictive limit is the $H_{MPE,train}=0.001429$ J/m^2
$E_{MPE,train}=H_{MPE,train}/t_p=2.86*10^5$ W/m^2

So the nominal hazard distance for direct intrabeam viewing without cylindrical lens is:
(As from equation 1 in section 6, page 26 of BS:EN 60825-1:1994)
$r_{NOHD}=1/\phi(\sqrt{((4*P_p)/(\pi*E_{MPE}))}-a)$
$r_{NOHD}=1/2.0*10^{-3}(\sqrt{((4*24*10^6)/(\pi*2.86*10^5))}-4.5*10^{-3})$
$r_{NOHD}=5.17$ km

So direct beam viewing is safe at a distance of 5.17 km

2.2 Direct beam viewing with cylindrical lens:

Assuming the beam can still be considered as an apparent point source, the MPE for direct ocular exposure are:

C_6=1 for point sources (From notes to table 1 to 4, page 39 BS:EN 60825-1:1994)

Therefore the restrictive H_{MPE} remains unchanged from the direct intrabeam viewing

H_{MPE}=0.0014285 J/m^2
E_{MPE}=2.86 *10^5 W/m^2

But the hazard distance for the beam with cylindrical lens is
(As from equation 4 from section 6, page 26 of BS:EN 60825-1:1994)
$r_{NOHD} = f/a\ (\sqrt{((4*P_p)/(\pi*E_{MPE}))}-f$
$r_{NOHD} =(15*10^{-3}/4.5*10^{-3})(\sqrt{((4*24*10^6)/(\pi*\ 2.86*10^5)))}-15*10^{-3}$
r_{NOHD} =34.5 m

So diameter of the beam at a distance of 34.5 m
(As from equation 3 from chapter 6)
$D_l= a*(f+ r_{NOHD}) / (f)$
D_l=10.04 m
So the beam height at a distance of 34.5 m is 10.04 m
Area of the beam with diameter of 10.04 m is 79.12 m^2
For a laser beam to have a rectangular image of equivalent area the distance the beam has to travel can be found by
By trial and error method
r_{NOHD}=362 m
The rectangular image dimensions are
Length=L=109 m
Width=W=0.729 m

2.3 Diffuse reflections of direct beam

The nominal hazard zone for diffuse reflections of direct beam without cylindrical lens is given by the formula:
(As from equation 6 in section 6, page 26 of BS:EN 60825-1:1994)

$r_{NHZ}=\sqrt{((\rho*P_p \cos\theta)/(\pi*E_{MPE}))}$

Assuming the spectral reflectance $\rho=1$ and the viewing angle $\theta=45^0$

The E_{MPE} in the above formula is for the direct beam viewing under small source conditions

$E_{MPE} =2.86*10^5$ W/m^2

$r_{NHZ} =\sqrt{((\rho*P_p \cos\theta)/(\pi* E_{MPE}))}$

$r_{NHZ} =\sqrt{((1* 24*10^6*\cos 45^0)/(\pi*2.86*10^5)}$

$r_{NHZ} =4.34$ m

Nominal hazard zones at different angles of viewing:

Spectral Reflectance	Angle of viewing at eye θ (degrees)	Cosθ	Irradiance E_{MPE} W/m^2	Peak Power P_p W	Nominal Hazard Zone r_{NHZ}(m)
1	0	1			5.167964407
1	15	0.9659			5.079086357
1	30	0.866	2.86E+05	2.40E+07	4.809262251
1	45	0.707			4.345394605
1	60	0.5			3.654302677

2.4 Diffuse reflections of the laser beam as expanded by the cylindrical lens

2.4.1 Area of the laser beam on the diffusing surface:

The diffusing surface is at a distance of 1000 mm from the focal length of the cylindrical lens.

The beam height and width on the diffusing surface is:

(As from equation 3 in chapter 6 of BS:EN 60825-1:1994)

$D_l = a*L/(f)$

$D_l = (0.0045*1)/0.015$

$D_l = 30.5$ cm

Beam Width on the diffusing surface is

$W = a + r\phi$ where r=1

$W = 0.0045 + (1*2*10^{-3})$

W=6.5 mm

So, the rectangular cross-section of the laser beam incident on the diffusing surface is

$A_s = D_l * W$

$A_s = 19.79\ cm^2$

We can assume it a laser beam of similar area with a circular cross-section diameter of

$A_s = \pi * d^2/4$

D=5.01 cm

So the equivalent diameter D=5.01 cm

At a distance of 1000 mm from the diffusing surface

The effective equivalent viewing angle for rectangular image

$\alpha = d/100$

$\alpha = 5.01/100$

$\alpha = 0.05$ rad

Since $\alpha<100$ mrad

$C_6=\alpha/\alpha min$

$C_6=33.5$

Maximum permissible exposure for diffused reflections:

2.4.2 Single Pulse assessment:

From table 6 in the BS:EN 60825-1:1994 for $\lambda=534$ nm and $t_p=5ns$

$H_{MPE}=5*10^{-3}*C_6$ J/m^2

$C_6=33.5$

Therefore $H_{MPE}=5*10^{-3}*33.5=0.1673$ J/m^2

2.4.3 Average Exposure Assessment:

The MPE for average exposure duration of 10 seconds

For t=10 seconds

Since $\alpha>1.5$ mrad and $T2=10*10[(\alpha-1.5mrad)/98.5]$

From table 6 in the BS:EN 60825-1:1994

$H_{MPE}=18t^{0.75}\ C_6$

$H_{MPE}=6.37*10^4$ J/m^2

The number of pulses in exposure duration of 10 seconds is

$N=f*t=15*100=150$

Therefore $H_{MPE,avg}=(6.37*10^4/150)$ W/m^2

$H_{MPE,avg}=4.25*10^2$ J/m^2

2.4.4 Multiple Pulse Assessment:

The criterion is the average exposure from pulses within a pulse train shall not exceed the MPE for a single pulse multiplied by a correction factor C_5.

The maximum exposure duration for which this requirement is applied is T_2 in the 400 nm to 1400 nm range

$T_2=10*10[(\alpha-1.5mrad)/98.5]$ for $\alpha>\alpha_{min}$

$T_2=10.011$ seconds

$H_{MPE,\ single}=5*10^{-3}$ J/m^2

$H_{MPE,train}=H_{MPE,\ single}*N^{-0.25}$

Number of pulses=N=(F *T2)

N=150

$H_{MPE,train}=5*10^{-3}*0.2856*C6$

$H_{MPE,train}=0.0478$ J/m2

So the most restrictive limit is the $H_{MPE,train}=0.0478$ J/m^2

$E_{MPE,train}=H_{MPE,train}/tp=9.56*10^6$W/m^2

2.4.5 Actual exposure from the diffusing surface:

Irradiance E_s on the diffusing surface with peak power of laser and cross-sectional area A_s

(As from equation 8 in chapter 6 of BS:EN 60825-1:1994)

$E_s=P_p/A_s=24*10^6/0.0019$

$E_s=1.21*10^{10}$ W/m^2

By assuming a lambertian surface, Radiance L of a diffuse reflection is given by

(As from equation 9 in chapter 6)

$L=(\rho*P_p)/(A*\pi)$

Assuming a spectral reflectance of 1 for the diffusing surface

$L=1*24*10^7/(0.0019*3.142)$

$L=385.926*10^7$ W/m^2-sr

The irradiance at the eye for a diffused reflection with a radiance L is given by
(As from equation 10 in chapter 6 of BS:EN 60825-1:1994)
E_{eye}= L*Area of the diffused surface*Cosθ/r^2

Irradiance for exposure duration of 10 seconds at a distance of 1m from the diffuser and at an angle of viewing of 45^0 is given by

E_{eye}= L*Area of the diffused surface*Cosθ/r^2
E_{eye}=385.926*10^7 *0.0019*0.707/ (1*1)
E_{eye}=5.184*10^6 W/m^2

But the E_{MPE}=9.56*10^6 W/m^2
So, the diffused reflections are safe for viewing.

2.4.6 Nominal Hazard Zone for diffused reflections with cylindrical lens:
So the nominal hazard zone for diffused reflections with cylindrical lens is given by
(As from equation 10 in chapter 6 of BS:EN 60825-1:1994)
r_{NHD}= √(L*Area of the diffused surface*Cosθ)/ E_{MPE}
r_{NHD}=√(385.926*10^7 *0.0019*0.707/9.56*10^6)
r_{NHD} =73.63 cm
So at a zone of around 73.63 cm, safe viewing conditions exist.

2.4.6 Nominal hazard zones at different angles of viewing:

Area of the image m^2	Angle of viewing at eye θ (degrees)	Cosθ	Irradiance E_{MPE} (W/m^2)	Radiance L (W/m^2-sr)	r_{NHZ} (m)
0.0019	0	1	9.56E+06	3.86E+09	0.875874
0.0019	15	0.9659	9.56E+06	3.86E+09	0.860811
0.0019	30	0.866	9.56E+06	3.86E+09	0.81508
0.0019	45	0.707	9.56E+06	3.86E+09	0.736463
0.0019	60	0.5	9.56E+06	3.86E+09	0.619336

2.5 Summary for 10 seconds viewing conditions:

r_{NOHD} (Without cylindrical lens) m	r_{NOHD} (With cylindrical lens) m	r_{NHZ} (direct diffused reflections) m	r_{NHZ} (diffused reflections with cylindrical lens) m
5170	362	4.34	0.736

3. 0.25 seconds viewing case

3.1 Direct intrabeam viewing without cylindrical lens

Maximum permissible exposure for ocular hazard calculations:

3.1.1 Single Pulse Assessment:

From 2.1.1 $H_{MPE} = 5*10^{-3}*1 = 5*10^{-3}$ J/m^2

$E_{MPE} = 1*10^{6}$ J/m^2

3.1.2 Average Exposure Aassessment:

The MPE for average exposure duration of 0.25 seconds

Since $\alpha \leq 1.5$ mrad and $T_2 = 0.25$ s

$H_{MPE} = 18t^{0.75}$ C6

$H_{MPE} = 6.36$ J/m^2

The number of pulses in exposure duration of 0.25 seconds is

$N = f*t = 15*0.25 = 3.7$

Therefore $H_{MPE,avg} = 6.36/3.75$

$H_{MPE,avg} = 1.7$ J/m^2

3.1.3 Multiple Pulses Assessment:

The maximum exposure duration for which this requirement is applied is T_2 in the 400 nm to 1400 nm range

Assuming $T_2 = 0.25$ s for $\alpha \leq \alpha_{min}$

$H_{MPE,\ single} = 5*10^{-3}$ J/m^2

$H_{MPE,train} = H_{MPE,single}*N^{-0.25}$

Number of pulses $= N = (F*T_2)^{-0.25}$

$N = 0.7186$

$H_{MPE,train} = 5*10^{-3}*0.7186$

$H_{MPE,train}$ =0.0035 J/m^2

So the most restrictive limit is the $H_{MPE,train}$ =0.0035 J/m^2

$E_{MPE,train}=H_{MPE}/t_p=7.19*10^5$ W/m^2

So the nominal hazard distance for direct intrabeam viewing without cylindrical lens is:

(As from equation 1 in section 6, page 26 of BS:EN 60825-1:1994)

$r_{NOHD}=1/\phi(\sqrt{((4*Pp)/(\pi*E_{MPE}))}-a)$

$r_{NOHD} =1/2.0*10^{-3}(\sqrt{((4*24*10^6)/(\pi*\ 7.19*10^5))}-\ 4.5\ *10^{-3})$

r_{NOHD} =3.26 km

So direct beam viewing is safe at a distance of 3.26 km

3.2 Direct beam viewing with cylindrical lens

Assuming the beam can still be considered as an apparent point source, the MPE for direct ocular exposure are:

C_6=1 for point sources (From notes to table 1 to 4, page 39 BS:EN 60825-1:1994)
Therefore the restrictive H_{MPE} remains unchanged from the direct intrabeam viewing

H_{MPE}=0.003593 J/m^2
E_{MPE}=7.19 *10^5 W/m^2

But the hazard distance for the beam with cylindrical lens is
(As from equation 4 from section 6, page 26 of BS:EN 60825-1:1994)
$r_{NOHD} = (f/a (\sqrt{((4*Pp)/(\pi*E_{MPE}))}-f$
$r_{NOHD} =(15*10^{-03}/4.5*10^{-3})(\sqrt{((4*24*10^6)/(\pi* 7.19*10^5))}-15*10^{-3}$

r_{NOHD} =21.7 m

So diameter of the beam at a distance of 21.7 m
(As from equation 3 from chapter 6)
$D_l= a*(f+ r_{NOHD}) / (f)$
D_l=6.51 m
So the beam height at a distance of 34.5 m is 6.51 m
Area of the beam with diameter of 6.51 m is 33.28 m^2
For a laser beam to have a rectangular image of equivalent area the distance the beam has to travel can be found by
By trial and error method
r_{NOHD}=234 m
The rectangular image dimensions are
Length=L=70.2 m
Width=W=0.472 m

3.3 Diffuse reflections of the direct beam

The nominal hazard zone for diffuse reflections of direct beam without cylindrical lens is given by the formula:
(As from equation 6 in section 6, page 26 of BS:EN 60825-1:1994)

$r_{NHZ}=\sqrt{((\rho * P_p \cos\theta)/(\pi * E_{MPE}))}$

Assuming the spectral reflectance $\rho=1$ and the viewing angle $\theta=45^0$

The E_{MPE} in the above formula is for the direct beam viewing under small source conditions

$E_{MPE} = 7.19*10^5$ W/m^2

$r_{NHZ} = \sqrt{((\rho * P_p \cos\theta)/(\pi * E_{MPE}))}$

$r_{NHZ} = \sqrt{((1 * 24*10^6 * \cos 45^0)/(\pi * 7.19*10^5))}$

$r_{NHZ} = 2.74$ m

Nominal hazard zones at different angles of viewing:

Spectral Reflectance	Angle of viewing at eye θ (degrees)	Cosθ	Irradiance E_{MPE} W/m^2	Peak Power P_p W	Nominal Hazard Zone r_{NHZ}(m)
1	0	1			3.259403183
1	15	0.9659			3.203348346
1	30	0.866	7.19E+05	2.40E+07	3.033171952
1	45	0.707			2.740613497
1	60	0.5			2.304746093

3.4 Diffuse reflections of the laser beam as expanded by the cylindrical lens

3.4.1 Area of the laser beam on the diffusing surface:

From section 2.4.1

A_s= Rectangular cross sectional area=19.79 cm^2

D_l=Beam Height=30.5 cm

W=Beam Width=6.5 mm

D=Equivalent circular diameter=5.01 cm

α=Effective equivalent angle for rectangular image=0.05 rad

C_6=33.5

Maximum permissible exposure for diffused reflections:

3.4.2 Single Pulse Assessment:

From section 2.4.2:

H_{MPE}=0.1673 J/m^2

3.4.3 Average Exposure Assessment:

The MPE for average exposure duration of 0.25 seconds

For t=0.25 seconds

Since α>1.5 mrad and T_2=0.25 seconds

From table 6 in the BS:EN 60825-1:1994

$H_{MPE} = 18t^{0.75}$ C6

The number of pulses in exposure duration of 0.25 seconds is

N=F*t=15*0.25=3.75

Therefore $H_{MPE,avg} = 2.13*10^2/3.7$ W/m^2

$H_{MPE,avg}$ =5.68*10 J/m^2

3.4.4 Multiple Pulse Assessment:

The maximum exposure duration for which this requirement is applied is T_2 in the 400 nm to 1400 nm range

T_2=0.25 s

$H_{MPE, single}$ =5*10^{-3}* C_6 J/m^2

From the BS:EN 60825-1:1994

$H_{MPE,train}$ =$H_{MPE,single}$*$N^{-0.25}$

Number of pulses=N= (F *T_2)

$H_{MPE,train}$ =5*10^{-3}*0.7186*C_6

$H_{MPE,train}$ =1.2 *10^{-1} J/m^2

So the most restrictive limit is the $H_{MPE,train}$ =0.12 J/m^2

$E_{MPE,train}$ = $H_{MPE,train}$ /tp=2.4*10^7 W/m^2

3.4.5 Actual exposure from the diffusing surface:

From section 2.4.5 we have

E_s=Irradiance on the diffusing surface=1.21*10^{10} W/m^2

L=Radiance of the diffusing surface=385.926*10^7 W/m^2-sr

E_{eye}= Irradiance at the eye at a distance of 1metre=5.184*10^6 J/m^2

But the E_{MPE}=2.4*10^7 W/m^2

So the diffused reflections are safe to view.

3.4.6 Nominal Hazard Zone for diffused reflections with cylindrical lens:

So the nominal hazard zone for diffused reflections with cylindrical lens is given by (As from equation 10 in chapter 6)

r_{NHD}= √(L*Area of the diffused surface*Cosθ/ E_{MPE})

r_{NHD}=√(385.926*10^7 *0.0019*0.707/2.4*10^7)

r_{NHD} =46.48 cm

So at a zone of around 46.48 cm the safe viewing conditions exists.

3.4.7 Nominal hazard zones at different angles of viewing

Area of the image m^2	Angle of viewing at eye θ (degrees)	Cosθ	Irradiance E_{MPE} (W/m^2)	Radiance L (W/m^2-sr)	r_{NHZ} (m)
0.0019	0	1	2.40E+07	3.86E+09	0.552796
0.0019	15	0.9659	2.40E+07	3.86E+09	0.543289
0.0019	30	0.866	2.40E+07	3.86E+09	0.514427
0.0019	45	0.707	2.40E+07	3.86E+09	0.464809
0.0019	60	0.5	2.40E+07	3.86E+09	0.390886

3.5 Summary for 0.25 seconds viewing conditions:

r_{NOHD} (Without cylindrical lens) m	r_{NOHD} (With cylindrical lens) m	r_{NHZ} (direct diffused reflections) m	r_{NHZ} (diffused reflections with cylindrical lens) m
3260	234	2.74	0.4648

4. 100 seconds viewing case

4.1 Direct intrabeam viewing without cylindrical lens

Maximum permissible exposure for ocular hazard calculations:

4.1.1 Single Pulse Assessment:

From 2.1.1 $H_{MPE} = 5*10^{-3}*1 = 5*10^{-3}$ J/m^2

$E_{MPE} = 1*10^{6}$ J/m^2

4.1.2 Average Exposure Assessment:

The MPE for average exposure duration of 100 seconds

For t=100 seconds

Since $\alpha \leq 1.5$ mrad and $T_2 = 10$ s

For an exposure duration between 10 s and $3*10^4$ s, the appropriate MPE is given in table 6 BS:EN 60825-1:1994 as one of the three possibilities depending on the exposure duration t, relative to the breakpoint T_2 and for $t > T_2$ on the value of α:

$H_{MPE} = 18t^{0.75}C_6$ J/m^2

$E_{MPE} = 18t^{-0.25}C_6$ W/m^2

Or for $t > T_2$

$E_{MPE} = 10$ W/m^2

Thus, for this problem with an exposure duration of $t > T_2$ the MPE is constant and independent of exposure duration

The number of pulses in exposure duration of 100 seconds is

$N = f*t = 15*100 = 1500$

Therefore $E_{MPE,avg} = 10/1500$

$E_{MPE,avg} = 6.67 *10^{-3}$ W/m^2

4.1.3 Multiple Pulses assessment

The maximum exposure duration for which this requirement is applied is T_2 in the 400 nm to 1400 nm range

T_2=10 s for $\alpha \leq \alpha_{min}$

$H_{MPE,\ single}$=5*10-3 J/m^2

$H_{MPE,train} = H_{MPE,single} * N^{-0.25}$

Number of pulses=$N=(F * T_2)^{-0.25}$

$H_{MPE,train}=5*10^{-3}*0.2857$

$H_{MPE,train}$ =0.001429 J/m^2

$E_{MPE,train}=2.86*10^5$ W/m^2

So the most restrictive limit is the E_{MPE},avg =6.67 *10^{-3} W/m^2

So the nominal hazard distance for direct intrabeam viewing without cylindrical lens is:

(As from equation 2 in section 6, page 26 of BS:EN 60825-1:1994)

$r_{NOHD}=1/\phi(\sqrt{((4*Po)/(\pi*E_{MPE}))}-a)$

r_{NOHD} =1/2.0*10^{-3}($\sqrt{((4*1.8)/(\pi*$ 6.67*10^{-3}))- 4.5 *10^{-3})

r_{NOHD} =9.27 km

4.2 Direct beam viewing with cylindrical lens

Assuming the beam can still be considered as an apparent point source, the MPE for direct ocular exposure are:

C_6=1 for point sources (From notes to table 1 to 4, page 39 of BS:EN 60825-1:1994)
Therefore the restrictive H_{MPE} remains unchanged from the direct intrabeam viewing

$E_{MPE}=6.67*10^{-3}$ W/m^2

But the hazard distance for the beam with cylindrical lens is
(As from equation 5 in section 6, page 26 of BS:EN 60825-1:1994)

$r_{NOHD} = (f/a\ (\sqrt{((4*P_o)/(\pi*E_{MPE}))}-f$
$r_{NOHD} =(15*10^{-03}/4.5*10^{-3})(\sqrt{((4*1.8)/(\pi*\ 6.67*10^{-3}))}-15*10^{-3}$

r_{NOHD} =61.12 m

So diameter of the beam at a distance of 21.7 m
(As from equation 3 in chapter 6)
$D_l= a*(f+ r_{NOHD}) / (f)$
D_l=18.4 m
So the beam height at a distance of 61.12 m is 18.4 m
Area of the beam with diameter of 18.4 m is 265.93 m^2
For a laser beam to have a rectangular image of equivalent area the distance the beam has to travel can be found by
By trial and error method
r_{NOHD}=664 m
The rectangular image dimensions are
Length=L=199 m
Width=W=1.33 m

4.3 Diffuse reflections of the direct beam

The nominal hazard zone for diffuse reflections of direct beam without cylindrical lens is given by the formula:
(As from equation 7 in section 6, page 26 of BS:EN 60825-1:1994)

$r_{NHZ}=\sqrt{((\rho*P_o \cos\theta)/(\pi*E_{MPE}))}$

Assuming the spectral reflectance $\rho=1$ and the viewing angle $\theta=45^0$

The E_{MPE} in the above formula is for the direct beam viewing under small source conditions

$E_{MPE} =6.67*10^{-3}$ W/m^2

$r_{NHZ} =\sqrt{((\rho*P_o \cos\theta)/(\pi* E_{MPE}))}$

$r_{NHZ} =\sqrt{((1* 24*10^6*\cos 45^0)/(\pi*7.19*10^5)}$

$r_{NHZ} =7.79$ m

Nominal hazard zones at different angles of viewing:

Spectral Reflectance	Angle of viewing at eye θ (degrees)	Cosθ	Irradiance E_{MPE} W/m^2	Peak Power P_o W	Nominal Hazard Zone r_{NHZ}(m)
1	0	1			9.264
1	15	0.9659			9.11
1	30	0.866	6.67E-03	1.8	8.62
1	45	0.707			7.79
1	60	0.5			6.55

4.4 Diffuse reflections of the laser beam as expanded by the cylindrical lens

4.4.1 Area of the laser beam on the diffusing surface:

From section 2.4.1

A_s= Rectangular cross sectional area=19.79 cm^2

D_l=Beam Height=30.5 cm

W=Beam Width=6.5 mm

D=Equivalent circular diameter=5.01 cm

α=Effective equivalent angle for rectangular image=0.05 rad

C_6=33.5

Maximum permissible exposure for diffused reflections:

4.4.2 Single Pulse Assessment:

From section 2.4.2:

H_{MPE}=0.1673 J/m^2

4.4.3 Average Exposure Assessment:

For t=100 seconds

Since α>1.5 mrad, T_2=100 seconds

From table 6 in the BS:EN 60825-1:1994

$E_{MPE} = 18T_2^{-0.25}C6$

E_{MPE} =339 W/m^2

The number of pulses in exposure duration of 100 seconds is

N=F*t=15*100=1500

$E_{MPE,avg}$ =0.226 W/m^2

4.4.4 Multiple Pulse Assessment:

The maximum exposure duration for which this requirement is applied is T_2 in the 400 nm to 1400 nm range

T_2=100 s

$H_{MPE,\ single}$ =5*10^{-3}* C_6 J/m^2
From the BS:EN 60825-1:1994

$H_{MPE,train}$ =Hmpe,single*$N^{-0.25}$
Number of pulses=N=(F *T_2)
$H_{MPE,train}$ =5*10^{-3}*0.2857*C_6
$H_{MPE,train}$ =1.2 *10^{-1} J/m^2

So the most restrictive limit is the $E_{MPE,avg}$ =0.226 W/m^2

4.4.5 Actual exposure from the diffusing surface:

Irradiance E_s on the diffusing surface with average power of laser and cross-sectional area A_s:
(As from equation 11 in section 6, page 26 of BS:EN 60825-1:1994)

E_s= Es=P_o/A_s=1.8/0.0019
E_s=9.09*10^2 W/m^2

Radiance L from the diffuse surface
(As from equation 12 in section 6, page 26 of BS:EN 60825-1:1994)
L=(ρ* P_o)/(A*π)
L=1*1.8/(0.0019*3.142)
L=289.44 W/m^2-sr

The irradiance at the eye for a diffused reflection with a radiance L is given by
E_{eye}= L*Area of the diffused surface*Cosθ/r^2

Irradiance for exposure duration of 10 seconds at a distance of 1m from the diffuser and at an angle of viewing of 45^0 is given by
E_{eye}= L*Area of the diffused surface*Cosθ/r^2

E_{eye}=289.44 *0.0019*10*0.707/ (1*1)

E_{eye}=0.388 W/m^2

But the E_{MPE}=0.266 W/m^2

So the diffused reflections are not safe for viewing.

4.4.6 Nominal Hazard Zone for diffused reflections with cylindrical lens:

So the nominal hazard zone for diffused reflections with cylindrical lens is given by (As from equation 13 in chapter 6 of BS:EN 60825-1:1994)

r_{NHD}= √(L*Area of the diffused surface*Cosθ/ E_{MPE})

r_{NHD}=√(289.44 *0.0019*0.707/0.266)

r_{NHD} =1.31 m

So at a zone of around 1.31 m, the safe viewing condition exists.

4.4.7 Nominal hazard zones at different angles of viewing

Area of the image m^2	Angle of viewing at eye θ (degrees)	Cosθ	Irradiance E_{MPE} (W/m^2)	Radiance L (W/m^2-sr)	r_{NHZ} (m)
0.0019	0	1	2.26E-01	2.89E+02	1.559918
0.0019	15	0.9659	2.26E-01	2.89E+02	1.533091
0.0019	30	0.866	2.26E-01	2.89E+02	1.451646
0.0019	45	0.707	2.26E-01	2.89E+02	1.311631
0.0019	60	0.5	2.26E-01	2.89E+02	1.103029

4.5 Summary for 100 seconds viewing conditions:

r_{NOHD} (Without cylindrical lens) m	r_{NOHD} (With cylindrical lens) m	r_{NHZ} (direct diffused reflections) m	r_{NHZ} (diffused reflections with cylindrical lens) m
9270	664	7.79	1.31

5. Summary:

5.1 Direct intrabeam viewing conditions:

Exposure duration t (sec)	H_{MPE} (J/m^2)	E_{MPE} (W/m^2)	r_{NOHD} (Without cylindrical lens) m	r_{NOHD} (With cylindrical lens) m
0.25	0.0035	$7.19*10^5$	3260	234
10	0.001429	$2.86*10^5$	5170	362
100 (Average power used)	3.33*10-[11]	$6.67*10^{-3}$	9270	664

5.2 Diffused reflections viewing condition:

Exposure duration t (sec)	H_{MPE} (J/m^2)	E_{MPE} (W/m^2)	r_{NHZ} (direct diffused reflections) m	r_{NHZ} (diffused reflections with cylindrical lens) m
0.25	0.12	$2.4*10^7$	2.74	0.4648
10	0.0478	$9.56*10^6$	4.34	0.736
100 (Average power used)	$1.13*10^{-9}$	0.226	7.79	1.31

6. Appendix- Derivation of formulae and figures:

6.1 Direct beam viewing without lens:

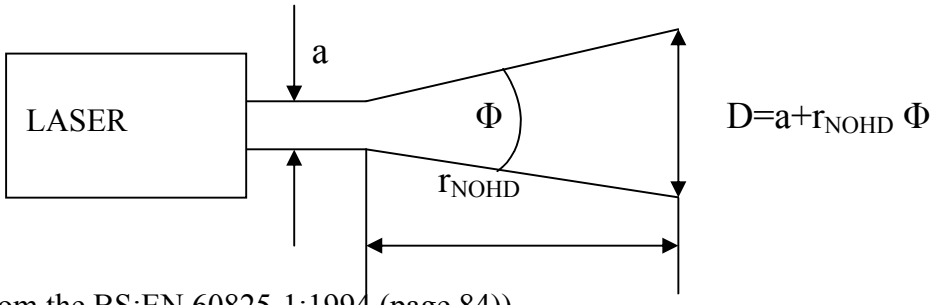

(From the BS:EN 60825-1:1994 (page 84))

$r_{NOHD} = 1/\phi(\sqrt{((4*P_p)/(\pi*E_{MPE}))}-a)$----------(1)

If E_{MPE} is due to the average exposure duration then

$r_{NOHD} = 1/\phi(\sqrt{((4*P_o)/(\pi*E_{MPE}))}-a)$----------(2)

6.2 Direct beam viewing with diverging lens:

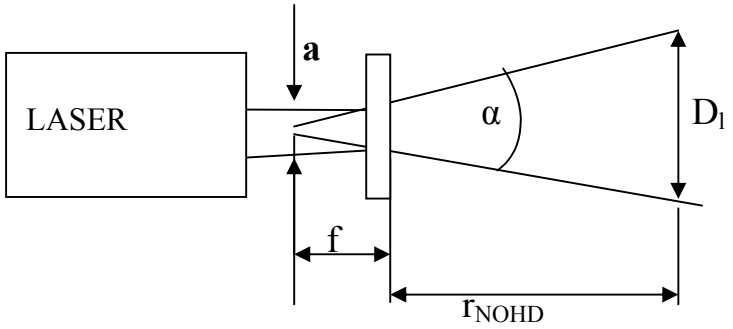

$E_{MPE}=4*P_p/(\pi*D_l*D_l)$

$D_l= \sqrt{(4*P_p)/(\pi*E_{MPE})}$

$Tan\alpha/2=\alpha/2=(D_l/2)/(r_{NOHD}+f)$

$D_l= \alpha*(f+r_{NOHD})$

$\alpha/2=(a/2)/f$

$\alpha=a/f$

$D_l= (a/f)*(f+ r_{NOHD})$----------(3)

$r_{NOHD} = (f/a)(\sqrt{((4*P_p)/(\pi*E_{MPE}))}-f$ ----------(4)

If E_{MPE} is due to the average exposure duration then

$r_{NOHD} = (f/a)(\sqrt{((4*P_o)/(\pi*E_{MPE}))}-f$ ----------(5)

6.3 Diffused reflections without diverging lens:

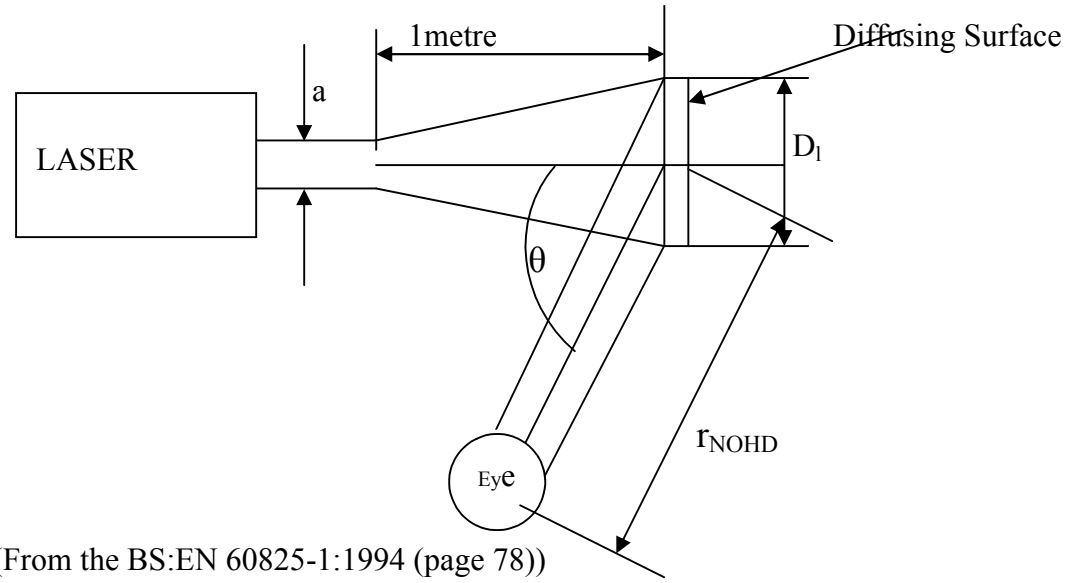

(From the BS:EN 60825-1:1994 (page 78))

$r_{NHZ} = \sqrt{((\rho*P_p \cos\theta)/(\pi* E_{MPE}))}$----------(6)

If E_{MPE} is due to the average exposure duration then

$r_{NHZ} = \sqrt{((\rho*P_o \cos\theta)/(\pi* E_{MPE}))}$----------(7)

6.4 Diffused reflections with diverging lens:

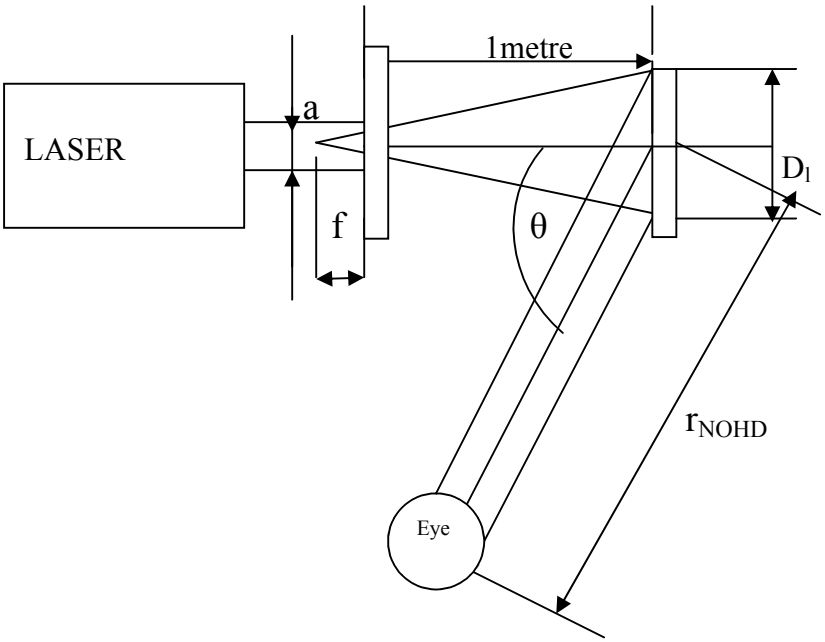

Irradiance E_s on the diffusing surface with average power of laser and cross-sectional area A_s

$E_s = P_p/A_s$----------(8)

Radiance L from the diffuse surface

$L=(\rho * P_p)/(A_s*\pi)$----------(9)

$r_{NHD}=\sqrt{}(L*\text{Area of the diffused surface}*\text{Cos}\theta/ E_{MPE})$----------(10)

If E_{MPE} is due to the average exposure duration then

$E_s = P_o/A_s$----------(11)

$L=(\rho * P_o)/(A_s*\pi)$----------(12)

7. References:

1. BS:EN 60825-1:1994

Appendix: E

Comparison of different grid engine algorithms

Comparison of different grid engine algorithms

A brief introduction regarding the Nyquist, recursive Nyquist and deformation grid was given in Chapter 3 Section 3.3.2. The experimental data from the half-field of view measurements for 100 mm monolith at Re 27400 was used to compare the three different grid algorithms. Generally the higher order grid methods like the recursive Nyquist and the deformation grid are more accurate as they use multiple passes. This again depends on the quality of the data obtained. If the obtained measurement contains spurious vectors, then using higher order grid methods would not produce a high SNR. The experimental data was processed using the three grid methods. The Nyquist grid was a single pass covering an area of 32 × 32 pixels. The recursive Nyquist grid had two passes with an initial grid of 64 × 64 pixels and the vectors from the first pass were used to optimise the next processing pass of 32 × 32 pixels. The deformation grid is a higher order grid with an initial grid of 64 × 64 pixels and the next processing pass is similar to the recursive Nyquist gird. It contains a third processing pass wherein the four corner neighbouring vectors are used to deform the spot in an attempt to eliminate the gradient in the raw image data. This is extremely useful in high shear flows.

The computational time required for the Nyquist grid is the shortest and is almost four times for the recursive Nyquist grid. The deformation grid is the slowest and takes up about ten times the processing time required for a Nyquist grid for a single image process. So for a large sample, the deformation grid processing tends to be very slow. The results from the three grid methods are shown in Figs. 1-4.

From the results there seems to be no difference in the quality of data obtained from the three methods although a higher SNR is expected from higher order grid methods. This might be due to the fact the vectors obtained from the Nyquist grid are good enough and hence improving the obtained vectors further using higher order grid methods does not have any significant effect on the quality of the vectors. Considering the amount of time required to process a deformation grid, it was thought to be the best compromise to use a recursive Nyquist grid in order to process the obtained experimental data. Hence the

recursive Nyquist grid with an initial grid size of 64 × 64 pixels and a final grid of 32 × 32 pixels have been used to process all the experimental data.

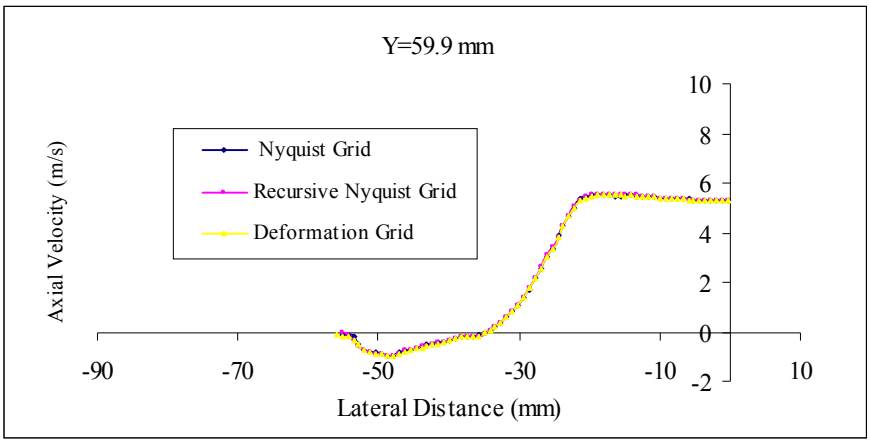

Figure 1: Comparison of axial velocity profiles for 100 mm monolith at Re: 27400 using different algorithms

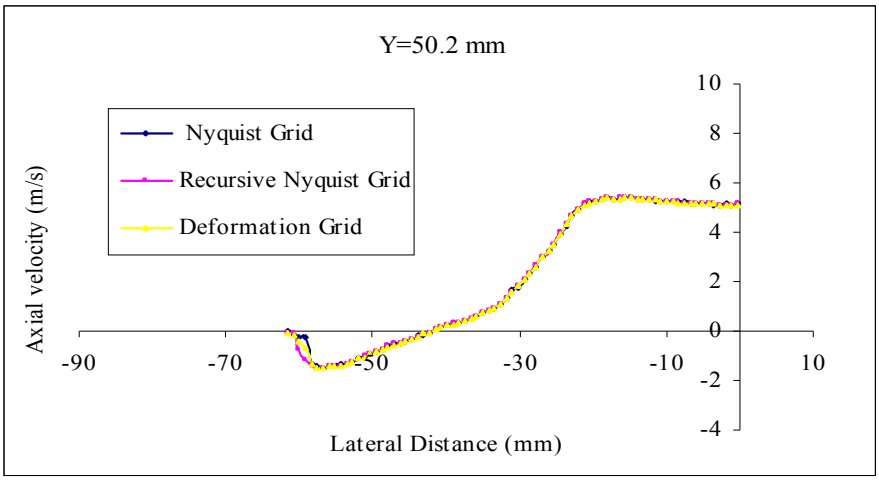

Figure 2: Comparison of axial velocity profiles for 100 mm monolith at Re: 27400 using different algorithms

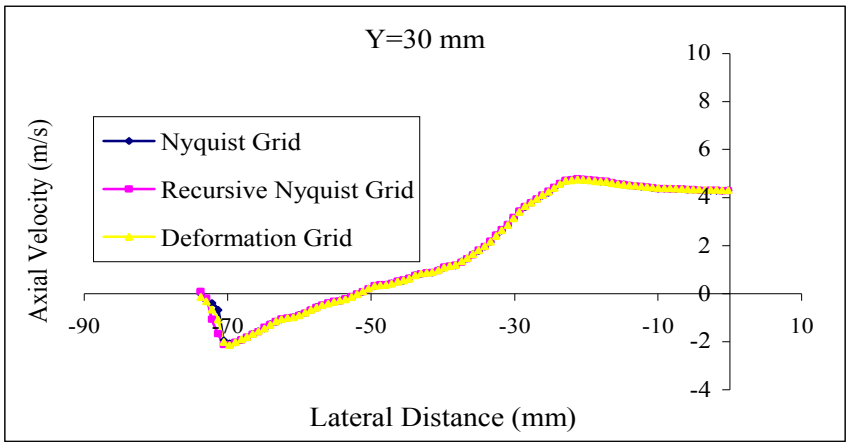

Figure 3: Comparison of axial velocity profiles for 100 mm monolith at Re: 27400 using different algorithms

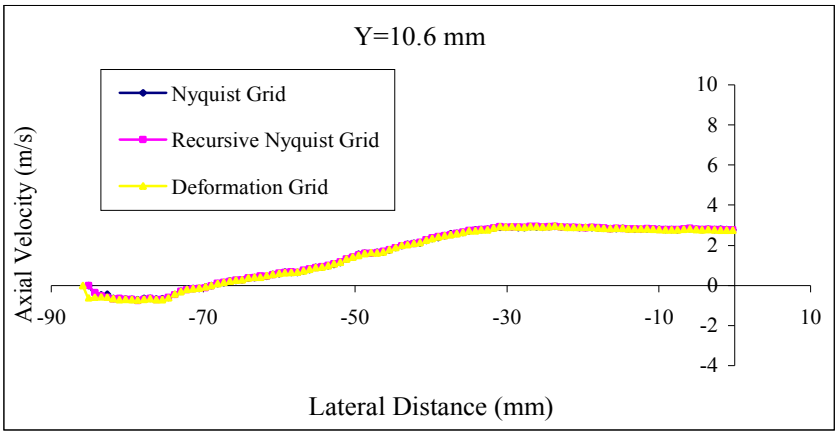

Figure 4: Comparison of axial velocity profiles for 100 mm monolith at Re: 27400 using different algorithms

Appendix: F
User Subroutine poros1.f

User Subroutine poros1.f for the 27 mm monolith

```
C************************************************************************
      SUBROUTINE POROS1(ALI,ALJ,ALK,BTI,BTJ,BTK,POROS)
C     Porous Resistance
C************************************************************************
C-----------------------------------------------------------------------*
C     STAR VERSION 3.26.000                                             *
C-----------------------------------------------------------------------*
      INCLUDE 'comdb.inc'

      COMMON/USR001/INTFLG(100)

      INCLUDE 'usrdat.inc'
      DIMENSION SCALAR(50)
      EQUIVALENCE( UDAT12(001), ICTID )
      EQUIVALENCE( UDAT04(001), CP )
      EQUIVALENCE( UDAT04(002), DEN )
      EQUIVALENCE( UDAT04(005), PR )
      EQUIVALENCE( UDAT04(009), SCALAR(01) )
      EQUIVALENCE( UDAT04(059), U )
      EQUIVALENCE( UDAT04(060), V )
      EQUIVALENCE( UDAT04(061), W )
      EQUIVALENCE( UDAT04(064), UL )
      EQUIVALENCE( UDAT04(065), VL )
      EQUIVALENCE( UDAT04(066), WL )
      EQUIVALENCE( UDAT04(062), VISM )
      EQUIVALENCE( UDAT04(063), VIST )
      EQUIVALENCE( UDAT04(007), T )
      EQUIVALENCE( UDAT04(067), X )
      EQUIVALENCE( UDAT04(068), Y )
      EQUIVALENCE( UDAT04(069), Z )
      EQUIVALENCE( UDAT04(070), XL )
      EQUIVALENCE( UDAT04(071), YL )
      EQUIVALENCE( UDAT04(072), ZL )
C-----------------------------------------------------------------------
C
C    This subroutine enables the user to specify resistance coefficients
C    ALI,ALJ,ALK,BTI,BTJ,BTK and porosity POROS in an arbitrary manner.
C
C    ** Parameters to be returned to STAR: ALI,ALJ,ALK,BTI,BTJ,BTK,POROS
C
C-----------------------------------------------------------------------

C     Sample coding: To specify resistance coefficients as functions
C                    of velocity and porosity as a function of
C                    temperature for porous cells in fluid 2
C
C     IF(IMAT.EQ.2.AND.IPOR.GT.0) THEN
C       ALI=100.*U**0.2
C       BTI=10.
C       ALJ=100.*V**0.2
C       BTJ=10.
```

```
C       ALK=0.
C       BTK=1.E10
C       POROS=1.-0.1*T/TREF
C     ENDIF
C-------------------------------------------------------------------------C
C           DIMENSION ICGMAP(1:NCTMXU*2)
C      SAVE ICGMAP
            REAL XWQ,BTIO,FQ,k,f,ANGR, YBIGST,XWP,XWO
      DIMENSION BTID(100)
      COMMON UME(100),VME(100)
C           OPEN(86,FILE='Permeability',form='formatted',Status='Unknown')
C           Write(86,61)ICNO,BOB,BTI,ANG
C61     format('',I5,2X,E15.7,2X,E15.7,2X,F4.1)



C           Alpha and Beta values for the 27 mm monolith


      IF(ICTID.EQ.4)THEN
      ALI=40.806
      BTI=609.48
      ALJ=1000000
      BTJ=1000000
      ALK=1000000
      BTK=1000000
      BTIO=609.48
      POROS=0.7744

C     GO TO 100
            END IF



      IF(ITER.LE.2)THEN
      DO 44 ICNO=1,99,1
      UME(ICNO)=0.1
      VME(ICNO)=0.1
44    CONTINUE
            GO TO 100
            END IF
C           CRITIR is the fixed critical angle of attack
             CRITIR=2*3.141592564*81/360

C           Entrance effect in the high Reynolds region

      IF(ICTID.EQ.4) THEN
      IF(Y.LE.0.0825)THEN
      FQ=(Y*1000)/1.375
      ICNO=INT(FQ)+1
      BOB=ABS(VME(ICNO))
      BIL=ABS(UME(ICNO))
      f=sqrt(BOB**2+BIL**2)
      g=BIL/0.7744
            Re=(DEN*g*0.001118)/(1.81E-05)
```

```
      ANG=ATAN(BOB/BIL)
C           WRITE(6,*)'ICNO IS',ICNO

      IF(ANG.GT.CRITIR)THEN
      BOB=BIL*TAN(CRITIR)
      END IF

      BTID(ICNO)=(0.5*DEN*f*f)*0.67473*((BOB/f)**2.466)*(Re**0.0756)

       BTI=BTIO+(BTID(ICNO)/(0.02741*U))
C           WRITE(6,*)'ICNO IS',ICNO,BTI

      END IF

C     Near wall region
       IF(Y.GT.0.0825)THEN
       YBIGST=0.0075*(1-0.94)/(1-0.94**20)
       XWO=2*YBIGST-0.12*(Y-0.0825)
       XWP=XWO/(YBIGST*(1+1/0.94))
       XWQ=LOG(XWP)/LOG(0.94)
       IWANT=NINT(XWQ)
              ICNO=IWANT+60
C        WRITE(6,*)'ICNO IS',ICNO
        BOB=ABS(VME(ICNO))
      BIL=ABS(UME(ICNO))
      f=sqrt(BOB**2+BIL**2)
      g=BIL/0.7744
     Re=(DEN*g*0.001118)/(1.81E-05)
      ANG=ATAN(BOB/BIL)

      IF(ANG.GT.CRITIR)THEN
      BOB=BIL*TAN(CRITIR)
      END IF

      BTID(ICNO)=(0.5*DEN*f*f)*0.67473*((BOB/f)**2.466)*(Re**0.0756)

       BTI=BTIO+(BTID(ICNO)/(0.02741*U))

          END IF


59       END IF

100   RETURN
     END

C
```